

# The role of turbulence on the bubble-particle collision – An experimental study with particle tracking methods

Dipl.-Ing. Anna-Elisabeth Sommer

Born on: 19.07.1990 in Sömmerda, Germany

## Dissertation

to achieve the academic degree

## Doktoringenieur (Dr.-Ing.)

First referee

Prof. Dr. rer. nat. et Ing. habil. Kerstin Eckert

Second referee

Prof. Dr.-Ing. Michael Schlüter

Prof. Stephen Neethling

Submitted on: 14.01.2022

Defended on: 06.05.2022

Big whirls have little whirls,  
that feed on their velocity.  
And little whirls have littler whirls,  
and so on to viscosity.

---

*Lewis Fry Richardson,  
British scientist*

## Acknowledgments

This thesis was written while I was working as a research assistant at the Helmholtz-Zentrum Dresden-Rossendorf (HZDR) within the framework of the European Union's Horizon 2020 research and innovation program FineFuture under grant agreement No 821265. Throughout the writing of this dissertation I have received a great deal of support and assistance. Therefore, I sincerely thank all those who have contributed in various ways to the successful outcome of this work.

On the 6th of May 2022, I have successfully passed my doctoral defense and express my gratitude to all members of the doctoral committee - Prof. Uwe Hampel, Prof. Kerstin Eckert, Prof. Michael Schlüter, Prof. Stephen Neethling and Prof. Jochen Fröhlich.

I would first like to thank my supervisors, Prof. Kerstin Eckert and Dr. Sascha Heitkam, whose expertise was invaluable in formulating the research questions and methodology. They always found time to give me helpful advice and discuss the current research results. Your insightful feedback pushed me to sharpen my thinking and brought my work to a higher level.

Additionally, I would like to thank Dr. Pablo Brito-Parada, Dr. Tom Leadbeater, Michael Van Heerden, Thomas Richter, Dr. Katie Cole, Prof. Stephen Neethling and Dr. Angus Morrison for their technical and scientific support before, during and after the Positron Emission Particle Tracking (PEPT) measurement campaigns at the iThemba LABS, South Africa. Thanks are also due to Kilian Ortmann for his calm and patient support next to PEPT scanner, finding the radioactive-labeled tracer particles and convincing them to collide with the stagnant bubble.

I am also grateful for the support and friendship from the varied members of the Chair of transport processes at interfaces, especially Peggy Jähnigen for her laboratory assistance, Teresa Schurz for her administrative support, Heiko Kunadt and Bernd Nowak for their precise mechanical productions. Further, I express my gratitude to Dr. Tobias Lappan, Aleksandr Bashkatov, Milad Eftekhari, Sahil Hossain, Mengyuan Huang and Anahita Keshmiri not only for their technical help and proofreading, but also their great friendship.

Warm thanks to Silvia Scheinert, Pengyu Shi and Colin Marquardt for their careful proofreading of this dissertation.

I would not have been able to do this PhD without the fantastic support of all of my friends and family. *Meinem Ehemann und meinen Eltern danke ich ganz besonders, die mich auf dem Weg zu meiner Promotion begleitet und mich dabei moralisch unterstützt haben. Dankeschön!*

## Abstract

The analysis of collisions between particles and bubbles in a turbulent flow is a fundamental problem of high technological relevance, e.g. for the separation of valuable mineral particles by froth flotation. That relevance contrasts with an apparent lack of experimental data and insights into this collision process. A major issue is the limitation of available measurement techniques to directly observe the collisions between particles and bubbles.

In this dissertation, novel methodologies are developed to measure the interaction between bubbles and particles under defined hydrodynamic conditions. These methodologies comprise particle tracking techniques such as 4D PTV and PEPT to triangulate the Lagrangian particle trajectories in the vicinity of a bubble and classify those which are colliding.

In two experimental setups, these techniques are applied to investigate the bubble-particle interaction in turbulent flows. In a bubble column, turbulence is generated in the wake of a freely rising bubble chain, whereas in a water channel, a fluid passing through grid produces a turbulent flow upstream of a stagnant bubble. Accordingly, the turbulent flow field around these bubbles is characterized by TPIV.

Firstly, the influence of the bubble wake on the bubble-particle collision is analyzed for both experimental setups with 4D PTV. It is shown that the collision of fluorescent fine particles take place not only at the leading edge but also at the trailing edge of the bubble, independently of the experimental setup. These findings are correlated with the measured TKE and dissipation rates around the bubble and in the bubble wake. Subsequently, the experimental TKE and dissipation rates are applied to existing models for collision frequency, and their predictions are discussed.

Secondly, the impact of the turbulent liquid flow on the collision between a stagnant bubble and model particles is studied for a range of turbulent length scales. Besides the investigation in a dilute solid suspension, the bubble-particle interaction is also examined in a dense flow with PEPT. PEPT has the potential to measure suspensions with a high solid fraction, which could not be achieved with optical particle tracking methods. For the detection of individual particles with PEPT, radioactive tracer particles were designed to represent the bulk particles. The trajectories of the labeled particles are used to determine the average particle distribution in the turbulent field and describe the bubble-particle interactions.

Overall, the developed methodologies in this dissertation provide a framework to investigate directly the collision between particles and bubble in a turbulent flow. The gained experimental validation data allows to verify existing collision models and to advance our understanding of the role of turbulence in froth flotation.

## Zusammenfassung

Die Analyse von Kollisionen zwischen Partikeln und Blasen in einer turbulenten Strömung ist ein grundlegendes Problem von hoher technologischer Relevanz, z. B. für die Abtrennung wertvoller Mineralpartikel durch Schaumflotation. Dieser Relevanz steht ein Defizit an experimentellen Daten und Erkenntnissen über den Kollisionsprozess gegenüber. Ein Hauptproblem ist die geringe Anzahl der verfügbaren Messtechniken zur direkten Beobachtung der Kollisionen zwischen Partikeln und Blasen.

Daher besteht das Ziel dieser Dissertation darin, neue Methoden zu entwickeln, um die Wechselwirkung zwischen Blasen und Partikeln unter definierten hydrodynamischen Bedingungen zu messen. Diese Methoden beruhen auf der Verfolgung von einzelnen Partikeln mit 4D Particle Tracking Velocimetry (PTV) und Positron Emission Particle Tracking (PEPT), um die Lagrangeschen Partikeltrajektorien in der Nähe einer Blase zu bestimmen und die kollidierenden Partikel zu klassifizieren.

In zwei Versuchsaufbauten werden diese Messmethoden angewandt, um die Wechselwirkung zwischen Blasen und Partikeln in turbulenten Strömungen zu untersuchen. In einer Blasensäule wird die Turbulenz im Nachlauf einer frei aufsteigenden Blasenkette erzeugt, während in einem Wasserkanal die Turbulenz durch die Umströmung eines Gitters produziert wird. In beiden Fällen wird das vorhandene turbulente Strömungsfeld um die Blasen mittels Tomographic Particle Image Velocimetry (TPIV) charakterisiert.

Zunächst wird der Einfluss des Blasennachlaufs auf die Blasen-Partikel-Kollision für beide Versuchsaufbauten mit dem 4D-PTV-Verfahren analysiert. Es wird gezeigt, dass in beiden Versuchsanordnungen die Kollision von feinen Partikeln nicht nur an der Vorderseite, sondern auch an der Hinterseite der Blase stattfindet. Diese Ergebnisse werden mit der gemessenen turbulenten kinetischen Energie und der Dissipationsrate um die Blase korreliert. Anschließend werden die experimentell ermittelte turbulente kinetische Energie und Dissipationsrate genutzt, um die Kollisionsfrequenz vorherzusagen. Dafür werden bestehende Modelle angewendet und deren Vorhersagen den experimentellen Ergebnissen gegenübergestellt.

Weiterhin wird der Wasserkanal genutzt, um den Einfluss der turbulenten Flüssigkeitsströmung auf die Kollision zwischen einer stagnierenden Blase und den Modellpartikeln zu verdeutlichen. Neben der Untersuchung in einer verdünnten Feststoffsuspension wird auch die Blasen-Partikel-Wechselwirkung in einer dichten Strömung mit dem PEPT-Verfahren untersucht. Das PEPT-Verfahren hat das Potenzial, Suspensionen mit einem hohen Feststoffanteil zu messen, was mit optischen Trackingverfahren, wie 4D-PTV, nicht möglich ist. Für den Nachweis einzelner Partikel mit dem PEPT-Verfahren wurden radioaktive Tracerpartikel entwickelt, welche repräsentativ für die Modellpartikeln sind. Die Trajektorien der markierten Partikel werden verwendet, um die durchschnittliche Partikelverteilung im turbulenten Feld zu bestimmen und die Blasen-Partikel-Wechselwirkung zu beschreiben.

Insgesamt bieten die entwickelten Methoden eine Möglichkeit die Kollision zwischen Partikeln und Blasen in einer turbulenten Strömung direkt zu untersuchen. Die gewonnenen experimentellen Daten ermöglichen es, bestehende Kollisionsmodelle zu überprüfen und das Verständnis über die Rolle von Turbulenzen in der Schaumflotation zu verbessern.

# Contents

<b>1. Introduction</b>	<b>1</b>
1.1. Motivation . . . . .	1
1.2. Objectives . . . . .	3
1.3. Structure of the thesis . . . . .	3
<b>2. Background on turbulent multiphase flows</b>	<b>5</b>
2.1. Turbulent flow . . . . .	5
2.1.1. Governing equations of a fluid flow . . . . .	5
2.1.2. Energy cascade . . . . .	7
2.1.3. Grid turbulence . . . . .	8
2.2. Bubble dynamics . . . . .	9
2.2.1. Bubble formation . . . . .	9
2.2.2. Bubble shape and motion . . . . .	11
2.2.3. Bubble wake . . . . .	14
2.2.4. Surface mobility . . . . .	16
2.3. Particle dynamics . . . . .	17
2.3.1. Motion of a single particle . . . . .	17
2.3.2. Dense particle suspension . . . . .	19
2.4. Bubble-particle collision . . . . .	21
2.4.1. Numerical investigations . . . . .	21
2.4.2. Experimental investigations . . . . .	24
<b>3. Materials and Methods</b>	<b>26</b>
3.1. Experimental setups . . . . .	26
3.1.1. Freely rising bubble chain in a bubble column . . . . .	26
3.1.2. Turbulent flow upstream of a stagnant bubble in a water channel . . . . .	27
3.2. Tomographic Particle Image Velocimetry (TPIV) . . . . .	29
3.2.1. Principle of TPIV . . . . .	29
3.2.2. Measurement setup and tracer particle system . . . . .	30
3.2.3. Data analysis . . . . .	32

3.2.4. Uncertainty analysis . . . . .	36
3.3. 4D Particle Tracking Velocimetry (PTV) . . . . .	40
3.3.1. Principle of PTV and Shake-the-box (STB) . . . . .	40
3.3.2. Measurement setup and particle systems to model mineral particles . .	41
3.3.3. Identification of particle trajectories colliding with bubbles . . . . .	43
3.4. Positron Emission Particle Tracking (PEPT) . . . . .	46
3.4.1. Principle of PEPT . . . . .	46
3.4.2. Measurement setup and radioactive tracer particles . . . . .	47
3.4.3. Data analysis . . . . .	49
3.4.4. Uncertainty analysis . . . . .	51
3.5. Discussion and Conclusion . . . . .	52
<b>4. Flow characterization measured with shadowgraphy and TPIV</b>	<b>55</b>
4.1. Introduction . . . . .	55
4.2. Freely rising bubble chain in the bubble column . . . . .	55
4.2.1. Shape and motion of bubbles . . . . .	56
4.2.2. Flow field around bubbles . . . . .	58
4.3. Stagnant bubbles in the turbulent water channel . . . . .	62
4.3.1. Turbulent flow field in the water channel . . . . .	63
4.3.2. Shape and motion of bubbles . . . . .	66
4.3.3. Flow field around bubbles . . . . .	68
4.4. Discussion and Conclusion . . . . .	70
<b>5. Particle motion in the vicinity of bubbles measured with 4D PTV and PEPT</b>	<b>75</b>
5.1. Freely rising bubble chain measured with 4D PTV . . . . .	75
5.1.1. Verification of collision criteria . . . . .	76
5.1.2. Bubble-particle collision . . . . .	78
5.1.3. Interaction of the flow field on the trailing edge collision . . . . .	79
5.1.4. Comparison of the collision frequency with available models . . . . .	83
5.1.5. Limitations on the detection of the bubble-particle collision . . . . .	85
5.2. Stagnant bubbles in the water channel measured with 4D PTV . . . . .	87
5.2.1. Bubble-particle collision . . . . .	87
5.2.2. Interaction of the turbulent flow field on the collision phenomena . . .	89
5.2.3. Comparison of the collision frequency with available models . . . . .	94
5.2.4. Limitations on the detection of the bubble-particle collision . . . . .	96
5.3. Stagnant bubbles in the water channel measured with PEPT . . . . .	97
5.3.1. Particle distribution in the channel cross-section . . . . .	97
5.3.2. Radial particle displacement in the bubble vicinity . . . . .	99
5.3.3. Bubble-particle collision . . . . .	101
5.3.4. Limitations on the detection of the bubble-particle collision . . . . .	102
5.4. Discussion and Conclusion . . . . .	104
<b>6. Concluding remarks</b>	<b>107</b>
6.1. Conclusions . . . . .	107

6.2. Outlook . . . . .	110
<b>A. Appendix</b>	<b>112</b>
A.1. Physical properties of the model particle systems . . . . .	112
A.2. Measurement of the contact angle with the Washburn method . . . . .	112
A.3. Specifications of the calibration targets . . . . .	114
A.4. Collision models . . . . .	114
A.5. Calculation of the values of the box plot . . . . .	119
<b>Bibliography</b>	<b>120</b>



# 1. Introduction

## 1.1. Motivation

The collision between fluid objects (drops and bubbles), and particles in turbulent flows belongs to the class of generic problems with widespread occurrence in both nature [1–3] and technology [4–8]. One example is froth flotation, which is the most important and widely used operation in mineral processing to separate valuable ore particles from gangue materials. Billions of tonnes of ores are beneficiated by froth flotation to extract base and critical raw materials such as particles bearing copper and rare-earth elements [9, 10]. Thus, even small enhancements of this separation process will lead to significant economic benefits.

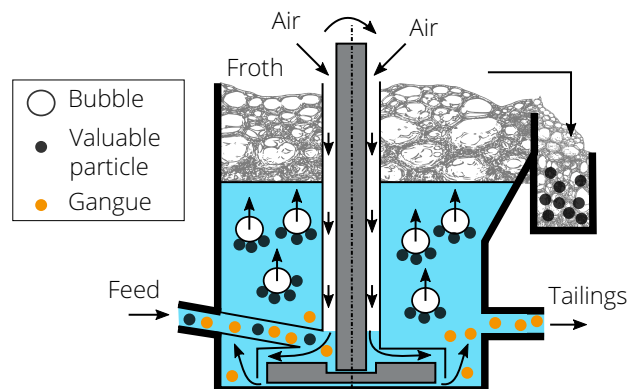
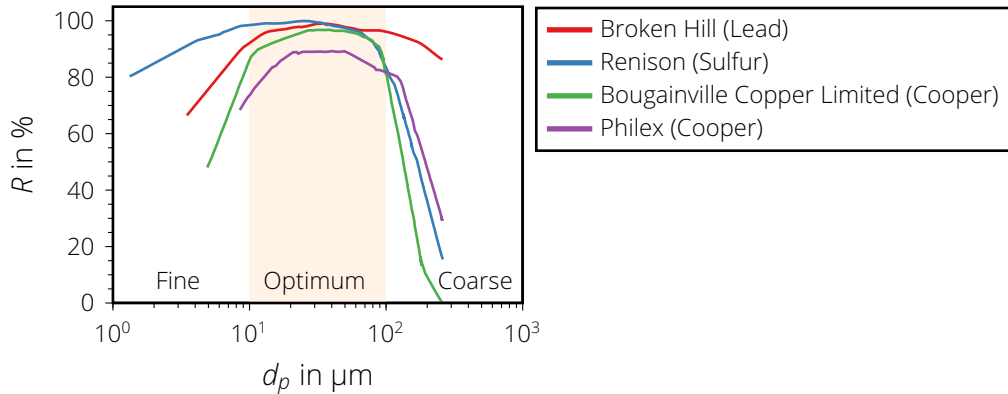


Figure 1.1. Sketch of a flotation cell.

This separation process takes place in a flotation cell (Fig. 1.1) where the multiphase flow is e.g. mechanically mixed by an impeller to agitate the slurry and disperse the air bubbles. During the attachment process, due to hydrodynamic conditions in the cell, hydrophobized particles collide with a bubble. Together, they form a stable three-phase contact line on the fluidic interface during the attachment. The formed particle-bubble aggregate rises into the froth, while the undesired hydrophilic gangue material remains in the pulp. The froth is skimmed to obtain the concentrate of the valuable particles. Only if the detaching forces, e.g. due to turbulent stresses, are higher than the attaching forces, the particle detaches from

the bubble again. To sum up, the success of the process, defined as recovery, depends on both the surface chemistry for the hydrophobization of particles and the hydrodynamics for an encounter between bubble and particle [11].



**Figure 1.2.** Recovery,  $R$ , by particle size,  $d_p$ , from industrial flotation of a variety of different sulfide ores. Optimal particle size for a high recovery lies between  $10\ \mu\text{m}$  and  $100\ \mu\text{m}$ . For finer and coarser particle sizes, the recovery suddenly drops (adapted from [12]).

The optimal particle size for a high recovery lies between  $10\ \mu\text{m}$  and  $100\ \mu\text{m}$ . For smaller particle sizes, the recovery suddenly drops as shown in Fig. 1.2 [13–15]. Finer particles are less likely to exhibit bubble-particle collisions. Consequently, these fine particles are mostly lost in the tailings [13, 14, 16]. One reason for that is their small particle mass, leading to a small inertia. As illustrated in Fig. 1.3a, intermediate particles deviate from the fluid streamlines through factors e.g. interception, inertial, gravitational and turbulent effects [17]. But in the case of fine particles (Fig. 1.3b), they tend to follow the fluid streamlines because of their low inertia resulting in a low collision probability. Therefore, the process of recovery of this type of particles has a low efficiency [12, 14, 15, 18–20].

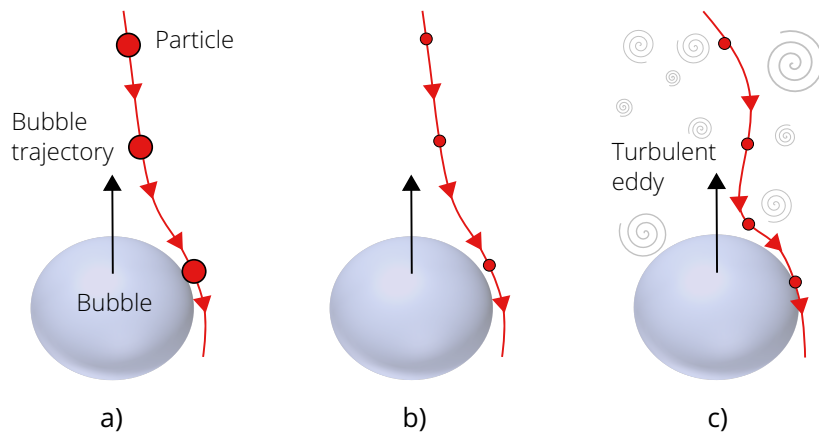


**Figure 1.3.** Bubble-particle collision for a) intermediate and b) fine particle sizes. c) Enhancement of the collision between fine particles and bubbles due to turbulent eddies.

One approach to enhance the collision between fine particles and bubbles is to increase

the shear rate (Fig. 1.3c) [7, 21]. In recent years, a novel flotation cell design has been developed to expose the particles to higher shear rates as such as the Concorde Cell [21] or the REFLUX Flotation Cell [22]. But research on a direct observation of the collision process under a high shear rate to get a deeper understanding of the effect is still lacking. Mainly, the overall recovery of the novel flotation cell designs was measured and their improved performance was observed [12, 20].

The missing insight into this topic is caused by the restrictions in measurement technique to directly observe the collision between particles and bubble [23, 24]. Thus, experimental validation data for the developed collision models are limited [24]. The validation data rely mainly on direct numerical simulation (DNS), allowing the primary variables and the collision to be controlled with high accuracy [25–29]. Due to the high computational effort required, DNS is however only applicable to a certain range of Reynolds numbers. Previous experimental studies applied high-speed imaging methods to record particle trajectories colliding with a stagnant bubble in quiescent flow [17, 30–34]. However, from these experimental results, no conclusions can be drawn on the collision mechanisms between particles and bubbles in turbulent flows.

## 1.2. Objectives

It is desired to develop a direct way to measure the interaction between bubbles and particles under defined hydrodynamic conditions. The gained experimental validation data would allow to verify existing collision models and to advance our understanding of the role of turbulence in froth flotation. Therefore, this thesis aims to answer the following questions:

- Q.1 How to measure directly the collision between bubbles and particles?
- Q.2 How to generate a generic turbulent flow which influences the collision between bubbles and particles?
- Q.3 Which role does the turbulence in the bubble wake play on the collision between bubbles and particles?
- Q.4 How can different turbulent length scales upstream of a bubble influence the collision between bubbles and particles?
- Q.5 Can the well-known collision models proposed by Saffman et al. [35], Abrahamson [36] and Kostoglou et al. [37] predict the experimentally detected collision frequencies between bubbles and particles?

## 1.3. Structure of the thesis

In order to investigate the questions raised in Sec. 1.2, the dissertation is organized as follows. Chapter 2 introduces the basic concepts of turbulent multiphase flows. Starting with a brief overview of each phase, this chapter provides a discussion of hydrodynamic effects on the bubble-particle collision in froth flotation. The lack of insight into this topic due to the limited measurement techniques available is again highlighted.

Chapter 3 attempts to fill this gap in knowledge by describing the novel methodologies, advanced in this dissertation. These methodologies deal with the experimental investigation of the bubble-particle interaction in a turbulent flow. This chapter is subdivided into the designed generic experimental setups (Sec. 3.1) and the applied measurement techniques (Sec. 3.2 - Sec. 3.4). The experimental setups comprise a freely rising bubble chain in a bubble column and a stagnant bubble in a water channel. The bubble-particle interaction in these two setups are analyzed with a combination of Tomographic Particle Image Velocimetry (TPIV), 4D Particle Tracking Velocimetry (PTV) and Positron Emission Particle Tracking (PEPT). In particular, the flow field in the vicinity of the bubble is characterized with TPIV. 4D PTV and PEPT are applied to triangulate the particle trajectories, to classify the colliding particles and to calculate the collision frequency.

Chapter 4 and Chapter 5 summarize and discuss the results obtained by the proposed methodologies. Chapter 4 gives a framework of the existing turbulent flow field in the bubble column and in the water channel. This insight provides a basis to understand the motion of the particles in the vicinity of the bubbles. In Sec. 5.1, the interaction between fine particles and freely rising bubbles is analyzed in the bubble column with 4D PTV. The defined collision criteria are proven and the population of the collision positions is described. The thereby discovered phenomena of the trailing edge collision is tracked down to the turbulent parameters in the bubble wake. While Sec. 5.1 focuses on a freely rising bubble chain, Sec. 5.2 considers a stagnant bubble in the turbulent flow of the water channel. The analysis of the bubble-particle interactions with 4D PTV is in-line with the previous section. Until now, the particle suspension had to be diluted to be applicable to the optical 4D PTV. However, in Sec. 5.3, PEPT is employed to investigate the bubble-particle interaction in a dense turbulent flow. Chapter 6 summarizes the essential findings of the thesis and outlines open questions for following research.

In the following publications, partial results of this dissertation are published:

- [38]: A.-E. Sommer, M. Nikpay, S. Heitkam, M. Rudolph, and K. Eckert. "A novel method for measuring flotation recovery by means of 4D particle tracking velocimetry". In: *Minerals Engineering* 124 (2018), pp. 116–122.
- [39]: A.-E. Sommer, K. Ortmann, M. V. Heerden, T. Richter, T. Leadbeater, K. Cole, S. Heitkam, P. Brito-Parada, and K. Eckert. "Application of Positron Emission Particle Tracking (PEPT) to measure the bubble-particle interaction in a turbulent and dense flow". In: *Minerals Engineering* 156 (2020), p. 106410.
- [40]: A.-E. Sommer, H. Rox, P. Shi, K. Eckert, and R. Rzehak. "Solid-liquid flow in stirred Tanks: "CFD-grade" experimental investigation". In: *Chemical Engineering and Science* (2021), p. 116743.
- [41]: A.-E. Sommer, S. Heitkam, and K. Eckert. "Particle-bubble collisions in a turbulent flow: an experimental study with 4D Particle Tracking Velocimetry and Tomographic Particle Image Velocimetry". Submitted to *Journal of Fluid Mechanics* (2021).

## 2. Background on turbulent multiphase flows

In froth flotation, valuable minerals are separated from gangue materials based on their physicochemical properties. The efficiency of this process is not only controlled by surface chemistry, but also by the hydrodynamics in the flotation cell. The flow generated from the rotor-stator in a mechanical flotation cell enhances the suspension of the solid particles, the dispersion of the air and the interaction between bubbles and particles [7, 42]. The resulting multiphase flow is characterized by the motions of the liquid, gas and solid phases. Each individual phase contributes to the dominating fluid flow in a flotation cell and only a smooth interaction between them leads to a high recovery rate of the valuable mineral particles. These fundamental processes were investigated over decades by many researchers [43–49]. Therefore, this chapter is only a brief overview to describe the basic concepts used in this thesis and does not claim for completeness. In particular, this chapter introduces the basic concepts of a turbulent multiphase flow which dominates the hydrodynamics in a flotation cell. The individual phases are discussed separately, in the form of the turbulent flow, the bubble and particle dynamics. At the end, the influence of the hydrodynamics on the collision process between bubbles and particles is presented based on previous experimental and numerical investigations.

### 2.1. Turbulent flow

#### 2.1.1. Governing equations of a fluid flow

In general, the incompressible fluid flow,  $u_i$ , is described by continuity (Eq. 2.1) and Navier-Stokes equations (NSE) of motion (Eq. 2.2):

$$\frac{\partial u_i}{\partial x_i} = 0, \quad (2.1)$$

$$\underbrace{\frac{Du_i}{Dt}}_{\text{material derivative}} = \underbrace{\frac{\partial u_i}{\partial t}}_{\text{change of velocity with time}} + \underbrace{u_j \frac{\partial u_i}{\partial x_j}}_{\text{convective term}} = \underbrace{-\frac{1}{\rho_L} \frac{\partial p}{\partial x_i}}_{\text{pressure force}} + \underbrace{\nu \frac{\partial^2 u_i}{\partial x_j^2}}_{\text{viscous force}} + \underbrace{F_i}_{\text{body force}}. \quad (2.2)$$

The NSE is the application of Newton's second law of motion to an infinitesimal element at position,  $x_i$ , of an incompressible Newtonian fluid acting upon gravity as the only body force,  $F_i$  [44]. The incompressible Newtonian fluid is characterized by its density,  $\rho_L$ , and constant kinematic viscosity,  $\nu$ . On the left side of Eq. 2.2, the material derivative accounts for changes of the moving fluid. The terms on the right side show the pressure force, viscous force and body force acting on the fluid element, where  $p$  represents the static pressure.

To estimate the relative importance of the inertial to the viscous forces, the Reynolds number,  $Re$ , is used

$$Re = \frac{LU_0}{\nu}, \quad (2.3)$$

where  $L$  denotes the characteristic length and  $U_0$  the approaching velocity. If a flow reaches a Reynolds number beyond a certain critical Reynolds number, a laminar flow becomes turbulent.

This turbulent flow is specified by its chaotic and diffuse nature, and consists of many different scales, named eddies. To describe these complex motions, statistical techniques are applied in the form of the Reynolds decomposition [50], as illustrated in Fig. 2.1a. Here, the instantaneous velocity field component,  $u_i$ , is divided into its mean,  $\bar{u}_i$ , and fluctuation component,  $u'_i$ , by

$$u_i = \bar{u}_i + u'_i. \quad (2.4)$$

Several averaging methods are used to define the means that are related to  $\bar{u}_i$ . For example, the time-average over a time interval,  $T$ , is defined by

$$\bar{u}_{T,i} = \frac{1}{T} \sum_{t=0}^T u_i(t). \quad (2.5)$$

The governing equations of these instantaneous fluid motions, named Reynolds-averaged Navier–Stokes equations (RANS), are derived from the application of the Reynolds decomposition (Eq. 2.4) in the NSE (Eq. 2.2),

$$\frac{D\bar{u}_i}{Dt} = -\frac{1}{\rho_L} \frac{\partial \bar{p}}{\partial x_i} + \frac{\partial}{\partial x_j} \left( \nu \frac{\partial \bar{u}_i}{\partial x_j} - \overbrace{u'_i u'_j}^{\text{Reynolds stress term}} \right) + \bar{F}_i. \quad (2.6)$$

In appearance, the RANS equations and the NSE equations are the same, except the Reynolds stress term,  $R_{ij} = -\overline{u'_i u'_j}$ , resulting from the fluctuating velocity field. The Reynolds stress term poses the challenge of the numerical solution of the RANS equations, described by the closure problem. The number of unknown variables exceeds the available RANS equations. To close the system of equations, turbulent models are needed [40].

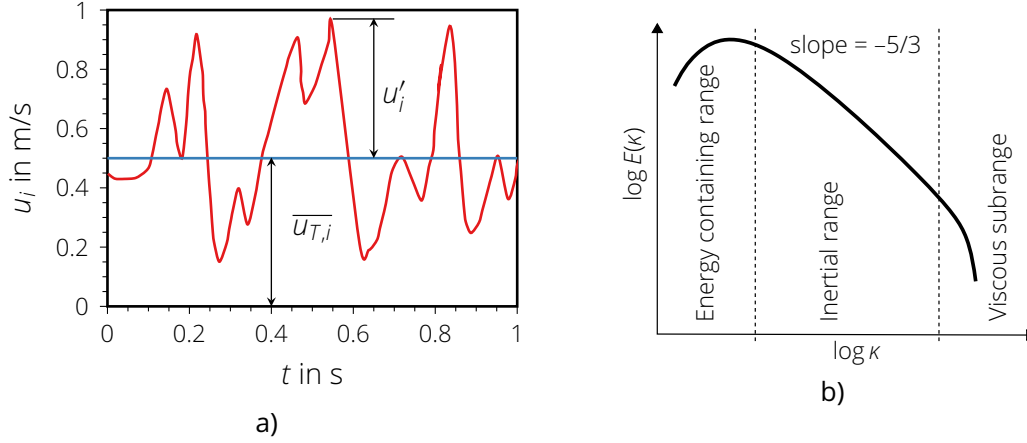


**Figure 2.1.** Schematic illustrations of a turbulent flow. a) Instantaneous velocity field component,  $u_i$ , by time,  $t$ , to explain the Reynolds decomposition (Eq. 2.4). Meaning, the instantaneous velocity field component is divided into its time-average,  $\overline{u_{T,i}}$ , and fluctuation component,  $u'_i$  (adapted from [51]). b) Spatial power spectrum of the energy cascade showing the containing turbulent kinetic energy (TKE) for each eddy size in the form of its wavenumber,  $\kappa$  (adapted from [52]).

### 2.1.2. Energy cascade

Turbulence is sustained by a continuous energy supply because turbulent kinetic energy (TKE) dissipates rapidly by viscosity from mechanical into thermal energy. In this process, many differently sized eddies are formed containing a varying amount of energy. The transfer of the TKE from the largest to the smallest eddies is described by an energy cascade. Fig. 2.1b shows a schematic spatial power spectrum of the energy cascade, representing the containing TKE of each eddy length scale,  $l_e$ , denoted by its wavenumber,

$$\kappa = \frac{2\pi}{l_e}. \quad (2.7)$$

In general, the power spectrum is a discrete-time Fourier transformation of the fluctuation component,  $u'_i(x_i, t)$ . Meaning, the discrete-time Fourier transforms the signal of the fluctuation component at a given point,  $x_i$ , from the time,  $t$ , into the frequency domain,  $f_e$ . The obtained frequencies can be converted in the spatial power spectrum by applying Taylor's frozen turbulence hypothesis,

$$\kappa = \frac{2\pi}{|\overline{U}|} f_e. \quad (2.8)$$

This assumption is valid as long as the relative turbulence intensity,  $U'$ , is small compared to the averaged velocity field,  $\overline{U}$  ( $|U'| \ll |\overline{U}|$ ) [53].

Through fluid shear, friction, buoyancy, or external forces, TKE is produced at the largest length scales - the integral length scales,  $\Lambda$ . These length scales correspond to the dimensions of the turbulence-generating system as for example the stirrer in a flotation cell [7]. In the inertial range, the TKE is transferred into smaller scales, due to the break up of the unstable large eddies into smaller eddies. If the smallest eddies reach the Kolmogorov length scale,  $\eta$ ,

their TKE dissipates by viscosity from mechanical into thermal energy [54].

In the energy containing range of the power spectrum, the eddy scales are anisotropic. A universal form does not exist because the length scales and their containing TKE depend strongly on the turbulence generating system. In contrast, the eddy scales in the inertial and viscous range are statistically isotropic and are determined by the viscous dissipation. Therefore, the turbulent scales in these ranges can be approximated in the following universal forms using the hypothesis of Kolmogorov [55]. In the inertial range, the power spectrum can be estimated as

$$E = C\varepsilon^{2/3} \kappa^{-5/3}, \quad (2.9)$$

with a value of  $C = 2$  which fits for a wide range of experimental studies [43]. The viscous range is characterized by the smallest eddy scale, named Kolmogorov scale

$$\eta = \left( \frac{\nu^3}{\varepsilon} \right)^{1/4}, \quad (2.10)$$

which depends only on  $\varepsilon$  the dissipation rate and  $\nu$  the kinematic viscosity. If the dissipation rate is scaled by  $\varepsilon \approx U_0^3 L^{-1}$  [43], Eq. 2.10 becomes

$$\eta = \left( \frac{\nu^3 L}{U_0} \right)^{1/4} = L Re^{-3/4}, \quad (2.11)$$

where  $L$  denotes the characteristic length,  $U_0$  the approaching velocity and  $Re$  the Reynolds number (Eq. 2.3).

These approximations of the turbulent scales (Eq. 2.9 - Eq. 2.11) are valid for flows with a high Reynolds number and a good separation between the largest and smallest scales. A detailed discussion on the limitations of the Kolmogorov [55] theory can be found in Pope [43] or Lesieur [56].

### 2.1.3. Grid turbulence

One way to produce experimentally defined, reproducible, homogeneous and isotropic turbulence is by passing a uniform flow through a grid [53, 57, 58]. Through the absence of a mean flow gradient, the large scale eddies can decay homogeneously, because no further turbulence is produced (Fig. 2.2a). The most common grid design consists of cylindrical rods, defined by their rod diameter,  $d_r$ , and the mesh width,  $M$  (Fig. 2.2b).

The range of turbulent length scales generated by a grid can be approximated as follows. The Kolmogorov length scale,  $\eta$ , can be estimated as (Eq. 2.11)

$$\eta = d_r Re_d^{-3/4}, \quad (2.12)$$

with  $Re_d$  as the Reynolds number based on the rod diameter.

The integral length scale depends on the shedding frequency of the rods which can be estimated using the Strouhal number,  $Sr$  [61]. The Strouhal number depicts a dimensionless



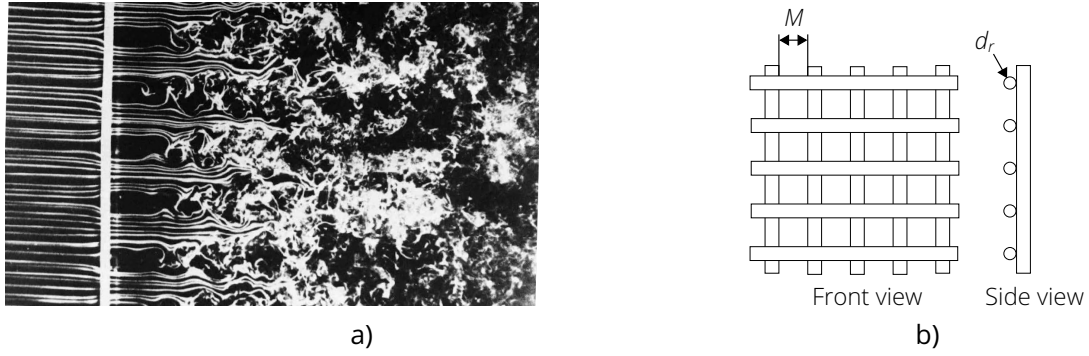


Figure 2.2. Grid turbulence. a) A photograph of a grid turbulence experiment (from [59]). b) A mesh grid defined by its rod diameter,  $d_r$ , and its mesh width,  $M$ , (from [60]).

shedding frequency,  $f_s$ , of an obstacle

$$Sr = \frac{f_s L}{U_0}, \quad (2.13)$$

where  $L$  denotes the characteristic length scale of the obstacle and  $U_0$  the approaching velocity. It is well known that  $Sr$  depends on  $Re$  [62, 63]. In the case of a circular cylinder, the Strouhal number remains close to the value of 0.21 for Reynolds number ranging between 150 and 1400 [64]. Thus,  $f_s$  can be used to estimate the integral time scale,

$$\tau_\Lambda = \frac{1}{f_s} = \frac{d_r}{Sr U_0}. \quad (2.14)$$

Besides, the integral length scale,  $\Lambda$ , can be approximated with the Taylor hypothesis [53] as

$$\Lambda = \tau_\Lambda U_0 = \frac{d_r}{Sr}. \quad (2.15)$$

## 2.2. Bubble dynamics

### 2.2.1. Bubble formation

One way to slowly form bubbles in a liquid phase is by flowing air with a constant flow rate,  $Q_G$ , through a upwards facing orifice with a radius,  $r_i$  [65]. In the stationary regime, the process involves the creation and deformation of a gas-liquid interface, which is dominated by viscous forces instead of inertial forces. The quasi-static regime persists as long as

$$f_{bub} = \frac{Q_G}{V_{bub}} \ll \frac{\Delta\rho}{\nu} r_i, \quad (2.16)$$

with  $f_{bub}$  as the bubble formation frequency,  $V_{bub}$  as the bubble volume, and  $\Delta\rho$  as the density difference between continuous and dispersed phase.

During the bubble formation process in the quasi-static regime, the bubble goes through well-defined pressure and shape states (Fig. 2.3). Firstly, the bubble pressure increases till

it reaches its maximum,  $\Delta p^{max}$ . At this point, the bubble is shaped as a hemisphere, where bubble radius and orifice radius are equal. If the applied pressure rises above the maximum pressure, the bubble grows beyond its hemispherical shape. Thus, the bubble pressure decreases till the bubble detaches from the orifice.

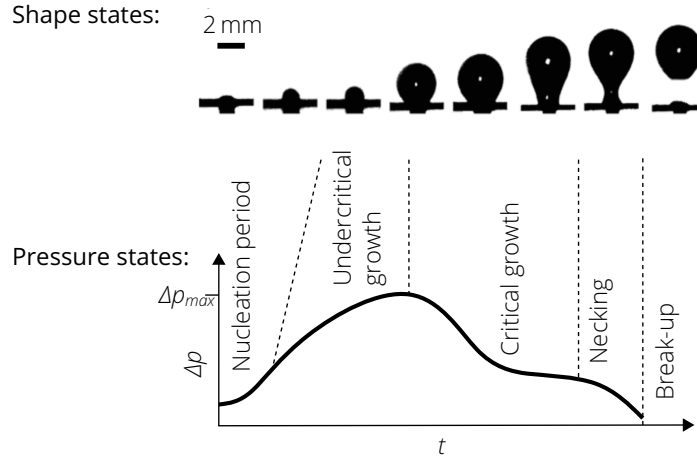


**Figure 2.3.** Illustration of the bubble formation process through an orifice in the quasi-static regime. The bubble goes through well-defined pressure and shape states, where  $\Delta p^{max}$  denotes the maximum pressure difference (adapted from [65–67]).

The resulting diameter of the detached bubble can be estimated based on a force balance. The force balance consists of the surface tension force,  $F_\sigma$ , keeping the bubble on the orifice,

$$F_\sigma = 2\pi\sigma_{lg}r_i, \quad (2.17)$$

and the buoyancy force,  $F_G$ , releasing the bubble from the orifice,

$$F_G = \Delta\rho g V_{bub}. \quad (2.18)$$

Assuming a spherical bubble with a volume of

$$V_{bub} = \frac{\pi d_b^3}{6}, \quad (2.19)$$

the diameter of the detached bubble can be approximated as

$$d_b \approx 2\sqrt[3]{\frac{1.5\sigma_{lg}}{\Delta\rho g}r_i}. \quad (2.20)$$

This approximation of  $d_b$  is valid for the following range of capillary length scales,

$$l_c = \sqrt{\frac{\sigma_{lg}}{\Delta\rho g}} \gg r_i. \quad (2.21)$$

Otherwise, gravity-driven deformation and instabilities of the bubble have to be considered.

All in all, Eq. 2.20 illustrates a strong dependency of the liquid phase and the orifice radius

on the detached bubble diameter. Therefore, a change in the air flow rate,  $Q_G$ , only varies the bubble formation frequency,  $f_{bub}$ .

### 2.2.2. Bubble shape and motion

The shape of the formed bubble can be classified in three categories: spherical (Fig. 2.4a), ellipsoidal (Fig. 2.4b), and spherical or ellipsoidal cap (Fig. 2.4c) [44]. Assuming a freely rising bubble in water, a bubble with a diameter below 2 mm is shaped as a sphere (Fig. 2.4a) and is defined by its diameter,  $d_b$ . With increasing gas volume, the bubble adapts to an oblate ellipsoidal shape with a major semi-axis,  $a$ , and minor semi-axis,  $c$  (Fig. 2.4b). As first approximation of the ellipsoidal size, the volume equivalent diameter can be used

$$d_b = \sqrt[3]{8a^2c}, \quad (2.22)$$

which is the diameter of a sphere of equivalent volume [68]. A further increase of the bubble volume leads to an asymptotic shape, known as spherical or ellipsoidal cap bubbles (Fig. 2.4c).

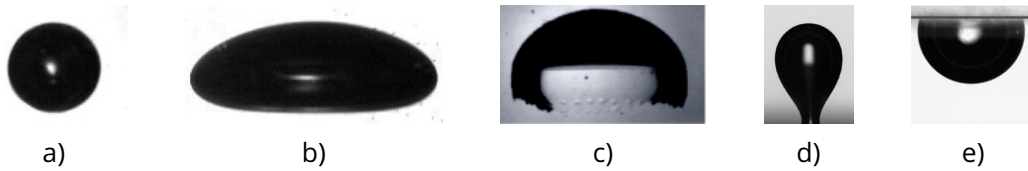


**Figure 2.4.** Typical bubble shapes. a) Spherical bubble (from [69]). b) Ellipsoidal bubble (from [69]). c) Ellipsoidal cap bubble (from [70]). d) A pendant bubble during the formation of a bubble at an orifice (from [71]). e) A sessile bubble captured on a hydrophobic surface in water (from [72]).

The shape of a freely rising bubble can be predicted using the bubble Reynolds number,

$$Re_b = \frac{d_b \bar{u}_b}{\nu}, \quad (2.23)$$

the Eötvös number, as ratio of the gravitational to surface tension forces,

$$Eo = \frac{\rho_L g d_b^2}{\sigma_{lg}}, \quad (2.24)$$

and Morton number, depending only on the material properties in the form of the ratio of viscous to surface forces,

$$Mo = \frac{g \mu^4}{\sigma_{lg}^3 \rho_L}, \quad (2.25)$$

with  $\rho_L$  as the liquid density,  $\nu$  and  $\mu$  as the kinematic and dynamic viscosity, respectively,  $\sigma_{lg}$  as the surface tension between liquid and gas phase, and  $\bar{u}_b$  as the averaged rising velocity of the bubble. From two of these three dimensionless numbers,  $Re_b$ ,  $Eo$  and  $Mo$ , the bubble shape can be classified with the well-known bubble-shape regime diagram by Clift et al. [44] (Fig. 2.5).

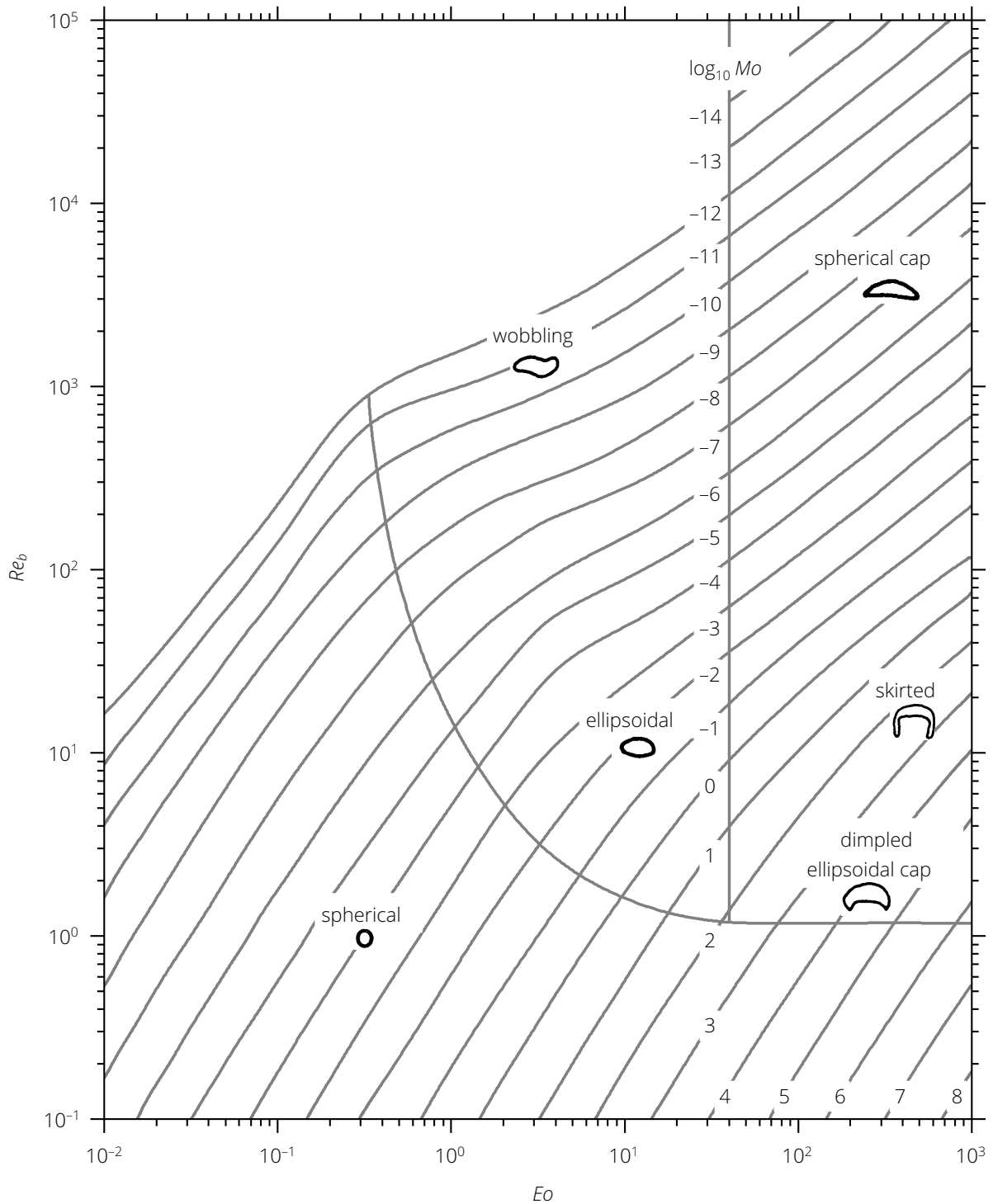


**Figure 2.5.** Bubble-shape regime diagram depending on the Reynolds,  $Re_b$  (Eq. 2.23), Eötvös,  $Eo$  (Eq. 2.24), and Morton number,  $Mo$  (Eq. 2.25), of a freely rising bubble (adapted from [44]).

After the detachment of a single bubble from an orifice, the bubble rises either rectilinearly (Fig. 2.6a) or exhibits an oscillating motion [73]. The rectilinear motion is described

as a straight vertical trajectory. Contrarily, the oscillating motions are quite complex due to the coupled action between shape oscillation, wake instability and impurities of the liquid phase [45]. These motions are mainly related to a zigzagging (Fig. 2.6b) or a spiraling motion (Fig. 2.6c) [74]. A zigzagging motion means that the bubble drifts periodically from one side to the other, remaining in one horizontal plane. A spiraling motion means that the bubble follows an elliptic spiraling path whose ratio from the minor to major axis increases [75].

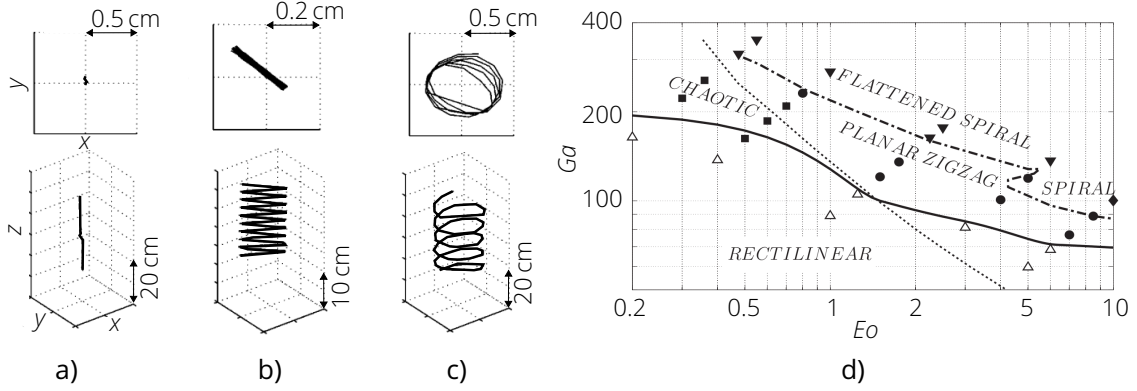


**Figure 2.6.** Trajectories of a freely rising bubble. Top and side view of a) a rectilinear, b) a zigzagging and c) a spiral motion (adapted from [76]). d) Phase diagram of the bubble rising trajectory depending on Eötvös,  $Eo$  (Eq. 2.24), and Galilei number,  $Ga$  (Eq. 2.26), (adapted from [75]).

The transition from a rectilinear to an oscillating motion is caused by the onset of a path instability which was investigated extensively by previous researchers [45]. Until now, several criteria to define the onset of path instability have been proposed e.g. depending on a critical Reynolds numbers, a critical Weber number, the aspect ratio of the bubble or the Morton number [e.g. 77–80]. Recently, Cano-Lozano et al. [75] summarized the threshold of the path instability of a freely rising bubble under surfactant-free conditions. A phase diagram (Fig. 2.6d) classifies the rising bubble trajectory according to its Eötvös and Galilei number,

$$Ga = \frac{\rho_L \sqrt{gd_b^3}}{\mu}. \quad (2.26)$$

The Galilei number is the ratio of the gravity to the viscous forces.

Besides freely rising bubbles, also static ones exist in the form of a pendant (Fig. 2.4d) or sessile bubble (Fig. 2.4e). The pendant bubble remains attached to a surface with gravity acting to pull it away. In contrast, the sessile one is prevented from moving upwards by a flat plate. The resulting profiles of pendant and sessile bubbles have been studied extensively [81–85]. The shape of the liquid-gas interface of quiescent fluids results from the equilibrium formed by the gravity and capillary forces, where at any point on the interface the following equation is valid,

$$\Delta p = \sigma_{lg} \left( \frac{1}{r_1} + \frac{1}{r_2} \right) \quad (2.27)$$

with  $\Delta p$  as the pressure difference (Laplace pressure) at the interface and  $r_i$  as the principal radii of the curvature.

### 2.2.3. Bubble wake

In general, the rise of a single bubble changes the surrounding liquid flow field due to the relative velocity between these two phases. For low Reynolds numbers, the viscous forces dominate over the inertial forces. The resulting flow is named Stokes flow. In the Stokes flow, the liquid streamlines follow the bubble contour. If the Reynolds number exceeds a critical value,  $Re_b^{crit}$ , the boundary layer, a thin layer of liquid close to the bubble interface, separates and forms a wake behind the bubble [86]

The phenomena of the boundary layer separation is illustrated for a spherical bubble in Fig. 2.7a. The upper part of Fig. 2.7a illustrates the streamlines around the bubble. Four significant points,  $D$ ,  $E$ ,  $F$  and  $S$  are marked, highlighting the leading edge, equator, trailing edge and separation point. The lower part focuses on the pressure distribution of the liquid flow by flowing around the spherical bubble.

Assuming a laminar liquid flow upwards of the spherical bubble, the liquid flow accelerates from point  $D$  to  $E$  and the pressure drops. Passing point  $E$ , the pressure increases again. At point  $S$ , the boundary layer starts to separate from the bubble surface by rolling up and forming vortices. This effect is combined with the onset of the path instability and a change in the rising trajectory of the bubble (Sec. 2.2.2) [86, 87]. At a moderate value of the bubble Reynolds number, the separated streamlines will rejoin in some distance behind the bubble and form a closed region, defined as a standing eddy (laminar regime in Fig. 2.7b). For higher values of  $Re_b$ , the standing eddy transits into an unsteady wake with vortex shedding until it forms a highly turbulent wake (Fig. 2.7b) [88, 89].

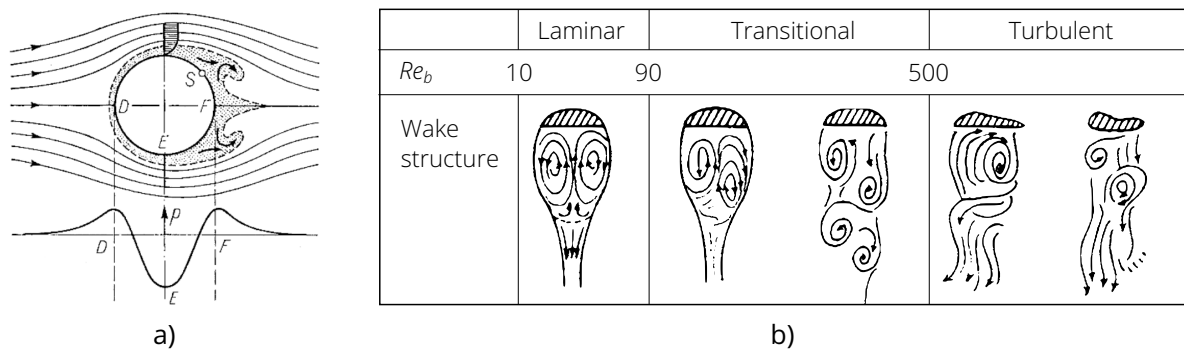


**Figure 2.7.** Formation of a bubble wake. a) Illustration of the boundary layer separation and the vortex formation downstream of a spherical bubble. The upper part illustrates the streamlines around the bubble and the lower part the corresponding pressure profile. Four significant points,  $D$ ,  $E$ ,  $F$  and  $S$ , are marked, highlighting the leading edge, equator, trailing edge and separation point, respectively (from [86]). b) Illustration of the bubble wake structure for different bubble Reynolds numbers,  $Re_b$ , (from [88]).

Besides the bubble Reynolds number, also the aspect ratio and surface mobility of the bubble have an impact on the wake structure. Mougin et al. [90] showed a strong dependency of the local value of the surface vorticity on the curvature and the tangential velocity. The combination of the viscous diffusion and axisymmetric transport carries the vorticity away in the form of an axisymmetric wake. If the generated vorticity reaches a critical value, the

described mechanism is not valid anymore. The axisymmetric wake becomes unstable and breaks into a double-threaded open wake. A typical critical vorticity is reached if the bubbles aspect ratio is larger than 1.65 (Fig. 2.8a) [91]. Likewise, Fan et al. [89] investigated the effect of the bubble surface mobility on the wake structure. In a pure system, the onset of wake formation occurs later and leads to a smaller wake volume than in a system contaminated with surface active substances (Fig. 2.8b, c).

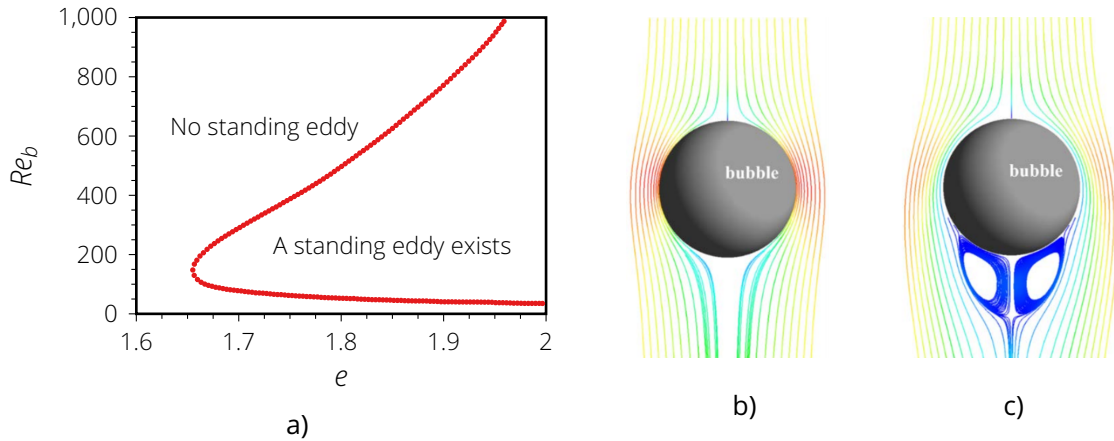


**Figure 2.8.** Wake structure depending on the aspect ratio and surface mobility of the bubble. a) Classification of the existence of a standing eddy behind an ellipsoidal bubble depending on the aspect ratio of the bubble,  $e$ , and the bubble Reynolds number,  $Re_b$ , (adapted from [91]). b)-c) Liquid streamlines around a freely rising bubble ( $d_b = 0.9$  mm) under different conditions of surface mobility (from [92]). b) Pure system. c) System contaminated with surface active substances.

Turning now from a single freely rising bubble to a bubble swarmed, the formed bubble wakes influence the bubble-bubble interactions. The dynamics of multiple bubbles rising together are different from that of a single freely rising bubble [93–95]. Assuming the simplified case of two bubbles rising in an in-line configuration, the trailing bubble is affected by the liquid flow structure of the leading bubble, and in particular its wake [93, 96–98]. The interaction among these two bubbles is manifold. For example, both bubbles could collide and coalesce. The wake of the leading bubble reduces the drag acting on the trailing bubble, so that the trailing bubble rises faster than their terminal velocity in isolation [99, 100]. The trailing bubble can approach the leading bubble closely, resulting into a coalescence of these two successive bubbles (Fig. 2.9a) [88].

Furthermore, the trailing bubble could escape from the vertical line of the leading bubble (Fig. 2.9b) as experimentally observed by Watanabe et al. [95] for spherical bubbles ( $Re_b = 40$ ,  $d_b = 1.4$  mm). Gumulya et al. [94] showed that for high Reynolds numbers ( $Re_b = 890$ ,  $Eu = 0.5$ ), the path of the trailing bubble deviated strongly from the leading bubble. The leading bubble remained a rectilinear rising path, whereas the trailing bubble inhibited a planar zig-zagging motion. Kusuno et al. [101] attributed the deviation of the rising paths between leading and trailing bubble to the lift force in the wake. A spherical trailing bubble migrates from the in-line configuration, due to the shear-induced lift in the wake. However, with increasing oblateness of the trailing bubble and the onset of the formation of a standing

eddy, the lift mechanism reverses, keeping the trailing bubble in-line.

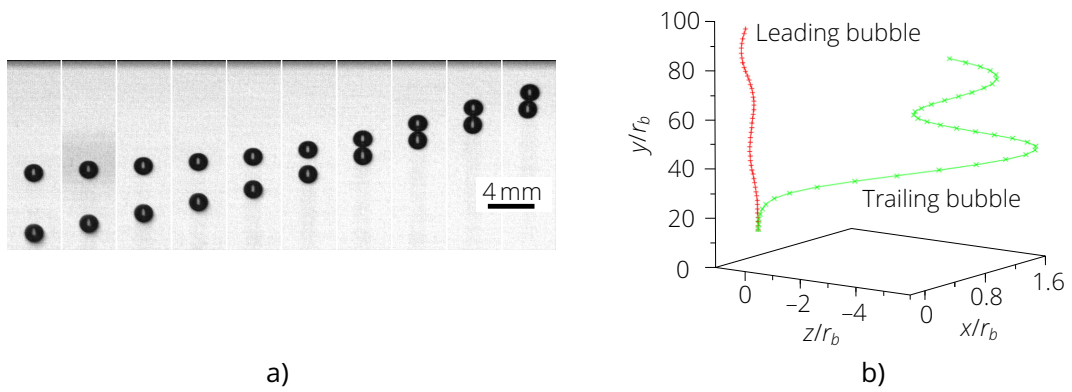


**Figure 2.9.** Dynamics of two bubbles rising in an in-line configuration. a) Coalescence between leading and trailing bubble (adapted from [95]). b) Trajectories of the leading and the trailing bubble, where the trailing bubble escapes from the in-line configuration (adapted from [94]).

### 2.2.4. Surface mobility

In a flotation cell, normally surface active substances, named surfactants, are used e.g. to hydrophobize the mineral particles or generate a stable froth. Consequently, the formed bubbles are released mainly into a contaminated liquid phase. These contaminants affect the surface mobility of the bubbles, changing from a mobile to an immobile surface (Fig. 2.10). The change in surface mobility is accompanied by a shift in the slip condition on the gas-liquid interface. Further, the adsorption of the surfactant molecules at the bubble surface limit the internal circulation of the bubble.

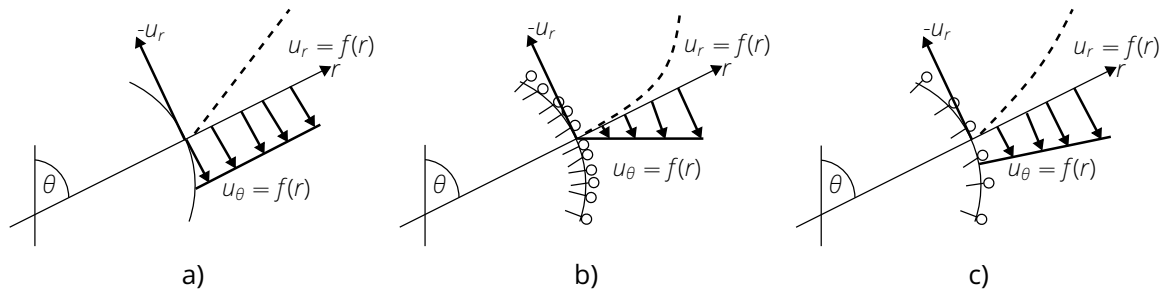


**Figure 2.10.** Effect of adsorbed surfactant molecules (line+circle) and other surface contaminants on the liquid velocity components at the bubble surface. The tangential liquid velocity as a function of the radial distance,  $r$ , measured from the bubble center is shown by the parallel lines with the arrows. The profiles of the radial,  $u_r$ , and tangential,  $u_\theta$ , components of liquid velocity at the bubble surface are shown by the dashed lines (from [102]). a) Fully mobile surface. b) Fully immobile surface. c) Partially immobile surface.

In general, two extrema of boundary conditions on the liquid-gas interface exist for the



normal,  $u_r$ , and tangential component,  $u_\theta$ , of the fluid flow, named free-slip (Fig. 2.10a) and no-slip condition (Fig. 2.10b). For both conditions, no-penetration yields to  $u_r = 0$ . The free-slip condition can be described by

$$\frac{\partial u_\theta}{\partial \theta} = 0, \quad (2.28)$$

thus a mobile bubble is free of shear stress. In comparison, the no-slip condition sets  $u_\theta = 0$  at the gas-liquid interface. The no-slip condition together with the incompressibility of the flow leads to

$$\frac{\partial u_r}{\partial r} = \frac{\partial u_\theta}{\partial \theta} = 0, \quad (2.29)$$

thus an immobile bubble is always free of normal viscous stress.

After the formation of a bubble in a contaminated solution, the fresh surface is mobile. Subsequently, the surfactants can be adsorbed onto the bubble surface. Due to the rising motion of the bubble, the adsorbed surfactants can be swept towards the rear of the bubble forming an immobile cap, whereas the leading edge of the bubble becomes partially mobile (Fig. 2.10c) [102]. Consequently, there is no strict line between mobile and immobile bubble surface [103]. Instead, all states in between mobile and immobile are possible and depend for example on the type of surfactant adsorbed at the liquid-gas interface [104–106] or the approaching liquid flow [107–109].

Due to the fact that the bubble mobility changes the flow field around the bubble, it affects also the terminal velocity of the rising bubble, its rising trajectory and the bubble-particle interaction. The mobile surface leads to a smaller drag force on the bubble, resulting in a higher terminal velocity and an earlier onset of path instabilities [45, 49, 110]. For example, Hartunian et al. [78] observed the onset of path instabilities for a critical Reynolds number of 206 in tap water, but 670 in distilled water.

In the context of the bubble-particle interaction, the collision probability for coarse particles is greater for an immobile bubble surface, whereas a mobile bubble surface is more suitable for fine particles [92]. According to Schulze [103], a mobile bubble surface offers a longer residence time to form a three-phase contact line, due to the smaller relative velocity between particles and bubbles. Additionally, the degree of mobility can vary over time. For example during laboratory batch flotation experiments, the concentration of surfactants decreases due to output of surface active minerals [103].

## 2.3. Particle dynamics

### 2.3.1. Motion of a single particle

The motion of a single non-deformable spherical particle,  $W$ , with the mass,  $m_p$ , is governed by the Basset–Boussinesq–Oseen (BBO)-equations in the form of [111–113]

$$m_p \frac{\partial W}{\partial t} = m_p G + m_f \left( \frac{DU}{Dt} - G \right) + F_p, \quad (2.30)$$

with  $\mathbf{G}$  as the gravity field,  $m_f$  as the mass of the fluid enclosed in the volume of the particle and  $\mathbf{U}$  as the liquid velocity field. The force,  $\mathbf{F}_P$ , groups the hydrodynamic forces resulting from the presence of the particle in the flow as follows

$$\mathbf{F}_P = \mathbf{F}_D + \mathbf{F}_B + \mathbf{F}_{VM} + \mathbf{F}_L, \quad (2.31)$$

with  $\mathbf{F}_D$  as the drag force,  $\mathbf{F}_{VM}$  as the added mass force,  $\mathbf{F}_B$  as the Basset force and  $\mathbf{F}_L$  as the lift force. The drag force acts on the opposite direction of the motion of particle. The added mass and Basset force describe the unsteady forces acting on the particle due to acceleration with respect to surrounding fluid. The lift force defines the force exerting on a particle due to the liquid flowing around the object.

Normally, mineral particles have a higher density than water leading to a tendency of settling to the bottom due to gravity. After a short transition period, the particle sinks into water and reaches its settling velocity,  $w_S$ . To compute the settling velocity, the BBO-equations (Eq. 2.30) are reduced to the drag and body forces as

$$0 = m_p \mathbf{G} + \mathbf{F}_D. \quad (2.32)$$

If the particle is spherical, the body forces contain the gravity directed downward and buoyancy force directed upward as

$$m_p \mathbf{G} = \frac{\pi d_p^3 \rho_S \mathbf{G}}{6} - \frac{\pi d_p^3 \rho_L \mathbf{G}}{6}. \quad (2.33)$$

The drag force is defined as

$$\mathbf{F}_D = C_D \rho_L \frac{\pi d_p^2}{8} |\Delta \mathbf{U}| \Delta \mathbf{U}, \quad (2.34)$$

where  $C_D$  denotes the particle's drag coefficient and  $\Delta \mathbf{U} = \mathbf{W} - \mathbf{U}$  the relative velocity between particle and liquid phase. For the drag coefficient, only limited analytical solutions are available [114]. Generally, the coefficient is defined as

$$C_D = \frac{24}{Re_p} f_D, \quad (2.35)$$

with the particle Reynolds number

$$Re_p = \frac{d_p |\Delta \mathbf{U}| \rho_L}{\mu}. \quad (2.36)$$

In the case of a sphere in the Stokes Regime ( $Re_p \ll 1$ ), the nonlinear term of the drag coefficient is  $f_D = 1$ . For higher Reynolds numbers,  $Re_p < 1000$ , the Schiller-Naumann drag coefficient applies with  $f_D = 1 + 0.15 Re_p^{0.687}$  [115]. In the case of a Stokes flow, the settling velocity of a spherical particle can be calculated as [49]

$$w_S = \sqrt{\frac{1}{6} \frac{d_p (\rho_S - \rho_L) g}{C_D \rho_L}}. \quad (2.37)$$

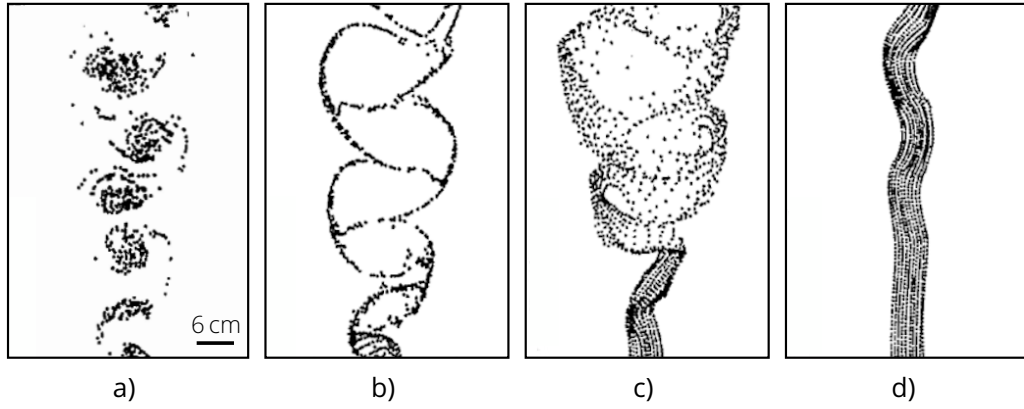


**Figure 2.11.** Instantaneous particle dispersion patterns from numerical simulation of the plane wake for different Stokes numbers,  $St$  (Eq. 2.38), (adapted from [116]). a)  $St = 0.01$ . b)  $St = 1.0$ . c)  $St = 10$ . d)  $St = 100$ .

If a particle is exposed to a moving fluid, the particle responds differently to the changes in the liquid velocity depending on its diameter and material properties (Fig. 2.11). This particle behavior is characterized by the Stokes number

$$St = \frac{\tau_p}{\tau_l}, \quad (2.38)$$

where  $\tau_p$  denotes the time required for particle to respond to change in velocity and  $\tau_l$  the characteristic time scale of the liquid flow. The characteristic time scale of a particle can be estimated as [48]

$$\tau_p = \frac{1}{18} \frac{(\rho_s + 0.5\rho_L)d_p^2}{\mu f_D}. \quad (2.39)$$

If  $St \ll 1$ , the characteristic time scale of the liquid flow exceeds the characteristic time scale of the particle. Thus, the particle can respond and follows the sudden changes of the liquid flow (Fig. 2.11a). If  $St > 1$ , the characteristic time scale of the liquid flow stays below the characteristic time scale of the particle. In this case, the particle motion is dominated by its inertia and passes through the liquid flow with a low response to sudden changes of the liquid flow. Thus, the particle trajectory remains mainly along its initial trajectory (Fig. 2.11b-d).

Another typical dimensionless number to describe the particle motion in the liquid phase is the Archimedes number,  $Ar$ ,

$$Ar = \frac{gd_p^3\rho_L(\rho_s - \rho_L)}{\mu^2}, \quad (2.40)$$

as the ratio of gravitational forces to viscous forces [117].

### 2.3.2. Dense particle suspension

The previous part focused mainly on the behavior of a single particle. If multiple particles are present, the particles may be influenced by the neighboring particles depending on the

spacing between them [118],

$$\frac{L_p}{d_p} = \sqrt[3]{\frac{\pi}{6\alpha_p}}, \quad (2.41)$$

with  $\alpha_p$  as the particle volume fraction,  $V_p$  as the particle volume and  $L_p$  as the distance between the particle centers.

Sommerfeld [48] classified the particle-laden flows into two regimes: dilute and dense flows (Fig. 2.12). In a dilute system, the particle volume fraction is low, so that particles can be treated as an isolated element and may influence the surrounding liquid. Thus, a dilute flow is dominated by the fluid-dynamic transport of particles. With an increase of the particle volume fraction, a dilute flow becomes dense. The particle-particle interaction gains in significance, leading to a collision-driven or a contact-driven transport.

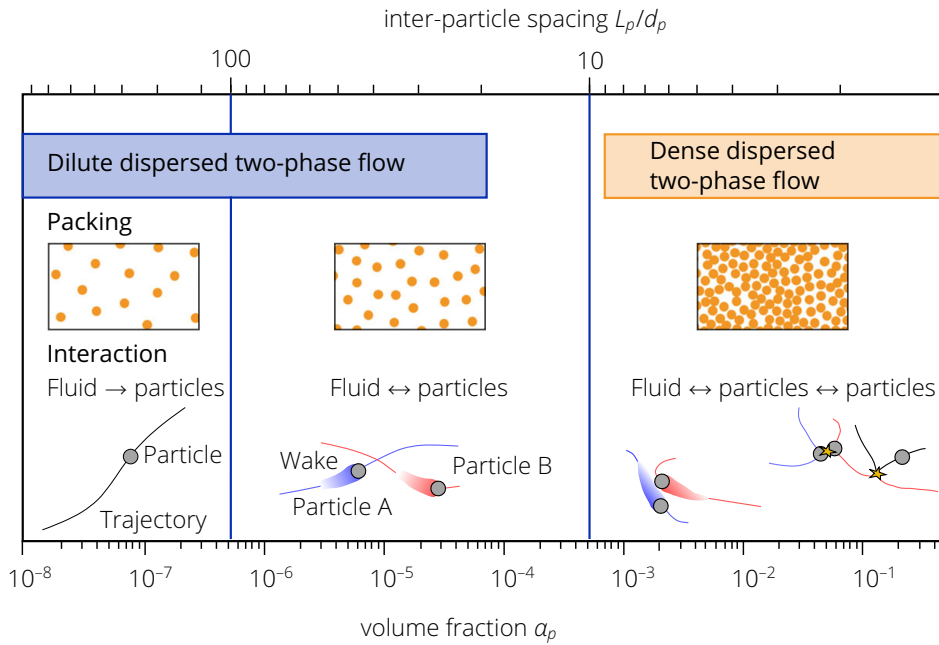


**Figure 2.12.** Classification of particle-laden flows in dilute and dense dispersed two-phase flows depending on the inter-particle spacing,  $L_p/d_p$ , and volume fraction,  $\alpha_p$ . For each class, typical mechanisms driving the flow and the interaction between the particles are illustrated as grey spheres denoting the particle combined with their trajectory and formed wake (marked red or blue). In a dilute flow, the particle motion is dominated by the surrounding liquid flow and may modify the characteristic of the carrier phase turbulence. In a dense flow, a particle-particle interaction is more significant leading to a collision-driven or a contact-driven transport (adapted from [48, 119]).

The presence of particles in a liquid flow field affects not only the motion of the individual particle, but the particles also modify the characteristic of the carrier phase turbulence compared to the single phase flow. Since the early 1990s, researchers have experimentally investigated the effect of particles on turbulence modulation [120]. In turbulent jets and pipe flows, Crowe et al. [47] have pointed out that particles which are small compared to the turbulent integral length scale attenuate turbulence, while relatively larger particle en-

hance turbulence in the continuous phase. In stirred tanks however, recent experimental investigations found contradicting results with data from Montante et al. [121] conforming to the criterion of Crowe et al. [47], while data from Unadkat et al. [122] and Gabriele et al. [123] showed turbulence attenuation for rather large particles. Moreover, recent literature [40, 124–127] shows that the mechanism of turbulence modulation is more complex. Accordingly, it is likely that the turbulence modulation does not only depend on the ratio of the particle diameter to the turbulent length scales, but on other dimensionless parameters as well, e.g. the Stokes number, particle-to-fluid density ratio, and solid concentration.

Balachandar et al. [126] summarized the mechanisms to enhance the velocity fluctuations, which are due to the wake dynamics, self-induced vortex shedding and buoyancy-induced instabilities based on density variation arising from preferential particle concentration. The mechanisms for reductions are the enhanced inertia, effective viscosity of the particle-laden flow and the dissipation rate increase due to particle drag. The effect of turbulent modulation of the liquid phase is not limited to particles. Bubbles also contribute to the turbulence production e.g. through their wake (Sec. 2.2) [98].

Additionally, the presence of particles can affect the motion of bubbles depending on the particle inertia [128]. Besides the increase of the viscosity of the suspension, particles can entrain in the bubble wake resulting into a higher mass force acting on the bubble [89, 129, 130]. Experiments on this effect of particles were conducted by Schlüter et al. [130]. They chose glass beads as solid particles with varying diameters ( $d_p = 150 \mu\text{m}; 500 \mu\text{m}$ ). The smaller particles had a low inertia and could follow the liquid flow in the wake. In the wake, these particles increased the mass force acting on the bubble resulting in a lower rising velocity. But not only the bubble rising velocity decreased, also the volume of the wake which is affected by the terminal velocity of the bubble did so. The larger particles had a higher inertia and were not able to follow the wake structure. Thus, a decrease of the rising velocity could be contributed to the increase of the overall viscosity of the suspension.

## 2.4. Bubble-particle collision

### 2.4.1. Numerical investigations

In froth flotation, valuable minerals are separated from gangue materials based on their physicochemical properties. They form a bubble-particle aggregate and rise into the froth. The collision between particles and bubbles is, besides attachment, the key process behind the formation of a bubble-particle aggregate in this process (Fig. 2.13a). A particle collides with the bubble surface due to a sufficiently close encounter. This process is governed by the hydrodynamics in the flotation cell. After the collision, the particle slides along the bubble surface. When the particles are sufficiently hydrophobic, the liquid film between the bubble and the particle thins and finally ruptures due to the interfacial forces. Only if the detaching forces, e.g. due to turbulent stresses, are higher than the attaching forces, the particle detaches from the bubble again [17, 23, 49, 131, 132]. To sum up, the success of the froth flotation process depends on both the surface chemistry for the hydrophobization of particles and the hydrodynamics for an encounter between bubble and particle.

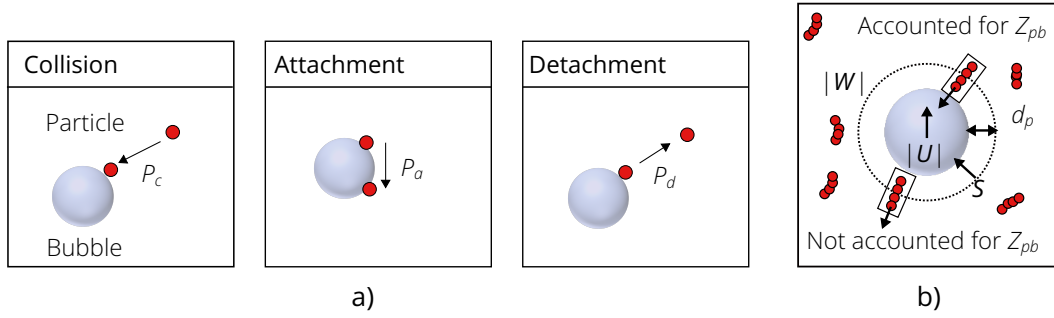


**Figure 2.13.** Interaction between particle and bubbles. a) Three sub-processes of the bubble-particle interaction: collision, attachment and detachment. The probability of each sub-process is denoted by  $P$  (adapted from [131]). b) Definition of the collision frequency,  $Z_{pb}$ , with  $|W|$  as the particle velocity,  $|U|$  as the bubble rising velocity and  $S$  as the bubble surface vector.

One important parameter to quantify the recovery of froth flotation is the collision rate,  $\dot{N}_c$ . In general terms, the collision rate is defined as the number of particles colliding with a bubble per unit of time,

$$\dot{N}_c = N_p Z_{pb} P \quad (2.42a)$$

$$= \oint \Lambda(\mathcal{J} \cdot d\mathcal{S}) \text{ with } \begin{cases} \Lambda(\mathcal{J} \cdot d\mathcal{S}) = \mathcal{J} \cdot d\mathcal{S} & \text{if } \mathcal{J} \cdot d\mathcal{S} > 0, \\ \Lambda(\mathcal{J} \cdot d\mathcal{S}) = 0 & \text{if } \mathcal{J} \cdot d\mathcal{S} \leq 0, \end{cases} \quad (2.42b)$$

where  $N_p$  is the particle number density,  $Z_{pb}$  refers to the collision frequency between particle and bubble, and  $P = P_c P_a (1 - P_d)$  is the overall probability of the particle collection process. Thus, the collision rate corresponds to the particle flux,  $\mathcal{J} = N_p \Delta W$ , of the relative velocity between the bubble and the particle,  $\Delta W$ , along the bubble surface element vector,  $S$  [133]. The vector,  $S$ , points inwards as illustrated in Fig. 2.13b. It is noted that only particle fluxes pointing towards the bubble surface are taken into account by applying the function  $\Lambda$  [37].

Many works [102, 134–136] are devoted to model the collision frequency in the form of

$$Z_{pb} = \oint \Lambda(\Delta W dS). \quad (2.43)$$

In particular, the modeling of the relative velocity between bubbles and particles has comprised a large part of the work, due to its deterministic and stochastic components. Initial studies assumed that the motions of bubbles and particles were deterministic, excluding the effect of the fluctuating components of turbulence. These motions are primarily governed by interception, inertia and gravity, as illustrated in Fig. 2.14 [49]. They can be used to describe collisions between bubbles and particles at a low degree of turbulence, for instance in a flotation column or in the relaxation area of an industrial flotation cell [136].

To account also for a high degree of turbulence, i.e. close to the stirrer in an industrial flotation cell, the stochastic motion of bubbles and particles has to be included in the models. For this purpose, the well-known collision models developed by Saffman et al. [35] for

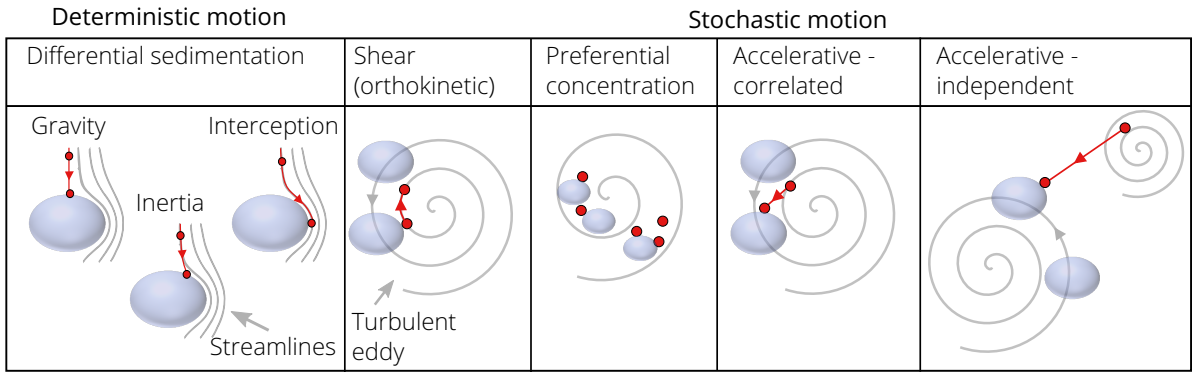


**Figure 2.14.** Schematic of deterministic and stochastic collision mechanisms (adapted from [24, 136]).

raindrops or by Abrahamson [36] for heavy particles were mainly applied, depending on the primary collision mechanism. An overview of these mechanisms is shown in Fig. 2.14. For a detailed review on further collision models, see Meyer et al. [24] and Kostoglou et al. [136].

There are four categories of collision mechanisms in turbulent flows: orthokinetic mechanism, preferential concentration, correlated and uncorrelated accelerative mechanism. If a particle can follow the fluid streamline of the turbulent eddy perfectly, it either collides with a bubble due to their different positions in the shear flow field (orthokinetic mechanism) or due to the spatial non-uniformity concentration of bubbles (preferential concentration). Otherwise, the particle deviates from the fluid streamline of a turbulent eddy and collides with a bubble moving in a partly correlated (accelerative - correlated) or uncorrelated turbulent eddy (accelerative - uncorrelated).

Saffman et al. [35] assumed that raindrops follow the atmospheric turbulence completely (orthokinetic mechanism), proposing

$$Z_{pb}^{ST} = \sqrt{\frac{8\pi}{15}}(r_1 + r_2)^3 \sqrt{\frac{\varepsilon}{\nu}}, \quad (2.44)$$

with  $r_i$  referring to the radii of the particles,  $\varepsilon$  to the dissipation rate and  $\nu$  to the kinematic viscosity. The model is valid for mono-dispersed particles with a radius smaller than the Kolmogorov scale of the fluid flow.

In contrast, the study by Abrahamson [36] analyzed the motion of heavy particles suspended in high-intensity isotropic turbulence (uncorrelated accelerative mechanism)

$$Z_{pb}^A = 5(r_1 + r_2)^2 \sqrt{W_1'^2 + W_2'^2}, \quad (2.45)$$

with  $W'$  as the turbulent fluctuations of the particles (Eq. A.85). This model is valid for particle radii exceeding the Kolmogorov length scale by far and if no external forces act on the particle motion.

However, it is well known that the models proposed by Saffman et al. [35] and Abrahamson [36] are just extremal cases to approximate the collision frequency. They are rarely found in the flotation process, where the collisions between various length scales of bubbles and

particles are of great importance. That means the motions of the smaller particles are disturbed by the flow field around the bubble. The particle could follow the streamlines around the bubble, rather than collide, leading to a decrease in the collision frequency. This effect can be described by the collision efficiency, the ratio of the number of detected collisions to the number of particles in the volumes swept out by the bubble. In the case of Saffman et al. [35] and Abrahamson [36], the collision efficiency is one. Further, as discussed critically by Kostoglou et al. [37], the TKE and dissipation rate should be two independent input parameters into the collision model. The turbulent power spectrum reveals that the energy-containing range is governed by the TKE. In contrast, the dissipation range is characterized by the dissipation rate (Sec. 2.1.2). The models proposed by Saffman et al. [35] and Abrahamson [36] depend only on one parameter. Consequently, Kostoglou et al. [37] developed a new collision model to overcome the previous shortcomings and adapted it for the process of froth flotation.

Kostoglou et al. [37] split the relative velocity between bubble and particles,  $\Delta W$ , into three major components

1. total relative velocity between bubble and liquid phase,  $|\Delta W_{bl}|$ ,
2. turbulent relative velocity between bubble and particle,  $|\Delta W_{bp}|$ , and
3. gravitational relative motion between particle and liquid phase,  $|\Delta W_{pl}|$ .

Consequently, integrating Eq. 2.43 along the polar angle around the bubble,  $\theta$ , results in

$$Z_{pb}^K = 2\pi(r_b + r_p)^2 \int_0^\pi \Lambda(\Omega(\theta)|\Delta W_{bl}| + |\Delta W_{bp}| + f \cos \theta |\Delta W_{pl}|) \sin \theta d\theta, \quad (2.46)$$

with  $r_b$  as the bubble radius,  $r_p$  as the particle radius,  $\Omega$  as a function of the normalized local radial liquid velocity distribution at the bubble surface [49], and  $f$  as a function of the normalized magnitude of the particle velocity. The calculation of all parameters is summarized in Appendix A.4.

## 2.4.2. Experimental investigations

One main problem for the developed collision models is the limitation of available validation data [24]. The validation data rely mainly on direct numerical simulation (DNS), allowing the primary variables and the collision to be controlled with high accuracy [25–29]. However, DNS is restricted to a certain range of Reynolds numbers due to high computational efforts.

Previous experimental studies are divided into indirect and direct methods [49]. The indirect methods determine the collision probability by measuring the overall recovery rate,  $R$ , of a particle system. Many researches focused on freely rising bubbles in a simplified fluid flow as for example in a Hallimond tube (Fig. 2.15a). The particle system consisted of mainly strongly hydrophobic fine particles. This system allowed to assume the attachment probability as unity and detachment probability as zero [49, 137, 138]. The key advantage of the indirect methods is the usage of freely rising bubbles, considering the bubble dynamics. A major drawback of this method is the assumption of an attachment probability of unity and no detachment. There is only a limited number of particles available meeting these criteria.



Additionally, the bubbles were released into a quiescent liquid leading to a high discrepancy to the high turbulence in a flotation cell.

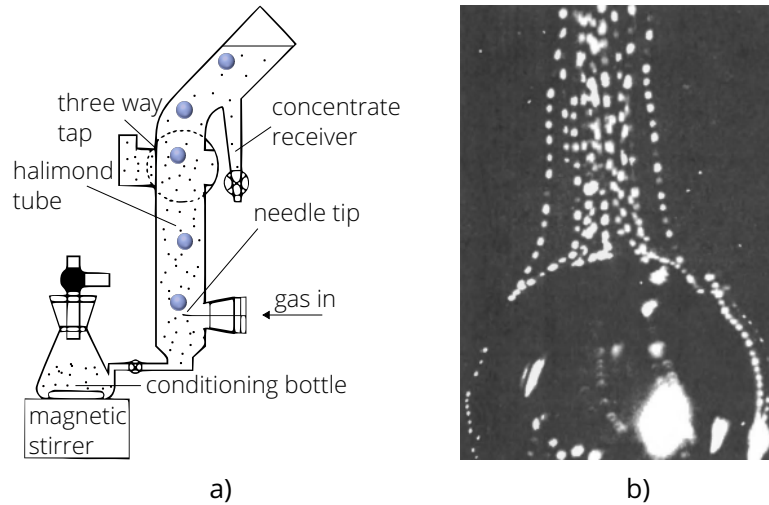


**Figure 2.15.** Measurement techniques to investigate the bubble-particle interaction. a) Indirect method by measuring the recovery rate in a Hallimond tube (from [139]). b) Direct method by recording the particle trajectories with high-speed imaging methods (from [140]).

The direct method comprises high-speed imaging methods to record particle trajectories. Applying this technique, mainly the collision between a particle with a stagnant bubble was investigated in a quiescent or laminar flow (Fig. 2.15b) [17, 30–33, 92]. This method enables an intensive study of a wide range of parameters as e.g. the particle shape or bubble surface mobility on the bubble-particle collision and attachment behavior. However, usage of a captive bubble is not comparable to freely rising bubbles. In particular, in the sense of their hydrodynamics and surface interactions (Sec. 2.2). Thus, from these experimental results, no conclusion can be drawn on the collision mechanisms between particles and freely rising bubbles in turbulent flows. Until now, only a few researchers have focused on the particle trajectories colliding with freely rising bubbles [34, 141]. These works are limited by particles with a high inertia such as galena or soda lime glass.

## 3. Materials and Methods

The investigation of the bubble-particle interaction is based on the development of generic experimental setups and the application of suitable measurement methods. Sec. 3.1 describes the designed experimental setups. The generic experiments comprise on the one hand a freely rising bubble chain in a quiescent liquid [38, 41]. On the other hand, a water channel is constructed to generate a generic turbulent flow. A defined range of turbulent length scales is produced by a liquid flow passing through a grid upstream of a stagnant bubble [39]. The applied experimental methods include Tomographic Particle Image Velocimetry (TPIV) (Sec. 3.2), 4D Particle Tracking Velocimetry (PTV) (Sec. 3.3) and Positron Emission Particle Tracking (PEPT) (Sec. 3.4). The liquid flow field around the individual bubbles is measured with TPIV, to understand the flow conditions which the particles are exposed to [39, 41]. With 4D PTV (Sec. 3.3) and PEPT (Sec. 3.4), the trajectories of the model particle systems are triangulated and classified according to their collision performance [38, 39, 41]. The respective sections describe the principle, the measurement setup, the particle systems, the data and uncertainty analysis of the particular measurement technique. In Sec. 3.5, the advantages and disadvantages of each measurement technique are discussed to determine their field of application.

### 3.1. Experimental setups

#### 3.1.1. Freely rising bubble chain in a bubble column

The experimental setup of the bubble column was adapted from Ziegenhein et al. [142] and is shown in Fig. 3.1a. The cell (90 mm × 220 mm × 25 mm, width × height × depth) was filled with deionized (DI) water and 0.01 M potassium chloride (KCl). KCl was added as an electrolyte background to compress the repulsive surface force due to overlapping of electrostatic double layers [49]. The physical and chemical values of the DI water are summarized in Tab. A.3.

Nearly monodisperse air bubbles are introduced by a single blunt needle with an inner diameter of  $d_i = 120 \mu\text{m}; 300 \mu\text{m}; 600 \mu\text{m}$ . The properties of the generated bubbles are summarized in Tab. 3.1, stating their bubble formation frequency,  $f_{bub}$ , their eccentricity (ratio of major to minor axis),  $e$ , the bubble diameter,  $d_b$ , and the mean bubble rising velocity,  $\bar{u}_b$ .

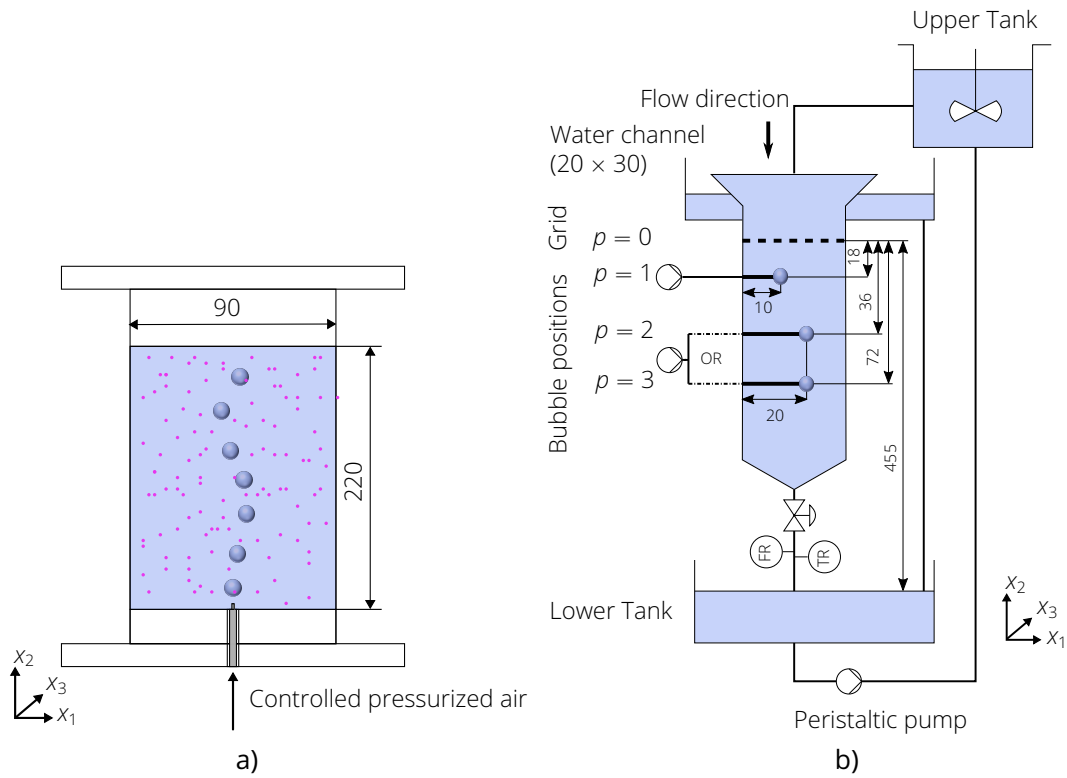


**Figure 3.1.** Experimental setups: a) Bubble column. Nearly monodisperse air bubbles are introduced by a single blunt needle. The global coordinate system originates from the bubble orifice. b) Water channel. A defined range of turbulent length scales is produced by a liquid flow passing through a grid. The downwards flow is set by an electrical valve and controlled by a volumetric flowmeter (FR) and an integrated temperature sensor (TR). The flow recirculates by pumping the suspension upwards into the upper tank with a peristaltic pump. The origin of the coordinate system is located, according to the bubble position,  $p$ , where the needle penetrates the wall of the water channel. Units are displayed in mm.

The air flow rate,  $Q_G$ , was controlled by a mass flow controller (FMA 1604A, OMEGA Engineering, Inc., USA) to achieve a distance of  $8d_b$  between two consecutive bubbles ( $\approx \overline{u_b} f_{bub}^{-1}$ ). The resulting bubble shapes and trajectories were characterized by their bubble Reynolds,  $Re_b$  (Eq. 2.23), their Eötvös,  $Eu$  (Eq. 2.24), and the Galilei number,  $Ga$  (Eq. 2.26). The associate Morton number (Eq. 2.25) was  $Mo = 2.6 \cdot 10^{-11}$ .

The global coordinate system was defined by the needle orifice, which represented the origin. The  $x_2$ -axis pointed to the upward direction of the orifice which corresponded to the rising direction of the bubbles. The  $x_1$ -axis and the  $x_3$ -axis were perpendicular to the  $x_2$ -axis.

### 3.1.2. Turbulent flow upstream of a stagnant bubble in a water channel

The water channel generated a large range of turbulent length scales by the fluid flow passing through the grid upstream of a bubble (Fig. 3.1b). The setup was adapted from the investigations by Haase et al. [143] and Tokuhiro et al. [144] who produced similarly a downward

**Table 3.1.** Bubble column: Properties of the gas phase. The measurement configurations depended on the inner diameter of the orifice,  $d_i$ , and its associated volume flow rate,  $Q_G$ . The produced bubble chains are specified by their bubble formation frequency,  $f_{bub}$ , their aspect ratio as the ratio of the major to minor axis,  $e$ , their diameter,  $d_b$ , and their rising velocity,  $|\overline{U}_b|$ . Additionally, the resulting Eötvös,  $Eu$  (Eq. 2.24), bubble Reynolds numbers,  $Re_b$  (Eq. 2.23), and Galilei number,  $Gal$  (Eq. 2.26), are summarized.

$d_i$ in $\mu\text{m}$	120	300	600
$Q_G$ in ml/min	$3.00 \pm 0.13$	$6.00 \pm 0.15$	$11.00 \pm 0.19$
$f_{bub}$ in Hz	$28 \pm 3$	$17 \pm 2$	$13 \pm 1$
$e$	$1.35 \pm 0.10$	$2.00 \pm 0.10$	$2.36 \pm 0.10$
$d_b$ in mm	$1.4 \pm 0.1$	$2.4 \pm 0.1$	$3.3 \pm 0.1$
$ \overline{U}_b $ in m/s	0.33	0.33	0.31
$Eu$	0.3	0.8	1.5
$Re_b$	446	780	1010
$Gal$	164	268	567

flow in a water channel. The flow recirculated from the upper tank through the water channel into the lower tank, where the suspension was pumped upwards again by a peristaltic pump (730SN/RE, Watson Marlow, United Kingdom). In order to ensure a uniform suspension of the particles, a mechanical stirrer was installed in the upper tank. Excess suspension, which could not fit into the water channel, flowed over the overflow tank directly into the lower tank to remain in the system. Consequently, the water height was automatically kept constant, and thus, the flow rate depended only on the valve position. During the experiments, the valve was completely open resulting in a flow rate of  $Q_L = 6.1$  l/min. This rate was checked with a volumetric flowmeter and an integrated temperature sensor (VTI 15, SIKA Dr. Siebert & Kühn GmbH & Co. KG, Germany) during all measurements.

Besides a wide range of turbulent length scales, a grid has the advantage of producing isotropic turbulence (Sec. 2.1). Similar to Fig. 2.2b, a grid with cylindrical rods,  $d_r = 1$  mm, and a mesh width,  $M = 3.2$  mm, was used to achieve a Kolmogorov length scale,  $\eta$ , of  $20 \mu\text{m}$  (Eq. 2.12) with the Reynolds number based on the rod diameter,  $Re_d = 180$  (Eq. 2.3). The range of turbulent length scales and their intensity depended on the distance to the grid, according to the energy cascade. With increasing distance to the grid, larger vortices broke down to smaller ones until they reached the Kolmogorov length scale and dissipated. Consequently, bubbles were placed at three distances to the grid ( $p = 1 \dots 3$  in Fig. 3.1b) for different turbulent conditions.

To enhance the number of collisions between bubble and particle, two bubbles were employed simultaneously at two of the three possible vertical positions. The horizontal separation between both bubbles was 10 mm to minimize the effect of the upper bubble on the lower one. Special care was taken to fix the bubble positions in the  $x_1$ - and  $x_3$ -direction, directly downstream from a loop of the grid, in order to generate symmetrical conditions. Each bubble ( $d_b = (2.3 \pm 0.2)$  mm) was produced individually with a needle ( $d_o = 0.9$  mm) and a syringe pump to control their size independently (NE-1000, New Era Pump Systems, Inc.,

USA or Pump 33, Harvard Apparatus, USA). To hinder the detachment of a bubble, the needles were hydrophobized with tetradecyltrimethylammonium bromide (TTAB) (Sigma-Aldrich, USA). Accordingly, the needles were placed into the TTAB solution ( $c_f = 4.14 \text{ g/l}$ ) overnight. Before the installation in the water channel, each needle was rinsed carefully with DI water to remove excess surfactant.

The origin of the coordinate system of the setup depended on the investigated bubble position,  $p$ . For each position, the origin was defined at the location, where the corresponding needle penetrates the wall of the water channel. The  $x_2$ -axis pointed against the main flow direction. The  $x_1$ -axis was perpendicular to the  $x_2$ -axis corresponding to the horizontal alignment of the needle. The  $x_3$ -axis was perpendicular to both axes.

## 3.2. Tomographic Particle Image Velocimetry (TPIV)

### 3.2.1. Principle of TPIV

Particle Image Velocimetry (PIV) is a well-established method to measure the velocity of liquid flows. The basic idea of PIV is that sufficiently small and neutrally buoyant tracers follow the streamlines of the fluid flow with negligible deviation. Thus, the velocity of the tracer particles is assumed to be equal to the fluid velocity. By measuring their position in time, their velocity is calculated by the displacement of tracer particles between two time steps.

Fig. 3.2a illustrates more precisely the measurement principle of PIV for an exemplary flow in a wind tunnel. The flow in the wind tunnel is seeded with tracer particles. The particles in the field of view (FOV) are illuminated twice by a laser sheet with a defined time delay between the pulses. The scattered light of the particles is captured by a camera on two separated frames. During the evaluation, the captured images are divided into subareas, named interrogation windows. The displacement of the particles in the interrogation windows is calculated with a cross-correlation method. Considering the time delay and a calibration of the imaging system, the velocity vector field is computed for the illuminated FOV. This method allows the measurement of the planar velocity field in 2D-2C, meaning the velocity components  $v_1$  and  $v_2$  at the positions  $y_1$  and  $y_2$  inside the laser sheet [145].

An extension of PIV is TPIV, which resolves the instantaneous velocity field,  $\mathbf{V} = (v_1, v_2, v_3)^T$ , in all three directions,  $\mathbf{Y} = (y_1, y_2, y_3)^T$  (Fig. 3.2b). In this case, the tracer particles in a defined volume are illuminated by a laser. The scattered light of the tracer particles is captured with multiple cameras from different viewing angles. The different viewing angles lead to a reconstruction of the particle field as a 3D distribution of light in the form of volume elements, named voxels. One common iterative algebraic reconstruction method is the multiplicative algebraic reconstruction technique (MART) [147] which requires a precise calibration in the order of a fraction of the particle diameter. Otherwise, the lines of sight corresponding to the imaged particle are not intersecting leading to a rapid loss in the reconstruction quality [148].

Therefore, the calibration procedure in TPIV consists of two parts, the usage of a two- or multi-layered calibration plate and a subsequent volumetric self-calibration (VSC) to correct a possible misalignment among the cameras [149]. The main idea of the VSC method is

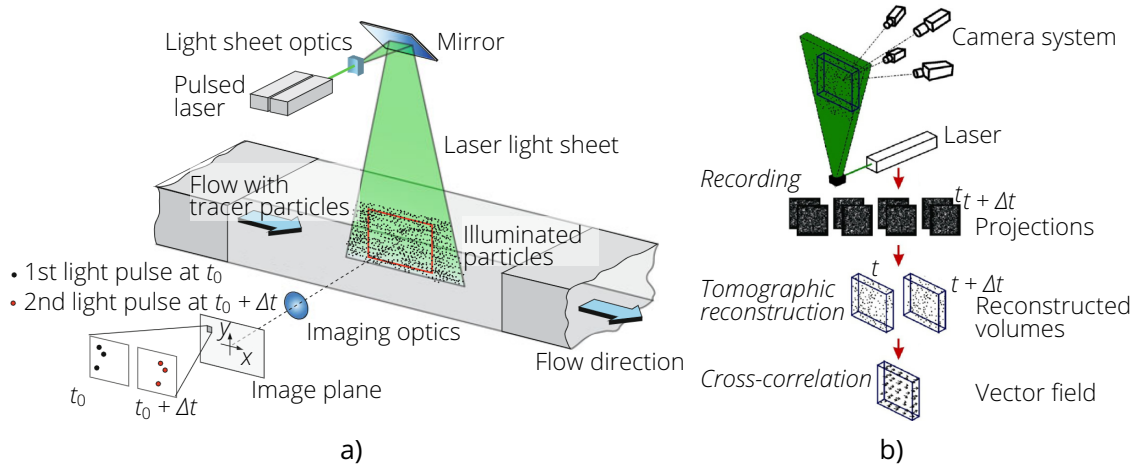


Figure 3.2. Principle of PIV. a) 2D-2C PIV (adapted from [145]). b) 3D-3C TPIV (adapted from [146]).

that particles are detected in the individual images of the cameras and are triangulated in 3D space. Afterwards, the triangulated particle positions are back-projected on the camera images. The offset between original and back-projected particle position is named disparity vector. The disparity vector is calculated for a large number of detected particles for each camera image,  $N_p = O(10^4)$ , providing a statistical estimate of the local disparity vector to correct the calibration for all cameras (Fig. 3.3). This method enables the reduction of the calibration uncertainty to below 0.1 px [145, 146].

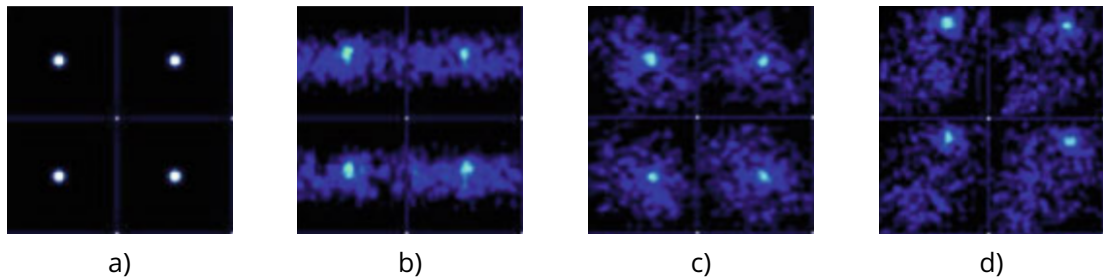


Figure 3.3. Disparity maps for a four-camera tomographic system obtained with the VSC method (adapted from [145]). a) Camera 1 is considered as the reference. b) Camera 2. c) Camera 3. d) Camera 4 shows the triangulation of particle images with displaced peaks, indicating a motion of the camera has occurred after calibration.

The final analysis of the particle displacement between two time-consecutive voxels is performed by a three-dimensional cross-correlation using a multi-grid and iterative window deformation [150]. Further details of TPIV are given by Scarano [146].

### 3.2.2. Measurement setup and tracer particle system

In this dissertation, TPIV was applied to investigate the turbulent liquid flow field around the individual bubbles. The arrangement and recording of TPIV was specific for each ex-

perimental setup. Therefore, Fig. 3.4 and Tab. 3.2 summarize the alignment and recording parameters, respectively, for the bubble column and for the water channel experiments.

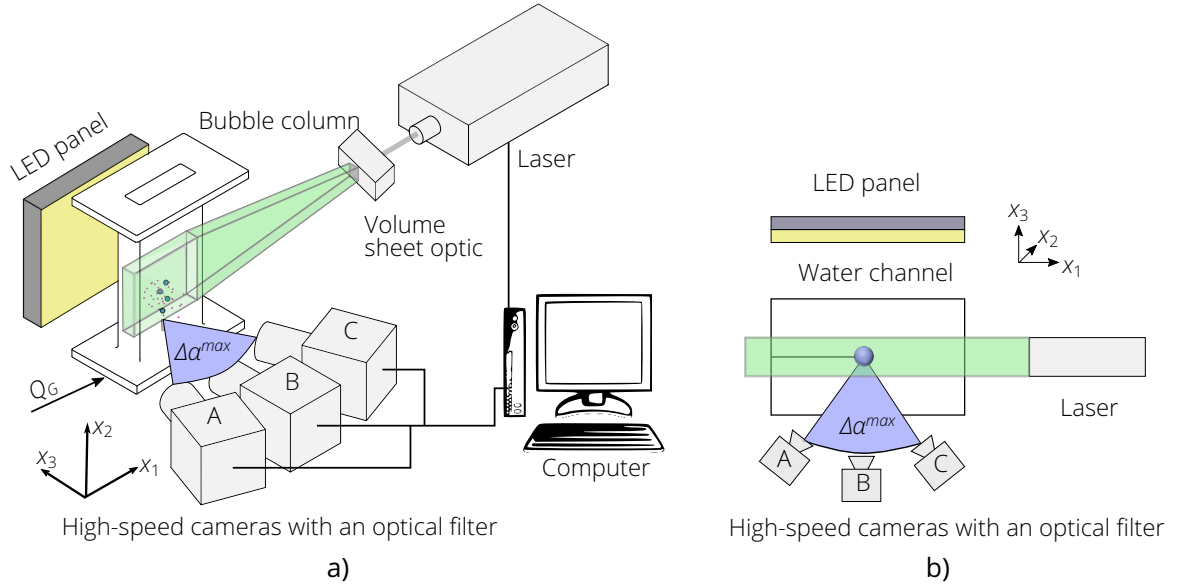


**Figure 3.4.** Arrangement of the experimental rigs in the measurement setup of TPIV and 4D PTV: a) Bubble column. b) Water channel.  $\Delta\alpha^{max}$  denotes the maximum azimuthal angle observable by all three cameras.

During the experiment, images were taken with three CMOS cameras (Phantom VEO 410 L, Vision research, USA). The three cameras were arranged linearly with an overall aperture of approx.  $90^\circ$ . The cameras were equipped with 100 mm objectives (AT-X Pro D, Kenko Tokina Co., Ltd, Japan), to achieve a spatial resolution of  $\Delta x$ . An optical band pass filter was inserted into the optical path to block the reflected laser light from the bubbles. The FOV was illuminated with two light sources: a Nd:YAG laser (DM20-527DH, Photonic Industries, USA, wavelength,  $\lambda = 532$  nm) and a light-emitting diode (LED) backlight (FR, Metaphase Technologies, Inc., USA). The laser light excited the fluorescent particles, whereas the LED backlight enhanced the detectability of the bubble shape. The laser light was arranged perpendicular to the optical axis of camera B. The resulting illuminated volume was aligned to the needle orifice.

To capture the light signals of the tracer particles and the bubbles nearly simultaneously but also on two separate frames, the cameras were run in a double frame mode. In the first frame, the cameras recorded the fluorescent tracer particles which were illuminated by the laser light. Meanwhile, in the second frame, the cameras recorded the shadow of the bubbles, which were illuminated by the LED backlight. The time delay between these two frames was  $2 \mu\text{s}$ . This short time duration ensured that the particles and bubbles scarcely moved between the two frames. In the case of the bubble column, the maximum velocity of the tracer particles was in the order of  $0.4$  m/s; they shifted by only  $0.8 \mu\text{m}$  or  $0.02$  px. In the case of the water channel, the maximum particle velocity was  $|\mathbf{W}| \approx 0.3$  m/s, resulting into a shift of  $0.6 \mu\text{m}$  or  $0.015$  px.

The double frames were recorded in a time-series sequence with a measurement fre-

**Table 3.2.** Recording parameters used during the TPIV measurements in the bubble column (Sec. 3.1.1) and in the water channel (Sec. 3.1.2), where  $\Delta x$  denotes the spatial resolution,  $f_{meas}$  the measurement frequency,  $t_{rec}$  the recording time and  $N_{rec}$  the number of recorded images. The field of view (FOV) is defined as height  $\times$  width  $\times$  depth. The specification of the used calibration targets is summarized in Tab. A.4. The properties of the tracer particle systems are listed in Tab. 3.3.

Experimental setup	Bubble column [41]	Water channel [39]
FOV in mm <sup>3</sup>	38 $\times$ 24 $\times$ 10	46 $\times$ 29 $\times$ 10
$\Delta x$ in mm/px	0.03	0.04
$f_{meas}$ in fps	1300	2000
$t_{rec}$ in s	3.3...7.1	0.5
$N_{rec}$	4290...9230	1000
Calibration target	058-5	025-3.3
Tracer particle system	PS33	PS1

quency,  $f_{meas}$ . The measurement frequency during the recordings in the water channel was increased to enhance the resolution of the turbulent length scales. Each measurement configuration lasted for a recording time duration,  $t_{rec}$ , leading to a corresponding number of double frames,  $N_{rec} = t_{rec}f_{meas}$ . For the bubble column, the recording time equaled the rise of approximately 100 bubbles.

As tracer particles, the fluorescent polystyrene (PS) particles *PS-FluoRed* (microParticles GmbH, Germany) were used. Their material properties are summarized in Tab. 3.3 in the form of particle diameter,  $d_p$ , particle imaged diameter,  $d_{pix}$ , concentration in the suspension,  $c_s$ , associated number of particles per pixel,  $ppp$ , and Stokes number,  $St$  (Eq. 2.38). The Stokes number was calculated with the associated inverse Nyquist frequency as fluid time scale,  $\tau_l = f_N^{-1} = 2f_{meas}^{-1}$ . The particle types varied between the experimental setup, because the monodisperse *PS-FluoRed* particles were not available in such quantities as to reach a sufficient particle concentration in the water channel ( $V_{wc} = 7$  l). Instead, the hetero-dispersed *PS-FluoRed* were applied. All in all, Samimy et al. [151] stated that a value of the Stokes number below  $10^{-1}$  yields an acceptable flow tracing accuracy. This was achieved with these tracer particles (Tab. 3.3).

### 3.2.3. Data analysis

After the recording of the time-series sequences, the data were evaluated according to the work flow illustrated in Fig. 3.5. For the data analysis, the commercial Software DaVis 10.1 (LaVision GmbH, Germany) was employed to calculate the 3D-3C liquid velocity field.

In the image preprocessing, the laser and shadow images were split into particle and bubble images. The shape of the bubble was extracted from the shadow image using the algorithm proposed by Lindken et al. [152]. Firstly, an ellipse was fitted to each bubble contour with the center point,  $x_1$  and  $x_2$ , the semi-major axis,  $a$ , the semi-minor axis,  $c$ , and the tilt angle around the  $x_3$ -axis,  $\theta$ , as marked red in the bubble image in Fig. 3.5. Secondly, the resulting bubble shape was assumed to be an oblate ellipsoid with the values  $a$ ,  $c$  and  $\theta$  extracted



**Table 3.3.** Properties of the tracer particles used during the TPIV measurements in the bubble column (Sec. 3.1.1) and in the water channel (Sec. 3.1.2), where  $d_p$  denotes the particle diameter,  $d_{pix}$  the particle image diameter,  $c_s$  the concentration of the tracer particles in the experimental setup,  $ppp$  the number of particles per pixel and  $St$  the Stokes number. The Stokes number,  $St$  (Eq. 2.38), was calculated with the associated inverse Nyquist frequency as fluid time scale,  $\tau_l = f_N^{-1} = 2 \cdot f_{meas}^{-1}$ . Further information about the physical properties of the particle material are summarized in Tab. A.1.

Experimental setup	Bubble column [41]	Water channel [39]
Symbol	<i>PS33</i>	<i>PS1</i>
Product name	<i>PS-FluoRed</i>	
$d_p$ in $\mu\text{m}$	$33.03 \pm 0.62$	1...20
$d_{pix}$ in px	1...3	1...2
$c_s$ in g/l	0.05...1	0.06...0.1
$ppp$	0.02	0.01
$St$	0.06	0.0001...0.3

from the images of camera *B* (Fig. 3.4). The corresponding volume equivalent diameter was calculated as defined in Eq. 2.22. Finally, the position of the bubble was triangulated based on the center points from all three cameras using the 3D PTV algorithm of Maas et al. [153]. This led to the 3D trajectory of each bubble, in the form of its position,  $\mathbf{X}$ , and its velocity,  $\mathbf{U}$ , for each time step.

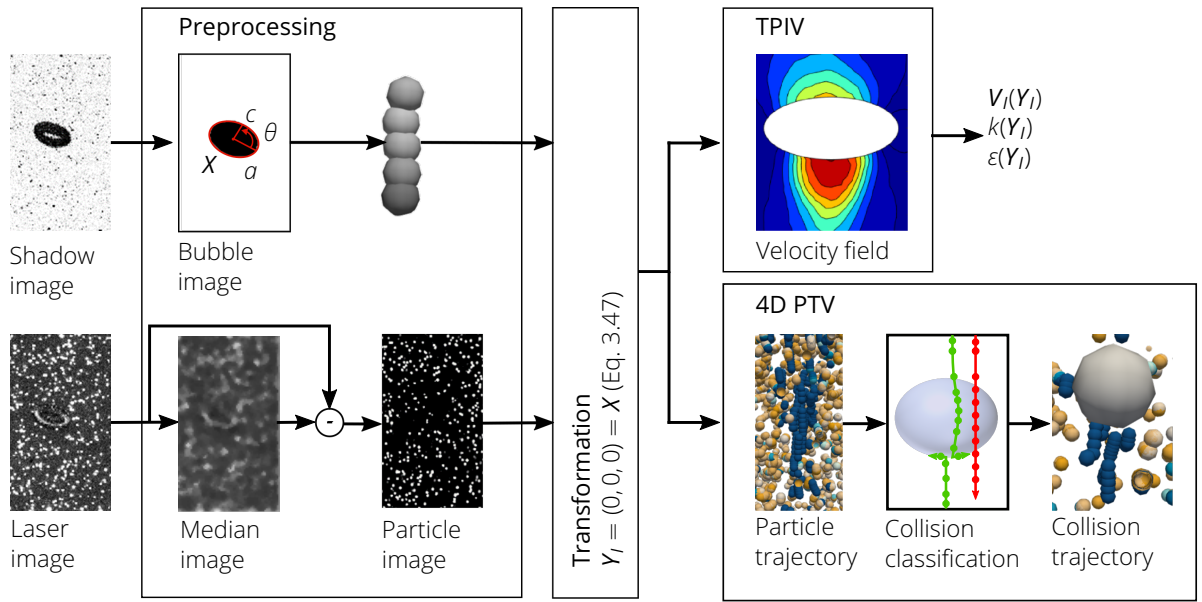


**Figure 3.5.** Workflow of the data analysis for TPIV and 4D PTV. TPIV: Calculation of the 3D-3C velocity field,  $\mathbf{V}_I(\mathbf{Y}_I)$ , turbulent kinetic energy (TKE),  $k(\mathbf{Y}_I)$ , and dissipation rate,  $\epsilon(\mathbf{Y}_I)$ . 4D PTV: Triangulation and classification of the colliding particle trajectories.

The laser images were preprocessed by removing the diffuse fluorescent light that was

reflected by the bubble surface to produce a particle image showing exclusively the particles without any disturbance. To achieve this, a median filter (7 px × 7 px) was applied to the laser image. The filter enabled the removal of small objects such as the tracers, so that only the large bubble surface remained in the median image. Afterwards, the median image was subtracted from the laser image. Remaining unwanted distortions were suppressed using the image preprocessing toolbox from DaVis 10.1. The image preprocessing included the background removal via the subtraction of a sliding minimum filter (3 px × 3 px), a Gaussian smoothing filter (3 px × 3 px) and a sharpening filter.

After the preprocessing, the particle images from different viewing angles were used to reconstruct the particle field as a 3D distribution of light. For the reconstruction, MART was employed as implemented in DaVis 10.1. Subsequently, a 3D cross-correlation method calculated the instantaneous velocity field,  $\mathbf{V}$ , in all three directions,  $\mathbf{Y}$ . Therefore, the reconstructed volume was split into interrogation volumes with a size of 32 px × 32 px × 32 px and an overlap of 75 %. Consequently, a spatial resolution of 0.24 mm × 0.24 mm × 0.24 mm and 0.32 mm × 0.32 mm × 0.32 mm was gained of the vector grid in the bubble column and water channel, respectively.

The described flow field in the global coordinate system corresponded to the Eulerian specification. To also obtain the Lagrangian specification of the flow field, the global coordinate system was transformed into a local coordinate system by a translation of the origin to the individual bubble center,

$$\begin{aligned} Y_l &= Y - X, \\ V_l &= V - U. \end{aligned} \quad (3.47)$$

In the resulting local coordinate system,  $y_{l,2}$  corresponded to the minor axis,  $y_{l,1}$  to the major axis of the bubble and  $y_{l,3}$  to the reconstructed direction.

The measured instantaneous velocity field,  $\mathbf{V}$ , was decomposed into an averaged velocity field,  $\bar{\mathbf{V}}$ , and its fluctuations,  $\mathbf{V}'$  (Fig. 2.1a). The averaging method varied between the data analysis of the freely rising bubble chain and the stagnant bubble. Due to the path instabilities of the freely rising bubble, its tilt angle varied over time. Therefore, a conditional average based on the tilt angle,  $\theta$ , was performed for all bubbles,

$$\bar{\mathbf{V}}_i = \frac{1}{N(\theta_{i,0} < \theta(t) \leq \theta_{i,1})} \sum_{t=0}^T \mathbf{V}_i(\theta_{i,0} < \theta(t) \leq \theta_{i,1}, t). \quad (3.48)$$

Each conditional group was defined by a start tilt angle,  $\theta_{i,0} = 5^\circ n_i$ , and an end tilt angle,  $\theta_{i,1} = 5^\circ n_{i+1}$ , for  $n = \{-3, -2, -1, 0, 1, 2, 3\}$ , covering the overall tilt angle range from  $-15^\circ$  to  $15^\circ$ . Consequently, the fluctuations,  $\mathbf{V}' = \mathbf{V} - \bar{\mathbf{V}}$ , depended on the tilt angle and varied with the conditional group, too. The averaging method in the case of the stagnant bubble in the water channel differed from the previous one. A time-averaging method was applied using  $N_{rec}$  consecutive time steps (Eq. 2.5) because the bubble position and tilt angle remained nearly constant during the measurement time.

Below the quantities depending on the measured averaged velocity field,  $\bar{\mathbf{V}}$ , and its fluctuations,  $\mathbf{V}'$ , are summarized, in particular the magnitude of the velocity field,  $|\bar{\mathbf{V}}|$ , the vorticity

vector,  $\boldsymbol{\omega}$ , TKE,  $k$ , degree of turbulence,  $Tu_{ij}$ , and dissipation rate,  $\varepsilon$ . The magnitude of the liquid velocity field was computed as

$$|\bar{\mathbf{V}}| = \sqrt{\bar{v}_1^2 + \bar{v}_2^2 + \bar{v}_3^2}. \quad (3.49)$$

The three components of the vorticity vector,  $\boldsymbol{\omega}$ , were calculated as

$$\omega_1 = \frac{v_3}{y_1} - \frac{v_1}{y_3} \quad (3.50a)$$

$$\omega_2 = \frac{v_2}{y_3} - \frac{v_3}{y_2} \quad (3.50b)$$

$$\omega_3 = \frac{v_2}{y_1} - \frac{v_1}{y_2}. \quad (3.50c)$$

The turbulent parameters depended on the fluctuations,  $\mathbf{V}'$ , and comprised the TKE

$$k = \frac{1}{2} \overline{v'_i v'_i}, \quad (3.51)$$

and the degree of turbulence,

$$Tu_{ij} = \frac{\sqrt{R_{ij}}}{|\bar{\mathbf{V}}|} \text{ with } i, j \in 1, 2, 3, \quad (3.52)$$

where  $R_{ij} = \overline{v'_i v'_j}$  denotes the Reynolds stress tensor component. Additionally, the dissipation rate was defined as [154]

$$\varepsilon = \nu \overline{\frac{\partial v_i}{\partial y_k} \frac{\partial v_i}{\partial y_k}}, \quad (3.53)$$

where  $\partial v_i / \partial y_k$  denotes the gradient of the instantaneous velocity, using either the conditional averaged values in the bubble column or the time-averaged values in the water channel.

A deeper insight into the turbulent energy cascade was gained by calculating the power spectrum,  $\mathbf{E}$ , based on the wavenumber,  $\kappa$ . In particular, at a given point,  $\mathbf{Y}$ , the fluctuation components,  $\mathbf{V}'(\mathbf{Y}, t)$ , were transformed from the time into the frequency domain,  $f_e$ ,

$$\mathbf{E} = \frac{1}{2\pi} \mathbf{F} \times \mathbf{F}^*, \quad (3.54)$$

where  $\mathbf{F}$  denotes the discrete-time Fourier transform and  $\mathbf{F}^*$  its complex conjugate. Subsequently, the frequencies were converted into their wavenumber using the frozen turbulence approach by Taylor [155]

$$\kappa = \frac{2\pi}{|\bar{\mathbf{V}}|} f_e. \quad (3.55)$$

Typical wavenumbers of a turbulent flow field are the wavenumber of the integral scale,

$$\kappa_\lambda = \frac{2\pi}{|\bar{\mathbf{V}}|} \frac{1}{\tau_\lambda}, \quad (3.56)$$

and Kolomogorov scale,

$$\kappa_\eta = \frac{2\pi}{|\bar{V}|} \frac{1}{\tau_\eta}, \quad (3.57)$$

where  $\tau_\lambda$  (Eq. 2.15) denotes the integral time scale and  $\tau_\eta$  the Kolomogorov time scale,

$$\tau_\eta = \left(\frac{\nu}{\varepsilon}\right)^{1/2}. \quad (3.58)$$

In the same way, the wavenumbers associated to the particle motion and to the bubble wake were calculated, named the particle wavenumber,  $\kappa_p$ ,

$$\kappa_p = \frac{2\pi}{|\bar{V}|} \frac{1}{\tau_p} = \frac{36\pi\mu}{(\rho_s + 0.5\rho_L)d_p^2 |\bar{V}|}, \quad (3.59)$$

where  $\tau_p$  (Eq. 2.39) denotes the particle response time.

The two typical wavenumbers of the bubble wake were the shedding wavenumber,

$$\kappa_s = \frac{2\pi}{|\mathbf{U}_b|} \frac{1}{\tau_s} = \frac{0.4\pi}{d_b}, \quad (3.60)$$

and the Kolomogorov wavenumber of the bubble wake,

$$\kappa_\eta^b = \frac{2\pi}{|\mathbf{U}_b|} \frac{1}{\tau_\eta} = \frac{2\pi}{d_b} Re_b^{1/2}, \quad (3.61)$$

where  $\mathbf{U}_b$  denotes the bubble rising velocity,  $\tau_s = d_b Sr^{-1} |\bar{\mathbf{U}}_b|^{-1}$  the shedding time scale,  $Sr = 0.21$  the Strouhal number (Sec. 2.1.2) and  $\tau_\eta^b = d_b Re_b^{-1/2} \bar{\mathbf{U}}_b^{-1}$  the Kolmogorov time scale of the bubble wake [156].

### 3.2.4. Uncertainty analysis

Although special care was taken for the alignment, calibration and conducting experiments, still uncertainties remained to a limited extend. The main quantities affected by these uncertainties were the bubble shape and the liquid velocity field.

For the bubble column, one parameter to describe the bubble shape was the volume equivalent diameter (Eq. 2.22). The bubble diameter was analyzed based on the planar projection of the bubble shape as observed by camera *B* (Fig. 3.4). This method was subjected to errors due to the tilt angle,  $\beta$ , of the bubble around the  $x_1$ -axis. As seen in Fig. 3.6a, the measured minor axis in the image plane,  $c$ , was larger than the actual minor axis of the bubble,  $c^*$ . Bröder et al. [157] calculated the maximum increase of the estimated area-equivalent diameter to the real diameter based on the tilt angle,  $\beta$ , and the eccentricity of the bubble,  $e$ . Adapting their methods for the uncertainty of the volume equivalent diameter led to

$$\frac{d_b}{d_b^*} = (e^2 \sin^2 \beta + \cos^2 \beta)^{1/6}. \quad (3.62)$$

Fig. 3.6b illustrates the uncertainty of the maximum increase of the estimated volume equiv-

alent diameter to the real diameter for all three bubble size configurations. However, the tilt angle around the  $x_1$ -axis,  $\beta$ , could not be measured in the current experimental setup. Instead, it was assumed that  $\beta$  was in the same order of magnitude as the measured tilt angle around the  $x_3$ -axis,  $\theta$  (Fig. 3.6c). Consequently, the measured volume equivalent bubble diameter was approximately 10 % larger than the real bubble diameter, assuming an oblate ellipsoidal shape of the bubbles.

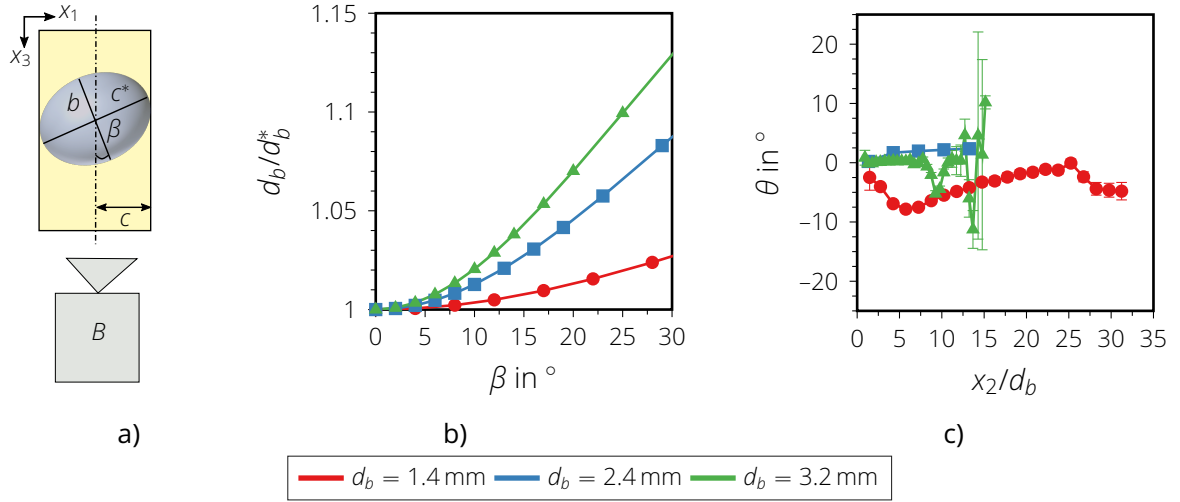


**Figure 3.6.** Uncertainty of the volume equivalent bubble diameter,  $d_b$  (Eq. 2.22), based on the tilt angle of the bubble around the  $x_1$ -axis,  $\beta$ . a) Definition of the tilt angle,  $\beta$ , the measured minor axis in the image plane,  $c$ , and the actual minor axis of the ellipsoid,  $c^*$  (adapted from [157]). b) Expansion of the estimated  $d_b$  due to the tilting of the bubble (estimated diameter normalized by the real diameter,  $d_b^*$ , as defined in Eq. 3.62). c) Measured tilt angle of the bubble around the  $x_3$ -axis,  $\theta$ , along the normalized  $x_2$ -axis.

During the measurements of the liquid phase velocity, random uncertainties occurred e.g. due to the particle image size, particle image density, turbulent fluctuations, and interrogation window size. These uncertainties of the velocity field,  $\Xi(u_i)$ , and degree of turbulence,  $\Xi(Tu_{ij})$ , were quantified with a confidence interval of 95.4 % as

$$\Xi(u_i) = \sigma_i \sqrt{\frac{1}{N_{rec}}}, \quad (3.63)$$

with the standard deviation,

$$\sigma_i = \sqrt{\frac{1}{N_{rec} - 1} \sum_{j=1}^{N_{rec}} (u_{ij} - \bar{u}_{ij})^2}. \quad (3.64)$$

The uncertainty of the degree of turbulence,  $\Xi(Tu_{ij})$ , was calculated based on the propagation

of uncertainty, incorporating the uncertainty of the Reynolds stress,

$$\Xi(Tu_{ij}) = \sigma_i \sigma_j \sqrt{\frac{1 + \rho_{ij}^2}{N_{rec} - 1}}, \quad (3.65)$$

where  $\rho_{ij}$  denotes the cross-correlation coefficient. This yields to

$$\Xi(Tu_{ij}) = \left| \frac{\partial Tu_{ij}}{\partial R_{ij}} \right| \cdot \Xi(|\bar{U}|) + \left| \frac{\partial Tu_{ij}}{\partial |\bar{U}|} \right| \cdot \Xi(R_{ij}) \quad (3.66)$$

$$= \left| \frac{1}{2\sqrt{R_{ij}}} |\bar{U}| \right| \cdot \Xi(|\bar{U}|) + \left| \frac{\sqrt{R_{ij}}}{|\bar{U}|^2} \right| \cdot \Xi(R_{ij}). \quad (3.67)$$

These methods to quantify the uncertainty of PIV measurements have been described previously by Sciacchitano et al. [158], further details can be found there.

Furthermore, these random uncertainties can affect the spatial power spectrum. The resolution of the turbulent length scales in the power spectrum was limited spatially by the cut-off wavenumber,  $\kappa_c$ , and temporally by the Nyquist frequency,  $f_N = 0.5f_{meas}$ . The cut-off wavenumber,

$$\kappa_c = \frac{2.8}{IW} = 2.92 \text{ 1/mm} \dots 8.75 \text{ 1/mm}, \quad (3.68)$$

depends on  $IW$  the interrogation window size, because the interrogation window caused a low-pass filtering of the data [159]. Converting the Nyquist frequency into the Nyquist wavenumber,  $\kappa_n = 13.6 \text{ 1/mm} \dots 69.8 \text{ 1/mm}$ , via the frozen turbulence approach (Eq. 3.55) reveals that for both experimental setups the cut-off wavenumber is smaller than the Nyquist wavenumber. Therefore, the cut-off wavenumber is the significant limit of the turbulent length scales in the TPIV measurement. However, the cut-off wavenumber represents only the upper limit of the resolvable wavenumber [160]. Due to noise in the TPIV measurement, the maximum measurable wavenumber could be smaller.

Another source of uncertainty in TPIV was the reconstruction noise, known as ghost particles [146]. Due to an imperfect calibration or a limited number of camera views, particles could artificially be added into the volume elements during the reconstruction process. These ghost particles could bias the cross-correlation. Meaning, the physical location of the ghost particles differs from the location of the actual particles. Consequently, ghost particles have a smoothing effect on the resulting velocity field [161].

For example, Fig. 3.7 illustrates the formation of ghost particles due to a limited number of camera views and a high seeding density. If two particles are observed by two cameras, the reconstruction algorithm would compute four possible locations of these particles as shown in Fig. 3.7a. This ambiguity can be solved by adding a third camera view (Fig. 3.7b). Additionally, ambiguities can occur due to a high seeding concentration of the tracer particles in the FOV (Fig. 3.7c). An accurate reconstruction is only possible, as long as most of the tracer particles are imaged distinctly [146].

To evaluate the number of ghost particles in the reconstruction volume, the light intensities of the particles were analyzed along the reconstructed  $y_3$ -axis (Fig. 3.8) [146]. Here, the reconstruction range in the  $y_3$ -axis was intentionally larger than the illuminated volume.

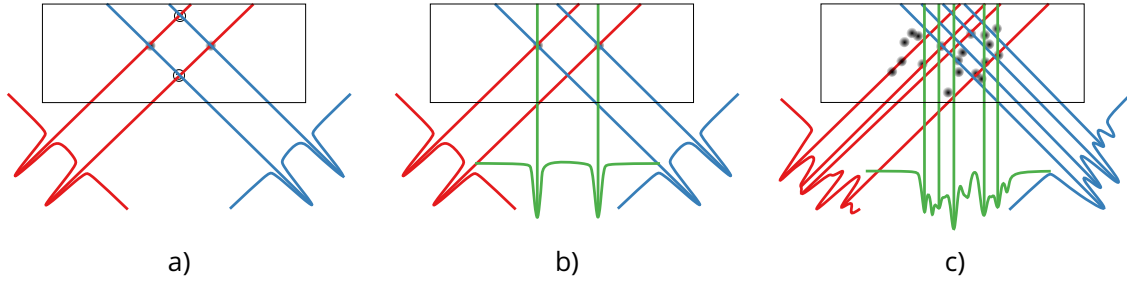


**Figure 3.7.** Formation of ghost particles (adapted from [146]). a) Two camera views for two particles yield four potential reconstructions. The view from camera 1 and camera 2 is marked red and blue, respectively. Potential ghost particles are illustrated as  $\odot$ . b) Adding a third camera view (marked green) eliminates potential ghost particles. c) Increasing the seeding density worsens a distinctive imaging of the particles.

Inside the illuminated volume, real and ghost particles were reconstructed, whereas outside the illuminated volume, only ghost particles were reconstructed. Consequently, the signal-to-noise ratio,  $SNR$ , between the averaged intensity inside,  $I_i$ , and the averaged intensity outside,  $I_o$ , of the illuminated volume gives an estimation of the ratio of the ghost particles,

$$SNR = \frac{I_i}{I_o}. \quad (3.69)$$

According to Scarano [146], the reconstruction of the tomographic experiments is of good quality if  $SNR \geq 2$ . Fig. 3.8 illustrates the  $SNR$  values averaged over 30 time steps for both experimental setups.  $SNR$  values below 2 are reached mainly on the edges of the reconstruction volume, whereas inside the  $SNR$  values exceed 2. Additionally, the number of particles per pixel,  $ppp$ , was below 0.05 (Tab. 3.3), as recommended by [162]. Consequently, the quality of the particle reconstruction was sufficient for the conducted experiments [146, 162].

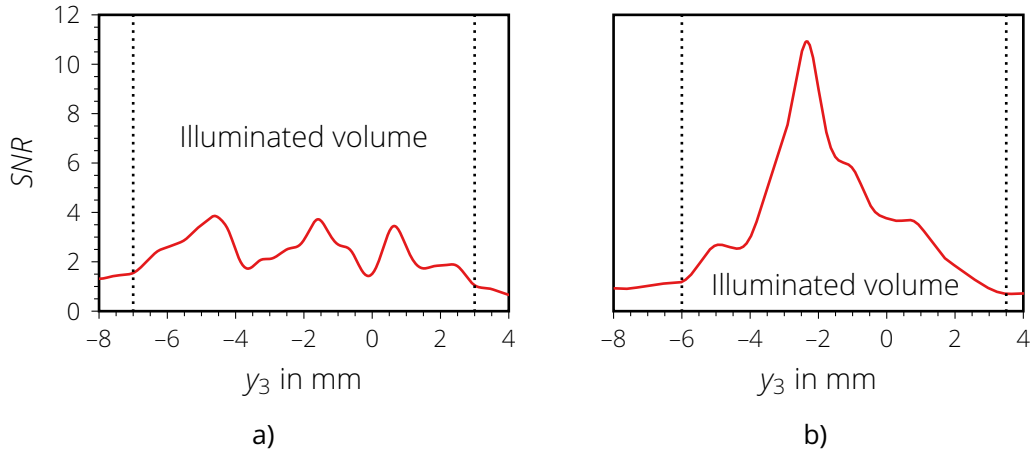


**Figure 3.8.** Signal-to-noise,  $SNR$ , profiles along the reconstructed  $y_3$ -axis in a) the bubble column and b) in the water channel. The dotted lines mark the illuminated volume.

### 3.3. 4D Particle Tracking Velocimetry (PTV)

#### 3.3.1. Principle of PTV and Shake-the-box (STB)

Typically, PTV is another method to measure the liquid field velocity by triangulating the individual particle trajectories [145, 163, 164]. It allows to enhance the spatial resolution and the measurement accuracy compared to correlation-based approaches [145]. If the trajectory of inertial particles (e.g. glass beads [165–167]) are tracked instead of small and neutrally buoyant tracer particles, the particle dynamics of the solid phase can also be investigated with PTV. However, one of the main challenges of PTV is the matching of the corresponding particle in each camera image and its tracking over time, especially for a high particle seeding concentration where the particle images start to overlap [145, 168, 169].

One way to overcome the challenge of the particle seeding concentration is the STB algorithm by Schanz et al. [170]. Instead of the individual treatment of each particle snapshot, the STB method utilizes as much temporal and spatial information of the particle trajectory as possible to predict the consecutive particle position. Thus, nearly all ghost particles are suppressed because of their shorter lifetime compared to actual particles. If no information of the particle trajectory is available, the particle positions are triangulated accurately with the iterative particle reconstruction (IPR) algorithm by Wieneke [171]. To put it simply, the IPR detects the 2D particle position in each image plane and matches the 2D particle positions among all camera views, to gain the possible 3D particle position. If the difference between projected and measured 2D particle location remains below a set triangulation error, the 3D particle position is valid. Otherwise, the particle is neglected for the further analysis.

Fig. 3.9 illustrates the main steps of the STB algorithm in the convergence phase. To reach the convergence stage, the particle positions are triangulated with the IPR algorithm over approx. four time steps to gain reliable particle trajectories. Afterwards, the positions of the known particle trajectories are predicted for the subsequent time step (Fig. 3.9). If the predicted particle positions do not exactly fit the particle position in the image, the predicted position is shifted by a fraction of a voxel to minimize the uncertainty, named shaking. The remaining particles in the residual image are triangulated with the IPR algorithm. If particles are overlapping, the number of utilized cameras are reduced during the triangulation leading to a nearly blank residual image. Therefore, the STB method enables a rapid triangulation of the 3D particle trajectories for a high particle seeding concentration.

Similar to TPIV, an accurate calibration is required, which is achieved by a combination of the volumetric self-calibration (VSC) method [149] and an optical transfer function (OTF) [172]. The first one assures the precise location of the projected particle position, whereas the latter one accounts for particle shape distortions, e.g. due to astigmatisms. The prediction of the OTF can be incorporated into the VSC, where not only the position but also the shape parameters are extracted and averaged for all triangulated particles in a certain sub-volume.



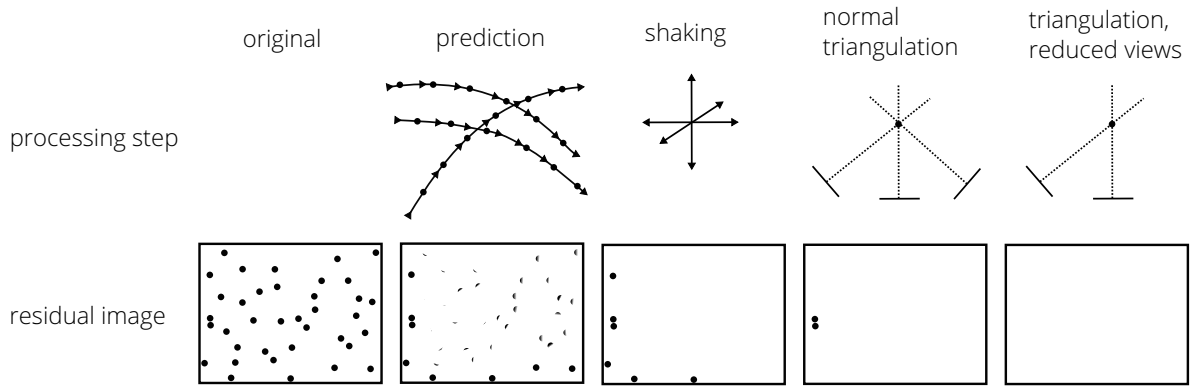


**Figure 3.9.** Schematic description of the STB procedure for one time-step in the converged state by illustrating the effects of the different computation steps on the residual image of one single camera out of multiple (from [170]).

### 3.3.2. Measurement setup and particle systems to model mineral particles

In this dissertation, 4D PTV was applied to investigate the collisions between particles and bubbles. Meaning, the trajectories of model particles were triangulated and classified according to their collision performance. The trajectories comprised the particle position  $\mathbf{Z}(t)$  and velocity  $\mathbf{W}(t)$  for each time step. The utilized measurement setup of 4D PTV was essentially the same as for TPIV. To avoid duplications, please refer to Sec. 3.2.2 for the description of the measurement setup. The corresponding experimental recording parameters for 4D PTV are summarized in Tab. 3.4.

**Table 3.4.** Recording parameters used during the 4D PTV measurements in the bubble column (Sec. 3.1.1) and in the water channel (Sec. 3.1.2), where  $\Delta x$  denotes the spatial resolution,  $f_{meas}$  the measurement frequency,  $t_{rec}$  the recording time and  $N_{rec}$  the number of recorded images. The field of view (FOV) is defined as height  $\times$  width  $\times$  depth. The specifications of the used calibration targets are summarized in Tab. A.4. The properties of the model particle systems are listed in Tab. 3.5.

Experimental setup	Bubble column [41]	Water channel	
FOV in mm <sup>3</sup>	38 $\times$ 24 $\times$ 10	46 $\times$ 29 $\times$ 10	
$\Delta x$ in mm/px	0.03	0.04	
$f_{meas}$ in fps	1300	2000	1000
$t_{rec}$ in s	23.9	9.3	25.9
$N_{rec}$	31 120	18 672	25 923
Calibration target	058-5	025-3.3	
Model particle system	PS33, PS95	PS33	PMMA200

The main difference in the measurement setup between TPIV and 4D PTV lies in the applied particle system. The major requirement on the tracer system in TPIV was to be sufficiently small and neutrally buoyant to follow the streamlines of the fluid flow with negligible deviation. In contrast, the model particle systems for 4D PTV were chosen based on the following criteria

- applicability to 4D PTV and PEPT,
- comparability to mineral particles in froth flotation and
- hydrophobicity.

The chosen model particle systems consisted of either monodispersed fluorescent PS particles, *PS-FluoRed* (microParticles GmbH, Germany), or heterodispersed fluorescent polymethylmethacrylate (PMMA) particles, *PMMA-RhB* (microParticles GmbH, Germany). The properties of these particle systems and their associated experimental setup are summarized in Tab. 3.5. All model particles had a spherical shape.

**Table 3.5.** Model particle systems used during the 4D PTV measurements in the bubble column (Sec. 3.1.1) and in the water channel (Sec. 3.1.2), where  $d_p$  denotes the particle diameter,  $d_{pix}$  the particle image diameter,  $c_s$  the concentration of the particles in the experimental setup,  $n_p$  the particle number density,  $St$  the Stokes number (Eq. 2.38),  $Re_p$  the particle Reynolds number (Eq. 2.36) and  $Ar$  the Archimedes number (Eq. 2.40). The Stokes number,  $St$  (Eq. 2.38), was calculated with the associated inverse Nyquist frequency as fluid time scale,  $\tau_l = f_N^{-1} = 2 \cdot f_{meas}^{-1}$ . Further information about the physical properties of the particle material are summarized in Tab. A.1.

Experimental setup Symbol	Bubble column [41]		Water channel	
	<i>PS33</i>	<i>PS95</i>	<i>PS33</i>	<i>PMMA200</i>
Product name	<i>PS-FluoRed</i>	<i>PS-FluoRed</i>	<i>PS-FluoRed</i>	<i>PMMA-RhB</i>
$d_p$ in $\mu\text{m}$	$33.03 \pm 0.62$	$95.07 \pm 1.50$	$33.03 \pm 0.62$	200...400
$d_{pix}$ in px	2...3	3...4	2...3	5...10
$c_s$ in g/l	0.03	0.05	0.01...0.02	0.3...1.7
$n_p$ in $1/\text{m}^3$	$1.5 \cdot 10^9$	$6.4 \cdot 10^9$	$1 \cdot 10^9$	$1.8 \cdot 10^7$
$St$	0.01	0.18	0.02	0.7...2.7
$Re_p$	0.0005	0.01	0.0005	0.8...4.9
$Ar$	0.19	0.44	0.19	16...127

The particle systems are applicable to 4D PTV if they are fluorescent and their exciting wavelength matches the wavelength of the laser light (532 nm). As seen in Tab. A.1, this is the case for *PS-FluoRed* and *PMMA-RhB*. The applicability of these model particle systems to PEPT is discussed in detail in Sec. 3.4.2.

A comparability of the model particle system to mineral particles was achieved if the model particles deviate in the same way from the fluid streamlines as the mineral ones [17]. Meaning, the Stokes number,  $St$  (Eq. 2.38), the particle Reynolds number,  $Re_p$  (Eq. 2.36) and Archimedes number,  $Ar$  (Eq. 2.40) are in the same order of magnitude (Sec. 2.3.1).

Taking, for example, the widespread ore galena ( $\text{PbS}$ ,  $\rho_s = 7.85 \text{ g/cm}^3$ ) with a particle diameter between  $15 \mu\text{m}$  and  $40 \mu\text{m}$ ,  $St$  is in the order of 0.01 to 0.17,  $Re_p$  in the order of 0.01 to 0.2 and  $Ar$  ranges between 0.22 and 4.3. This is also achieved with *PS33* and *PS95* particles as seen in Tab. 3.5. Consequently, it was possible to use *PS33* and *PS95* as model particle systems for the example of fine particle flotation with galena in the size range between  $15 \mu\text{m}$  and  $40 \mu\text{m}$ . The larger *PMMA200* particles for the PEPT measurements are not comparable with fine mineral particles. Instead, they are more suitable to observe the collision behavior

of coarse mineral particles. In the case of galena, *PMMA200* particles could mimic the motion of galena particles in the size range between 90  $\mu\text{m}$  and 180  $\mu\text{m}$ .

To prove that the fluorescent *PMMA-RhB* and *PS-FluoRed* particles are hydrophobic, their contact angle,  $\Theta$ , was measured in reference to the used liquid phase. The contact angle is defined as the angle at which the liquid–gas interface meets the solid–liquid interface, leading to the Young’s relation [173]

$$\sigma_{gs} = \sigma_{ls} + \sigma_{lg} \cdot \cos \Theta, \quad (3.70)$$

where  $\sigma_{lg}$  denotes the interfacial tension between liquid and gas phase,  $\sigma_{ls}$  the interfacial tension between liquid and solid phase, and  $\sigma_{gs}$  the interfacial tension between gas and solid phase (Fig. A.1b). Generally, a contact angle below 90° indicates a hydrophilic surface, whereas above 90° the solid surface would be classified as hydrophobic [174].

To measure these contact angles, the Washburn method for porous media [175] was used based on the measurement of the free surface energy with the force tensiometer K100 (KRÜSS GmbH, Germany). Appendix A.2 describes in detail this measurement technique and summarizes the received results. All in all, the resulting contact angles exceeded 90° (Tab. A.2) and proved that the suspended *PS-FluoRed* and *PMMA-RhB* particles were hydrophobic in DI water with 0.01 M KCl.

### 3.3.3. Identification of particle trajectories colliding with bubbles

As the measurement setup of 4D PTV was essentially the same as for TPIV, also the data analysis of 4D PTV was partially based on the TPIV data analysis (Fig. 3.5). In particular, the same preprocessing methods were applied for the images from the 4D PTV to define the bubble properties and to enhance the particle appearance (Sec. 3.2.3). The main difference among the data analysis methods occurred in the last step. In the TPIV analysis, the particle images were used to calculate the instantaneous velocity field around the bubble. In contrast, the 4D PTV analysis comprised the triangulation and the classification of the colliding particle trajectories.

After the preprocessing of the captured 4D PTV images, the particle trajectories were triangulated, using the STB method [170] as implemented in DaVis 10.1. The parameters of the triangulation algorithm differed to account for variations in the particle trajectories during the collision process. In total, each set of recorded images was analyzed with up to eight different settings. These settings were modified in terms of the allowed triangulation error ( $\bar{\epsilon}(\mathbf{Z}) = 2 \text{ voxel} \dots 4 \text{ voxel}$ ), the threshold of the used particle intensity and the minimum distance between two triangulated particle positions. The resulting particle trajectories of each parameter variation were combined into one particle trajectories ensemble. Overlapping particle positions/trajectories were removed and possible associated trajectories were linked using the nearest neighbor algorithm [176].

After the generation of the trajectory ensemble, the trajectories were preprocessed in three steps for the collision classification. Firstly, the particle trajectories were assigned to the closest bubble and were transformed into the local bubble coordinate system (Eq. 3.47),  $\mathbf{Z}_l$  and  $\mathbf{W}_l$ . Further, the particle positions were converted into the spherical coordinate system. This included the radial distance,  $r$ , polar angle,  $\theta$ , and azimuthal angle,  $\alpha$ , as illustrated in

Fig. 3.10a and d. The coordinates were transformed as

$$r = \sqrt{z_{l,1}^2 + z_{l,2}^2 + z_{l,3}^2}, \quad (3.71a)$$

$$\theta = \arccos \frac{z_{l,3}}{r} \text{ and} \quad (3.71b)$$

$$\alpha = \arctan \frac{z_{l,2}}{z_{l,1}}. \quad (3.71c)$$

Additionally, the radial velocity was computed as

$$w_r = \frac{\partial r}{\partial t}. \quad (3.72)$$

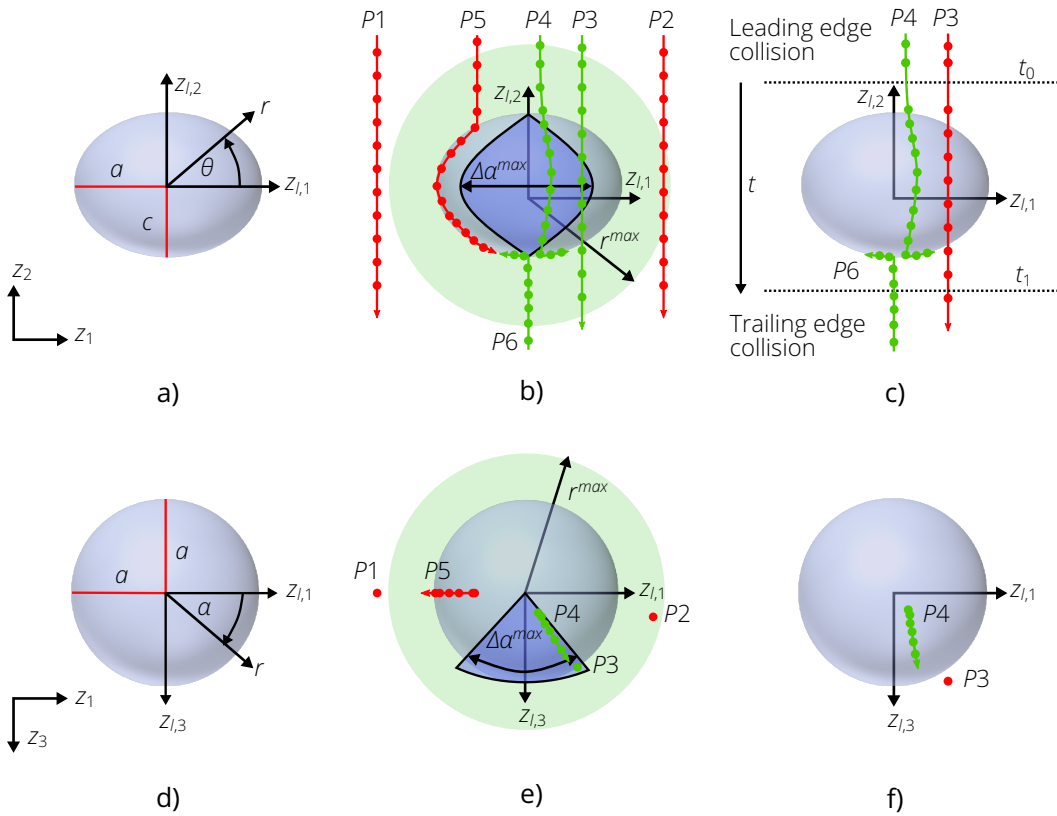


**Figure 3.10.** Workflow to classify particle collision trajectories. The first row displays the side view in the  $z_{l,1}z_{l,2}$ -plane. The second row displays the top view in the  $z_{l,1}z_{l,3}$ -plane. a), d) Definition of the global and the local, spherical coordinate system. b), e) Filtering out of particle trajectories (red) which are not compliant with the criteria in Eq. 3.73. The remaining valid particle trajectories are marked in green. c), f) Identification of colliding particle trajectories according to criteria in Eq. 3.75 and distinction between leading ( $0^\circ \leq \alpha < 180^\circ$ ) and trailing edge collision ( $180^\circ \leq \alpha < 360^\circ$ ).

Secondly, the first set of criteria focused on the location of the particle trajectory, in particular its radial distance,  $r$  (Eq. 3.71a), and its azimuthal angle,  $\alpha$  (Eq. 3.71b), in the spherical

coordinate system,

$$r < r^{max} = 1.6r_b \quad (3.73a)$$

$$45^\circ < \alpha < 135^\circ, \quad (3.73b)$$

where  $r_b = d_b/2$  denotes the bubble radius. These criteria (Eq. 3.73) ensured that only those trajectories remained that passed the bubble in a radial distance smaller than  $r^{max}$  (e.g.  $P1$  in Fig. 3.10b) and were detected by all three cameras.

The threshold  $r^{max}$  (Eq. 3.73a) was estimated based on the maximum grazing radius,

$$r_c = \bar{a} + d_p \approx 1 \dots 1.4\bar{r}_b \quad (3.74)$$

because it is the maximum radius where a particle interacts with a bubble [49]. To account for uncertainties in bubble shape and particle trajectory triangulation,  $r^{max}$  slightly exceeded  $r_c$ , resulting in  $r^{max} = 1.6r_b$ .

The latter criterion (Eq. 3.73b) came into effect if the azimuthal angle of the particle position,  $\alpha$ , was beyond the maximum detection angle of the cameras. The triangulation of particles based on two camera views could result in a higher uncertainty of the particle location. Therefore, the azimuthal angle of a valid particle position,  $\alpha$ , had to be between  $45^\circ$  and  $135^\circ$ , as marked in blue with  $\Delta\alpha^{max} = 90^\circ$  in Fig. 3.10b and e. If the particle was in this sphere segment, the particle was visible to all three cameras. An example is illustrated in Fig. 3.10d. Particle  $P2$  and  $P5$  do not satisfy criterion Eq. 3.73b, thus, they are filtered out.

Thirdly, a particle trajectory was classified as colliding (Fig. 3.10c and f) if the second set of criteria regarding the radial velocity,  $w_r$ , and residence time of the particle in the vicinity of the bubble,  $t_r$ , was fulfilled,

$$|w_r| < w_r^{max} = 0.05 \text{ m/s} \quad (3.75a)$$

$$t_r > t_r^{max} = 8 \text{ ms.} \quad (3.75b)$$

The second set of criteria guaranteed that a colliding particle moved towards the bubble surface with a radial velocity,  $w_r$ , decelerating over time to reach a value below  $w_r^{max}$ . Additionally, this particle remained for an extended time period,  $t_r^{max}$ , in the vicinity of the bubble.

For a particle approaching a bubble, the radial velocity decelerated until it reached theoretically 0 m/s at the collision point. A threshold of the radial velocity was chosen to account for uncertainties,  $w_r^{max} = -0.05 \text{ m/s}$ . The deceleration of the colliding particle trajectories was accompanied by a larger residence time,  $t_r$ , compared to a non-interacting particle trajectory. The average residence time of a non-interacting particle passing by the bubble was

$$t_r = \frac{2 \cdot \bar{c}}{\bar{u}_b} \quad (3.76)$$

covering a distance of twice the minor axis of the bubble,  $c$ . In the bubble column, the classification criteria,  $t_r^{max}$ , was set to 8 ms ( $\bar{c} = 1.2 \text{ mm}$ ,  $\bar{u}_b = 0.30 \text{ m/s}$ ) and in the water channel,  $t_r^{max} = 14 \text{ ms}$  ( $\bar{c} = 1.2 \text{ mm}$ ,  $\bar{u}_b = |\bar{V}| = 0.18 \text{ m/s}$ ).

Additionally, the analysis distinguished between leading ( $P4$ ) and trailing edge ( $P6$ ) colli-

sions. If the particle approached the bubble from above,  $0^\circ < \alpha < 180^\circ$ , the collision was classified as leading edge collision. Otherwise, the collision was classified as a trailing edge collision.

The detected particle collisions were used to calculate the collision frequency,

$$Z_{pb}^E = \frac{4 \cdot N_c}{N_p \cdot N_b \cdot \Delta t}, \quad (3.77)$$

with  $N_c$  and  $N_b$  as the total number of collisions and bubbles, respectively, and  $\Delta t$  as the measurement duration. The particle number densities, for each experimental setup, are summarized in Tab. 3.5.

The total number of collisions during experiments was restricted to the forequarter of the bubble surface due to the limited FOV. To also account for the particle collisions outside of the FOV, the multiplication factor of 4 was added to Eq. 3.77 assuming the same distribution of the unseen colliding particles behind the bubble ( $0^\circ < \alpha < 45^\circ$  and  $135^\circ < \alpha < 360^\circ$ ).

## 3.4. Positron Emission Particle Tracking (PEPT)

### 3.4.1. Principle of PEPT

Until now, the described measurement techniques, TPIV and 4D PTV, detect only the visible light. These techniques require transparency and are only applicable to dilute flows. However, typical flows in froth flotation are dense multiphase flows with a high gas and solid fraction [177]. The measurement in these dense flows is impossible for optical measurement techniques. To allow the measurements in opaque flows, non-optical signals have to be used as for example positrons in PEPT [178, 179].

The principle of PEPT is illustrated in Fig. 3.11. At the beginning, a model particle is radioactive-labeled with a positron emitting radionuclide, which undergoes a beta-plus decay. This, in turn, emits two photons in anti-parallel directions after annihilation with local electrons (Fig. 3.11a). If two detectors in an array simultaneously detect these gamma rays in coincidences, a line of response (LoR) can be defined between the two detection points (Fig. 3.11b). A sample of consecutive LoRs (typically 150...1000 events) are used to triangulate the instantaneous position of the radioactive model particle in three dimensions.

Several studies have successfully applied PEPT to measure the particle velocity field in the pulp and froth phase of a flotation cell [177, 180–182]. Most studies have only employed PEPT to determine the position of radioactive model particles and gain the 3D velocity field of the solid phase in a flotation cell. However, the observation of the interaction between bubbles and radioactive-labelled particles has not been addressed so far, because the position of gas bubbles is not detectable with PEPT. Instead, an additional measurement technique is required to observe the bubble positions. For example Cole et al. [183] measured simultaneously with a high-speed camera to gain the bubble positions.

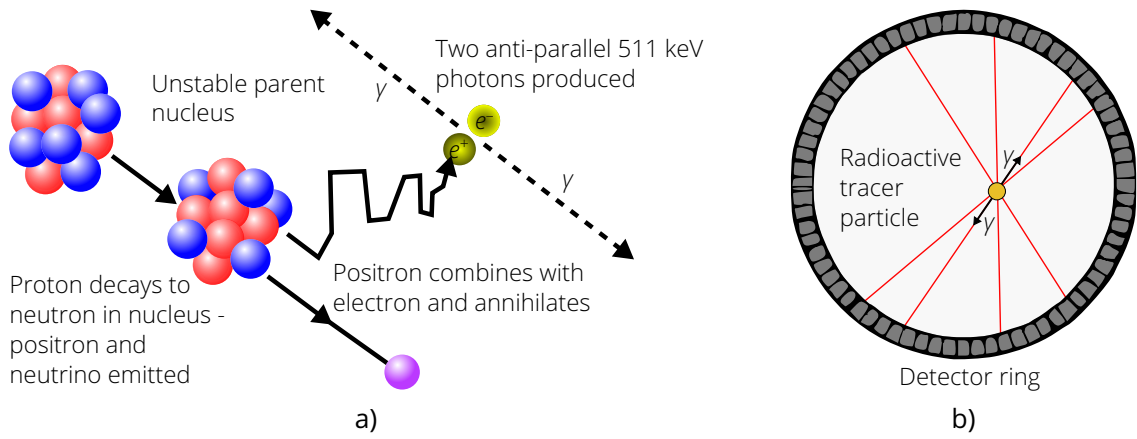


**Figure 3.11.** Illustration of the principle of PET (adapted from [184]). a) Mechanism of positron emission and interaction with matter, where a red sphere denotes a neutron and a blue sphere a proton b) Detection of the radioactive tracer particle by a detector ring. Triangulation of the position at the intersection of multiple lines of response (LoRs, marked as red lines).

### 3.4.2. Measurement setup and radioactive tracer particles

To investigate the bubble-particle interactions in a dense turbulent flow, the water channel (Sec. 3.1.2) was centered in the Positron Emission Tomography (PET) camera (ECAT HR++, Model: CTI/Siemens) at iThemba LABS, South Africa. The scanner detected the gamma rays of the inserted radioactive tracers.

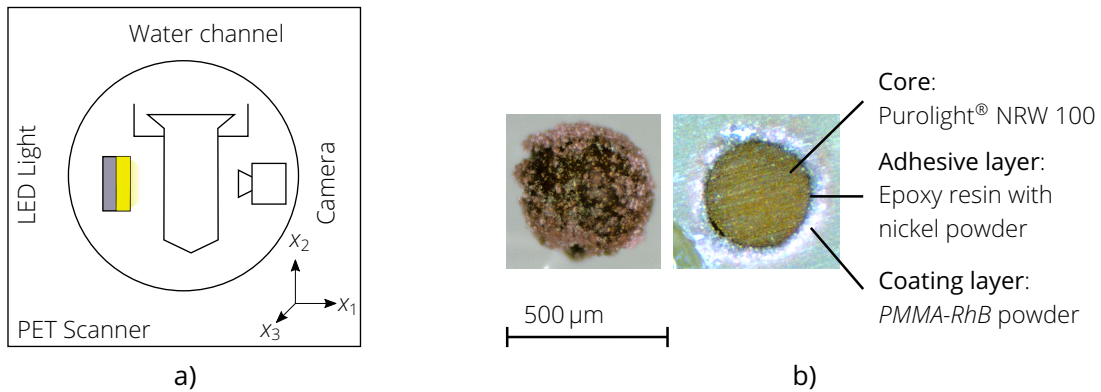


**Figure 3.12.** Application of PET to the water channel experiments. a) Arrangement of the water channel in the Positron Emission Tomography (PET) scanner. A camera recorded the bubble position and diameter. b) Radioactive tracer particle for measurements with PET (left) and micrograph of the same particle cut, grinded and polished along its diameter (right). The latter one was used to distinguish the three parts, namely, the core, the adhesive layer and the coating layer.

The gas phase was observed with a camera (GO-5100M-USB, JAI Ltd., Denmark) to account for small changes, e.g. due to switching needles during the measurement. The camera was located parallel to the water channel wall. It captured both bubbles in the  $x_2x_3$ -plane with a

frame rate of  $f_{meas} = 0.25$  fps. During the image analysis, a Hough transformation [185, 186] was applied to detect the stagnant bubble as a circle and obtain its center point,  $x_1$  and  $x_2$ , and its diameter,  $d_b$ .

The alignment of both coordinate systems, PET scanner and camera, was ensured by the following calibration. A radioactive particle was glued to a needle tip and placed at all bubble positions,  $p$ , in the water channel. Simultaneously, the known particle location was recorded by both systems, PEPT and camera, leading to an alignment of both coordinate systems with an uncertainty less than 2 mm.

For the investigation with PEPT, the solid suspension consisted of fluorescent PMMA model particles with a diameter of  $200 \mu\text{m} \dots 400 \mu\text{m}$  (*PMMA200*, Tab. 3.5) suspended in DI water with  $0.01 \text{ mol/l}$  KCl. These model particles were not only adaptable to radioactive tracer particles, but also applicable for 4D PTV (Sec. 3.3.2). The latter property was important for a subsequent comparison study between PEPT and 4D PTV. During the PEPT measurements, two different volume fractions were used - a dilute ( $\alpha_p = 1 \cdot 10^{-4}$ ) and a dense solid suspension ( $\alpha_p = 2.2 \cdot 10^{-3}$ ). These suspensions were classified as illustrated in Fig. 2.12, assuming a transition between both regimes at  $\alpha_p \approx 5 \cdot 10^{-4}$ .

For PEPT measurements, specific radioactive tracer particles were designed to represent the bulk *PMMA200* particles. These radioactive tracer particles had to fulfill two criteria. On the one hand, they had to be radioactive to be traceable in the PET scanner. On the other hand, their physical properties had to be similar to the suspended *PMMA200* particles. To meet all these criteria, the coating technique of Cole et al. [187], which used a silica coating and cyanoacrylate as an adhesive, was adapted for *PMMA200*. Accordingly, the radioactive model particle consisted of three parts, including a core in the form of an ion exchange resin, an adhesive layer containing epoxy resin with nickel powder, and a *PMMA-RhB* coating layer, as seen in Fig. 3.12b.

The core was composed of Purolight® NRW 100, an adapted spherical ion exchange resin for labeling with  $^{68}\text{Ga}$ . For the labeling, the techniques developed at PEPT Cape Town were used [181] and achieved an activity of  $I = (850 \pm 200) \mu\text{Ci}$  for the radioactive tracer particles at the beginning of each measurement. The adhesive layer was modified to prevent the dissolution of PMMA particles in the epoxy resin and provide additional physical strength of the coating to withstand the high stresses in the peristaltic pump. Therefore, a mixture of an epoxy resin and a nickel powder, each with a volume fraction of  $5 \cdot 10^{-1}$ , was applied. Finally, the radioactive model particle was coated with *PMMA-RhB* powder ( $d_p = 1 \mu\text{m} \dots 20 \mu\text{m}$ ) as an outer layer. A heat-treatment was applied during particle fabrication so that the coating was completely cured before the particles were added to the channel. The heat-treatment included three intervals of 15 s heating at  $160^\circ\text{C} \dots 180^\circ\text{C}$  and 15 s cooling at room temperature.

During the measurements, up to six radioactive tracer particles were added to the water channel. The rather high number of particles was chosen to increase the rate of bubble-particle interactions. The high residence time of the radioactive tracer particles in the whole system,  $\Delta t_{cir} \approx 1 \text{ min}$ , made it unlikely that multiple particles were in the region of interest (ROI),  $\Delta t_{roi} \approx 1 \text{ s}$ .

To conclude from the individual radioactive tracer particle to the overall *PMMA200* suspension, their physical properties had to be similar. Therefore, Tab. 3.6 summarizes the physical



properties of both particle types, in the form of surface material, diameter,  $d_p$ , density,  $\rho_s$ , the Stokes number,  $St$  (Eq. 2.38), the particle Reynolds number  $Re_p$  (Eq. 2.36) and the Archimedes number  $Ar$  (Eq. 2.40). The density of the PEPT,  $\rho_s = (1.5 \pm 0.2) \text{ g/cm}^3$ , was calculated based on its mass, measured with a microscale, and its volume, estimated by the micrograph image (Fig. 3.12b).

**Table 3.6.** Properties of the radioactive tracer particles and *PMMA-RhB* model particles. The particle types are compared in terms of their surface material,  $d_p$  the particle diameter,  $\rho_s$  particle density,  $St$  the Stokes number (Eq. 2.38),  $Re_p$  the particle Reynolds number (Eq. 2.36) and  $Ar$  the Archimedes number (Eq. 2.40). The Stokes number,  $St$  (Eq. 2.38), was calculated with the associated inverse Nyquist frequency as fluid time scale,  $\tau_l = f_N^{-1} = 2 \cdot f_{meas}^{-1}$ .

	Bulk suspension ( <i>PMMA200</i> )	Radioactive tracer particle (PEPT)
Surface material	<i>PMMA-RhB</i>	<i>PMMA-RhB</i> powder ( $d_p = 1 \mu\text{m} \dots 20 \mu\text{m}$ )
$d_p$ in $\mu\text{m}$	200...400	300...400
$\rho_s$ in $\text{g/cm}^3$	1.18	$1.5 \pm 0.2$
$St$	0.7...2.7	1.8...3.2
$Re_p$	0.8...4.9	5.1...10.1
$Ar$	16...127	133...315

Given these points, the *PMMA200* model particles have smaller inertia and drag than the radioactive ones. Thus, the dimensionless numbers, namely  $St$ ,  $Re_p$  and  $Ar$ , of the radioactive tracer particle exceed the ones from *PMMA200* particles. Regardless of this, the radioactive tracer particles are comparable and follow similarly the turbulent flow in the water channel.

### 3.4.3. Data analysis

The main idea of the PEPT data analysis is that the location of the inserted radioactive tracer particle is triangulated based on the detected LoRs, as shown in Fig. 3.13. Theoretically, the location of the tracer particle would correspond to the intersection point of all detected LoRs in the FOV at time step  $t$ . However, realistically some of these LoRs are corrupted e.g. due to Compton scattering or the simultaneous detection of two unrelated photons. These corrupted events are distributed across space, producing background noise and increasing the uncertainty of the tracer particle location. The number of corrupted events is specific for the individual setup and activity of the radioactive tracer particle. Additionally, the valid LoRs intersect in a minimum sphere of distance, not at a single point. Thus, the tracer particle is located at minimum distance to all the valid LoRs [178, 179, 188, 189].

The iterative triangulation algorithm of Parker et al. [178], adapted to the PEPT Cape Town system and described by Buffler et al. [190] was applied, to identify these corrupted events and triangulate the location of the tracer particle. Meaning, a specific number of consecutive LoRs,  $N$ , were used to compute an initial tracer location. Subsequently, corrupted events were discarded LoRs furthest away from the estimated tracer location. With the retained

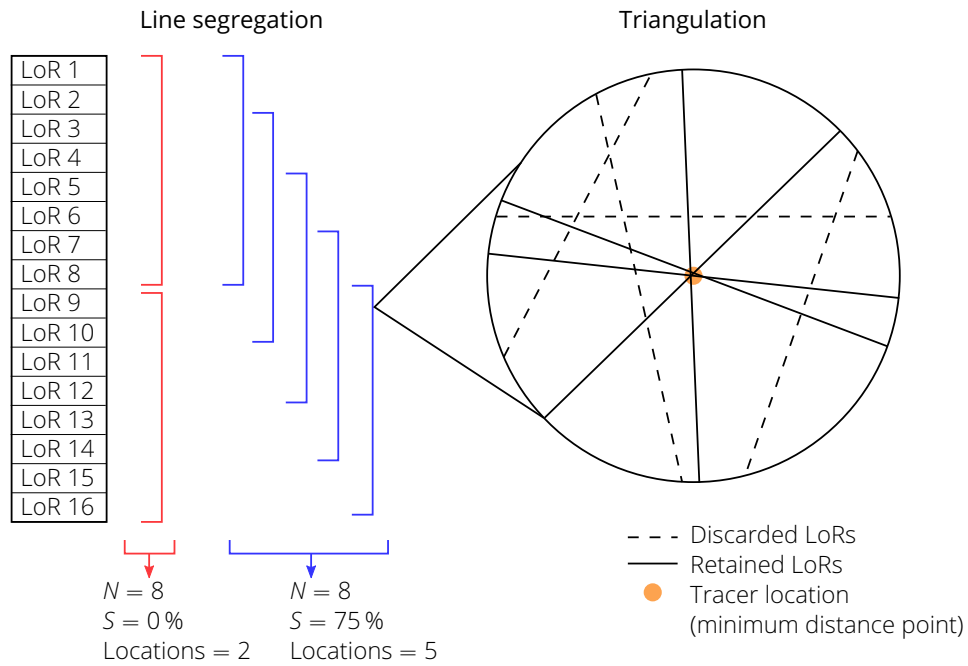


**Figure 3.13.** Diagram showing how LoRs first segregate into groups, using various numbers of consecutive LoRs,  $N$ , and different ratios of overlapping adjacent LoRs,  $S$ , followed by a representation of the 3D location triangulation process condensed to 2D. The proportion of corrupted LoRs is determined by  $f_{opt}$  (adapted from [188]).

LoRs, an improved approximation of the tracer location was determined. This iterative sequence was repeated until a predefined proportion of corrupted LoRs,  $f_{opt}$ , were discarded. Both values were optimized regarding the temporal and spatial resolution of the radioactive tracer particle location in the water channel as follows.

Concerning the temporal resolution, the goal was to achieve a resolution,  $\Delta t = 1$  ms, for each particle trajectory based on the location rate of the PET camera,  $F_{meas} = 1000$  Hz. However, the exponential decay of the particle radionuclide decreased the rate of an emitting positron, and thus, the temporal resolution. Therefore, the initial number of LoRs,  $N = 1000$ , was reduced continuously with decreasing particle activity to  $N = 50$  to calculate the particle location in time. Additionally, the sliding window technique of Sovechles et al. [188] was applied to artificially increase the number of LoRs, due to the usage of previously processed LoRs. The overlap of adjacent LoRs,  $S$ , ranged between 0 % and 75 %. If the temporal resolution of the particle trajectory exceeded 3 ms, the data were discarded for further calculations.

Besides an optimal number of LoRs,  $N$ , also the proportion of corrupted events of LoRs,  $f_{opt}$ , was needed to achieve a high spatial resolution. Consequently, the influence of  $f_{opt}$  on the standard deviation in radioactive particle location,  $\sigma_i$ , was measured with a stationary source under controlled conditions [179]. Fig. 3.14 illustrates the results for a radioactive particle glued to a needle tip which was placed one after another at each bubble position in the water channel (Fig. 3.1b). The number of LoRs was kept constant at 50, leading to the global minimum at  $f_{opt} = 70\%$  combining the results of all three bubble positions.

Finally, the particle trajectory was smoothed and interpolated with the method of Cole

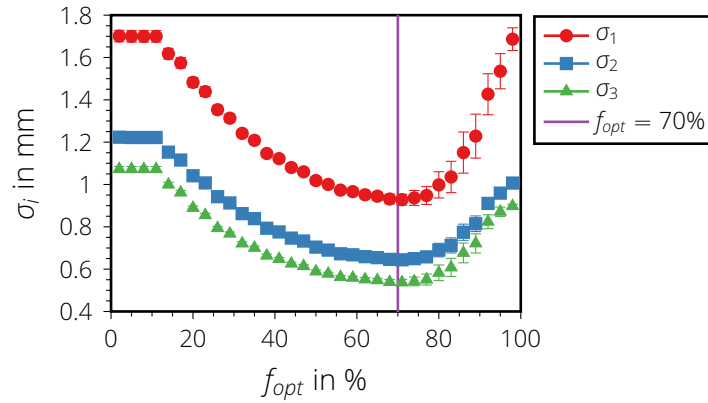


**Figure 3.14.** Uncertainty of the triangulated position of a radioactive tracer particle. The standard deviation,  $\sigma_i$ , of a stationary source depending on the proportion of corrupted LoRs,  $f_{opt}$ , evaluated in all three directions ( $i = 1 \dots 3$ ). The stationary source was a radioactive particle glued to a needle tip and was placed one after another at each bubble position in the water channel (Fig. 3.1b). For the triangulation, the specific number of LoRs  $N = 50$  was used.

et al. [191]. Cole et al. [191] used a time weighting function with a cubic spline to remove noise. Likewise, the kernel width was adapted to 10 ms, which is slightly less than the average residence time of a particle flowing around a bubble,  $t_r^{max} \approx 14$  ms (Eq. 3.76).

However, this triangulation method was developed for only one radioactive particle within the PET camera at a time. In order to take multiple particles into account, a ROI was set in the channel to avoid the interference of two or more particles on the triangulation of any single particle location. The ROI was defined as a sphere with the bubble center coordinates,  $\mathbf{X}_b$ , and radius,  $r_{roi}$ , which was evaluated separately for each bubble position,  $p$ . Therefore only instances of LoRs crossing the ROI were used for the triangulation of a particle. If multiple particles were in the ROI, their trajectories were rejected for further data analysis. The ROI radius was defined as  $r_{roi} = 9d_b$ , as a compromise between the enhancement of the small evaluation volume to increase the probability of detecting multiple particles and minimizing particle tracking errors close to the ROI boundaries.

#### 3.4.4. Uncertainty analysis

The uncertainty of the PEPT measurement method composed of a random triangulation error, a random experimental setup error and a systematic calibration error. The triangulation uncertainty was caused by physical effects in the measurement system, including low angle photon scatter and detector spatial resolution. In Fig. 3.14 the uncertainty ranged between 0.5 mm and 1 mm for the applied  $f_{opt}$  value of 70 % depending on the direction.

The experimental setup uncertainty was caused by e.g. a small variation of the concentration of the solid suspension, the properties of the radioactive model particle, the temperature or the flow. The uncertainty was quantified statistically by repeated measurement of the same experimental parameters, but a different set of radioactive model particles. The population of repetitions varied between four and nine times, depending on the experimental

parameter.

The calibration error included the positioning of the water channel in the PET scanner based on six reference points and the location of the bubble. The latter one was only checked in the  $x_1x_2$ -plane, and not in the  $x_1x_3$ - and  $x_2x_3$ -planes because of the planar camera image. The resulting uncertainties in the  $x_1$ - and  $x_2$ -direction were estimated to be in the order of 1 mm, whereas in the  $x_3$ -direction the uncertainty was approximated as 2 mm because of the limited verification by the camera during the measurements.

### 3.5. Discussion and Conclusion

Suitable generic experimental setups and measurement methods are crucial to investigate the bubble-particle interaction in turbulent flows. This chapter summarized the developed experimental setups and measurement methodologies. Hereby, questions Q.1 and Q.2 raised in Sec. 1.2 were answered.

The experiments were conducted in a bubble column (Sec. 3.1.1) and in a turbulent water channel (Sec. 3.1.2). In the bubble column, turbulence was generated in the wake of a freely rising bubble chain. In the turbulent water channel, the fluid flow passing through a grid produced turbulence. Depending from the distance between stagnant bubble and grid, different turbulent length scales influenced the bubble-particle interaction. A quantitative analysis of the generated turbulence in both experimental setups will be given in Chapter 4.

In this dissertation, these experimental setups were investigated by TPIV (Sec. 3.2) to measure the flow field in the vicinity of the bubble. 4D PTV (Sec. 3.3) and PEPT (Sec. 3.4) were applied to triangulate the trajectories of the model particle systems and classify these trajectories according to their collision performance. Tab. 3.7 summarizes the measurement principle, the restrictions on the measurement devices and the conditions of the model particle system to conclude their field of application.

TPIV and 4D PTV are optical measurement methods. The emitted visible light of the illuminated particles is detected by a camera. During the data analysis, the particle images are used either to compute the time-resolved flow field around a bubble based on a correlation-based approach (TPIV) or to triangulate the collision trajectories between particles and bubbles (4D PTV). To also account for the bubble position and shape, a combination of shadowgraphy and TPIV or 4D PTV were used, as described in Sec. 3.2.2.

In contrast, PEPT detects the emitted gamma photon of an annihilated positron. Consequently, PEPT can be applied to opaque flows, which is impossible for optical measurement techniques. For example, the PIV measurements of Sommer et al. [40] were limited to a solid volume fraction of approximately  $1 \cdot 10^{-3}$ . In comparison, Waters et al. [182] investigated flows with a solid volume fraction above  $1.3 \cdot 10^{-2}$  using PEPT. However, PEPT only detects the emitted positrons of a radioactive tracer particle, but not the position of the gas bubble. To overcome this limitation, the position of the bubble has to be known. Therefore, a stagnant bubble was used in the water channel (Sec. 3.1.2) to investigate the bubble-particle interaction with PEPT.

On the downside, PEPT is only available in two centers world wide, the Positron Imaging Center at the University of Birmingham (United Kingdom) and iThemba LABS at the University

**Table 3.7.** Comparison between the applied measurement techniques, namely TPIV, 4D PTV and PEPT, based on the measurement principle, the restrictions on the measurement devices and the conditions of the model particle system to conclude their field of application.

	TPIV	4D PTV	PEPT
Detected signal	Visible light		Gamma rays
Measurement parameter	Fluid flow field $U(X, t)$	Lagrangian particle trajectory $Z(t)$ and $W(t)$	
Detection of gas phase		Yes	No
Transparency		Yes	No
Availability	Commercially		Very limited
Restriction on rig size	No		Yes
Field of view	38 mm × 24 mm × 10 mm (height × width × depth)		600 mm × 230 mm (diameter × depth)
$\Delta x$ in mm	0.96	0.04	1
$\Delta t$ in $\mu s$	0.5	0.8	1
Property of tracer	Fluorescent, inertialess	Fluorescent	Radioactive
$d_{p,min}$ in $\mu m$	$\approx 30$	$\approx 30$	$\approx 300$
$N_p$ in FOV	$> 1000$		1
Availability	Commercially in larger quantities		Individually manufactured

of Cape Town (South Africa) [180]. Although PET scanners are commercially available for medical purpose, not all of them are suitable for PEPT. Nowadays these scanners are only available as a hybrid technique including a computed tomography or magnetic resonance imaging scanner. Besides the PET scanner, also a suitable facility is needed to generate the required isotopes and to produce radioactive tracer particles. Therefore, the number of PEPT centers are limited. To work with one of these devices, arrangements have to be made, in the form of application of measurement time and shipment of the experimental setup to the facility. Compared to TPIV and 4D PTV, the preparation of a measurement campaign is more challenging because TPIV and 4D PTV are commercially available systems by companies such as e.g. LaVision GmbH (Germany) or Dantec Dynamics A/S (Denmark). They supply not only the measurement technique, but also the suitable software to analyze the measurement data.

The optical measurement technique consists mainly of a camera, laser and backlight system. That means, this technique can be applied to a wide range of experimental rig sizes. As long as the visibility of the FOV is ensured, the cameras and laser optics can be mounted accordingly. Depending on the desired spatial resolution, the FOV is defined over the camera chip size, the aperture and the magnification factor of the lens system. For PEPT, the FOV is fixed by the size of the PET scanner, meaning also that the size of the experimental rig is limited by the PET scanner dimensions. In the case of the ECAT HR++ at iThemba LABS, the FOV had a diameter of 600 mm and a depth of 230 mm.

Further, the spatial,  $\Delta x$ , and temporal,  $\Delta t$ , resolution of the results vary with the measure-

ment technique. The values, summarized in Tab. 3.7, are based on the achieved resolutions during the experiments in this thesis. For the optical measurement techniques, the spatial resolution can be increased by the usage of larger objectives (e.g. 200 mm), which simultaneously decreases the depth of field (DOF). The temporal resolution can be enhanced by the usage of a higher frame rate. The described camera and laser system in Sec. 3.2.2 can achieve a maximum frame rate of 5200 fps at full resolution (1280 pix × 800 pix), resulting into a temporal resolution of 0.2 μs. An increase of the frame rate is associated with a smaller exposure time and an increase of the laser power. If the maximum of the laser power is reached, the particle contrast decreases. An additional increase would be possible with an update of the commercially available camera and laser system. In contrast, an improvement of the spatial and temporal resolution of the PET scanner is more challenging. This incorporates the development of smaller, local and specialized detectors and a change of the data acquisition system.

All applied measurement systems depend on the application of a suitable particle systems. On the one hand, for TPIV and 4D PTV, the particles need a matching fluorescent color, to pass through the optical filter of the cameras, in contrast to the scattered light of the bubbles. Further, the TPIV particles have to be small and inertialess to follow the liquid streamlines without any deviation. The minimal observable particle diameter,  $d_p$ , depends on the spatial resolution. Therefore, the commercially available *PS-FluoRed* and *PMMA-RhB* particles from microParticles GmbH were used.

On the other hand, PEPT requires radioactive tracer particles. The most common radioisotopes are  $^{18}\text{Fe}$ ,  $^{66}\text{Ga}$ ,  $^{68}\text{Ga}$ ,  $^{61}\text{Cu}$  and  $^{64}\text{Cu}$  [192, 193]. Depending on the production type, different particle diameters are achievable. With the coating technique used in this thesis, an extra layer of coating was applied on the radioactive tracer particle to mimic the material surface properties of the solid phase. The thickness of the coating is approx. 60 μm to 80 μm under optimum conditions, resulting in a radioactive particle diameter between 450 μm to 600 μm [187]. Additionally, the manual preparation of the radioactive tracer particles leads to a certain deviation in size and shape between the radioactive tracer particles and the particles in the bulk. Another possible technique would be the direct activation [180, 182], which directly activates the desired particles in the cyclotron. With this technique, particle diameters below 300 μm were reached. However, the smaller particle size goes along with less activity, a weak signal and a shorter measurement time.

To sum up, TPIV is a suitable technique to measure the prevailing flow around a bubble. These results can be correlated to the collision trajectories triangulated with 4D PTV and PEPT. At first sight, the comparison revealed an advantage of 4D PTV vis-à-vis PEPT, e.g. due to its better availability, higher spatial and temporal resolution. However, PEPT enables the measurement in opaque flows which is impossible for optical measurement techniques. This ability of PEPT allows the investigation of the bubble-particle interaction in dense flows with high solid fractions, typical for froth flotation.

TPIV enabled the characterization of the time-resolved 3D-3C flow field around a bubble. With 4D PTV and PEPT, the Lagrangian particle trajectories in vicinity of a bubble are triangulated, allowing the investigation of the bubble-particle interaction in turbulent flows. To conclude their field of application, Tab. 3.7 compares the applied measurement techniques.

# 4. Flow characterization measured with shadowgraphy and TPIV

## 4.1. Introduction

In this dissertation, two types of bubbles are investigated - a freely rising bubble chain in the bubble column (Fig. 3.1a) and a stagnant bubble in the water channel (Fig. 3.1b). This chapter focuses on the characterization of these generated bubbles and the liquid flow field around them, measured with shadowgraphy and Tomographic Particle Image Velocimetry (TPIV) (Sec. 3.2) [39, 41]. Starting with the freely rising bubble chain, the generated bubbles are examined regarding their shapes and motions. The resulting flow field around these bubbles and the turbulent length scales introduced here are specified. Subsequently, the focus is on the stagnant bubbles. Contrary to the freely rising bubble chain, these bubbles remain attached to their needle and are exposed to a turbulent flow. The turbulence generated by the flow passing through the grid is characterized, and its effects on the bubble shape, motion and resulting flow field around the bubble are analysed in detail. These characterization data give a framework of the bubble and grid-introduced turbulent flow field. The insight into the flow field provides the basis to understand the motion of the particles in the vicinity of the bubble. In the following chapter, the combination of the liquid flow field and the particle collision trajectories enables to understand where the model particles could deviate from the fluid streamlines and collide with the bubble surface.

## 4.2. Freely rising bubble chain in the bubble column

Starting with the freely rising bubble chain, the experiments were conducted in the bubble column (Fig. 4.1). Nearly monodisperse air bubbles were introduced by a single blunt needle with an inner diameter of  $d_i = 120 \mu\text{m}$ ,  $300 \mu\text{m}$  or  $600 \mu\text{m}$  (Sec. 3.1.1). Only one gas flow rate was used for each needle configuration to achieve a distance of  $8d_b$  between two consecutive bubbles. The dynamics of multiple freely rising bubbles are different from that of a single bubble [93–95].

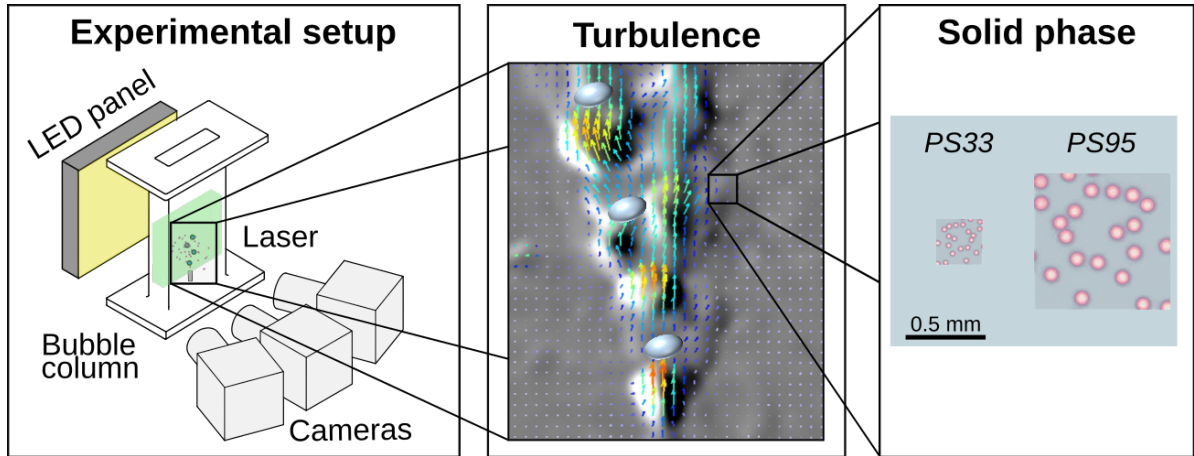


Figure 4.1. Bubble column: Graphical abstract of the experimental arrangement for the measurements in the bubble column with TPIV. The particle model system *PS33* and *PS95* consisted of fluorescent polystyrene (PS) particles with a diameter of 33  $\mu\text{m}$  and 95  $\mu\text{m}$ , respectively. Please refer to Sec. 3.1.1 for more details of the experimental setup and Tab. 3.5 for the properties of the model particle systems.

#### 4.2.1. Shape and motion of bubbles

The shape, rising trajectory and velocity of the trailing bubble are affected by the liquid flow structure of the leading bubble, and in particular its wake (Sec. 2.2.3). Therefore, the first part focused on characterizing the freely rising bubbles regarding their shapes (Fig. 4.2) and size distribution (Fig. 4.3a). Further, an example interaction between two consecutive bubbles was analyzed for each bubble configuration (Fig. 4.3b - d).

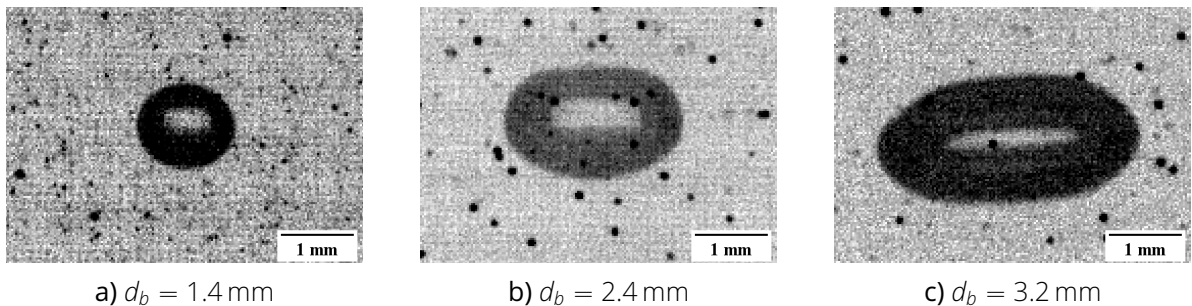
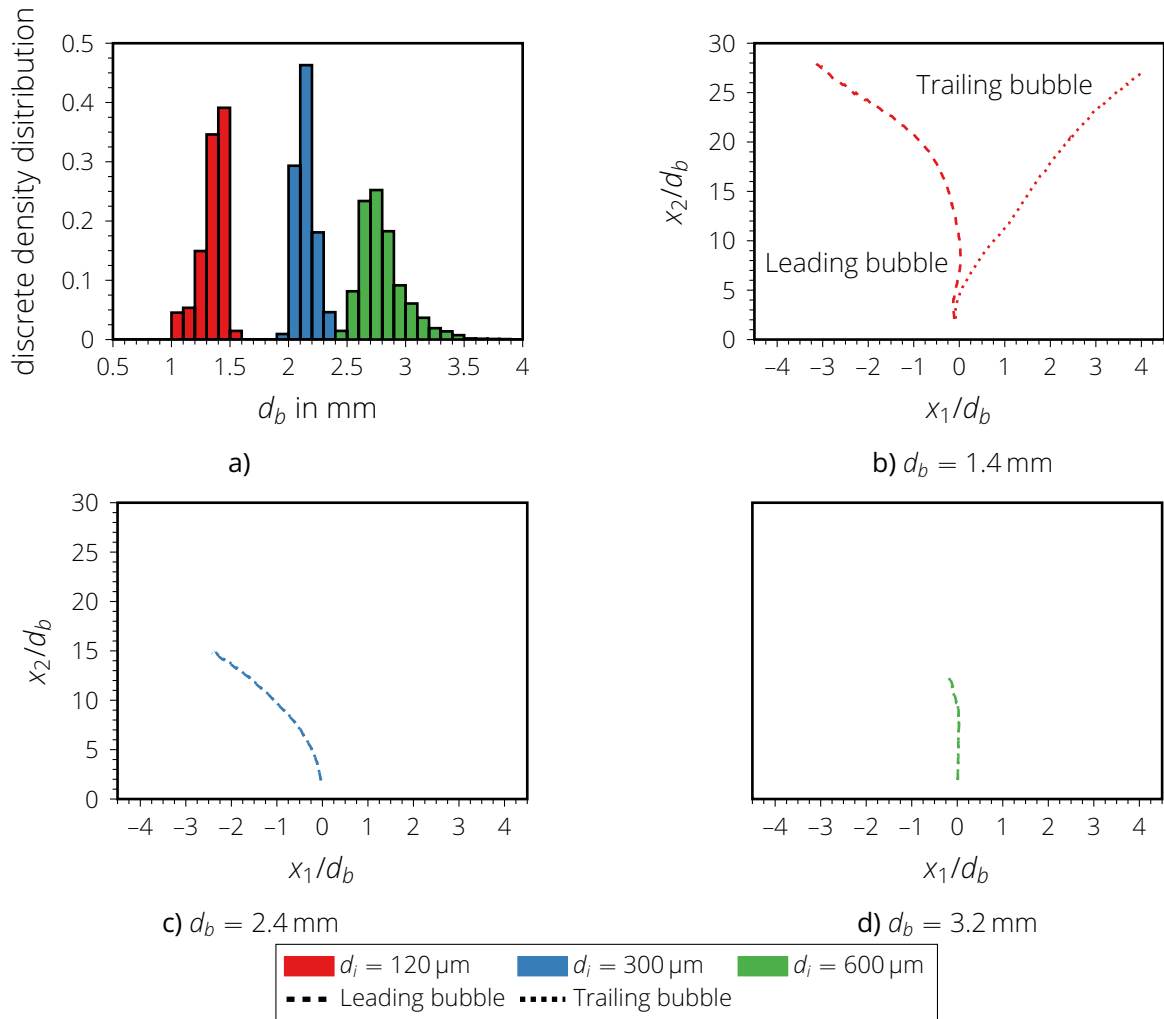


Figure 4.2. Bubble column: Typical shapes of the freely rising bubble chain. They were produced in the bubble column by different inner orifice diameters,  $d_i$ , at the position of  $3d_b$  above the needle orifice. a)  $d_i = 120 \mu\text{m}$ . b)  $d_i = 300 \mu\text{m}$ . c)  $d_i = 600 \mu\text{m}$ .

Fig. 4.2 shows example images of the formed bubbles at the position  $3d_b$  above the needle orifice. These images display that three types of bubbles were generated depending on the inner diameter of the needle,  $d_i$ . The smallest orifice,  $d_i = 120 \mu\text{m}$ , produced spherical to ellipsoidal bubbles, the middle one,  $d_i = 300 \mu\text{m}$ , generated ellipsoidal bubbles and the largest one,  $d_i = 600 \mu\text{m}$ , wobbling bubbles. This corresponded to the findings of Clift et al. [44], who classified the shape of a freely rising bubble based on its  $Re_b$  and  $Eo$  number (Fig. 2.5). For the investigated freely rising bubbles, these values are summarized in Tab. 3.1.





**Figure 4.3.** Bubble column: Characteristics of the freely rising bubble chain depending on the orifice diameter,  $d_i$ : a) Bubble size distribution with a bin with of 0.1 mm to reveal the underlying distribution. b) - d) Example rising trajectories of two consecutive bubbles in the  $x_1x_2$ -plane. In c) and d), the trajectories of leading and trailing bubble are matching.

The properties of the formed bubbles are illustrated in Fig. 4.3. Beginning with the bubble size distribution in Fig. 4.3a, the uniform bin width of the distribution is set to 0.1 mm and is adopted to reveal its underlying shape. In general, each orifice diameter,  $d_i$ , formed a homogeneous and reproducible bubble chain. The bubble diameter can be assigned directly to the inner diameter of the orifice because only one gas flow rate was used for each needle configuration. Thus, the mean bubble diameter was 1.4 mm, 2.4 mm, and 3.2 mm for  $d_i = 120 \mu\text{m}$ ,  $300 \mu\text{m}$  and  $600 \mu\text{m}$ , respectively. The bubble size distribution is narrow and does not overlap between the needle configurations. The measured bubble size distribution is only wider for  $d_i = 600 \mu\text{m}$ . Oscillations in the shape of the wobbling bubbles caused potential measurement uncertainties regarding the bubble diameter.

The measured bubble diameters agreed well with the theoretical findings of Drenckhan

et al. [65]. The generated bubbles were produced in the quasi-static regime because the capillary length,  $l_c = 2.7$  mm (Eq. 2.21), was much larger than  $r_i = 0.5 \cdot d_j$ . Therefore, the bubble diameter can be approximated with Eq. 2.20 to 1.8 mm, 2.4 mm, and 3.0 mm for  $d_j = 120$   $\mu\text{m}$ , 300  $\mu\text{m}$ , and 600  $\mu\text{m}$ , respectively. The difference between the theoretical and measured mean bubble diameter remained below 0.4 mm and could be attributed to the dynamics of multiple freely rising bubbles and the measurement uncertainty, as discussed in Sec. 3.2.4.

Turning now to the rising trajectories of two consecutive bubbles, Fig. 4.3b to d display the trajectories for each bubble configurations in the  $x_1x_2$ -plane. In general, all the trajectories exhibit firstly a rectilinear rising path and then transit into a presumably oscillating motion. The oscillation motion is mainly described as a zigzagging or a spiraling (helical) motion [74]. However, in this dissertation a classification of the oscillation path was challenging. The oscillation motion could not be observed over multiple cycles due to the limited field of view (FOV) along the  $x_2$ -axis.

Using Cano-Lozano et al. [75]'s phase diagram (Fig. 2.6d), the smallest bubble configuration would exhibit a rectilinear rising trajectory, whereas the other two bubble configurations ( $d_b = 2.4$  mm, 3.2 mm) would undergo a path instability in the form of a flattened spiral trajectory (the corresponding Eötvös and Galilei numbers are summarized in Tab. 3.1). This contradicts the experimental observation for the smallest bubble configuration, where a presumably oscillating trajectory was detected. One reason could be that Cano-Lozano et al. [75] investigated a single rising bubble, while the experiments comprised a bubble chain. Meaning, the trailing bubble could be affected by the liquid flow structure of the leading one, and in particular its wake.

Taking a closer look at the alignment of the two consecutive bubbles, the nearly spherical trailing bubble (Fig. 4.3b) is arranged coaxially to its corresponding leading bubble. In contrast, the ellipsoidal and wobbling trailing bubbles (Fig. 4.3c, d) remain in-line with their leading bubble. Kusuno et al. [101] attributed it to the lift force in the wake. A spherical trailing bubbles migrates from the in-line configuration, due to the shear-induced lift in the wake. However, with increasing oblateness of the trailing bubble and the onset of the formation of a standing eddy, the lift mechanism reverses, keeping the trailing bubble in-line (Sec. 2.2.3).

#### 4.2.2. Flow field around bubbles

Several studies have already demonstrated a strong connection between the path and the wake instabilities of freely rising bubbles [90, 194]. Thus, a variation of the bubble shape and sizes is accompanied by a change in the flow field around the bubble and the contribution to turbulence production in the liquid phase [98]. Therefore, Fig. 4.4 plots the averaged velocity magnitude, the vorticity in the  $y_1y_2$ -plane, turbulent kinetic energy (TKE) and dissipation rate around freely rising bubbles extracted from the TPIV measurements. Each column corresponds to one bubble configuration with a bubble diameter,  $d_b$ , varying from 1.4 mm to 3.2 mm. The averaging was performed as a conditional average based on the tilt angle of the bubble,  $\theta$  (Eq. 3.48). The results are discussed for the conditional group of  $0^\circ < \theta < 5^\circ$ .

For the smallest bubbles (Fig. 4.4a), the magnitude of the average flow velocity remains in the order of the bubble rising velocity, and the vorticity in the  $y_1y_2$ -plane,  $\omega_3$ , is approx-

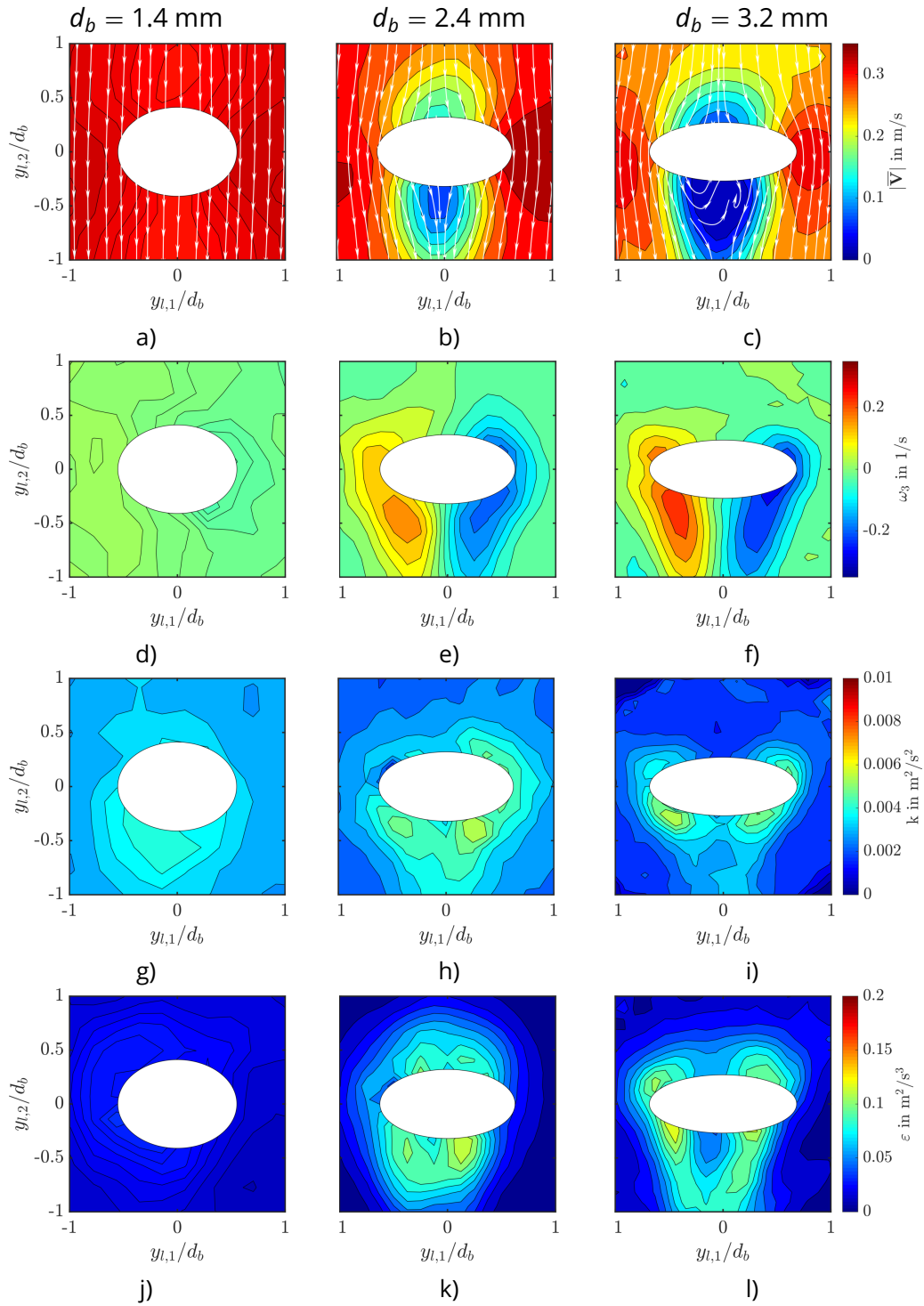


Figure 4.4. Bubble column: Flow field around a freely rising bubble with a diameter,  $d_b$ . a)-c) Magnitude of the averaged liquid velocity field,  $|\bar{\mathbf{V}}|$ . d)-f) Averaged vorticity,  $\omega_3$ , in the  $y_{l,1}y_{l,2}$ -plane. g)-i) Averaged turbulent kinetic energy,  $k$ . j)-l) Averaged dissipation rate,  $\epsilon$ . The values are conditionally averaged for the tilt angle of the bubble,  $\theta = 0^\circ \dots 5^\circ$ , around the  $y_{l,3}$ -axis from 0 mm to 0.3 mm.

imately zero (Fig. 4.4d). Theoretically, the averaged flow velocity has to reach zero at the boundary layer around the bubble surface. Due to the low spatial resolution and averaging process, the boundary layer could not be resolved during the experiments. The wake has an axisymmetric structure and no standing eddy exists, agreeing with the classification of Blanco et al. [91] for a rising bubble with an aspect ratio of 1.35 and a Reynolds number of 446.

As the aspect ratio of the bubble increases ( $e > 1.9$ , Fig. 4.4b and c), the magnitude of the velocity decreases upstream and downstream, forming two counter-rotating vortices at the trailing edge of the bubble (Fig. 4.4e and f). The vorticity in the  $y_{l,1}y_{l,2}$ -plane,  $\omega_3$ , starts to shed downstream of the bubble in the form of a double-threaded wake [90]. Due to the limited field of view above the needle, Fig. 4.4e and f show an intermediate step in the development of the double-threaded wake.

The turbulent characteristics of the formed wake structures are shown in the form of the TKE (Fig. 4.4g-i) and the dissipation rate (Fig. 4.4j-l). With an increasing magnitude of the vorticity in the  $y_{l,1}y_{l,2}$ -plane,  $\omega_3$ , downstream of the bubble, the values of TKE and the dissipation rate rise, too. Notably, the bubble with the largest diameter (Fig. 4.4f and i) has a striking pattern in terms of the TKE and the dissipation rate in the region of the counterrotating vortices. At the rear of the bubble, their magnitude is the lowest at the center line and increases towards the maximal expansion of the bubble in  $y_{l,1}$ -direction.

Besides the spatial distribution of the TKE and the dissipation rate around the rising bubble, also the range of turbulent length scales is important to characterize the turbulence induced by the bubble. Therefore, Fig. 4.5 illustrates the power spectra representing the containing TKE of turbulent length scale denoted by its wavenumber,  $\kappa$ . The power spectra were computed at two positions close to the freely rising bubble. The location of  $Y_{up}$ , upstream, and  $Y_{down}$ , downstream of the freely rising bubble, are marked in the inset of Fig. 4.5a. Starting with the power spectra of the largest bubble diameter (Fig. 4.5a), the TKE downstream of the bubble at  $Y_{down}$  is higher than upstream of the bubble  $Y_{up}$  due to the turbulence production in the double threaded wake (Fig. 4.4i). The energy difference,  $E(Y_{down}) - E(Y_{up})$ , decreases with increasing wavenumber. Thus, the wake formed downstream of the bubble only adds energy to the larger length scales.

Upstream of the freely rising bubble, the power spectrum remains in the same order of magnitude for the range of measurable wavenumbers. In contrast, downstream of the freely rising bubble, the largest turbulent length scales are in the range of the shedding wavenumber of the bubble (Eq. 3.60). With an increasing wavenumber (= decreasing turbulent length scale), the typical  $-5/3$  - rise is observed in the inertial range to the cut-off wavenumber  $\kappa_c \approx 2.92$  1/mm (Eq. 3.68). Afterwards, the power spectrum slightly increases again, due to noise in the TPIV measurements. Thus,  $\kappa_c$  represents the limit of the resolvable wavenumber but not the Kolmogorov length scale (Eq. 3.61), as shown in Fig. 4.5.

Additionally, the particle wavenumber,  $\kappa_p$  (Eq. 3.59), is marked in the power spectrum to investigate to which extend the particle systems respond to all turbulent length scales. In the case of the bubble column, the particle model systems of *PS33* and *PS95* were applied, noted as  $\kappa_{p33}$  and  $\kappa_{p95}$  in Fig. 4.5a, respectively (further details on the particle model systems in Tab. 3.5). Comparing the particle wavenumber with the Kolmogorov wavenumber, it is seen that, for *PS95*, the Kolmogorov wavenumber exceeded the particle wavenumber. In this case,

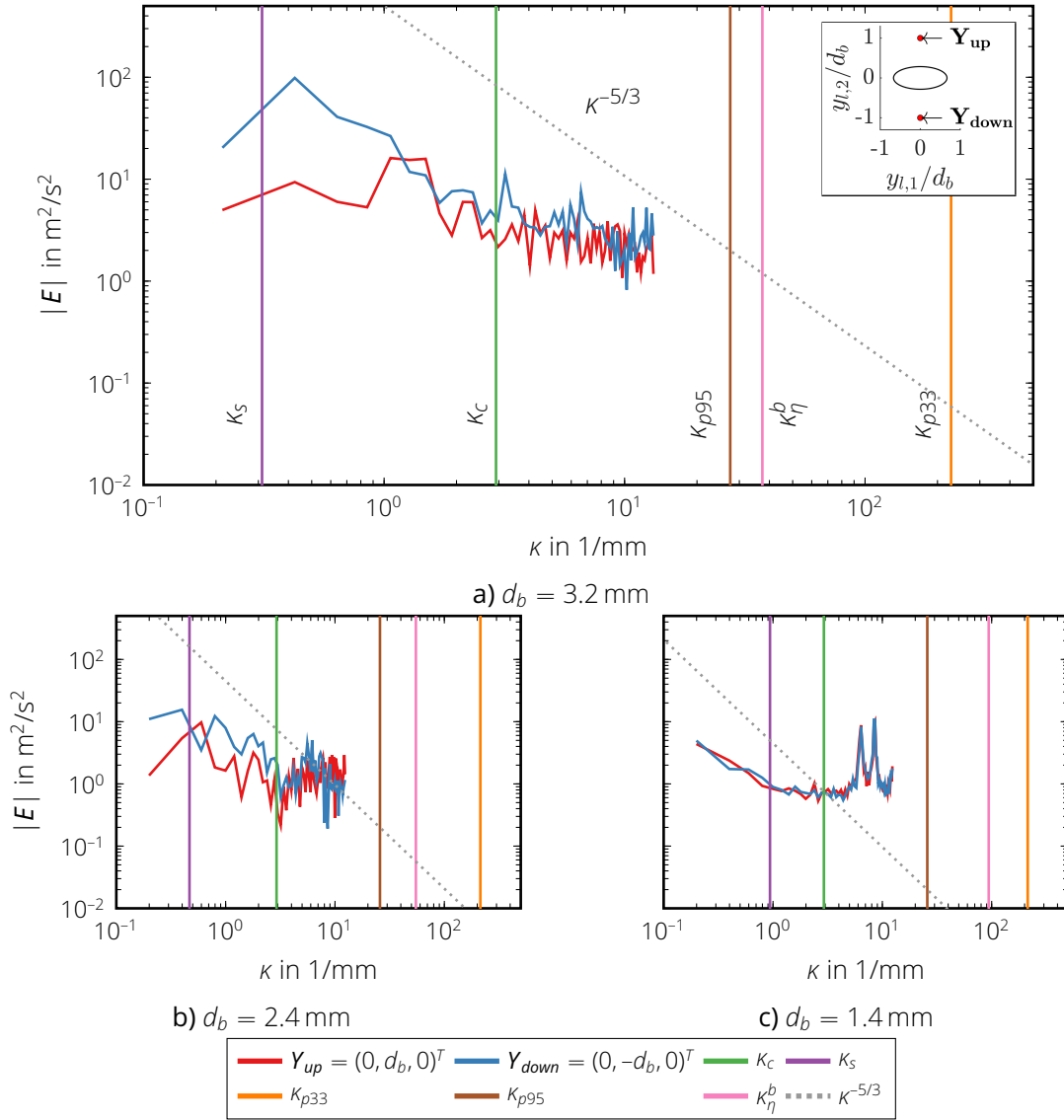


**Figure 4.5.** Bubble column: Power spectrum at point  $Y_{up}$  and  $Y_{down}$ , as marked with red dots in the inset of a), upstream and downstream of the freely rising bubble. Characteristic wavenumbers are plotted such as the limit of the resolvable wavenumber,  $\kappa_C$  (Eq. 3.68), the shedding wavenumber of the bubble,  $\kappa_S$  (Eq. 3.60), the maximum wavenumber of the particles,  $\kappa_{p33}$  and  $\kappa_{p95}$  (Eq. 3.59), and the Kolmogorov wavenumber,  $\kappa_\eta^b$  (Eq. 3.61).

the particle deviates significantly from the fluid streamline using the energy difference. For the smaller particles,  $PS33$ , the particle wavenumber goes beyond  $\kappa_\eta^b$ . Consequently, these particles responded to all changes of the fluid flow of the rising bubble chain.

Turning now to the power spectrum of the medium-sized bubble configuration in Fig. 4.5b, the distribution of energy along the wavenumbers is comparable to the largest bubble configuration (Fig. 4.5a). Only downstream of the bubble at  $Y_{up}$ , the magnitude of the power spectrum decreases with the bubble diameter due to the decreasing length of the double-threaded wake in Fig. 4.4d-f. Consequently, the wake of the leading bubble affects the inflow

conditions of the trailing bubble [101]. This influences both the wake structure [62] and the rising path of the trailing bubble [99].

For the smallest bubble diameter in Fig. 4.5c, the axisymmetric wake structure does not affect the power spectrum because the distribution of the energy along the wavenumbers is almost identical upstream and downstream of the bubble. This was also expected because of the low value of TKE around the freely rising bubble in Fig. 4.4g.

### 4.3. Stagnant bubbles in the turbulent water channel

In this thesis, bubbles were not only released in the quiescent flow of the bubble column, but they were also exposed to a turbulent flow in the water channel (Fig. 4.6). The turbulence was generated reproducibly by passing a uniform flow through a grid [53, 57, 58]. Through the absence of a mean flow gradient, the large scale can decay homogeneously, because no further turbulence is produced (Sec. 2.1.3). The decay of the large scale turbulence leads to a change of the characteristics of the turbulent flow with increasing distance to the grid.

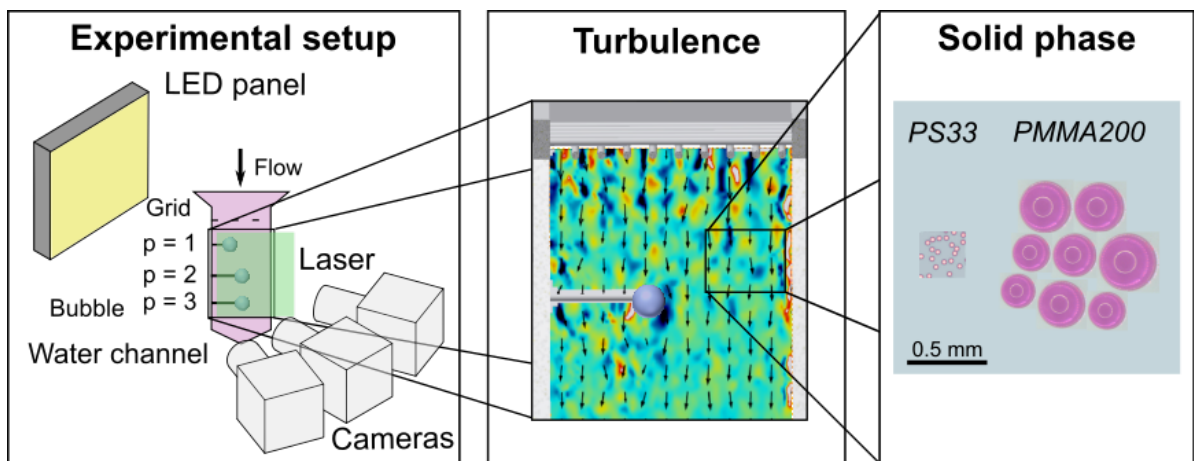
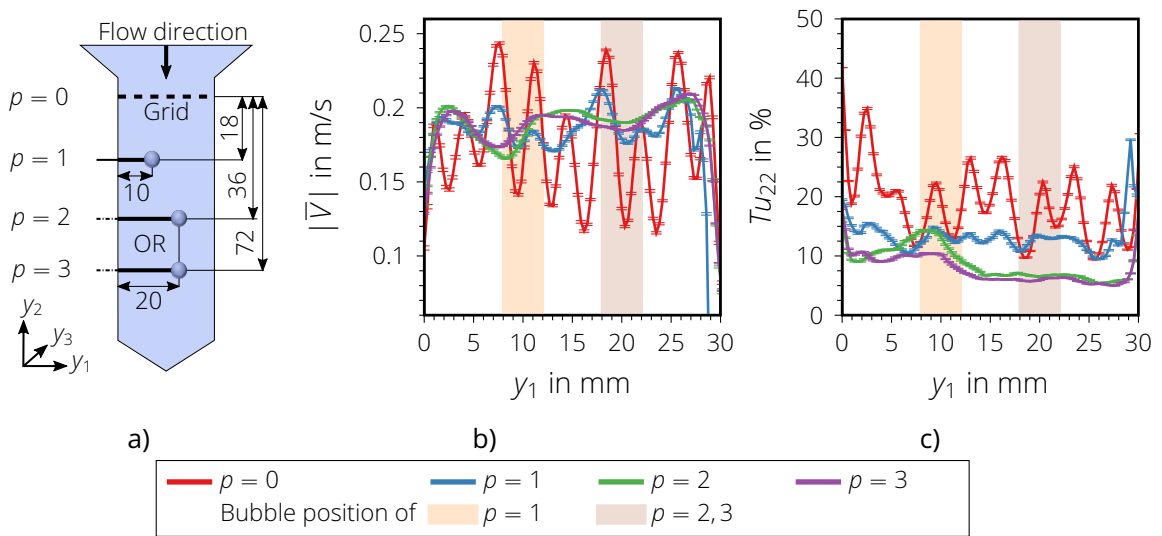


Figure 4.6. Water channel: Graphical abstract of the experimental arrangement for the measurements in the water channel with TPIV. The particle model system *PS33* and *PMMA200* consisted of fluorescent PS particles with a diameter of  $33\ \mu\text{m}$  and fluorescent polymethylmethacrylate (PMMA) particles with a diameter of  $200\ \mu\text{m}$ ...  $400\ \mu\text{m}$ , respectively. Please refer to Sec. 3.1.2 for more details of the experimental setup and Tab. 3.5 for the properties of the model particle systems.

To investigate the bubble-particle interaction under these well-defined turbulent conditions, stagnant bubbles were located at three positions,  $p$ . Thus, the flow upstream of each bubble consisted of different turbulent length scales and intensities. To minimize the effect of the upper bubble on the lower one, only two bubbles with a horizontal spacing of 10 mm were employed during the measurements. The first configuration consisted of the upper bubble position,  $p = 1$ , and the middle one,  $p = 2$ , whereas the second configuration included the upper one,  $p = 1$ , and the lower one,  $p = 3$ .

### 4.3.1. Turbulent flow field in the water channel

In the following section, the generated turbulent flow was measured with TPIV at these positions,  $p = 1 - 3$ , to characterize the single-phase flow in the water channel. Additionally, the flow directly downstream of the grid ( $p = 0$ ) was investigated to analyze the initially generated large scale turbulence. Starting with the time-averaged velocity magnitude,  $|\bar{\mathbf{V}}|$ , at  $p = 0$  (Fig. 4.7b),  $|\bar{\mathbf{V}}|$  varied strongly along the  $y_1$ -direction because of its deceleration at the rod position,  $|\bar{\mathbf{V}}| \approx 0.16$  m/s, and its acceleration by passing through the mesh,  $|\bar{\mathbf{V}}| \approx 0.23$  m/s. With increasing distance to the grid,  $p = 1$ , the oscillations of  $|\bar{\mathbf{V}}|$  along the  $y_1$ -direction are reduced until they are nearly depressed at  $p = 2$  and  $p = 3$ . To sum up, the time-averaged velocity magnitude was approximately 0.18 m/s (Fig. 4.7b). This velocity magnitude corresponded to the rising velocity of a 2.3 mm bubble in contaminated water [44], resulting in a bubble Reynolds number of approximately  $Re_b = 450$ . The remaining variations could be contributed to a slightly nonuniform spacing of the mesh grid.



**Figure 4.7.** Water channel: Characteristics of the single phase flow in the water channel. a) Definition of the grid ( $p = 0$ ) and bubble positions ( $p = 1 - 3$ ) in the water channel. Units are displayed in mm. b) Magnitude of the time-averaged velocity profile,  $|\bar{\mathbf{V}}|$  (Eq. 3.49). c) Degree of turbulence in  $y_2$ -direction,  $Tu_{22}$  (Eq. 3.52). The properties are evaluated along the  $y_1$ -direction where 0 mm and 30 mm define the channel walls. Additionally, the bubble positions in  $y_1$ -direction are marked as orange ( $p = 1$  at  $y_1 = 10$  mm) and brown ( $p = 2$  and  $p = 3$  at  $y_1 = 20$  mm) in both diagrams. Although the bubble positions were used for the analysis, no stagnant bubble was present during these measurements.

Similarly, the degree of turbulence in  $y_2$ -direction,  $Tu_{22}$  (Eq. 3.52), is illustrated in Fig. 4.7c. The degree of turbulence,  $Tu_{22}$ , decreases with increasing distance to the grid. The highest degree of turbulence is close to the grid,  $p = 0$ , and varies between 10% and 30%. At this position, the turbulence was produced by the wake of the grid rods. Increasing the distance to the grid and reaching the upper bubble position,  $p = 1$ , one part of the TKE still remains in the large turbulent length scales resulting into  $Tu_{22} = 15\%$ . These large length scales

dissipated further downstream, at the middle,  $p = 2$ , and lower bubble position,  $p = 3$ , thus,  $Tu_{22}$  decreases to approximately 5 %.

However, turbulence was not only generated by the flow passing through the grid, but also by a recirculation of the flow behind the needle. Generally, if a flow reaches a Reynolds number beyond a certain critical value, a laminar flow becomes turbulent. Approximating the needle as a cylinder, the critical Reynolds number,  $Re_c$ , is roughly 49 to form an unstable wake behind a cylinder [195]. During the measurements, the Reynolds number of the needle,  $Re_c(d_o) = d_o \cdot |\mathbf{V}| \cdot \nu^{-1} = 180$ , was above this critical Reynolds number, thus the needle introduced turbulence to the flow. Therefore, the higher turbulent intensities at  $y_1 < 10$  mm at the bubble positions  $p = 2$  and 3 could correspond to the wake of the upper needle. To avoid a disturbance of the flow by the upper needle, the lower bubble position ( $p = 2$  or  $p = 3$ ) had a horizontal offset of 10 mm. Consequently, the influence of the upper bubble position on the lower one was minor.

These variations in the degree of turbulence are connected to the distribution of turbulent length scales and their containing TKE. This distribution is quantified in the power spectra as shown in Fig. 4.8. Starting with the power spectrum in the main flow direction (Fig. 4.8a), the largest turbulent length scales are in the range of the integral wavenumber (Eq. 3.56). With an increasing wavenumber (= decreasing turbulent length scale), the typical  $-5/3$  - rise is observed in the inertial range to the cut-off wavenumber  $\kappa_c \approx 8.75$  1/mm (Eq. 3.68). Afterwards, the power spectrum slightly increases again, due to noise in the TPIV measurements. Thus,  $\kappa_c$  represents the limit of the resolvable wavenumber but not the Kolmogorov length scale (Eq. 3.57).

Focusing now on the distribution of TKE at the different bubble positions, the TKE decreases with increasing distance to the grid analogous to the degree of turbulence (Fig. 4.7c). In particular in the large turbulent length scales ( $\kappa < \kappa_\lambda$ ), the amount of TKE decreases by two orders of magnitude from the bubble position  $p = 0$  to 3, whereas in the smaller turbulent length scales ( $\kappa \gg \kappa_\lambda$ ), the amount of TKE remains in the same order of magnitude for these positions. These variations in the energy difference with the wavenumber are typical for turbulence generated by a grid. Through the absence of a mean flow gradient, no further turbulence is produced. Additionally, the energy difference between middle and lower bubble position,  $E_2(p = 2) - E_2(p = 3)$ , remains in the same order of magnitude for the range of measurable wavenumbers.

Turning now to the power spectrum in  $y_1$ -direction as shown in Fig. 4.8b, the distribution of energy along the wavenumbers is comparable to  $E_2$  (Fig. 4.8a). Only the magnitude of TKE at  $p = 0$  and  $p = 1$  is one order of magnitude smaller for  $E_1$  compared to  $E_2$ . For  $p = 2$  and  $p = 3$  the magnitude of TKE remains the same. In contrast, the power spectrum in  $y_3$ -direction (Fig. 4.8c) varies from the previous ones (Fig. 4.8a, b). Although the largest turbulent length scales are in the range of the integral wavenumber (Eq. 3.56), with increasing wavenumber the energy remains in the same order of magnitude. Thus, the typical  $-5/3$  - rise is not observed in the inertial range. One reason could be the high uncertainty of  $v_3$ , resulting from the reconstruction process in the TPIV algorithm. This uncertainty could add artificial turbulence to the spectrum.

Additionally, the power spectrum allows to evaluate whether the generated turbulence could be isotropic. Meaning in the case of isotropic turbulence, the magnitude and distribu-



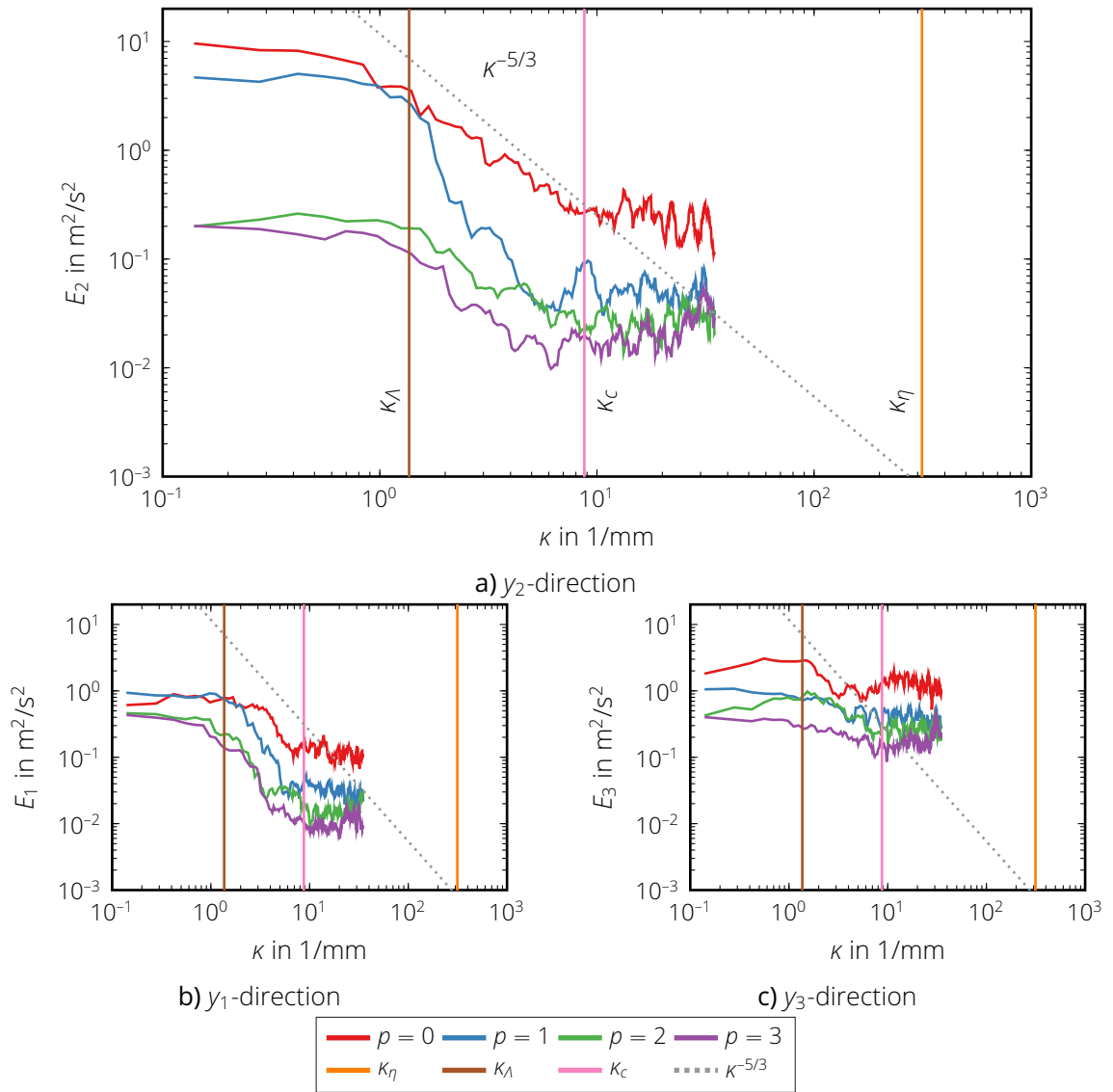


**Figure 4.8.** Water channel: Power spectrum of the single phase flow in the water channel. The measurement locations,  $p$ , were chosen based on the location of the bubble center (Fig. 4.7a). Additionally, the characteristic wavenumbers of the Komogorov scale,  $\kappa_\eta$  (Eq. 3.57), the integral scale,  $\kappa_L$  (Eq. 3.56), and the maximal resolvable wavenumber of the TPIV setup,  $\kappa_c$  (Eq. 3.68), are plotted. Although the bubble positions were used for the analysis, no stagnant bubble was present during these measurements.

tion of TKE along the wavenumbers are equivalent in all three dimensions. Therefore, Fig. 4.9 illustrates the ratio of the power spectra in  $y_1$ -direction,  $E_1$ , and  $y_3$ -direction,  $E_3$ , to the power spectra of the main flow direction,  $E_2$ . For the middle,  $p = 2$ , and lower bubble position,  $p = 3$ , these ratios remain in the order of one for the range of the small wavenumbers (= large turbulent length scales). Thus, it seems that at these bubble position the turbulent flow was isotropic.

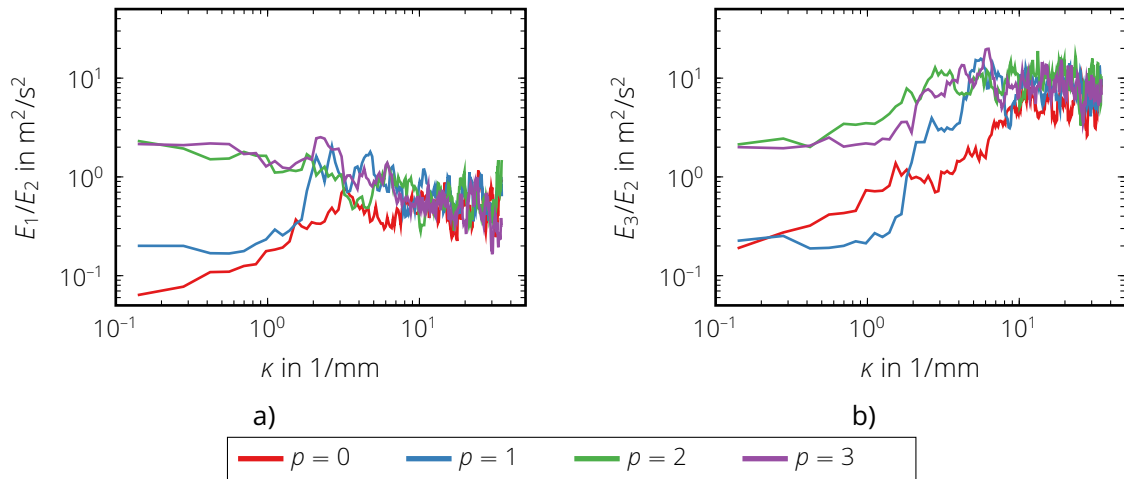


**Figure 4.9.** Water channel: Isotropy measure,  $E_i/E_2$ , of the single phase flow: a) The ratio of the power spectrum  $E_1$  to  $E_2$  and b) the ratio of the power spectrum  $E_3$  to  $E_2$ . The underlying power spectra were extracted from Fig. 4.8. The measurement locations,  $p$ , were chosen based on the location of the bubble center (Fig. 4.7a). Although the bubble positions were used for the analysis, no stagnant bubble was present during these measurements.

### 4.3.2. Shape and motion of bubbles

In the water channel, a more idealized bubble configuration was used to investigate bubble-particle interactions in a turbulent flow. A stagnant bubble attached on a needle allowed the measurements at a certain position, where the bubble was exposed to a defined turbulent flow. However, the attachment of the bubble to a needle led to a change of the bubble shape and motion, compared to a freely rising bubble. The properties of the stagnant bubbles are summarized in Fig. 4.10, in the form of their shape, their size distribution and shifting of the bubble center position.

An exemplary image of the bubble shape is illustrated in Fig. 4.10a, as typically captured with camera  $B$  (Fig. 3.4b) during the measurements. At first sight, the shape of the stagnant bubble would be comparable to an ellipsoidal bubble. However, Fig. 4.10a shows only the view of the bubble in the  $x_1x_2$ -plane. The stagnant bubble was still attached to the needle. Thus, viewing the bubble in the  $x_2x_3$ -plane, a pendant bubble shape would be observed similar to Fig. 2.4d. Nevertheless, for the further characterization of the bubble shape and motion, the stagnant bubble was assumed to be ellipsoidal in first approximation. At the center point, the semi-major and the semi-minor axis were extracted from the shadow image captured with camera  $B$  (Fig. 3.4b).

The repeatability of the formed stagnant bubbles is shown in Fig. 4.10b. Fig. 4.10b illustrates the bubble size distribution with a uniform bin width of 0.1 mm to reveal the underlying shape of the distribution. In general, the stagnant bubbles were produced in a narrow bubbles size distribution, independently from their position in the water channel,  $p$  (Fig. 3.1b). The diameter of the generated stagnant bubble was 2.3 mm, comparable to freely rising bubbles formed at the orifice with  $d_i = 300 \mu\text{m}$  (Fig. 4.3a).

The generation of stagnant bubbles with a considerably smaller or larger diameter was

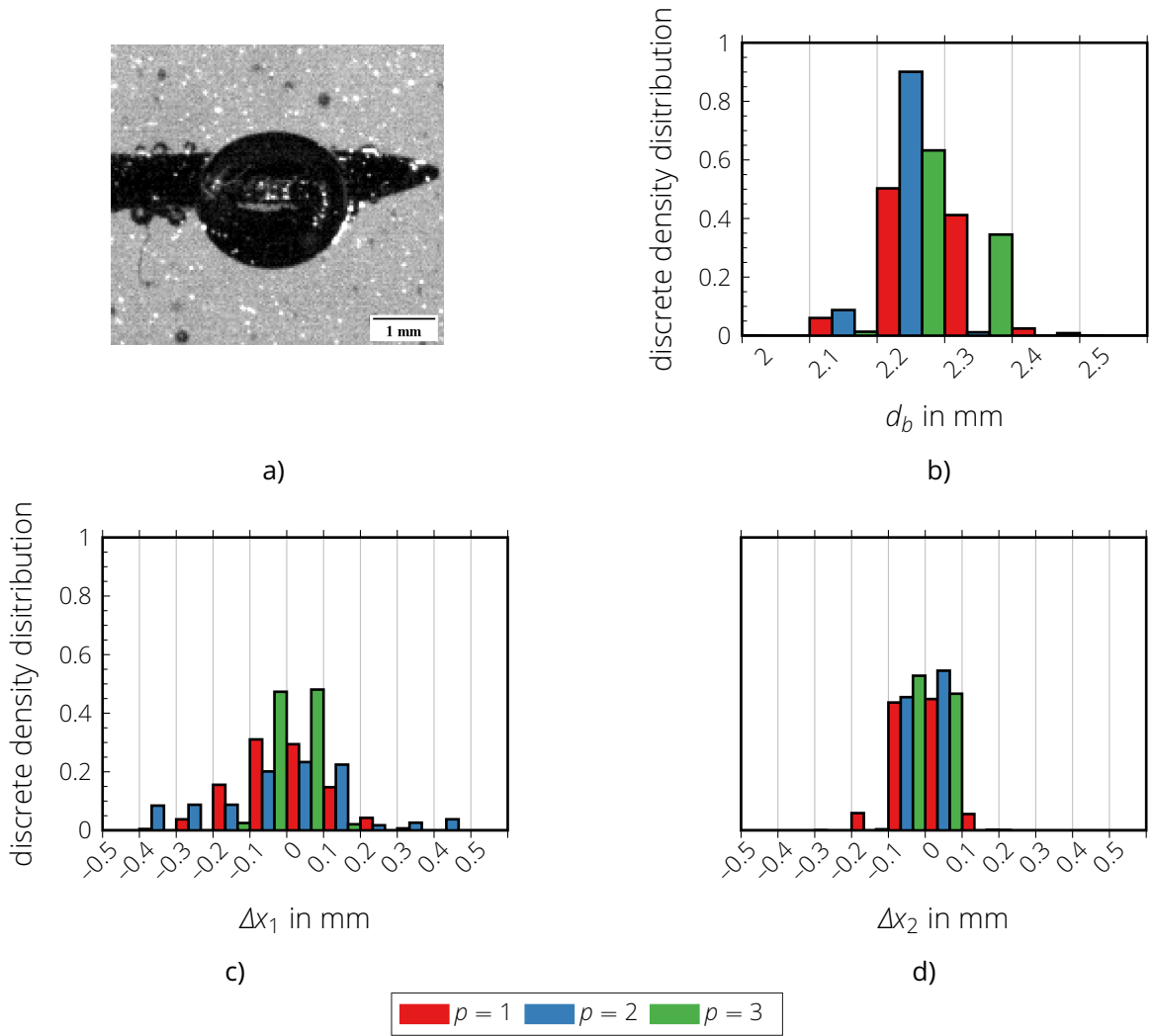


**Figure 4.10.** Water channel: Characteristics of the stagnant bubble depending on its distance to the grid,  $p$  (Fig. 3.1b): b) Bubble size distribution with a uniform bin with of 0.1 mm. c), d) Shifting of the bubble center position,  $\Delta x_i$  (Eq. 4.78), in  $x_1$ - and  $x_2$ -direction. The distributions have a uniform bin with of 0.1 mm.

challenging. On the one hand, decreasing the bubble diameter to  $d_b = 1.4$  mm, as generated by a orifice with  $d_i = 120 \mu\text{m}$  in the bubble column, would lead to a high distortion due to the needle. In this case, the bubble diameter would be slightly larger than the outer diameter of the needle ( $d_o = 0.9$  mm). On the other hand, increasing the bubble diameter to  $d_b = 3.2$  mm, as generated by a orifice with  $d_i = 600 \mu\text{m}$  in the bubble column, the stagnant bubble would detach before reaching the desired bubble diameter. In this case, the buoyancy force (Eq. 2.18) would exceed the surface tension force (Eq. 2.17). Therefore, only the bubble diameter of 2.3 mm was feasible during the water channel experiments.

For the direct measurement of the collision probability, Nguyen et al. [49] mainly observed the collision trajectories in quiescent and laminar flows. Their concern was that high velocities and fluctuations would lead to a varying shift of the bubble position and final detachment of

the stagnant bubble. To address these concerns, Fig. 4.10c and d illustrate the distribution of the shifting of the bubble center in  $x_1$ - and  $x_2$ -direction. The uniform bin width of the distribution is set to 0.1 mm and is adopted to reveal the underlying shape of the distribution. The shifting of the bubble center point is quantified as

$$\Delta x_j = x_j - \bar{x}_j. \quad (4.78)$$

The largest shift of the bubble position occurred in  $x_1$ -direction, ranging between  $-0.4$  mm and  $0.5$  mm. In  $x_2$ -direction, the shifting remained between  $-0.2$  mm and  $0.2$  mm. Although these variations in the bubble position were inevitable for the usage of a turbulent inflow of the bubble, they remained within a reasonable range.

### 4.3.3. Flow field around bubbles

The variation of the turbulent length scales upstream of each stagnant bubble (Sec. 4.3.1) changed also the flow around the bubble. Fig. 4.11 shows the influence of the different turbulent length scales on the magnitude of the average velocity (Fig. 4.11a-c), the vorticity in the  $y_{l,1}y_{l,2}$ -plane,  $\omega_3$  (Fig. 4.11d-f), the TKE (Fig. 4.11g-i) and the dissipation rate (Fig. 4.11j-l). In Fig. 4.11 each column denotes one bubble position,  $p$  (Fig. 3.1b), whereas each row represents one parameter of the fluid flow around the corresponding bubble. The averaging of these parameters was performed as a time-average (Eq. 2.5).

Independently of the bubble position, the averaged velocity magnitude (Fig. 4.11a-c) is in the order of the average channel flow,  $0.18$  m/s. At the upper bubble position ( $p = 1$ ), small variations can be contributed to remaining oscillation of the liquid flow as illustrated in Fig. 4.7b. Downstream of each bubble, the magnitude of the liquid velocity decelerates and forms two small counter-rotating vortices at the trailing edge of the bubble (Fig. 4.11d-f).

To quantify the effect of the generated turbulence on the turbulent parameters in the flow around the bubble, Fig. 4.11g-l illustrate the TKE and the dissipation rate. The highest values of TKE and dissipation rate are observed upstream and downstream of the upper bubble position (Fig. 4.11g,j). Besides the wake region of the stagnant bubble, also downstream of the needle, these values are enhanced compared to the flow upstream. This corresponds to the findings in Fig. 4.7c at  $p = 2$ , where the degree of turbulence is significantly higher at  $y_1 < 10$  mm, which corresponded to the wake of the upper needle. This supports that the mounting needle influenced the wake region behind the bubble.

Turning now to the other bubble positions, the values of TKE and dissipation rate decrease with increasing distance to the grid. One reason could be the degree of turbulence upstream of each bubble. A higher degree of turbulence led to a later detachment of the boundary layer [86, 196]. Thus, the detachment point of the boundary layer moved further to the trailing edge of the bubble (Sec. 2.2.3). Consequently, the generated turbulence in the water channel influenced not only the flow upstream of each bubble position, but also the recirculating flow in the bubble wake. Similarly, Rüttinger et al. [62] observed an influence of the turbulent structures of a vortex street behind a cylinder on the wake of a stagnant bubble.

The range of the turbulent length scales is illustrated via the power spectra in Fig. 4.12 at two positions. These positions are located upstream,  $Y_{up}$ , and downstream of the stagnant

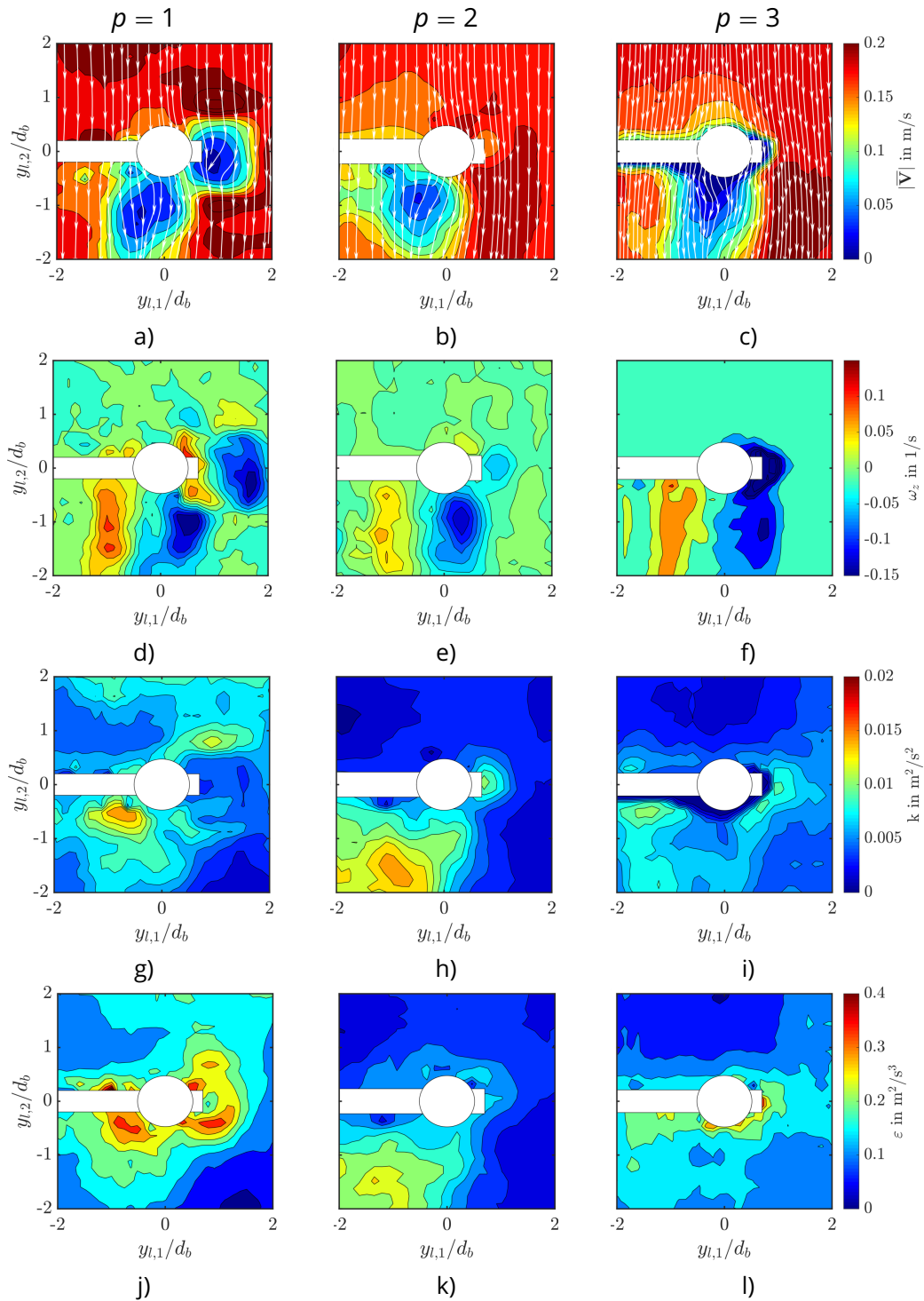


Figure 4.11. Water channel: Flow field around a stagnant bubble at different needle positions,  $p$ , in the water channel (Fig. 3.1b). a)-c) Magnitude of the averaged liquid velocity field,  $|\bar{\mathbf{V}}|$ . d)-f) Averaged vorticity in the  $y_{l,1}y_{l,2}$ -plane,  $\omega_3$ . g)-i) Averaged turbulent kinetic energy,  $k$ . j)-l) Averaged dissipation rate,  $\varepsilon$ . The values are time-averaged over 1.5 s using the  $y_{l,3}$ -axis from 0 mm to 0.3 mm.

bubble,  $Y_{down}$ , as marked in the inset of Fig. 4.12a. Firstly, the power spectrum of the stagnant bubble closest to the grid ( $\rho = 1$ ) is illustrated in Fig. 4.12a. Independently from the investigated position upstream or downstream of the bubble, the values of TKE remain in the same order of magnitude and only depend on the wavenumber. Meaning, the highest values of TKE are in the range of the integral wavenumber (Eq. 3.56) and decrease with an increasing wavenumber (= decreasing turbulent length scale) with the typical  $-5/3$  - rise in the inertial range to the cut-off wavenumber  $\kappa_c \approx 8.75$  1/mm (Eq. 3.68). The Kolmogorov length scale (Eq. 3.57) is not resolved due to noise of the TPIV.

Secondly, with increasing distance of the stagnant bubble to the grid (Fig. 4.12b,c), the magnitude of TKE reduces upstream of the bubble,  $Y_{up}$ , due to the decay of the large scale turbulence (Sec. 4.3.1). In contrast, the distribution of TKE downstream of the bubble remains in the same order of magnitude along the wavenumbers. Although Fig. 4.11g-l show a dependency between bubble position and turbulent parameter in the bubble wake, no influence is observed in the power spectrum of the bubble wake.

Additionally, the particle wavenumbers (Eq. 3.59) are marked in the power spectra. Due to the flow circulation in the water channel, not only the fine particle system, *PS33*, but also the coarse particle system, *PMMA200*, could be applied for the analysis of the particle collision behavior (further information on the particle systems are summarized in Tab. 3.5). The particle wavenumbers are denoted in Fig. 4.12 as  $\kappa_{p33}$  representing *PS33*, and  $\kappa_{p200}$  and  $\kappa_{p400}$  the lower ( $d_p = 200$   $\mu\text{m}$ ) and upper end ( $d_p = 400$   $\mu\text{m}$ ) of the heterodispersed particle size distribution of *PMMA200*. The small particles exceed the Kolmogorov wavenumber,  $\kappa_{p33}^b > \kappa_{\eta}^b$ . Consequently, these particles are expected to respond to all changes of the fluid flow in the water channel. In contrast, the coarse-sized particles are characterized by a lower wavenumber ( $\kappa_{p400} < \kappa_{p200} < \kappa_{\eta}^b$ ) and, thus, deviate from the fluid streamlines already in the large turbulent length scales. Therefore, this particle system was significantly less affected by the small turbulent length scales in the water channel and wake of the bubble.

## 4.4. Discussion and Conclusion

This chapter analyzed the multiphase flow generated in the two experimental setups - the bubble column and the water channel. In particular, the shape and size of the formed bubbles, and the accompanied turbulent flow fields were investigated in detail. The results demonstrated that the chosen experimental setups were eligible to generate a generic turbulent flow and were appropriate to answer Question **Q.2** in Sec. 1.2. The properties of the generated turbulent flows in both experimental setups are summarized in Tab. 4.1.

In the first step, the bubble size was investigated, showing that all bubbles were generated reproducibly with a distinctive diameter. In the bubble column, the bubbles varied in diameter and shape according to the inner diameter of the needle. As typical for these shape regimes, the bubble motion exhibited instabilities resulting in a spiral or zigzag path, and rotating movement. In contrast, the stagnant bubble lacked in diversity of size and shapes, but remained at a defined position. Only a small variation of the bubble position was observed due to the turbulent flow conditions upstream of the bubbles. A possible case for comparison would be the bubble configuration of  $d_b = 1.4$  mm in the bubble column because the

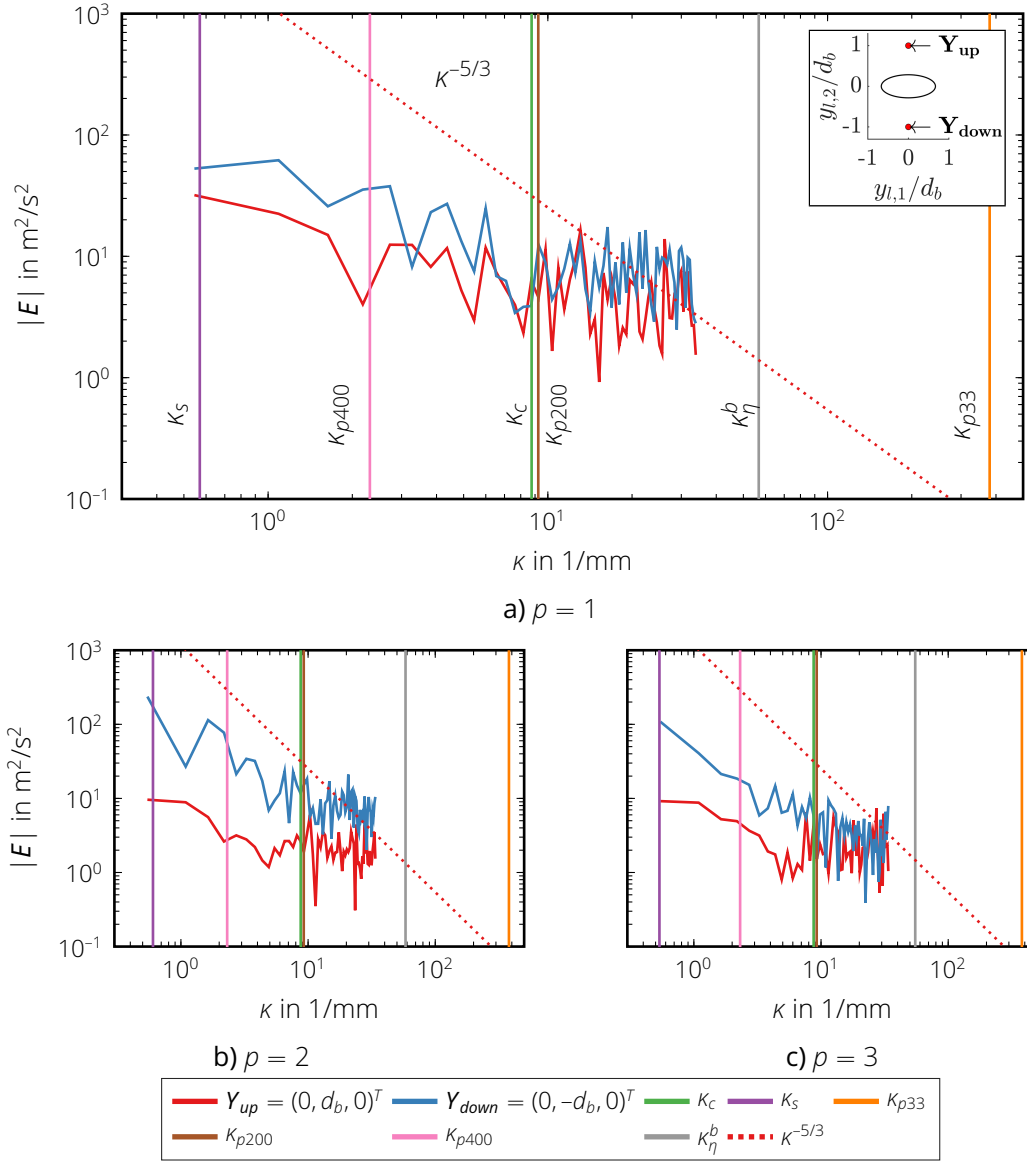


**Figure 4.12.** Water channel: Power spectrum of the velocity magnitude,  $|\bar{V}|$ , at two positions,  $Y_{up}$  upstream of the stagnant bubble;  $Y_{down}$  in the wake of the stagnant bubble. These analysis locations are marked as red dots in the inset of a). Furthermore, the characteristic wavenumbers are denoted as the maximal resolvable wavenumber of the current TPIV setup,  $\kappa_c$  (Eq. 3.68), the shedding wavenumber of the bubble,  $\kappa_s$  (Eq. 3.60), the maximum response wavenumber of the particles,  $\kappa_{p33}$ ,  $\kappa_{p200}$  and  $\kappa_{p400}$  (Eq. 3.59), and the Kolmogorov wavenumber,  $\kappa_{\eta}^b$  (Eq. 3.61).

bubble Reynolds number for both setups was approximately 450. It is noted that the comparison was only feasible to a certain extent due to their varying bubble dynamics (rising and stagnant).

These bubbles were either released in a quiescent liquid in the bubble column or remained attached on a needle exposed to a turbulent flow in the water channel. In the water channel, the highest degree of turbulence was measured at  $p = 1$ , and decreased from  $p = 2$  to

**Table 4.1.** Comparison of the flow characteristics between the freely rising bubble in the bubble column and the stagnant bubble in the water channel. The Stokes number is computed via Eq. 2.38, using the Kolmogorov time scale,  $\tau_\eta^b = d_b \cdot Re_b^{-1/2} \cdot \overline{u_b}^{-1}$  [156], as characteristic time scale of the liquid flow.

		Freely rising bubble	Stagnant bubble
Bubble	Shape	Spherical to wobbling	Pendant
	Size	1 mm...3.5 mm	2 mm...2.5 mm
	Position	Varying, due to path instability	Pinned to the orifice
	Wake formation	Yes, for $d_b = 2.4$ mm and 3.2 mm	Yes, but disturbed by mounting needle
	Surface mobility	Mobile	Immobile
Flow field	Inflow	Quiescent	Turbulent, $Tu_{22} = 5\% \dots 15\%$
Particles	Particle systems Stokes number	<i>PS33</i> and <i>PS95</i>	<i>PS33</i> and <i>PMMA200</i>
		<i>PS33</i> : $O(St) = 0.1$ <i>PS95</i> : $O(St) = 1$	<i>PMMA200</i> : $O(St) = 10$

$p = 3$  (Fig. 4.7c). The increasing distance to the grid led to a decay to the large turbulent length scales (Sec. 2.1.2). Therefore, the larger length scales were still observed at  $p = 1$ , whereas  $p = 2$  and  $p = 3$  had already developed isotropic turbulence (Fig. 4.8). Theoretically, the Kolmogorov scale of  $\eta^* = 20 \mu\text{m}$  (Eq. 2.12) was reached in the water channel. However, this value could not be quantified experimentally due to the limited spatial and temporal resolution of the TPIV setup.

All these varying conditions of the bubble properties and flow conditions affected the flow field around the bubbles. The changes were mainly analyzed in terms of the liquid velocity magnitude, the vorticity in the  $y_{l,1}y_{l,2}$ -plane, the TKE, the dissipation rate, and the power spectrum in the vicinity of the bubble. Starting with the freely rising bubble chain, the measured flow field revealed an axisymmetric wake structure downstream of the small-sized bubbles, whereas a double-threaded wake structure was shown downstream of the medium- and large-sized bubbles. In the literature [e.g. 90], the double-threaded wake corresponds to the onset of the path instability, resulting in a transition of the bubble rising trajectory from rectilinear to an oscillatory motion. Consequently,  $d_b = 1.4$  mm would exhibit a rectilinear rising path, whereas the trajectories of the  $d_b = 2.4$  mm and 3.2 mm would undergo a zigzag motion. However, a zigzagging rising path was also observed for the smallest bubble diameter. This path instability does not result from the standing eddy, but was instead connected to bubble-bubble interaction and its coupling to the surrounding flow.

The flow field around the freely rising bubble is connected not only to its rising path, but also to the state of its surface mobility. The mobility affects the boundary conditions of the bubble surface, leading to a change in the flow field around the bubble [49, 197]. In general, there are two limiting cases for bubble surface mobility: mobile and immobile (Sec. 2.2.4). As the spatial resolution of the TPIV measurements was lower than the micro-Particle Image



Velocimetry (PIV) measurement in Eftekhari et al. [109] the state of mobility of the bubble surface could not be evaluated. In the present case, the liquid phase consisted only of deionized (DI) water and potassium chloride (KCl), without any trace of surfactant. During the experiments, special care was taken to avoid contamination due to surfactants by repeated rinsing of the bubble column with deionized water. The measurement took place approximately 0.2 s after the bubble surface was generated. Consequently, the bubble surface could be approximated as mobile. This was confirmed by the high terminal velocity (Tab. 3.1). Clift et al. [44] estimated a terminal velocity of around 0.2 m/s for contaminated water, and around 0.3 m/s for pure water, using the flow parameters similar to the conducted experiments.

For the investigation of the particle collision trajectory, only fine particle systems, *PS33* and *PS95*, were applicable in the bubble column due to their low settling velocity. These two systems varied in their responses to turbulent length scales. For the characterization the Stokes number (Eq. 2.38) was used, applying the Kolmogorov time scale,  $\tau_{\eta}^b = d_b \cdot Re_b^{-1/2} \cdot \bar{u}_b^{-1}$  [156], as characteristic time scale of the liquid flow. In the case of *PS33*, the Stokes number was much smaller than one, thus these particles could respond to all changes in the fluid flow. In contrast, the Stokes number of *PS95* was approximately one, allowing these particles to deviate from the fluid streamline and collide with the bubble surface.

Turning now to the turbulent flow in the water channel, the stagnant bubbles were generated by means of a needle at different positions,  $p = 1 - 3$ . This configuration provided bubbles of constant diameter and at predefined positions. However, the flow around the bubble pinned to the needle was disturbed by the needle itself. For example, in Fig. 4.11g, also downstream of the needle, the TKE was enhanced compared to the flow upstream of the bubble.

In general, the influence of the turbulent inflow conditions was shown. With increasing degree of turbulence upstream of the stagnant bubble, the TKE and dissipation rate at the trailing edge of the bubble increased. The magnitude of the velocity and size of the two counter-rotating vortices remained in the same order of magnitude among the different bubble positions ( $p = 1 - 3$ ). In contrast, the two counter-rotating vortices were not observed for the freely rising bubble ( $d_b = 1.4$  mm,  $Re_b \approx 450$ ), as shown in Fig. 4.4d. There are several possible explanations for this result. Besides the distortion due to the needle, the generated turbulence in the water channel influenced not only the flow upstream of each bubble position, but also the recirculating flow in the bubble wake. Similarly, Rüttinger et al. [62] observed an influence of the turbulent structures of a vortex street behind a cylinder on the wake of a stagnant bubble. They showed that the vortex street amplified the fluctuation, and thus the TKE, in the bubble wake.

Additionally, the state of the bubbles surface mobility varied between the two setups. The bubble column investigated a nearly mobile bubble, whereas in the water channel, the bubble surface could be approximated as immobile. This immobility was caused by the hydrophobized mounting needle to overcome an easy detachment of the bubble due to the turbulent inflow. This immobile surface may change the flow field around the bubble, and thus the formation of the two counter-rotating vortices in the bubble wake could onset at lower bubble Reynolds numbers [45, 49, 110].

Due to the circulation of the fluid flow, the water channel enabled the usage of larger sized particle systems which were also applicable to be transformed into radioactive tracers

during the Positron Emission Particle Tracking (PEPT) measurements. Therefore, the particle systems *PS33* and *PMMA200* were applied. Similar to the bubble column, the Stokes number of the *PS33* particle system was far below one, thus these particles could respond to all changes in the fluid flow. In contrast, the *PMMA200* particle system exceeded the Stokes number of one by far. Consequently, the particles deviate from the fluid streamline already in the large turbulent length scales.

It is plausible that a number of limitations might have influenced the results obtained in the water channel. Although special care was taken during the experiments, the vibrations caused by the pump could only be damped within a certain range. Thus, uncertainties arose during the reconstruction of the velocity field, leading to inaccuracies in the computed velocity fields. Further, the gained results are applicable to a dilute system, as present during the 4D Particle Tracking Velocimetry (PTV) measurements. However, these findings are only partly relevant to a dense flow, as induced in the PEPT measurements (Sec. 5.3). With higher solid fraction, the particles may modify the carrier phase turbulence compared to the single phase flow (Sec. 2.3.2). Using only the particle's Reynolds number as approximation, similar to Hetsroni [198], the degree of turbulence in this dissertation should be reduced by adding the PMMA suspension (Tab. 3.5) because of its low particle Reynolds number ( $Re_p < 400$ ). However, the effect of the turbulent modulation cannot be reduced to one parameter, it is a combination of various mechanisms such as wake dynamics, self-induced vortex shedding and buoyancy-induced instabilities (Sec. 2.3.2). Therefore, an extrapolation of the degree of turbulence from the dilute to dense solid suspension is challenging. Other techniques as e.g. the piezo-electrical vibration sensor [199–201] or constant temperature anemometer [201–203] would be more suitable to measure the liquid phase velocity in a dense multiphase flow.

To sum up, the features of the fluid flow for both setups were investigated in this chapter. Although the freely rising bubble is closer to the bubble motion in a flotation cell, the stagnant bubble enabled a defined positioning in the turbulent flow. The slightly idealized system allowed to investigate separately and generically the defined turbulent inflow conditions on the bubble-particle interactions. Distortions from path instabilities or rotation, which are typical for freely rising bubbles in this size range, could be avoided. Therefore, both setups enable to investigate a range of flow fields and their influence on the collision between particles and bubbles. The measurement of the flow field with TPIV represented the framework to study the motions and collision behavior with 4D PTV (Sec. 5.1 and 5.2) and PEPT (Sec. 5.3).

## 5. Particle motion in the vicinity of bubbles measured with 4D PTV and PEPT

After the characterization of the generated bubbles and their surrounded liquid flow field, the results of the observed bubble-particle collision phenomena are summarized in the following sections. Beginning with the bubble column, Sec. 5.1 explores the collisions between fine particles and a freely rising bubble chain with 4D Particle Tracking Velocimetry (PTV) [38, 41]. Specifically, the collision positions on the bubble surface are examined carefully in context of the surrounding flow (Sec. 4.2.2). The collision frequencies are determined experimentally and are compared to those in the literature [36, 37, 79]. Similarly in Sec. 5.2, the interactions between particles and a stagnant bubble are examined in the turbulent flow of the water channel. Until now, the particle suspension had to be dilute to be applicable for 4D PTV. To also perform experiments in a dense particle suspension, Positron Emission Particle Tracking (PEPT) is employed to the water channel in Sec. 5.3 [39]. The analysis comprises the particle distribution and their deviation in the vicinity of the stagnant bubbles. Finally, Sec. 5.4 discusses the collision phenomena observed with a freely rising bubble chain and a stagnant bubble, and evaluates both particle tracking techniques, 4D PTV and PEPT.

### 5.1. Freely rising bubble chain measured with 4D PTV

As stated in Sec. 3.1.1, the experiments on the freely rising bubble chain were conducted in the bubble column (Fig. 5.1). They comprised three different bubble diameters ( $d_b = 1.4$  mm, 2.4 mm, 3.2 mm; Sec. 4.2.1) by varying the orifice of a single blunt needle. The variation of the bubble diameter went along with a change of the wake structure and turbulent length scales (Sec. 4.2.2). To observe the bubble-particle interactions, two sets of model particle systems (*PS33* and *PS95*; Tab. 3.5) were exposed to these varying liquid flow conditions. In the following, the results obtained from a freely rising bubble chain and fine particles are summarized applying 4D PTV.

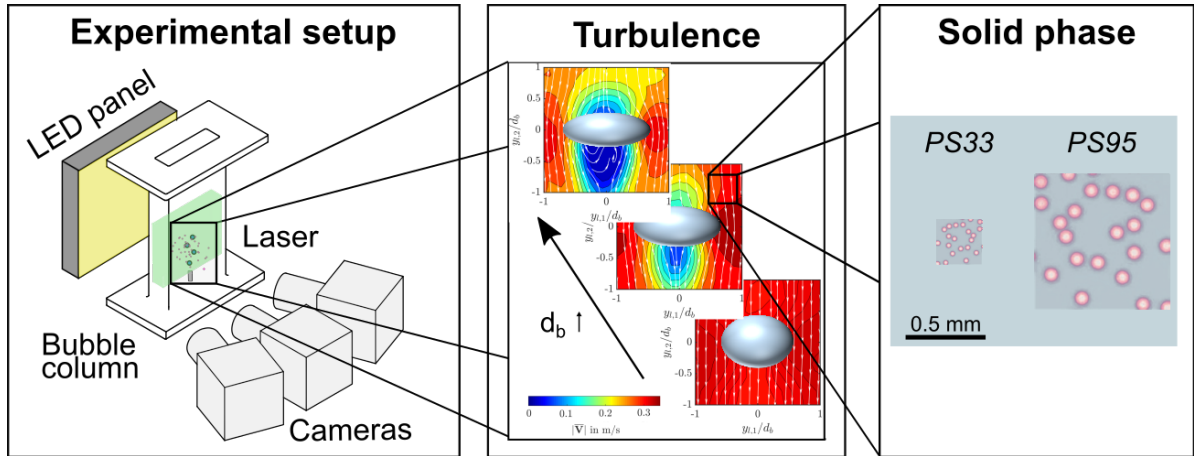


Figure 5.1. Bubble column: Graphical abstract of the experimental arrangement for the measurements in the bubble column with 4D PTV. The particle model system *PS33* and *PS95* consisted of fluorescent polystyrene (PS) particles with a diameter of  $33\ \mu\text{m}$  and  $95\ \mu\text{m}$ , respectively. Please refer to Sec. 3.1.1 for more details of the experimental setup and Tab. 3.5 for the properties of the model particle systems.

### 5.1.1. Verification of collision criteria

Before doing an in-depth analysis of the bubble-particle interactions, the defined collision criteria (Eq. 3.75) had to be proved. Therefore, an exemplary leading and trailing edge collision trajectory out of 578 are shown in Fig. 5.2. The corresponding raw data in the form of a video can be found in Sommer et al. [204]. The analyzed trajectories are illustrated as the triangulated particle position in the vicinity of the rising bubble (Fig. 5.2a and c) and the course of the radial velocity,  $w_r$ , and normalized radial position,  $r/r_b$ , over time,  $t$  (Fig. 5.2b,d). Additionally, the collision criteria of the radial velocity (Eq. 3.75a) and the residence time (Eq. 3.75b) are inserted as lines marked  $w_r^{\text{max}}$  and  $r^{\text{max}}/r_b$ , respectively. The resultant classified collisions are highlighted with a red circle.

The leading edge trajectory (Fig. 5.2b) can be divided into three stages: approach, collision and sliding phase along the bubble surface. Afterwards, the hydrophobic particle was supposed to attach to the bubble surface. Note that the limited spatial resolution excludes the observation of the rupture of the liquid film between the particle and the bubble - the basic condition for successful attachment. During the approach phase, the radial position,  $r$ , and the magnitude of the radial velocity decreased. The minimum of both values was reached at  $t \approx 5\ \text{ms}$  with  $r \approx 0.8r_b$  and  $w_r \approx 0\ \text{m/s}$ . Thus, at this time step, the particle trajectory collides on the bubble surface. In the sliding phase, the radial position increased slightly due to the particle movement from the minor to the major semi-axis of the ellipsoidal bubble. Consequently, the radial velocity also rose slightly. The trailing edge of the bubble was reached at  $t \approx 10\ \text{ms}$  with  $r \approx r_b$  and  $w_r \approx 0\ \text{m/s}$ . From that time step on, the particle trajectory retains its radial distance and velocity over more than 8 ms, fulfilling both classification criteria (Eq. 3.75).

The radial position and velocity of the trailing edge collision trajectory are shown in Fig. 5.2d. In general, the sliding phase vanishes for the trailing edge collision. The radial position of the

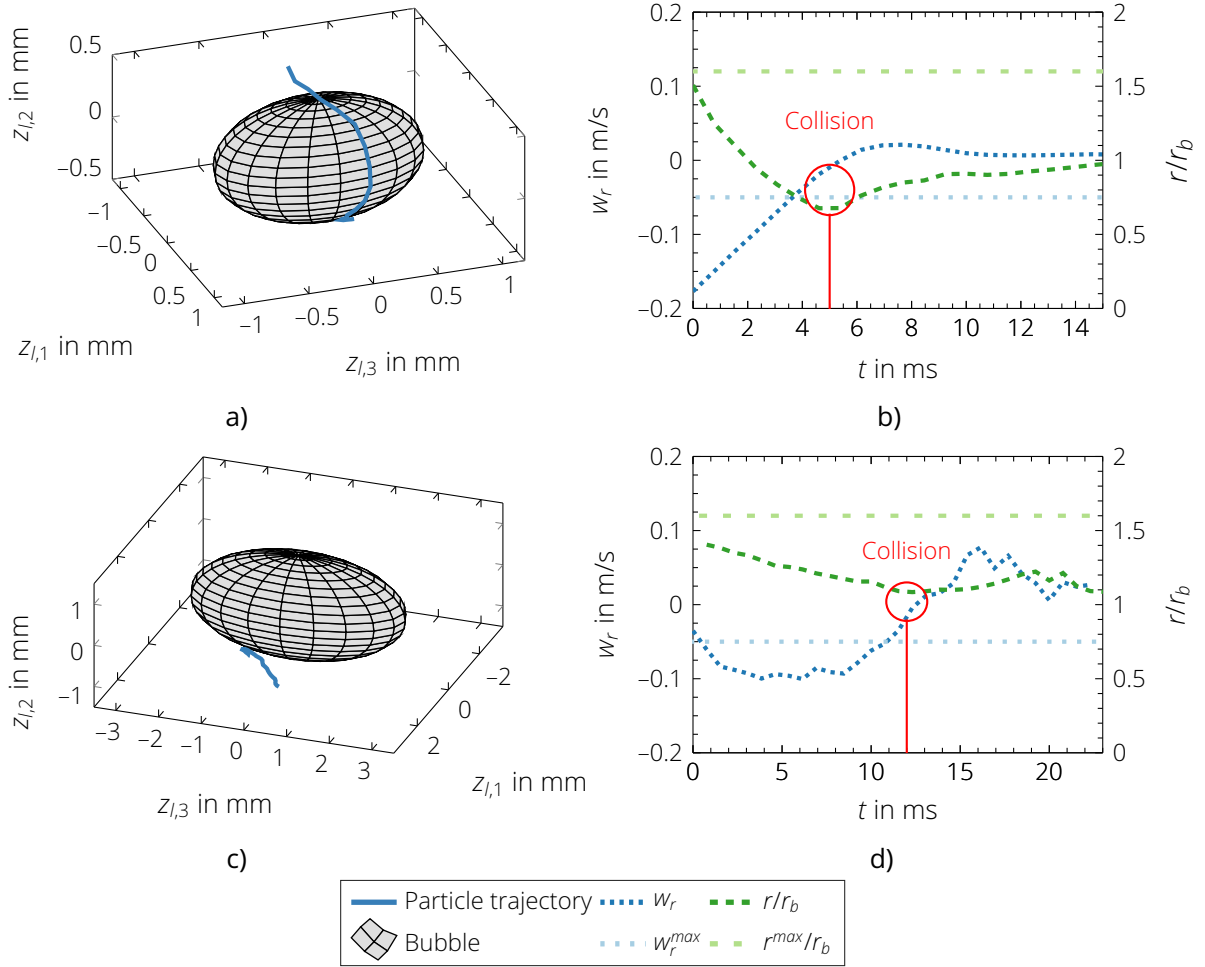


**Figure 5.2.** Bubble column: Classification of a leading (top row) and trailing (bottom row) edge collision of an exemplary trajectory as seen in Sommer et al. [204]. a), c) Particle trajectory in the local coordinate system of the averaged bubble dimension during this time. The bubble radius is illustrated 20 % smaller, to enhance the visibility of the particle trajectory. b), d) Diagram of the radial velocity,  $w_r$ , and radial distance normalized by the bubble radius,  $r/r_b$ , over time,  $t$ . Additionally, the collision criteria of the radial velocity (Eq. 3.75a) and the residence time (Eq. 3.75b) are inserted as a dotted line in light blue ( $w_r^{max}$ ) and a dashed line in light green ( $r^{max}/r_b$ ), respectively. The resultant classified collisions are highlighted with a red circle.

particle decreases slightly from  $1.6 r_b$  to approx.  $1.2 r_b$ . The magnitude of the radial velocity remains below  $0.05 \text{ m/s}$ . Thus, the collision point is at the plateau of the radial position ( $t \approx 12 \text{ ms}$ ). From that time step on, the particle trajectory retains its radial distance and velocity over more than 20 ms, meeting both classification criteria (Eq. 3.75).

To sum up, the defined classification criteria using the radial velocity and residence time (Eq. 3.75) are a suitable basis for detecting colliding particles at the leading and trailing edges of a bubble.

### 5.1.2. Bubble-particle collision

Applying these collision criteria (Eq. 3.75) to all detected particle trajectories, overall 578 trajectories were classified as colliding. Their preferred collision position on the bubble surface is illustrated in Fig. 5.3, in the form of the normalized distribution of collision events according to the bubble's polar angle,  $\theta$  (as shown in the inset of Fig. 5.3c). For each measurement configuration, the uniform bin width of the distribution is set to  $20^\circ$  to reveal its underlying shape. The number of collisions of each bin,  $N_{c,i}$ , is normalized by the overall number of collision events of the specific configuration,  $N_c$ . These configurations comprised three bubble diameters,  $d_b$ , denoted by each column, and two model particle systems (*PS33* or *PS95*), represented by each row.

For all configurations, a leading edge collision, see red bins, takes place along the entire range of polar angle between  $0^\circ$  and  $180^\circ$ . The peak in the number of collisions mainly occurs at the bin from  $80^\circ$  to  $100^\circ$ , including the stagnation point of the bubble at  $90^\circ$ . Trailing edge collisions, see the blue bins, are observed only for three configurations. For the medium-size bubble,  $d_b = 2.4$  mm (Fig. 5.3e), they are only detected for the largest particle system, *PS95*, and for the largest bubble diameter for both particle systems (Fig. 5.3c and f). In these three cases, the collision point varies between a polar angle of  $-140^\circ$  and  $-50^\circ$ , covering a smaller range than for the leading edge collision.

To quantify the statistical relevance of the collision points in Fig. 5.3, Fig. 5.4 summarizes the collision position in the form of a box plot for different time segments. In general, a box plot visualizes the distribution of a given sample through their percentiles, named median, 25th percentile, 75th percentile, upper and lower whisker (as shown in the legend below Fig. 5.4). More details on the computation of these percentiles is given in the Appendix A.5. In context of the statistical relevance, the aim was that the distribution of the collision events according to the bubble's polar angle,  $\theta$ , remained independent of the chosen sample. Therefore, three samples are selected for each configuration based on different time intervals. The first half of the measurement time, denoted by index 1, the second half of the measurement time, denoted by index 2, and the entire measurement time, denoted by index *A*, were applied as the underlying population.

The largest underlying population of detected collision events for the entire measurement time was  $N_c = 353$  in Fig. 5.4b. Comparing the box plots of the first half of the measurement time,  $L_1$ , and the second half,  $L_2$ , to the overall measurement time,  $L_A$ , the median and the spread of the 25th to 75th percentiles of the collision angle vary only by approximately  $10^\circ$ . Thus, the collision positions on the leading edge could be allocated to the same histogram bin width of  $20^\circ$  as shown in Fig. 5.3b. With a decreasing number of collision events as, for example in Fig. 5.4c with  $N_c = 112$ , the agreement of the median collision position and the spread of the data between the 25th and 75th percentiles remain in the same order of magnitude as in Fig. 5.4b. Only a slightly smaller median collision angle with a narrower spread of the population is shown for the first half of the measurement time of the trailing edge collision,  $T_1$ . However, the collision angles of  $T_1$  persist in the 25th to 75th percentiles of  $T_A$ .

To sum up, a reasonable agreement of the collision angle was achieved for all bubble and particle configurations in these three time segments. This confirms the statistical relevance

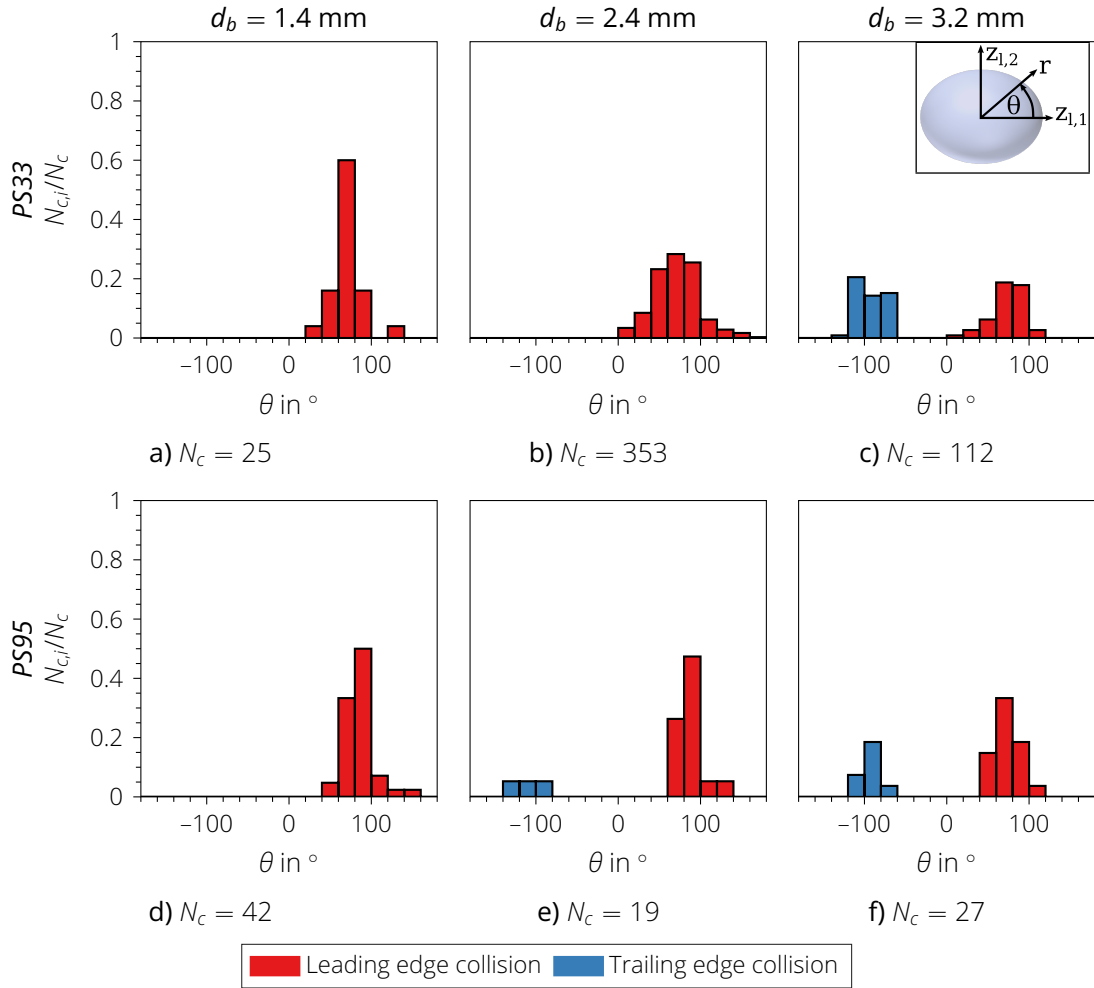


**Figure 5.3.** Bubble column: Normalized distribution of collision events according to their collision position at the bubble surface. The collision position is defined by the bubble's polar angle,  $\theta$ , as shown in the inset of c). The collision position is defined, where for the first time the particle trajectory reaches a minimum distance of  $r \approx 0.8r_b$  and minimum radial velocity of  $w_r \approx 0$  m/s. The uniform bin width of the distribution is set to  $20^\circ$ . For each bin, the number of collisions,  $N_{c,i}$ , is normalized by the overall number of collision events of the specific bubble diameter,  $d_b$ , and model particle system (PS33 or PS95).

of the detected collision positions, even for a modest underlying data population as, for example, in Fig. 5.4e with  $N_c = 19$ .

### 5.1.3. Interaction of the flow field on the trailing edge collision

The previous section showed that leading edge collisions occurred during all measurements, while trailing edge collisions appeared only for the larger bubble diameters ( $d_b \leq 2.4$  mm). One reason for these differing results was the fluid flow field around the freely rising bubbles because it influenced the particle trajectories. Therefore, Fig. 5.5 assesses the impact of

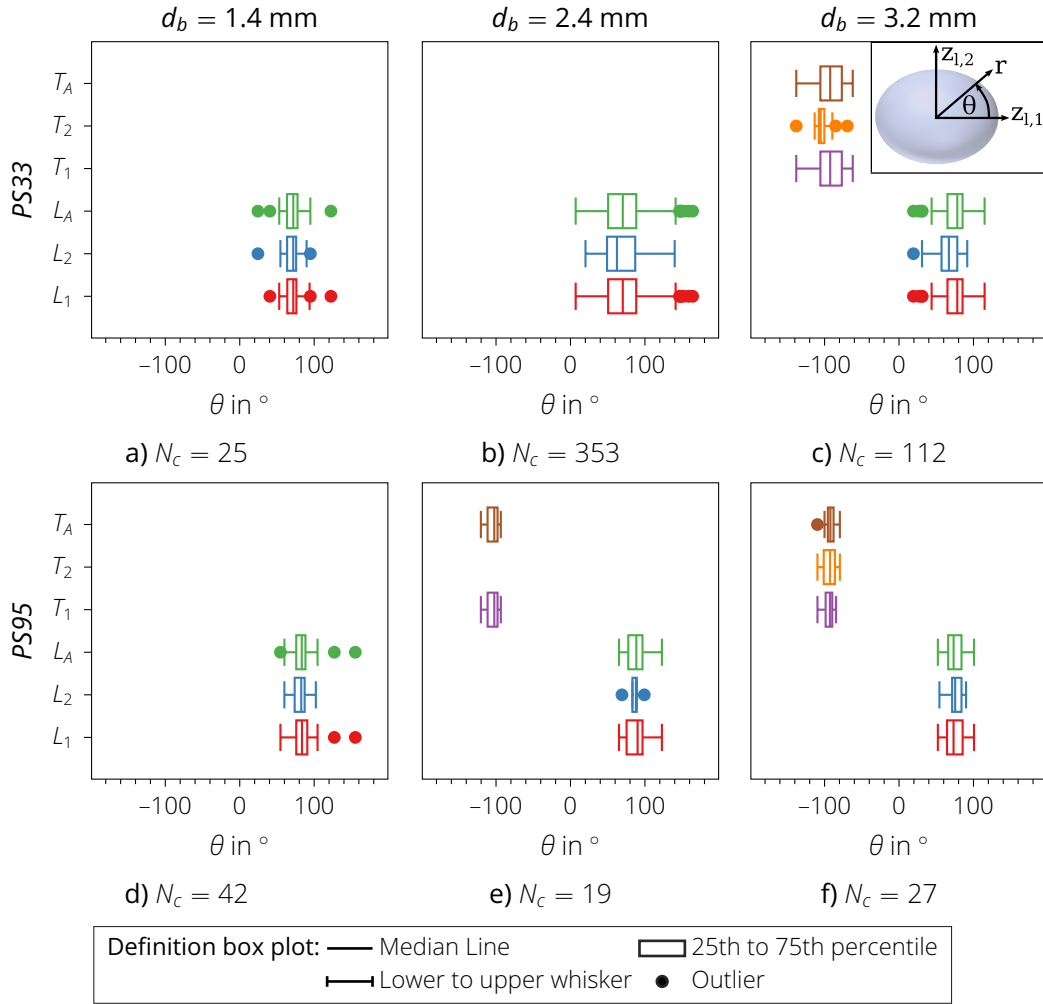


**Figure 5.4.** Bubble column: Box plots of the normalized distribution of the collision events according to the bubble's polar angle,  $\theta$ , as illustrated in the inset of c). Three sets of data are selected from the leading,  $L$ , and trailing,  $T$ , edge collision. They are chosen based on different time intervals for each measurement configuration. The underlying population of each sample is denoted by the indexes 1, 2 and  $A$  of  $L$  or  $T$  (y-axis). These samples are defined as the first half of the measurement time, represented by index 1, the second half of the measurement time, represented by index 2, or the complete measurement time, represented by index  $A$ . The variable  $N_c$  summarizes the underlying population of particle collision trajectories for the entire measurement time at the leading and trailing edge of the bubble. More details on the computation of the percentiles used in the box plot are given in the Appendix A.5.

turbulent parameters on the bubble-particle collision by plotting the dissipation rate and turbulent kinetic energy (TKE) (Fig. 4.4) together with the distribution of the collision position (Fig. 5.3) along the bubble's polar angle,  $\theta$  (Fig. 3.10a).

To determine the magnitude of these turbulent parameters along the bubble surface, the data shown in Fig. 4.4 are averaged over cylindrical sectors. Each cylindrical sector is defined,



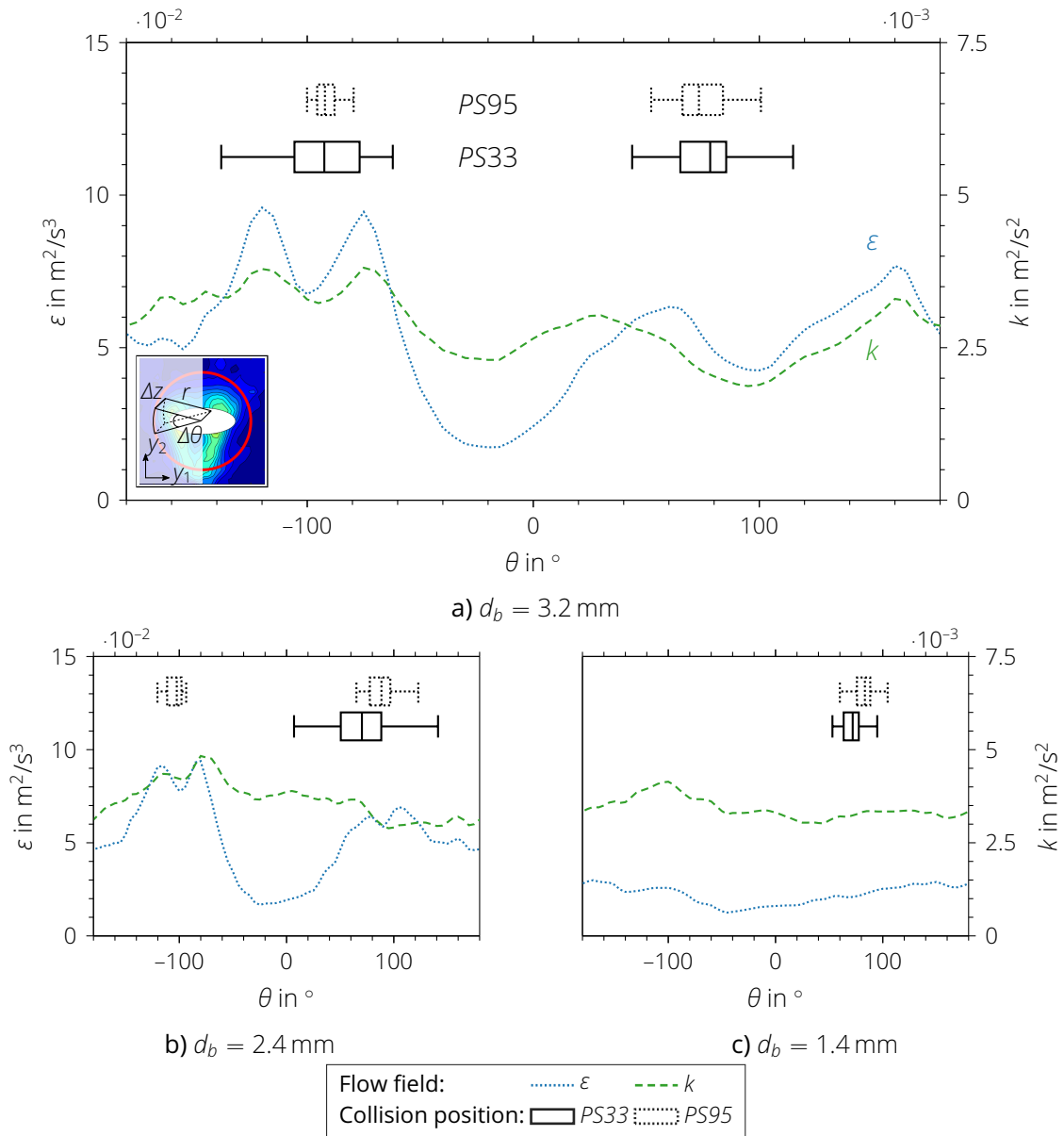


**Figure 5.5.** Bubble column: Combination of the flow field and the collision position. Course of the dissipation rate,  $\varepsilon$ , and TKE,  $k$ , on the bubble interface along the polar angle,  $\theta$ . The turbulent parameters are averaged over a cylinder segment, as marked in the inset of a), with a radius of  $r = 2 \cdot r_b$ , polar angle angle step width of  $\Delta\theta = 5^\circ$  and a thickness of  $\Delta y_{1,3} = 0.3 \text{ mm}$ . The collision positions are shown in the form of a box plot individually for each particle diameter,  $d_p$ . The outliers of the box plots are hidden to increase the visibility, please refer to Fig. 5.4 for the complete box plot.

as marked with a circle in the inset of Fig. 5.5a, by a radius equaling  $2 \cdot r_b$ , a polar angle with a step width of  $\Delta\theta = 5^\circ$  and a thickness of  $\Delta y_{1,3} = 0.3 \text{ mm}$ . Additionally, the collision positions on the leading and trailing edges for both particle diameters are plotted as box plots, similarly to Fig. 5.4. Only the outliers are neglected to increase the visibility.

Starting with the largest bubble diameter (Fig. 5.5a), the highest values of the dissipation rate and TKE are measured at the trailing edge. Two nearly symmetrical maxima for both turbulent parameters are located at approximately  $\theta = -125^\circ$  and  $-75^\circ$ , which clearly corresponds to the double-threaded wake, as discussed in Sec. 4.2.2. On the leading edge, peaks in the dissipation rate are smaller by about 30 % and occur at  $\theta = 50^\circ$  and  $150^\circ$ .

Turning now to the relationship between collision positions and the peak structure of the turbulent parameters, the collision positions for *PS33* are spread over a wide range of polar angles,  $75^\circ < |\theta| < 125^\circ$ , independently of the leading and trailing edges. Their distribution correlates with the maxima of both turbulent parameters. For *PS95*, the collision distribution is tighter, especially at the trailing edge. At the trailing edge, the majority of collisions take place approximately at a polar angle range between  $-75^\circ$  and  $-100^\circ$ .

With a decreasing bubble diameter (Fig. 5.5b), the course of the turbulent parameters remains similar: only the absolute values are slightly lower. Both particle systems collided with the bubble whereas only for *PS95* a trailing edge collision was observed. It seems that the dissipation rate is still sufficient for a trailing edge collision to occur in a small range of polar angles, varying from  $-120^\circ$  to  $-90^\circ$ . Here, they are located nearly symmetrically along the double-threaded wake. For the smallest bubble size (Fig. 5.5c), both turbulent parameters remain nearly constant around the bubble surface. Only a leading edge collision took place for both particle diameters around the stagnation point  $\theta = 90^\circ$  without any correlation with a particular peak structure in the dissipation rate.

Besides the flow field around the bubble, also the Stokes number can give a conclusion on the occurrence of trailing edge collision as it characterizes the behavior of particles suspended in a fluid flow. Previously, the defined Stokes number (Eq. 2.38) referred only to the characteristic fluid time scale based on the averaged rising velocity and diameter of the bubble. However, to also take into account the developed turbulent flow structures, a localized Stokes number is defined, which uses the Kolmogorov time scale,  $\tau_\eta$ , as the characteristic fluid time scale,

$$St_{local} = \frac{\tau_p}{\tau_\eta} = \frac{d_p^2(\rho_s + 0.5\rho_L)}{18\eta} \cdot \left(\frac{\varepsilon}{\nu}\right)^{\frac{1}{2}} \quad (5.79)$$

where  $\varepsilon$  denotes the measured dissipation rate (Fig. 4.4j-l).

The localized Stokes number,  $St_{local}$ , is illustrated in Fig. 5.6. The contour plots reveal possible locations where the particle trajectory could deviate from the fluid streamlines to collide with the bubble. The smallest Stokes numbers,  $St_{local} \ll 0.1$ , are found for the smallest particle diameter (*PS33*) independently of the bubble diameter (Fig. 5.6 a-c). Some variations occurred among the bubble diameters, but these seem insignificant compared to the localized Stokes number computed for *PS95* (Fig. 5.6d-f). Here, the highest values of the localized Stokes number,  $St_{local} \approx 0.3$ , are found in the wake region of the larger bubble diameters ( $d_b > 2$  mm), giving a possible explanation of the trailing edge collisions.

However, the previous results showed that also the smaller particle system underwent a trailing edge collision for the largest bubble diameter ( $d_b = 3.2$  mm). One possible source of error is the measured dissipation rate, as already discussed in Sec. 3.2.4. Fig. 4.5 shows that the power spectrum was only partially resolved during the Tomographic Particle Image Velocimetry (TPIV) measurements. This leads to the assumption that the dissipation rate

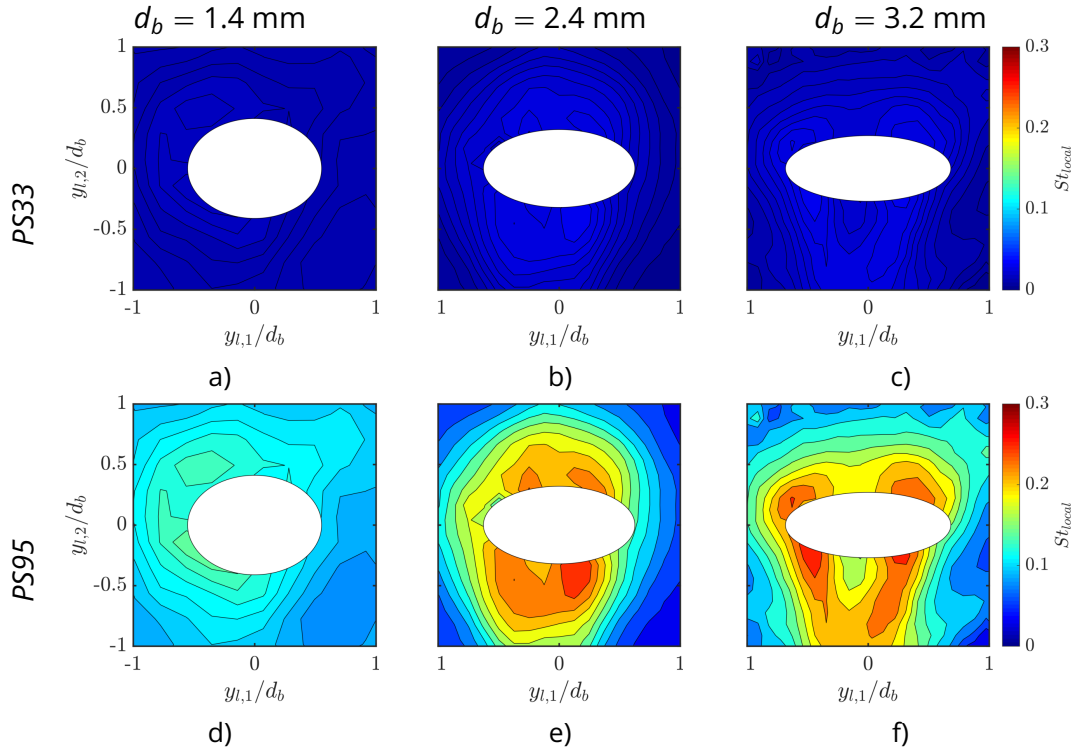


**Figure 5.6.** Bubble column: Localized Stokes number,  $St_l$ , of the model particle systems *PS33* (PS,  $d_p = 33 \mu\text{m}$ ) in the first row and *PS95* (PS,  $d_p = 95 \mu\text{m}$ ) in the second row. These model particle systems are exposed to the fluid flow around a freely rising bubble with a diameter  $d_b$ . The values are conditionally averaged for the tilt angle of the bubble  $\theta = 0^\circ \dots 5^\circ$  along the  $y_{3,l}$ -axis from 0 mm to 0.3 mm.

was under-resolved with the applied measurement setup. If the localized Stokes number was instead calculated with the theoretical Kolmogorov time scale of a freely rising bubble ( $\tau_\eta = d_b \cdot Re_b^{-1/2} \cdot \bar{u}_b^{-1}$  [156]), the localized Stokes numbers would vary between 0.28 and 3.6, exceeding the threshold of 1.0. This offers a prove that the trailing collision may occur due to higher dissipation rates in the bubble wake.

#### 5.1.4. Comparison of the collision frequency with available models

As described in Sec. 2.4.1, quite a considerable number of studies has been published on both inter-particle collisions and on collisions between bubbles and particles. Depending on the assumptions made, they can be applied to different ranges of Stokes numbers. The limiting cases of the Stokes number of monodispersed particle flows are described by Saffman et al. [35] and Abrahamson [36]. While the model developed by Saffman et al. [35] focused on Stokes numbers around zero, Abrahamson's model [36] relates to large Stokes numbers. In both models, the collision between monodispersed particles is not affected by the flow field around each particle. That means the value of the collision efficiency introduced in Sec. 2.4.1 equals unity [36]. However, three-phase flows provide different conditions where these limits are rarely met. There, the motion of the smaller particles is affected by the flow field

around the bubble. Instead of colliding with the bubble surface, the particle may follow the streamlines around the bubble, i.e. the collision efficiency is below unity. Consequently, Kostoglou et al. [37] developed a new collision model to overcome the previous shortcomings and adapted it for the process of froth flotation.

In Fig. 5.7, the collision frequency predicted by Saffman et al. [35], Abrahamson [36] and Kostoglou et al. [37], is plotted over the Stokes number. To feed the model developed by Saffman et al. [35] (Eq. 2.44) and Abrahamson [36] (Eq. 2.45), the experimentally measured dissipation rate,  $\varepsilon$ , and TKE,  $k$ , are used together with the bubble,  $r_b$ , and particle radii,  $r$ . The more complex model designated by Kostoglou et al. [37] depends additionally on the mean rising velocity of the bubble,  $|\mathbf{U}_b|$ , and is used as described in Appendix A.4. The corresponding TKE and dissipation rate equal the average around the freely rising bubbles and are taken from Fig. 5.5. The experimentally determined collision  $Z_{pb}^E$  follows Eq. 3.68, employing the number of collisions,  $N_c$ , in Fig. 5.3.

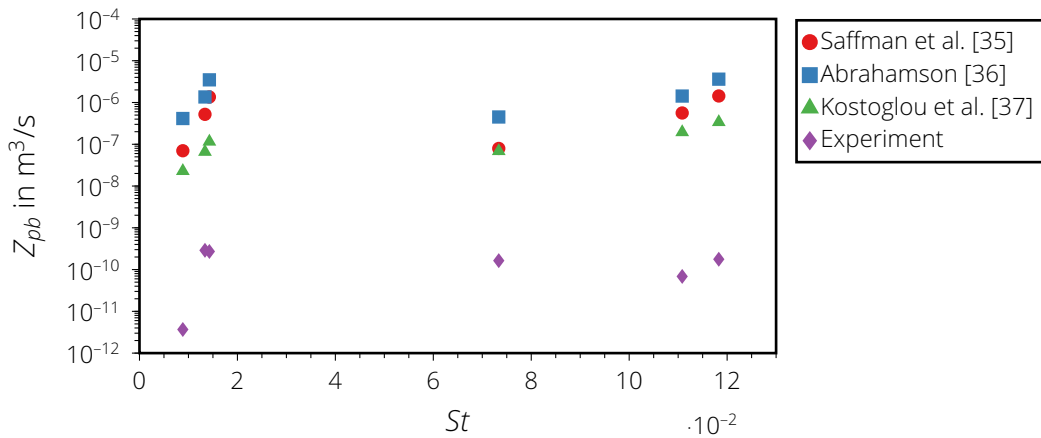


**Figure 5.7.** Bubble column: The collision frequency,  $Z_{pb}$ , depending on the Stokes number,  $St$  (Eq. 2.38).

The Stokes numbers equals the averaged localized Stokes number in the vicinity of each bubble position as shown in Fig. 5.6. Thus, the Stokes number of  $St < 0.02$  corresponds to the particle diameter of  $d_p = 33 \mu\text{m}$  and  $St > 0.06$  to  $d_p = 95 \mu\text{m}$ . In-line with the expectations, the predicted collision frequencies by Kostoglou et al. [37] are smaller than those predicted by the models proposed by Saffman et al. [35] and Abrahamson [36]. The experimentally detected collision frequencies are considerably smaller than those predicted by the three models.

There are several explanations for this outcome. The analytic theories put forward by Saffman et al. [35] and Abrahamson [36] arose from investigations into coagulation of drops in atmospheric turbulence and heavy particles in a highly turbulent gaseous flow, respectively. Both theories assumed that the density of the drop or the particle exceeds that of the carrier fluid by far, and that the particle sizes should be in a similar size range, while the flow conditions are isotropic [27]. These assumptions make it challenging to transfer their models directly to the interaction between bubbles and particles.

Both models neglect the added mass effect experienced by particles and bubbles moving through a liquid phase as water. Thus, their motion is not affected by the neighboring collid-

ing partner. This could be overcome by applying collision efficiency to the models proposed by Saffman et al. [35] and Abrahamson [36]. However, as noted by Nguyen et al. [49], a huge variation in the nominal collision frequencies exists, leading to a lack of comparability. Instead, Kostoglou et al. [37] consider these effects in their model by explicitly taking the flow around the bubble into account.

Still, the experimentally detected collision frequencies are two orders of magnitude smaller than those predicted by the developed model by Kostoglou et al. [37]. One possible source of uncertainty could be the state of the bubble surface mobility. Although the model by Kostoglou et al. [37] refers to the limited cases of either a mobile or immobile bubble surface, many intermediate stages of partial mobility exist [109]. The effect of the bubble surface mobility on the collision frequency was previously investigated by Dai et al. [205] and Schulze [103]. Both research groups emphasized that the collision frequency on an immobile bubble surface is approximately ten times lower than on a mobile bubble surface. Additionally, the existing flotation models mainly assume isotropic turbulence to describe the stochastic motions between bubble and particle. Discrepancies could occur due to non-isotropic turbulence in the bubble wake.

Another possible source of uncertainty could be missing collision trajectories, as discussed in the following section. These missing collision trajectories would lead to an underestimation of the number of colliding particles, and thus of the collision frequency.

### 5.1.5. Limitations on the detection of the bubble-particle collision

Theoretically, a bubble-particle encounter can be classified as a collision by measuring the exact distance between the particle and the bubble surface. Accordingly, an exact reconstruction of the bubble surface and the position of the particle at a high spatial resolution is indispensable. This criterion could not be deployed for the collision classification because of the limited spatial resolution in the upper micrometer scale of the applied experimental arrangement of 4D PTV. Instead, the particle's movement towards the bubble in the form of the radial velocity and the extended residence time (Eq. 3.75) in the vicinity of the bubble were applied as classification criteria.

Still, the chosen method has its limitations and could not detect all colliding events during the data analysis. These occurred either during the reconstruction of the bubble surface, the particle triangulation with the Shake-the-box (STB) algorithm or during the collision classification.

The bubble surface was reconstructed based on the assumption of an oblate ellipsoid. The major axis,  $a$ , and minor axis,  $c$ , of the ellipsoid were retrieved from the planar projection observed by camera  $B$  (Fig. 3.4). This method was subjected to errors. On the one hand, only the tilt angle along the  $x_3$ -axis was known. The other two tilt angles along the  $x_1$  and the  $x_2$ -axis could not be retrieved from the planar projection. On the other hand, the unknown tilt angles along the  $x_1$ - and the  $x_2$ -axis could lead to uncertainties on the major axis and minor axis of the reconstructed bubble surface. For example as seen in Fig. 3.6a, the measured minor axis in the image plane,  $c$ , was larger than the actual minor axis of the bubble,  $c^*$ . Consequently, the reconstructed bubble surface would be larger than the actual bubble surface.

In general, the STB algorithm predicts the particle position in the subsequent time step based on the previously known particle locations. However, the collision event was an exceptional case because most of the particles follow the fluid streamlines around the bubble. The triangulated colliding particles could not match the other circulating particle trajectories. The algorithm may have detected some of these colliding particles as outliers and removed them from the triangulated particle ensemble. Consequently, the outlier particle trajectories were not available for the collision classification.

These missing collision trajectories would lead to an underestimation of the number of colliding particles, and thus of the collision frequency. However, the key observation of the existence of collision events is not falsified by the neglect of certain collision events.

## 5.2. Stagnant bubbles in the water channel measured with 4D PTV

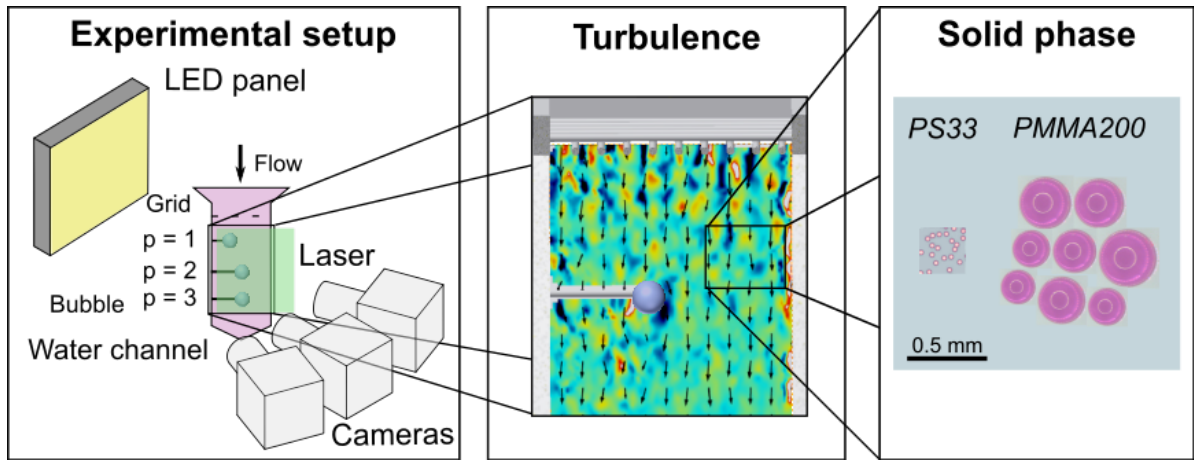


Figure 5.8. Water channel: Graphical abstract of the experimental arrangement for the measurements in the water channel with 4D PTV. The particle model system *PS33* and *PMMA200* consisted of fluorescent PS particles with a diameter of  $33\ \mu\text{m}$  and fluorescent polymethylmethacrylate (PMMA) particles with a diameter of  $200\ \mu\text{m}$ ...  $400\ \mu\text{m}$ , respectively. Please refer to Sec. 3.1.2 for more details of the experimental setup and Tab. 3.5 for the properties of the model particle systems.

While Sec. 5.1 focused on a freely rising bubble chain, this section considers stagnant bubbles in the turbulent flow of the water channel (Fig. 5.8). The experiments comprised three different bubble positions ( $p = 1 - 3$ ; Fig. 3.1b). To minimize the effect of the upper bubble on the lower one, only two bubbles with a horizontal spacing of  $10\ \text{mm}$  were employed during the measurements. The first configuration consisted of the upper bubble position,  $p = 1$ , and the middle one,  $p = 2$ , whereas the second configuration included the upper one,  $p = 1$ , and the lower one,  $p = 3$ . As shown in Sec. 4.3.1, these positions went along with varying turbulent length scales upstream of each stagnant bubble. The highest degree of turbulence was measured at the bubble position  $p = 1$ , and decreased from  $p = 2$  to  $p = 3$  (Fig. 4.7c). A dilute solid suspension was added to the water channel, containing either the particle model system *PS33* or *PMMA200* (Tab. 3.5). In the following, the observed interactions between a stagnant bubble and particles are summarized applying 4D PTV.

### 5.2.1. Bubble-particle collision

At first, the focus is on the preferred collision position of the particles on the bubble surface. Fig. 5.9 illustrates the normalized distribution of collision events according to the bubble's polar angle,  $\theta$ , as defined in the inset of Fig. 5.9c. For each measurement configuration, the uniform bin width of the distribution is set to  $20^\circ$  to reveal its underlying shape. The number of collisions of each bin,  $N_{c,i}$ , are normalized by the overall number of collision events of the specific configuration,  $N_c$ . These configurations consisted of three bubble positions,  $p$ ,

denoted by each column, and two model particle system (*PS33* or *PMMA200*), represented by each row.

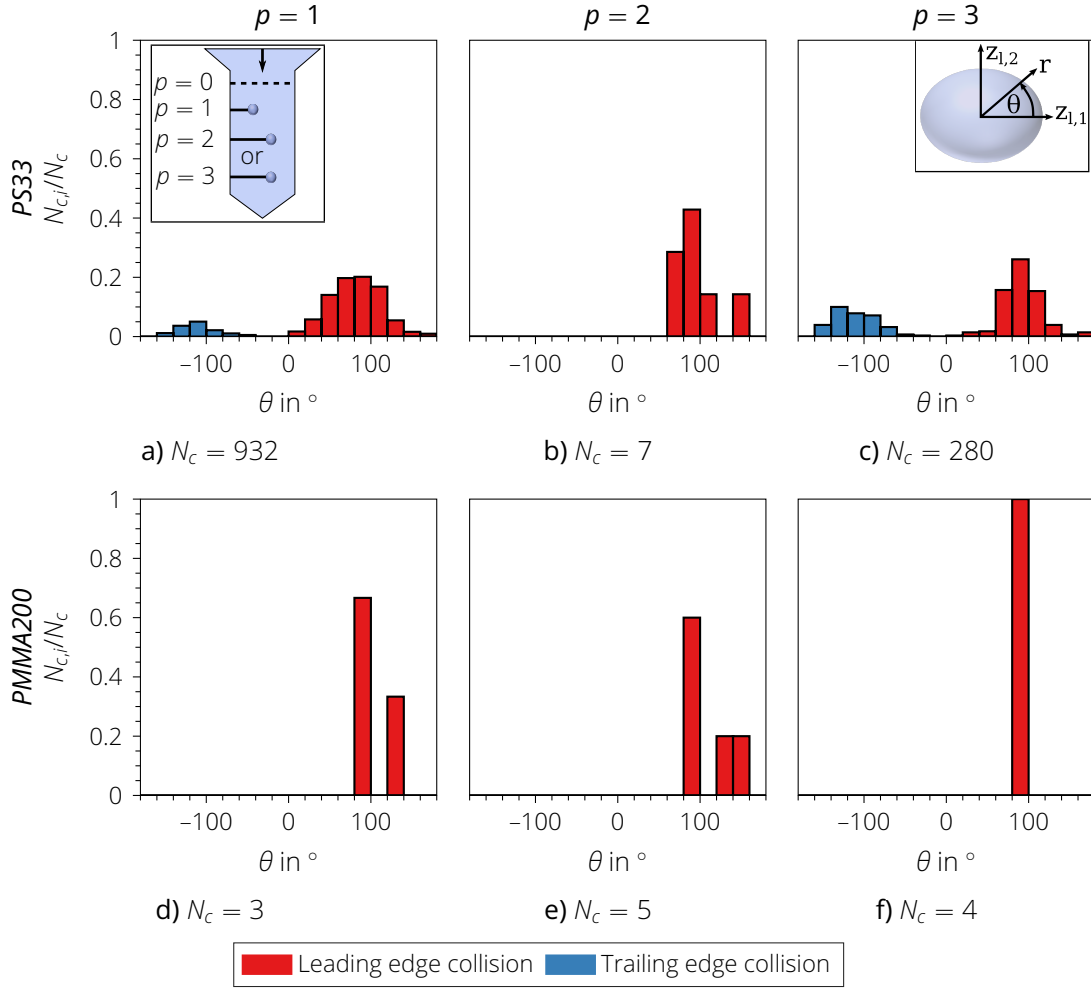


**Figure 5.9.** Water channel: Distribution of the collision positions along the polar angle of the bubble,  $\theta$ , as defined in the inset of c). Each row represents one model particle system, *PS33* and *PMMA200* (Tab. 3.5), whereas each column stands for one of the three bubble positions,  $\rho$ , as shown in the inset of a). The collision position is where for the first time the particle trajectory reaches a minimum distance of  $r \approx 0.8 r_b$  and minimum radial velocity of  $w_r \approx 0$  m/s. The uniform bin width of the distribution is set to  $20^\circ$ . For each bin, the number of collisions,  $N_{c,i}$ , is normalized by the overall number of collision events of the specific bubble position,  $\rho$ , and model particle system.

As expected, the measurement configurations containing the smallest particle system, *PS33*, demonstrate a leading and trailing edge collision. The leading edge collision angle varies from  $0^\circ$  to  $180^\circ$ . The peak in the number of collisions mainly occurs at the bin from  $80^\circ$  to  $100^\circ$ , including the stagnation point of the bubble at  $90^\circ$ . Similarly, the trailing edge collisions are distributed between  $-180^\circ$  and  $0^\circ$ . It seems that the fraction of trailing edge collisions slightly increases from the bubble position  $\rho = 1$  to  $\rho = 3$  (Fig. 5.9a and c).



Contrary to expectations, no trailing edge collisions are observed for the bubble position  $p = 2$  (Fig. 5.9b). One reason might be the low number of the detected collisions overall,  $N_c = 7$ . This value is two orders of magnitude smaller than the detected collisions at the bubble positions  $p = 1$  and  $p = 3$  with  $N_c = 932$  and  $280$ , respectively. It is likely that a precision of calibration below a value of  $0.1$  px was not reached at  $p = 2$ , leading to a lower number of detected particle trajectories and, thus, colliding particle trajectories. Please refer to the discussion in Sec. 5.2.4 for further details.

For the larger particle system, *PMMA200*, the results are in agreement with the expectation, meaning only leading edge collisions are detected. As summarized in Tab. 3.5, the Stokes number of *PMMA200* is in the order of 1, using the characteristic fluid time scale of the large turbulent length scales. Thus, this model particle system is only slightly affected by the larger turbulent length scales of the liquid flow field (Fig. 2.11). They cannot respond to the fast changes of the small turbulent length scales in the bubble wake. Consequently, a trailing edge collision is unlikely for the model particle system *PMMA200*.

To quantify the statistical relevance of the collision points in Fig. 5.9, Fig. 5.10 summarizes the collision position in the form of a box plot for different time segments. A box plot is generally understood as an illustration of the distribution of a given sample through their percentiles, named median, 25th percentile, 75th percentile, upper and lower whisker (as shown in the legend below Fig. 5.10). More details on the computation of these percentiles are given in the Appendix A.5. In context of the statistical relevance, the aim was that the distribution of the collision events according to the bubble's polar angle,  $\theta$ , remained comparable independent of the chosen sample. Therefore, three samples are selected for each configuration based on different time intervals. The first half of the measurement time, denoted by index 1, the second half of the measurement time, denoted by index 2, and the entire measurement time, denoted by index *A*, were applied as the underlying population.

The box plots in Fig. 5.10a and c have the largest underlying population during the entire measurement time, more precisely 932 and 280 collision events, respectively. Comparing the box plots of the first half of the measurement time,  $L_1$ , and the second half,  $L_2$ , to the overall measurement time,  $L_A$ , the median and the spread of the 25th to 75th percentiles of the collision angle vary only by approximately  $10^\circ$ . Thus, the collision positions could be allocated to the same histogram bin with a width of  $20^\circ$ , as shown in Fig. 5.9a and c.

With a decreasing number of collision events as, for example, in Fig. 5.10b with  $N_c = 7$ , the agreement of the median collision position and the spread of the data between the 25th and 75th percentiles remain in the same order of magnitude as in Fig. 5.10a and c.

To sum up, a reasonable agreement of the collision angle was achieved for all bubble and particle configurations in these three time segments. This confirms the statistical relevance of the detected collision positions, even for a modest underlying data population as, for example, in Fig. 5.10e with  $N_c = 3$ .

### 5.2.2. Interaction of the turbulent flow field on the collision phenomena

Important parameters influencing the particle trajectory are the turbulent length scales upstream of the stagnant bubble and the resulting fluid flow field around the stagnant bubble. Thus, Fig. 5.11 indicates the impact of the turbulent parameter on the bubble-particle inter-

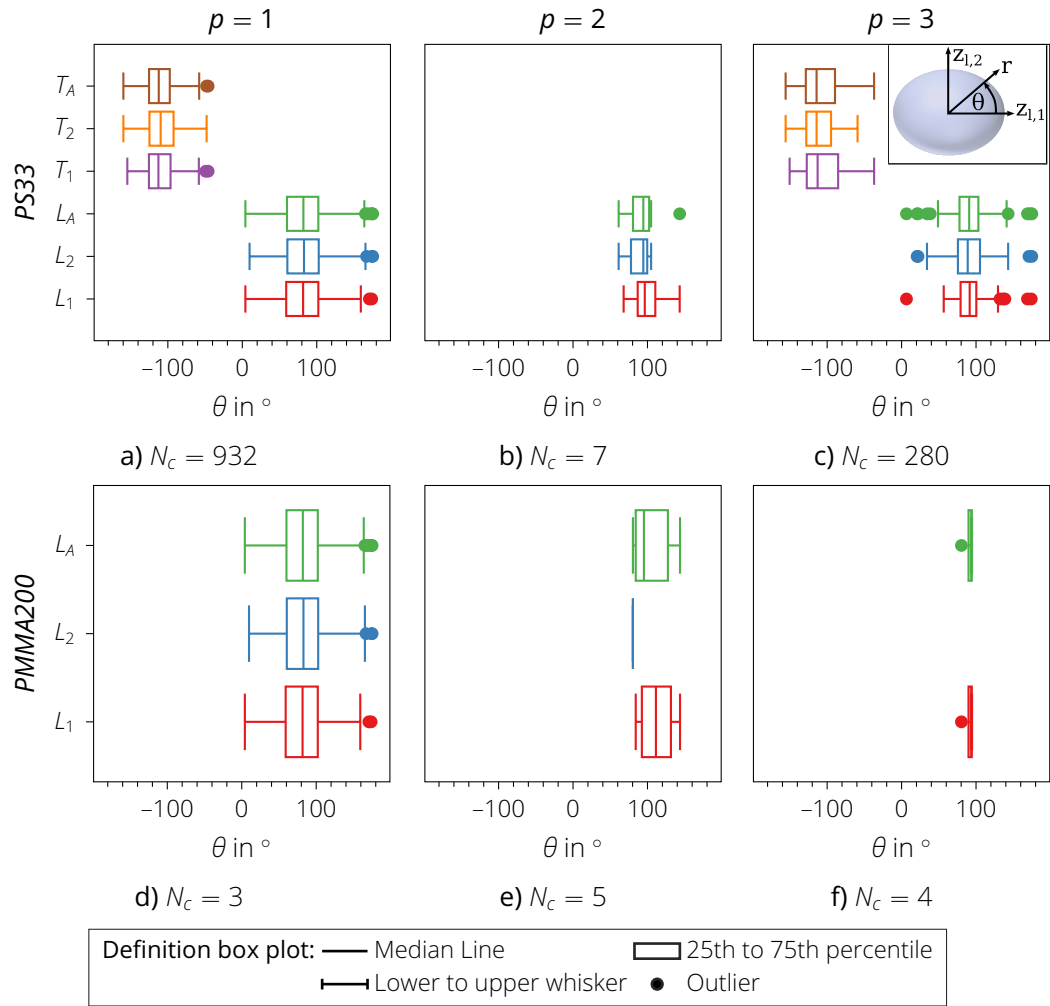


**Figure 5.10.** Water channel: Box plots to quantify the statistical relevance of the collision positions in Fig. 5.9 along the polar angle,  $\theta$ , as defined in the inset of c). Three sets of data are selected from the leading,  $L$ , and trailing,  $T$ , edge collision based on different time intervals. The underlying population of each sample is denoted by the indexes 1, 2 and  $A$  of  $L$  or  $T$  (y-axis). These samples are defined as the first half of the measurement time, represented by index 1, the second half of the measurement time, represented by index 2, or the complete measurement time, represented by index  $A$ . The variable,  $N_c$ , summarizes the underlying population of particle collision trajectories for the entire measurement time at the leading and trailing edges of the bubble. A detailed explanation of the calculation of the box plot values are summarized in Sec. A.5.

action along the bubble's polar angle,  $\theta$  (Fig. 3.10a). In particular, the dissipation rate and TKE (Fig. 4.11) are plotted together with the collision between particles and the bubble surface (Fig. 5.9), similar to Fig. 5.5.

To determine the magnitude of these turbulent parameters along the bubble surface, the data shown in Fig. 4.11 are averaged over cylindrical sectors. The definition of each cylindrical sector in the case of the stagnant bubbles matches the one for the freely rising bubble.

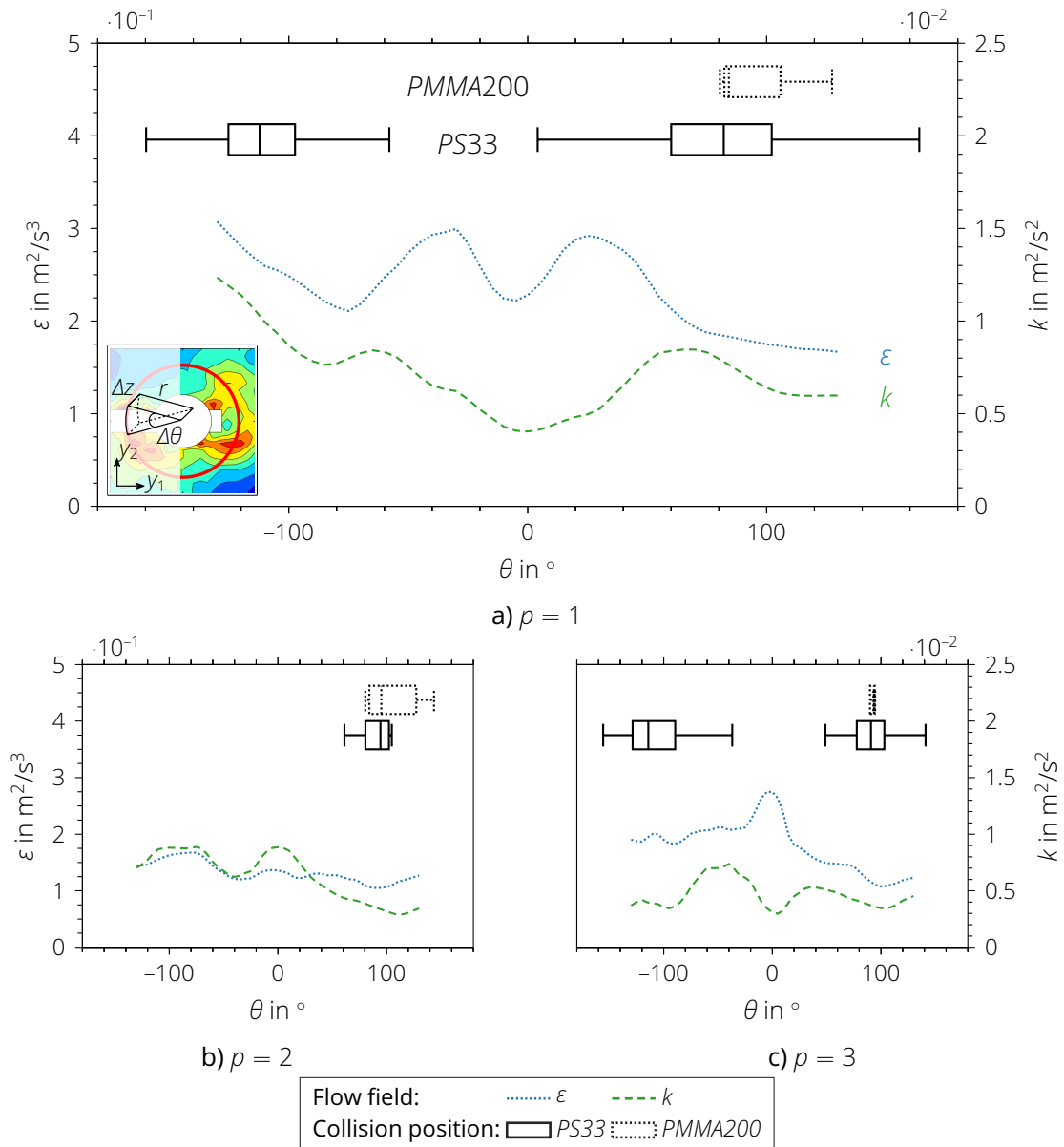


**Figure 5.11.** Water channel: Combination of the flow field and the collision position. Course of the dissipation rate,  $\varepsilon$ , and TKE,  $k$ , on the bubble interface along the polar angle,  $\theta$ . The turbulent parameters are averaged over a cylinder segment as marked in the inset of a) with a radius of  $r = 2 \cdot r_b$ , a polar angle step width of  $\Delta\theta = 5^\circ$  and a thickness of  $\Delta y_{1,3} = 0.3$  mm. The collision positions are shown in the form of a box plot individually for each particle diameter,  $d_p$ . The outliers of the box plots are hidden to increase the visibility, please refer to Fig. 5.10 for the complete box plot.

Therefore, each cylindrical sector is defined in the inset of Fig. 5.11a by a radius equaling  $2 \cdot r_b$ , a polar angle with a step width of  $\Delta\theta = 5^\circ$  and a thickness of  $\Delta y_{1,3} = 0.3$  mm. The polar angle range is only defined from  $-130^\circ$  to  $130^\circ$ , due to the masked out area of the needle, where the stagnant bubble is attached to. Positive values of  $\theta$  denote the leading edge of

the bubble, whereas negative ones belong to the trailing edge (Fig. 3.10a). Additionally, the collision positions on the leading and trailing edges for both particle diameters are plotted as box plots, similarly to Fig. 5.10. Only the outliers are neglected to increase the visibility.

The highest values of the dissipation rate are measured in the vicinity of the stagnant bubble at the position  $p = 1$  (Fig. 5.11a). This position corresponds to the highest degree of turbulence upstream of the bubble (Fig. 4.7c). The values remain in the same order of magnitude on the leading edge of the bubble, but they rise steadily on the trailing edge of the bubble. This can be contributed to the turbulent wake of the bubble and needle, as shown in Fig. 4.11. Additionally, two maxima evolve along the bubble surface at approximately  $-40^\circ$  and  $40^\circ$ . These maxima correspond to the location of the tip of the needle. Thus, the tip of the needle could be a possible distortion of the liquid flow around the bubble, too.

With an increasing distance of the bubble position to the grid from  $p = 2$  to  $p = 3$ , the degree of turbulence upstream of the stagnant bubble decreases. This corresponds in Fig. 5.11b and c to a slight reduction of the dissipation rate on the leading edge of the bubble. On the trailing edge of the bubble, these values rise moderately again from  $p = 2$  to  $p = 3$ . Regarding to the TKE, the course of the TKE remains in the same order of magnitude independently of the bubble position. Generally, a slight increase of the TKE is noticeable from the leading to the trailing edge of the bubble.

In the next step, the focus is on the relationship between the collision positions and the structure of TKE and dissipation rate. Starting at the bubble position  $p = 1$  (Fig. 5.11a) for the model particle system *PS33*, the collision positions are spread over nearly the complete range of polar angles, independently of the leading and trailing edges. This extraordinarily wide range of collisions positions could be contributed to the large range of turbulent length scales (Fig. 4.12a), allowing the fine particles to pass closely by the bubble and collide with its interface (as illustrated in Fig. 5.12b). The trailing edge collision could be attributed to the enhanced values of the turbulent parameters due to the wake of the bubble and needle.

Turning now to the position  $p = 2$ , where the findings are based on a limited number of collision events. Consequently, the results of the analysis should therefore be treated with considerable caution. At  $p = 2$  for *PS33* (Fig. 5.11b), the majority of the collision positions concentrate around the stagnation point of the bubble, from  $80^\circ$  to  $120^\circ$ . Despite the fact that the turbulent parameters are in the same order of magnitude on the trailing edge of the bubble at  $p = 1$  and  $p = 3$ . Theoretically, sufficient TKE and dissipation rate would be available to influence the motion of the model particle system, *PS33*, allowing a trailing edge collision to occur. There are several sources for possible limitations which are discussed in detail in Sec. 5.2.4.

At the lowest degree of turbulence ( $p = 3$ ; Fig. 5.11c), the turbulent parameters remain in the same order of magnitude. The distribution of the collision positions persists in the case of *PS33* for a wide range of polar angles on the leading and trailing edge of the bubble. Thus, no significant difference is observed between  $p = 1$  and  $p = 3$ .

In contrast, the large model particles, *PMMA200*, collide only around the stagnation point at the surface, precisely from  $80^\circ$  to  $120^\circ$ . These results are independent of the turbulent length scales upstream of each stagnant bubble. Consequently, even the magnitude of turbulent parameters associated to the highest degree of turbulence was still too low to influence the motion of the larger model particles of *PMMA200* on the trailing edge of the bubble, as shown

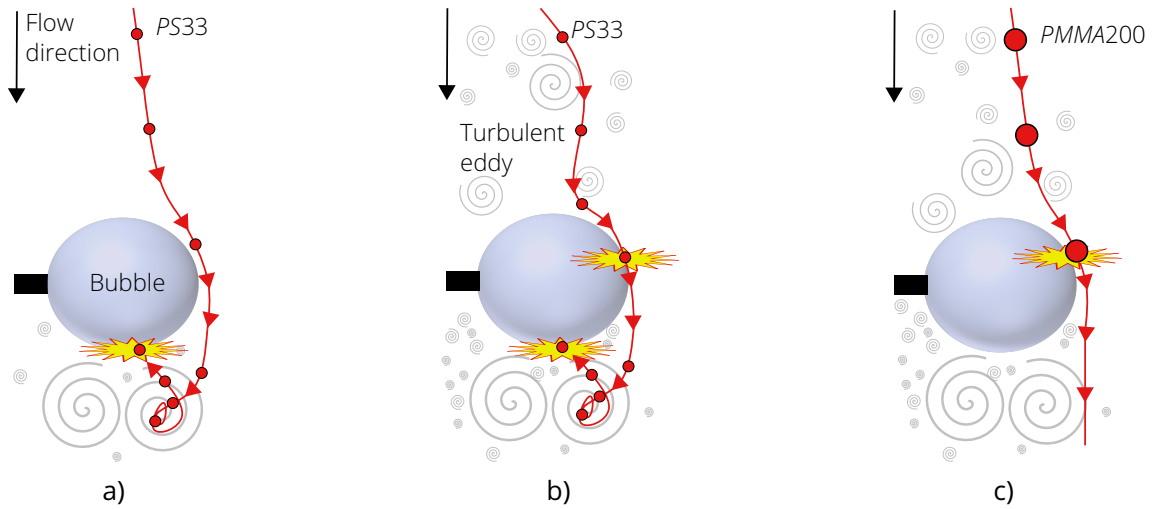


**Figure 5.12.** Sketch of the collision mechanism between a stagnant bubble and various model particle systems. a) No turbulent flow upstream of the bubble, the fine particle system, *PS33*, follows the fluid streamlines around the bubble and may collide with the trailing edge. b) Turbulent flow upstream of the bubble, the fine particle system, *PS33*, gets trapped in the turbulent eddies and collides in various positions on the bubble surface. c) Turbulent flow upstream of the bubble, the coarse particle system, *PMMA200*, is not affected by the turbulent eddies and collides only at the leading edge of the bubble.

in Fig. 5.12c.

Besides the flow field around the bubble, also the Stokes number can give a conclusion on the occurrence of trailing edge collision as it characterizes the behavior of particles suspended in a fluid flow. Therefore, also the localized Stokes number,  $St_{local}$  (Eq. 5.79) is analyzed accordingly for the stagnant bubbles in the water channel, as seen in Sec. 5.1.3. The localized Stokes number,  $St_{local}$  (Eq. 5.79), is illustrated in Fig. 5.13 and calculated using the measured dissipation rate as shown in Fig. 4.11j-l. Analogue to Fig. 5.6, the contour plots reveal possible locations where the particle trajectory could either deviate from the fluid streamlines colliding with the bubble or follow the liquid flow for a collision with the bubble.

The smallest Stokes numbers,  $St_{local} \ll 0.1$ , are found for the smallest particle diameter independently of the bubble position (Fig. 5.13 a-c). Significantly higher values of the localized Stokes number are computed for the larger particle system, *PMMA200* (Fig. 5.13d-f). Here, the highest values of the localized Stokes number,  $St_{local} > 2$ , are found close to the stagnant bubble for each position, independent from its leading or trailing edge.

As already discussed in Sec. 5.1.3, the current measurement configuration of TPIV lacks in resolving the complete power spectrum. Thus, the shown localized Stokes numbers in Eq. 5.79 are presumably underestimated. To verify this statement, an approximation of the Kolmogorov time scale,  $\tau_\eta$ , in the fluid flow around the stagnant bubble would be helpful. This approximation is challenging, because  $\tau_\eta$  is not only influenced by the turbulent length scales, but also due to the presence of the needle.

A rough estimation of  $\tau_\eta$  could be achieved, using the theoretical Kolmogorov time scale of a freely rising bubble ( $\tau_\eta = d_b \cdot Re_b^{-1/2} \cdot \bar{u}_b^{-1}$  [156]), assuming that the rising velocity of the

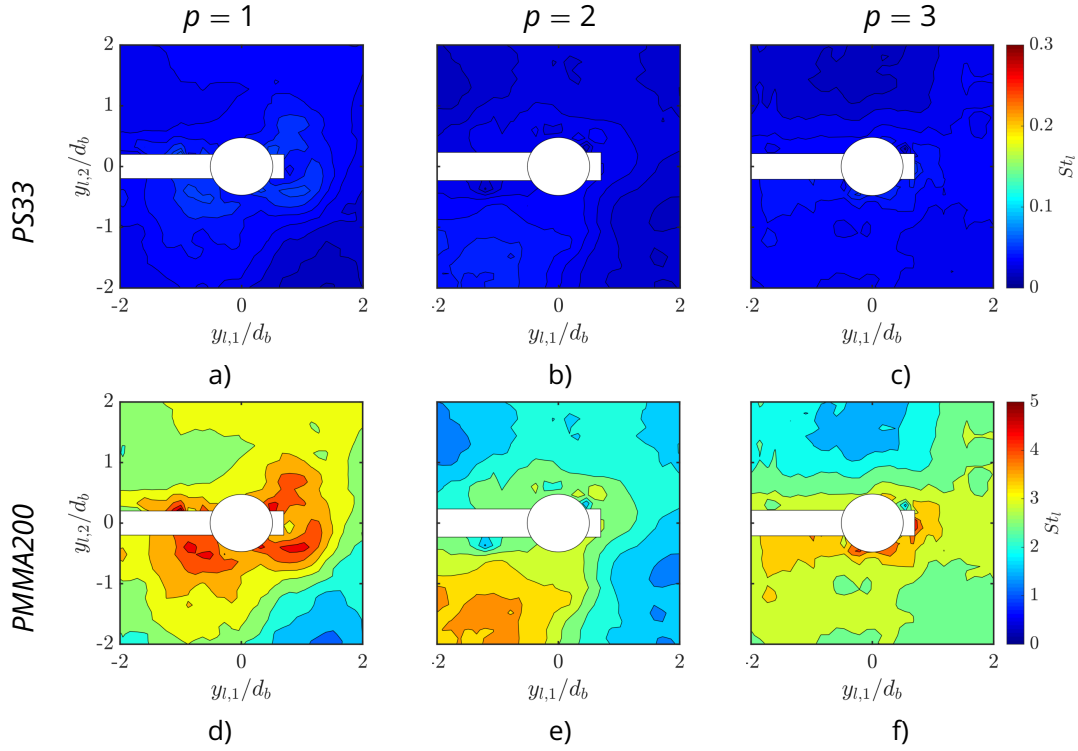


Figure 5.13. Water channel: Localized Stokes number,  $St_{local}$ , of the model particle systems *PS33* (PS,  $d_p = 33 \mu\text{m}$ ) in the first row and *PMMA200* (PMMA,  $d_p = 200 \mu\text{m} \dots 400 \mu\text{m}$ ) in the second row. These model particle systems are exposed to the fluid flow around a stagnant bubble in the water channel with various turbulent length scales upstream of each bubble position,  $p$  (Fig. 3.1b). The values are averaged along the  $y_{i,3}$ -axis from 0 mm to 0.3 mm.

bubble equals the averaged liquid velocity in the water channel. Applying this approximation, the theoretical Kolmogorov time scale is in the order of 0.6 ms. The associated localized Stokes numbers would be approximately 0.4 for *PS33* and 12 for *PMMA200*.

Consequently, in the case of *PS33*, the trailing edge collision may occur due to higher dissipation rates in the bubble wake. In the case of *PMMA200*, the localized Stokes number exceeds one by far. Thus, it is unlikely that these particles would deviate from the fluid streamline due to the turbulent length scales in the water channel.

### 5.2.3. Comparison of the collision frequency with available models

The measurement of the collision positions cannot only reveal the collision position of the particle on the bubble surface, it also allows to compute the collision frequency,  $Z_{pb}$  - an important parameter to predict the recovery of a flotation cell. Similar to Sec. 5.1.4, Fig. 5.14 compares the experimentally determined collision frequency with those predicted by Saffman et al. [35], Abrahamson [36] and Kostoglou et al. [37] for a range of Stokes numbers (Eq. 2.38). Here, the Stokes number equals the averaged localized Stokes number in the vicinity of each bubble position as shown in Fig. 5.13.

The models developed by Saffman et al. [35] (Eq. 2.44) and Abrahamson [36] (Eq. 2.45) are fed by the experimentally measured dissipation rate,  $\varepsilon$ , and TKE,  $k$ , and used together with the bubble,  $r_b$ , and particle radii,  $r$ . The more complex model developed by Kostoglou et al. [37] additionally depends on the mean rising velocity of the bubble,  $|\mathbf{U}_b|$ , and is used as described in Appendix A.4 for an immobile bubble. The corresponding TKE and dissipation rate equal the average around the stagnant bubble and are taken from Fig. 5.11. The experimentally determined collision frequency  $Z_{pb}^E$  follows Eq. 3.68, employing the number of collisions,  $N_C$ , from Fig. 5.9.

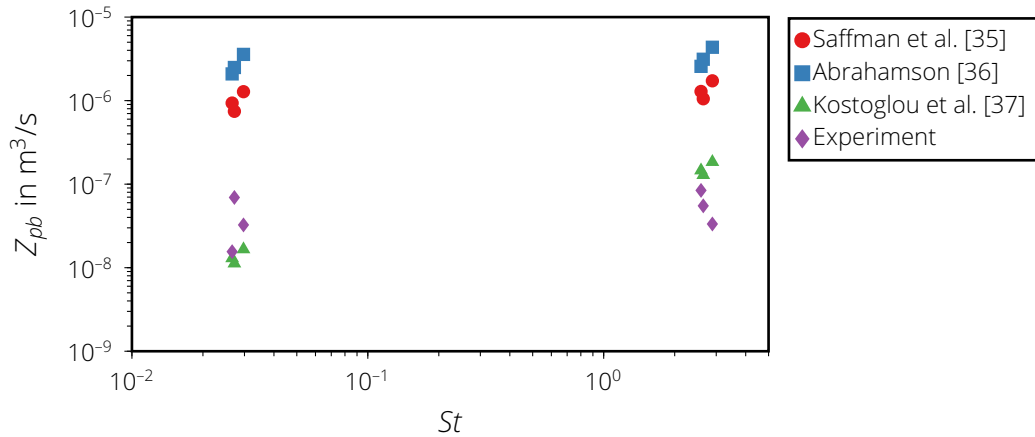


**Figure 5.14.** Water channel: The collision frequency,  $Z_{pb}$ , depending on the Stokes number,  $St$  (Eq. 2.38).

The calculated Stokes numbers depend on the particle diameter, where  $St < 0.01$  corresponds to *PS33* and  $St > 1$  to *PMMA200*. Similar to Fig. 5.7, the predicted collision frequencies by Kostoglou et al. [37] are smaller than those predicted by the models proposed by Saffman et al. [35] and Abrahamson [36]. Possible explanations for these deviations are already discussed in Sec. 5.1.4.

As expected, the experimentally detected collision frequencies are in the same order of magnitude as the prediction by the model proposed by Kostoglou et al. [37]. The assumptions made by Kostoglou et al. [37] fit well with the experimental setup: isotropic turbulence and state of the bubble surface mobility. Firstly, the turbulent flow is nearly isotropic at the stagnant bubble position  $p = 2$  and  $p = 3$ , as discussed in Sec. 4.3.1. Secondly, the state of the bubble surface mobility can be approximated as immobile due to the hydrophobization of the needle (Sec. 4.4).

However, these results should be interpreted with caution. The collision model proposed by Kostoglou et al. [37] was developed for the process of froth flotation, meaning the gas phase consisted of countless bubbles rising in a swarm. Their hydrodynamics and surface interaction differed from a stagnant bubble [49] as applied in the water channel. For example, the wake of the bubble was superimposed by the wake of the needle. Thus, the values of TKE and dissipation rate could enhance the trailing edge collision, compared to a freely rising bubble.

#### 5.2.4. Limitations on the detection of the bubble-particle collision

As discussed in Sec. 5.1.5, the application of 4D PTV had its limitations and could not detect all particle collision trajectories during the data analysis. Besides the addressed limitations in the context of the freely rising bubble, additionally the particle reconstruction with the iterative particle reconstruction (IPR) algorithm was challenging.

A basic requirement for the IPR algorithm to reconstruct the particle position in 3D is a calibration with a precision below a value of 0.1 px [171]. Therefore, a combination of multiple techniques was applied during the measurement and subsequent data analysis (Sec. 3.3.1): a multiplane calibration target (Appendix A.3), volumetric self-calibration (VSC) [149] and optical transfer function (OTF) [172]. These techniques required among others a calibration target covering the majority of the field of view (FOV) and a particle image diameter between 2 px and 6 px [171, 206]. Otherwise, the triangulation would get increasingly difficult, leading to a growing number of ghost particles due to the underdetermined nature of triangulation [206].

These requirements were easily achieved during the experiments in the bubble column (Tab. 3.4). However, it was challenging to meet all of these requirements during the experiments in the water channel. On the one hand, a smaller sized calibration target was used to fit into the water channel. The mounting of the calibration plate was limited to the positions  $p = 1$  and  $p = 3$ . Thus,  $p = 2$  was only partially covered by the calibration target as shown in Fig. A.2. This could be one reason, why the number of collision events at  $p = 2$  was remarkably smaller than at  $p = 1$  and  $p = 3$  (Fig. 5.9).

On the other hand, the particle image diameter of the particle system of *PMMA200* ranged between 5 px and 10 px (Tab. 3.4), exceeding the recommendations of 2 px...6 px [171, 206]. Consequently, the number of detected collisions for the model particle system *PS33* was significantly higher than for *PMMA200* (Fig. 5.9).

Additionally, the calibration precision was affected by vibrations of the peristaltic pump which continuously circulated the flow through the water channel. Although special care was taken during the experiments, it was difficult to damp these vibrations. Recently, Jahn et al. [206] proposed an advanced iterative particle reconstruction for 4D PTV, which can correct these instantaneous vibrations in the form of an in-situ single-image VSC.

Despite these limitations, the 4D PTV method and the classification of the collision trajectory were applied successfully to the turbulent flow in the water channel. This methodology allowed not only to investigate the influence of the turbulent length scales on the leading edge collision, but also on the trailing edge collision.



### 5.3. Stagnant bubbles in the water channel measured with PEPT

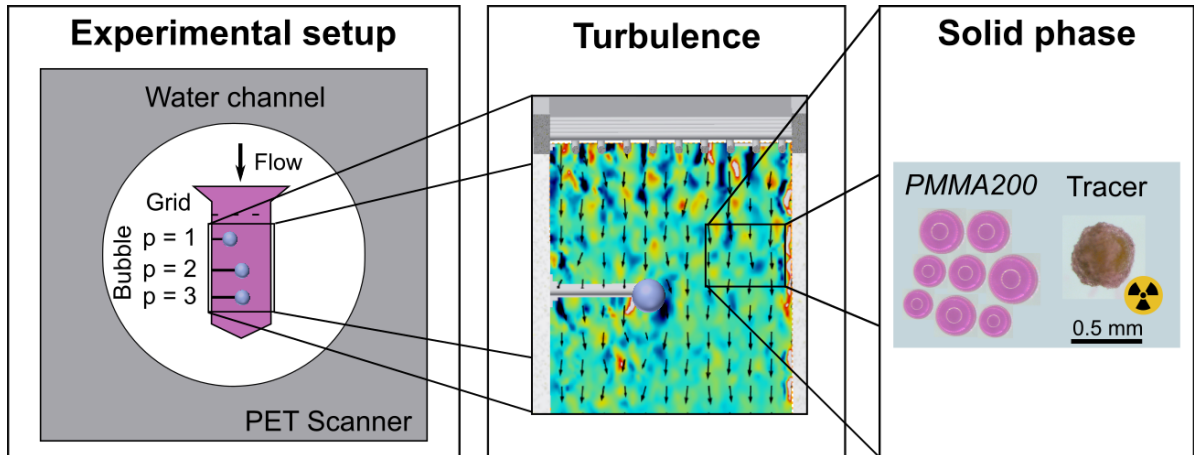


**Figure 5.15.** Water channel: Graphical abstract of the experimental arrangement for the measurements in the water channel with PEPT. The particle model system *PMMA200* consisted of fluorescent PMMA particles with a diameter of 200  $\mu\text{m}$ ... 400  $\mu\text{m}$ , including up to six radioactive tracer particles. Please refer to Sec. 3.1.2 for more details of the experimental setup, Tab. 3.5 for the properties of the model particle system and Tab. 3.6 for the properties of the radioactive tracer particles.

Until now, the particle suspension had to be diluted to be applicable to the optical 4D PTV. However, in this section, PEPT was employed to investigate the bubble-particle interaction in a dense turbulent flow. Emphasizing that PEPT represented a valuable alternative particle tracking method because of its applicability to optically opaque fluids. Similar to Sec. 5.2, the experimental setup consisted of a stagnant bubble in the turbulent flow of the water channel (Fig. 5.15). The experiments comprised three different bubble positions ( $p = 1 - 3$ ; Fig. 3.1b). As shown in Sec. 4.3.1, these positions went along with varying turbulent length scales upstream of each stagnant bubble. The highest turbulence degree was measured at the bubble position  $p = 1$ , and decreased from  $p = 2$  to  $p = 3$ . The solid suspension consisted of the particle model system *PMMA200* (Tab. 3.5), including up to six radioactive tracer particles which represented the bulk particles (Tab. 3.6). Two cases of particle concentrations were investigated, either a dilute or a dense suspension, having a particle volume fraction,  $a_p$ , of  $1 \cdot 10^{-4}$  or  $2.2 \cdot 10^{-3}$ , respectively. In the following, the observed interactions between a stagnant bubble and particles are summarized based on the results from the PEPT measurement campaign.

#### 5.3.1. Particle distribution in the channel cross-section

To begin with the distribution of the particles, Fig. 5.16 illustrates the occupancy of the radioactive-labeled tracer particles in the channel cross-section. As noted in Sec. 3.4.2, the tracer particles were designed to represent the bulk PMMA particles, *PMMA200*. Therefore,

the probability of the radioactive-labeled particles in Fig. 5.16 was supposed to indicate the distribution and concentration of *PMMA200* model particle system.

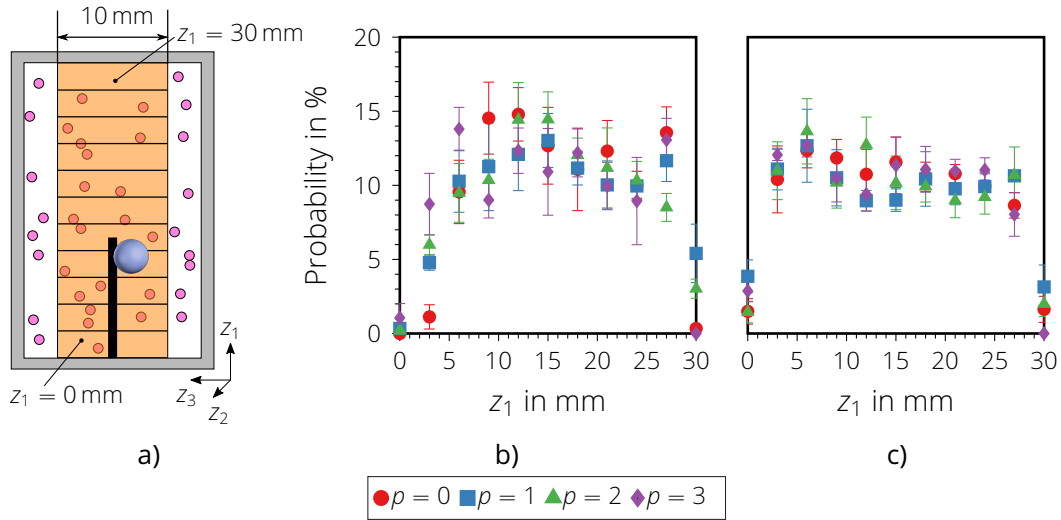


**Figure 5.16.** Water channel: Probability of the radioactive-labeled particle location along the  $z_1$ -direction measured with PEPT. a) Schematic illustration of the binning area of the particle locations in the  $z_1z_3$ -plane. b) Dilute flow with a volume fraction of  $\alpha_p = 1 \cdot 10^{-4}$ . c) Dense flow with volume fraction of  $\alpha_p = 2.2 \cdot 10^{-3}$ . The  $z_2$ -direction corresponds to the location of the grid and the bubble (Fig. 3.1b).

The distribution of tracer particles was measured in the  $z_1z_3$ -plane at four different heights,  $z_2$ . These heights equaled the position of the grid at  $p = 0$ , and the needle positions at  $p = 1 - 3$ . To quantify their preferential location along the  $z_1$ -direction, the particle positions are binned at these planes in  $z_3$ -direction from  $-5$  mm to  $5$  mm, as illustrated in Fig. 5.16a.

Although the bubble positions went along with varying turbulent length scales (Sec. 4.3.1), the particles are equally distributed along the  $z_1$ -direction independently of the bubble position. Additionally, the particle distribution is also independent of the volume fraction. Theoretically, the increase of the particle volume fraction from the dilute to the dense system would affect the particle movement because of the turbulent modulation, as described in Sec. 2.3.2. However, any differences in vertical positions are of the order less than uncertainty. Close to the vertical walls,  $z_1 = 0$  mm and  $z_1 = 30$  mm, a lower amount of particle passes is visible because of the low velocity in the boundary layer.

A major source of uncertainty in the particle distribution could be the high inertia of the PEPT tracer particles and, therefore, their low capability to follow the small eddies of the turbulent flow. This effect is quantified by the Stokes number,  $St$ , varying between 0.7 and 2.7 for the PEPT tracer in the water channel (Tab. 3.6). To reduce the particles' inertia and their Stokes number (Eq. 2.38), either the liquid velocity increases leading to a larger characteristic time scale of the liquid flow, or particles with a smaller density or diameter are used (Eq. 2.39). For example, Cole et al. [181] tried to downscale the particle size range of PEPT tracers to  $50 \mu\text{m}$ . However, they stated that the smaller tracer range comes along with lower labeling efficiency of the tracers, a challenging particle manufacturing process, as well as increased health and safety concerns.

### 5.3.2. Radial particle displacement in the bubble vicinity

In froth flotation, the particle trajectories near the bubble and their corresponding interaction are of particular interest. In the water channel, these particle trajectories can deviate either due to turbulent length scales upstream of the bubble or due to the turbulent bubble wake (Sec. 4.3.3). To distinguish the predominant effect in the current setup, the radial particle deviation,  $\Delta r(z_{l,2})$ , was computed from the PEPT experiment, as seen in Fig. 5.17.

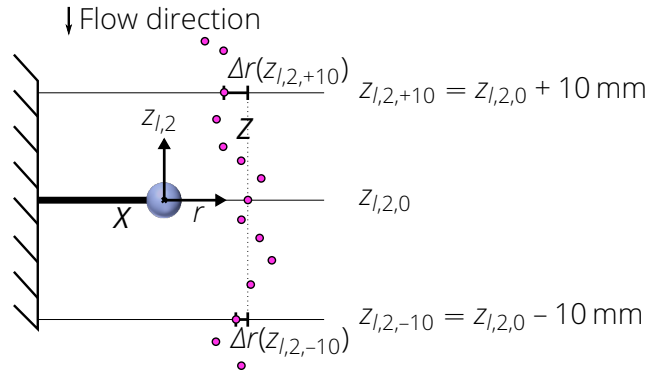


**Figure 5.17.** Schematic illustration of the radial deviation,  $\Delta r(z_{l,2})$ , of a tracer particle trajectory,  $\mathbf{Z}_c = (r, \alpha, z_{l,2})^T$ , around a bubble,  $\mathbf{X}$ . Hereby, the radial deviation is defined as the distance between the reference point,  $z_{l,2,0}$ , and the comparison point,  $z_{l,2,+10}$  or  $z_{l,2,-10}$ . The comparison points,  $z_{l,2,+10}$  and  $z_{l,2,-10}$ , mark the particle position 10 mm upstream and downstream of the bubble, respectively.

Firstly, each position of the particle trajectory was transformed into cylindrical coordinates,  $\mathbf{Z}_c = (r, \alpha, z_{l,2})^T$  (Eq. 3.71), based on the center point of the individual bubble,  $\mathbf{X} = (x_1, x_2, x_3)^T$ , as origin. Secondly, three positions of each trajectory were chosen, namely the reference point at the bubble center point,  $z_{l,2,0} = 0$  mm, the comparison points 10 mm upstream,  $z_{l,2,+10} = 10$  mm, and downstream of the bubble,  $z_{l,2,-10} = -10$  mm. Finally, the radial particle deviation,  $\Delta r(z_{l,2})$ , was calculated as the difference between the radial component of the reference point,  $r(z_{l,2,0})$ , and one of the comparison points,  $r(z_{l,2}) = r(z_{l,2,+10})$  or  $r(z_{l,2,-10})$ ,

$$\Delta r(z_{l,2}) = r(z_{l,2,0}) - r(z_{l,2}). \quad (5.80)$$

In Fig. 5.18,  $\Delta r(z_{l,2})$  is plotted over the corresponding radial position at the reference point of each particle trajectory,  $r(z_{l,2,0})$ . In this way, the effect of the deviation on the particle trajectory is distinguished between upstream and downstream of the bubble. For an increased visibility, the predominating tendency is emphasized by arrows in the plots. Meaning that the radial displacement of the particle trajectory is either in direction towards or away from the bubble. Only particle trajectories which passed by the bubble with a distance,  $|r(z_{l,2})| \leq 10$  mm, were used. Each column in Fig. 5.18 represents one bubble position,  $p = 1 \dots 3$ , and each row one volume fraction,  $\alpha_p, 1 \cdot 10^{-4}$  and  $2.2 \cdot 10^{-3}$ . Due to the limited measurement time, no data are available for the case  $p = 2$  at  $\alpha_p = 2.2 \cdot 10^{-3}$ .

The data show no significant difference between volume fractions, comparing Fig. 5.18a and Fig. 5.18d for  $p = 1$  or Fig. 5.18c and Fig. 5.18e for  $p = 3$ . Instead, the particle deviation decreases with the turbulence degree from  $p = 1$  to  $p = 3$  and the distance to the bubble.

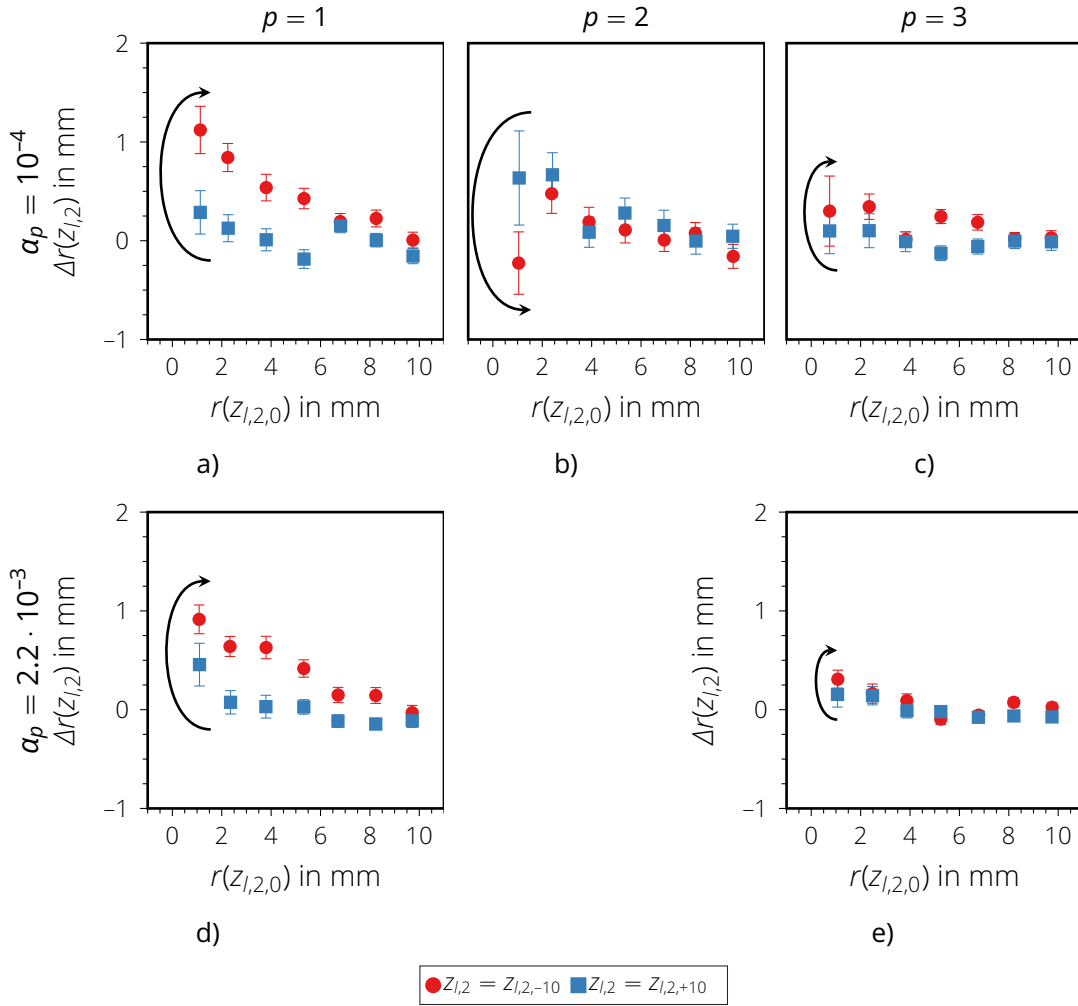


**Figure 5.18.** Water channel: Radial displacement,  $\Delta r(z_{l,2})$ , of tracer particles by passing by the stagnant bubble measured with PEPT, as illustrated in Fig. 5.17. With regard to the deviation on the particle trajectory, a distinction is made between upstream,  $z_{l,2,+10}$ , and downstream of the bubble,  $z_{l,2,-10}$ . The arrow emphasizes whether the radial displacement of the particle trajectory is in direction towards,  $\downarrow$ , or away from the bubble,  $\uparrow$ . The trajectory of the tracer particles are binned over the particle radial position at the height of  $z_{l,2} = 0 \text{ mm} = z_{l,2,0}$ .

But this effect is predominately observed downstream of the bubble at  $z_{l,2,-10}$ . This measurement result suggests that the flow in the bubble wake has a higher influence on the particle trajectory than the incident turbulent flow. Fig. 4.11 confirms this hypothesis because the highest TKE is observed in the wake of the bubble located at  $p = 1$  decreasing from location  $p = 2$  to  $p = 3$ . The lowest TKE are measured in the incident turbulent flow in the same order of magnitude among the bubble locations. Thus, there is a good probability that the high TKE in the bubble wake at  $p = 1$  was sufficient to push the particles further away.

These results might be affected by the shift of the bubble position in  $x_1$ -direction. Although a camera monitored the bubble position, it could not resolve all deviations of the bubble positions due to its low frame rate (0.25 fps). Therefore, the shift of the bubble position could

not be completely considered in the data analysis. As discussed in Sec. 4.3.2, the magnitude of the bubble shift decreased from 0.5 mm down to 0.2 mm with increasing distance from the grid,  $p = 1 \dots 3$ . Given that the measured radial displacement exceeds the variation of the bubble center in  $x_1$ -direction roughly by a factor of two, significance of the findings in Fig. 5.18 is suggested here.

### 5.3.3. Bubble-particle collision

Particles that deviate from the fluid streamlines may collide with a bubble. As reported above, a deviation in the form of a radial displacement of the particles was measured around the bubbles. This section focuses on the individual observation of particle trajectories close to a bubble surface for possible encounters. While measuring all in all 4599 trajectories in the region of interest (ROI) over 47.9 h acquisition time, none of the six radioactive-labeled PEPT tracer particles had been observed to attach to the bubble surface. Consequently, this PEPT measurement lacked a reliable validation case of a bubble-particle encounter prior to the particle attachment to the bubble surface. Therefore, possible particle encounters were classified based on their deceleration in the collision process, in the form of their enhanced residence time compared to a non-interacting particle.

The shift in residence time between an interacting and non-interacting particle is defined as

$$\Delta t_r = t_r - t_r^{non}, \quad (5.81)$$

with the residence time,  $t_r$ , of the particle and the theoretical residence time,  $t_r^{non}$ , of a non-interacting particle. The residence time,  $t_r$ , refers to the time a particle takes from the reference height,  $z_{l,2} = -5$  mm, to each triangulated position along the main flow direction till  $z_{l,2} = 5$  mm. The residence time of a non-interacting particle,  $t_r^{non}$ , equals the time of a particle moving with the average liquid velocity,  $|\bar{\mathbf{V}}|$ , from the reference height to each triangulated position along the main flow direction. Consequently, if  $\Delta t_r > 0$ , the residence time of the particle is extended and it may point towards a bubble-particle encounter.

Fig. 5.19 and Fig. 5.20 summarize the deviation of the residence time,  $\Delta t_r$ , close to the bubble. Each point corresponds to a triangulated particle position of a valid particle trajectory. To avoid uncertainties regarding the channel borders, the evaluated cross-section included only the area of in  $z_1$ -direction from 5 mm to 25 mm and in  $z_3$ -direction from -5 mm to 5 mm. Due to the change of needles during the measurements, an uncertainty of the bubble position arose in  $z_1$ -direction as marked in Fig. 5.19 and Fig. 5.20. The marked uncertainty only refers to the overall bubbles, and does not affect each individual bubble position. For them, the camera images were used for a continues calibration.

Fig. 5.19 illustrates that only a minority of particle trajectories extended their residence time above 20 ms in the vicinity of the bubble. These particle trajectories were located mainly around the upper bubble position with the highest turbulent degree. The majority of particles kept their velocity and even accelerated slightly downstream of the bubble. Only one trajectory had a remarkably higher normalized residence time of approximately 70 ms.

In addition to Fig. 5.19 highlighting the particles' prolonged residence time, Fig. 5.20 points out the dependency between the radial position,  $r$ , and the variation of the residence time,

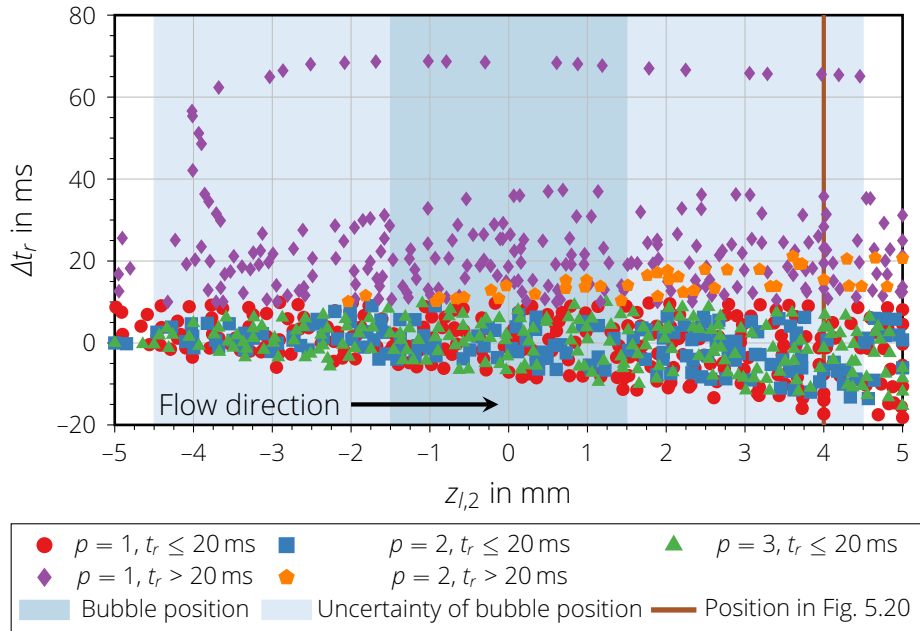


**Figure 5.19.** Water channel: Normalized residence time of particle trajectories,  $t_r$ , in the vicinity of the bubble in  $z_{l,2}$ -direction measured with PEPT. Each point corresponds to a triangulated particle position belonging in the vicinity of each bubble,  $z_{l,2}$  ranging from  $-5$  mm to  $5$  mm. The trajectories are classified by their bubble position,  $x_2$  ( $p = 1 \dots 3$ , see Fig. 3.1b), and whether they are above or below the limit of  $t_r = 20$  ms.

$\Delta t_r$ . The radial position equals the transformation of the particle position into cylindrical coordinates,  $\mathbf{Z}_c = (r, \alpha, z_{l,2})^T$ , with the bubble position,  $\mathbf{X}$ , as origin (Fig. 5.17). In Fig. 5.20, the radial position,  $r$ , of all particle trajectories at  $z_{l,2} = -4$  mm are summarized. The diagram emphasizes that an increase in residence time is not only caused by the bubble. Also, particle trajectories further away from the bubble surface exceed a residence time of 20 ms. The observed increase of the residence time could be attributed to the turbulent length scales upstream of the upper bubble. Presumably, the tracer particle was trapped in the larger eddies leading to higher residence time. The only promising trajectory in Fig. 5.19 was located in the vicinity of the bubble. But based on one individual event, no conclusion regarding a bubble-particle collision can be drawn.

### 5.3.4. Limitations on the detection of the bubble-particle collision

Contrary to exceptions, the PEPT measurements failed to detect a sufficient number of encounters between bubbles and PEPT tracer particles. Three main reasons for this shortcoming are discussed in the following.

Firstly, the manufactured PEPT tracers were supposed to represent the physical properties of the bulk *PMMA200* model particle system. Due to the manufacturing process, variations in size, density and shape (Sec. 3.4.2) were inevitable, which may lead to small deviations between the bulk *PMMA200* particles and PEPT tracers. However, there is no other tracer

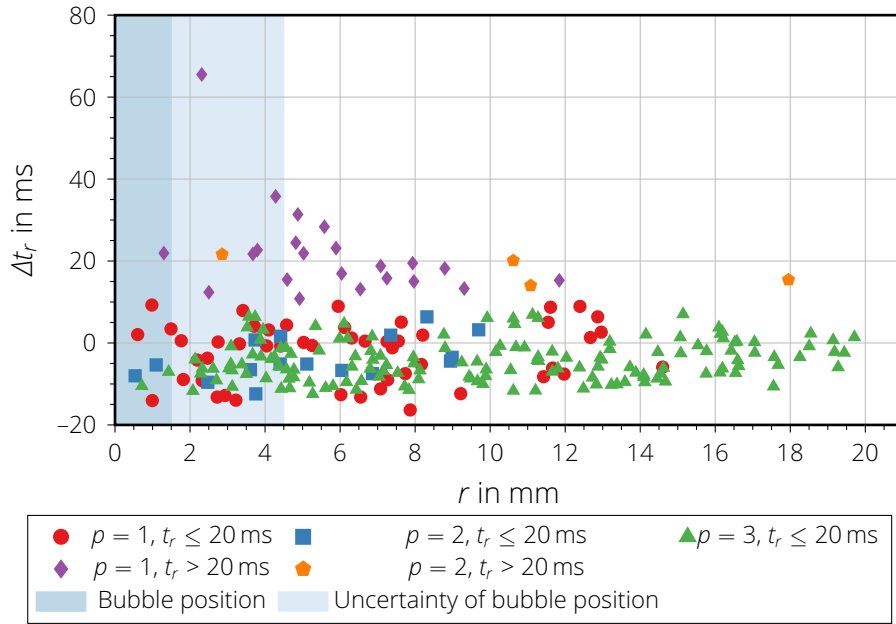


**Figure 5.20.** Water channel: Normalized residence time of particle trajectories,  $t_r$ , in the vicinity of the bubble, depending on its radial position,  $r$ , measured with PEPT. The radial position equals the transformation of the particle position into cylindrical coordinates,  $\mathbf{Z}_c = (r, \alpha, z_{l,2})^T$ , with the bubble position,  $\mathbf{X}$ , as origin (Fig. 5.17). Each point corresponds to a triangulated particle position of a valid particle trajectory at  $z_{l,2} = -4$  mm. The trajectories are classified by their bubble position,  $x_2$  ( $p = 1 - 3$ , see Fig. 3.1b) and whether they are above or below the limit of  $t_r = 20$  ms.

production technique available to be applicable for PMMA and achieving tracer sizes below  $500 \mu\text{m}$ . For example, the direct activation of  $^{18}\text{F}$  from  $^{16}\text{O}$  materials via a high-energy  $^3\text{He}$  beam is not applicable for PMMA [179]. Due to the low melting point of PMMA of  $125^\circ\text{C}$ , the polymer would not withstand the elevated temperatures above several hundred degrees [207].

Secondly, the main challenge of the water channel was that only the interaction of individual radioactive tracer particles with individual bubbles was observable with this technique. Therefore, the potential for a collision between bubble and particle was increased by employing two bubbles simultaneously at two of the three possible vertical positions. This enhanced the probability of a bubble-particle collision,  $P_c$ , from 0.8 % to 1.6 % per passage of the radioactive model particle. The values are quantified by the observation by Nguyen et al. [49], where only particles within the grazing trajectory of the bubble led to a collision,

$$P_c = \frac{N_b \cdot A_b}{A_{wc}} \cdot 100, \quad (5.82)$$

with the number of bubbles  $N_b$ , the cross-sectional area of the bubble,  $A_b = 0.25 \cdot \pi \cdot d_b^2$ , and the cross-sectional area of the water channel,  $A_{wc} = 600 \text{ mm}^2$ .

Additionally, up to six radioactive tracer particles were included into the solid phase at

once. Still, the probability of the interaction of an individual radioactive-labeled particles with a single bubble was lower during PEPT measurements than during the 4D PTV experiments, where hundreds of *PMMA200* particles were detected at the same time.

Finally, the dependency of the temporal and spatial resolution of the tracer position on its activity limited the quality of the triangulated trajectory. The exponential decay of the tracer radionuclide led to a decrease in the spatial resolution for a fixed temporal resolution over time. Consequently, even if an interaction took place, the event could not be resolved and detected.

## 5.4. Discussion and Conclusion

The collision between particles and bubbles is, besides attachment, the key process behind the formation of a bubble-particle aggregate in froth flotation. A particle collides with the bubble surface due to a sufficiently close encounter. This process is governed by the hydrodynamics in the flotation cell. After the collision, the particle slides along the bubble surface. When the particles are sufficiently hydrophobic, the liquid film between the bubble and the particle thins and finally ruptures due to the interfacial forces. This process takes place in the nanometer range [17].

Due to the importance of the collision process in froth flotation, this chapter investigated the role of turbulence on the collision between bubbles and particles. The range of conducted experiments is summarized in Tab. 5.1. By this means, the novel measurement methods, 4D PTV and PEPT, were applied to answer Questions **Q.3** and **Q.4** (Sec. 1.2). Additionally, the new experimental insight was used to compare the predicted collision frequencies from available collision models with the experimentally determined collision frequencies, responding to Question **Q.5** (Sec. 1.2).

**Table 5.1.** Summary of the conducted experiments regarding the applied measurement technique, experimental setup and model particle system.

Section	Particle tracking method	Experimental setup	Model particle system
5.1	4D PTV	Bubble column	<i>PS33, PS95</i>
5.2	4D PTV	Water channel	<i>PS33, PMMA200</i>
5.3	PEPT	Water channel	<i>PMMA200</i>

Comparing the conducted experiments in Tab. 5.1, it is notable that certain overlaps of either the applied measurement technique, the experimental setup, or the applied model particle systems existed among the three cases. Therefore, the influence of the particle tracking method or experimental setup can be discussed on a wider scope. In particular, the 4D PTV results of the bubble column (Sec. 5.1) could be compared with the ones in the water channel (Sec. 5.2). Additionally, the results in the water channel conducted with 4D PTV (Sec. 5.2) could be compared with the ones conducted with PEPT (Sec. 5.3).

In this chapter, 4D PTV was not only used to analyze the collision of particles with a freely rising bubble chain, but also with a stagnant bubble. For this purpose, experiments were conducted for a range of bubble diameters (Fig. 4.3a, Fig. 4.10b) and particle diameters (Tab. 3.5)



in the bubble column and the water channel. A suitable reference case for a comparison among these two setups would be the interaction between the model particle system *PS33* and the bubbles with a Reynolds number of approximately 450. This Reynolds number was achieved for all stagnant bubbles in the water channel and the smallest bubble diameter in the bubble column ( $d_b = 1.4$  mm).

In both experimental setups, a leading edge collision was observed over the entire range of investigated parameters (Fig. 5.3a and Fig. 5.9a-c). The trailing edge collision occurred only in the water channel at  $p = 1$  and  $p = 3$  (Fig. 5.9a and c). One reason might be the wake structure which was also influenced by the diverging surface mobility. In the case of the freely rising bubble, the mobile surface may have retarded the evolution of a double-threaded wake in comparison to the immobile surface of the stagnant bubble. Additionally, the distortions by the mounting needle could affect the wake structure of the stagnant bubble.

In the case of the freely rising bubble, the bubble wake was axisymmetric without a standing eddy (Fig. 4.4d). Thus, the values of dissipation rate and TKE were in the same order of magnitude upstream and downstream of the bubble ( $\varepsilon \approx 3 \cdot 10^{-2} \text{ m}^2/\text{s}^3$ ;  $k \approx 3.5 \cdot 10^{-3} \text{ m}^2/\text{s}^2$ ). In contrast, the trailing edge of the stagnant bubble not only had a double-threaded wake, but also the flow was superimposed by the wake of the needle. Thus, higher values of TKE and dissipation rate were reached downstream of the stagnant bubble ( $\varepsilon \approx 2.5 \cdot 10^{-1} \text{ m}^2/\text{s}^3$ ;  $k \approx 7.5 \cdot 10^{-3} \text{ m}^2/\text{s}^2$ ).

As a consequence of the higher TKE in the vicinity of the stagnant bubble a higher collision frequency ( $Z_{pb}^E \approx 10^{-8} \text{ m}^3/\text{s}$ ) was measured in the water channel than in the bubble column ( $Z_{pb}^E \approx 10^{-10} \text{ m}^3/\text{s}$ ). Thus, the experimentally detected collision frequencies for an immobile stagnant bubble with a turbulent inflow were in the same order of magnitude as the prediction by the model proposed by Kostoglou et al. [37]. In the case of the freely rising bubbles with a mobile surface, the experimentally detected collision frequencies were considerably smaller than the prediction by the model proposed by Kostoglou et al. [37].

Surprisingly, the difference between the values of the turbulent parameters of both experimental setups were lower than expected. For example, the values of the TKE in the vicinity of the stagnant bubble were only twice as high as in the vicinity of the freely rising bubble. There are several possible explanations for this. On the one hand, the generated turbulence by the applied grid was limited to a certain range of turbulent length scales and TKE, which are comparable to a freely rising bubble. Theoretically, the grid reached a Kolmogorov length scale of  $20 \mu\text{m}$  (Eq. 2.12), whereas the smallest freely rising bubble produced a Kolmogorov length scale of  $15 \mu\text{m}$  [156]. Consequently, they were both in the same order of magnitude. On the other hand, the uncertainty and limitations of the TPIV measurements as discussed in Sec. 4.4 and Sec. 5.2.4 led to an underestimation of the turbulent parameters.

Additionally, the comparability among the experimental results of these two experimental arrangements was limited as already discussed in Sec. 4.4. Just analysing the effect of the turbulent inflow conditions on the stagnant bubble compared to the freely rising bubble was challenging, because also the surface mobility (immobile for stagnant bubble, mobile for freely rising bubble) and the distortion of the needle (stagnant bubble) modified the flow field and collision behaviour. Given that the previous comparison should be treated with considerable caution. Further research is required to determine how the turbulent inflow influences the bubble-particle collision.

Turning now to the comparison of the results in the water channel conducted with 4D PTV and PEPT, a suitable reference point would be the dilute suspension of the model particle system *PMMA200*. In the 4D PTV experiments (Sec. 5.2), the PMMA model particles collided only with the leading edge of the bubble (Fig. 5.9d-f). One reason could be the high localized Stokes number in the wake of the bubble (Fig. 5.13d-f), emphasizing that the fluid time scale was too small to affect the particle motion of *PMMA200*.

These findings agreed with the measured particle distribution with PEPT (Sec. 5.3.1). The particle distribution remained nearly constant, independently of the turbulence degree upstream of the bubble. However, to establish a connection between the particle distribution and collision positions was challenging during the PEPT measurements because the PEPT measurements failed to detect a sufficient number of encounters between bubbles and PEPT tracer particles. Possible reasons have already been discussed in Sec. 5.3.4.

Still, PEPT is a promising measurement technique to investigate the bubble-particle interaction. Its ability to investigate dense solid suspensions makes PEPT indispensable for further research in this field. In particular, the recent developments of Cole et al. [181] allow the production of tracer particles below 50  $\mu\text{m}$ . Consequently, future PEPT studies can examine the interaction between fine particles and bubbles in dense flows with high solid fractions, typical for froth flotation.

# 6. Concluding remarks

## 6.1. Conclusions

This thesis aimed to measure directly the collisions between bubbles and particles under defined hydrodynamic conditions. The results should serve to verify existing collision models and to advance the understanding of the role of turbulence in the bubble-particle interaction. In model experiments, turbulence was either generated in the wake of a freely rising bubble chain or by a fluid passing through grid upstream of a stagnant bubble. The generated turbulence was characterized with Tomographic Particle Image Velocimetry (TPIV). This insight provided the basis to understand the motion of the model particles in the vicinity of the bubble, as observed by 4D Particle Tracking Velocimetry (PTV) and Positron Emission Particle Tracking (PEPT). The combination of both, the liquid flow field and the collision trajectories, was fed into existing collision models to obtain the collision frequency. Consequently, questions Q.1 to Q.5 (Sec. 1.2) have been answered in this dissertation.

Question Q.1 addressed the current limitations of suitable measurement techniques to observe the collision between particles and bubbles. In this thesis, two new methodologies were developed by applying 4D PTV and PEPT. These techniques observed the particle trajectories colliding with a bubble. Suitable particle systems were found to mimic mineral particles and be detectable in the according measurement systems (Tab. 3.5 and Fig. 3.12b).

In the case of 4D PTV, suitable criteria were developed which enabled the colliding particle trajectories to be classified (Eq. 3.75) based on distance, radial velocity and residence time. The applicability of these criteria were proven for exemplary cases of the leading and trailing edge collision (Fig. 5.2).

PEPT represented a valuable alternative to 4D PTV because of its applicability to optically opaque fluids. For the detection of individual particles with PEPT, radioactive tracer particles were designed to represent the bulk particles. This method allowed to research the particle distribution and bubble-particle interactions in a turbulent and dense flow field. A classification of colliding particle trajectories similar to 4D PTV was challenging due to the limited number of collision and attachment events of the radioactive tracers.

Thus, considerable progress has been made on the available measurement techniques in this field. In this thesis, 4D PTV and PEPT were applied to measure directly the bubble-particle

interaction for the first time. In particular, PEPT has the potential to measure suspensions with a high solid fraction as typical for froth flotation [177], which could not be achieved with optical particle tracking methods.

With respect to question **Q.2**, two experimental setups were developed to measure the bubble-particle interaction under turbulent conditions. The setups were adapted to the special needs of the applied measurement techniques - 4D PTV and PEPT.

The first experimental setup consisted of a freely rising bubble chain in a bubble column (Sec. 3.1.1). The freely rising bubble chain is a well-known and strongly investigated phenomenon [90, 91, 98]. There is a strong connection between the aspect ratio of the bubble and its wake structure. Thus, a variation in the bubble diameter went along with reproducible wake structures and turbulent length scales. However, this experimental setup was limited to the fine particle systems (*PS33* and *PS95*). The settling velocity of *PMMA200* was too high to be applicable in the quiescent flow of the bubble column.

The second experimental setup consisted of a water channel. A grid upstream of the stagnant bubbles produced a well-defined turbulence (Sec. 3.1.2). Stagnant bubbles were generated by means of a needle at three defined positions ( $p = 1 - 3$ ). The turbulent intensity changed with the distance to the grid, leading to different turbulent length scales upstream of each bubble position. Although the flow field could be distorted by the needle, the predefined position of the stagnant bubble was beneficial for multiple reasons. Firstly, PEPT only detected the emitted positrons of the radioactive-labelled tracer particle, excluding the gas phase. Therefore, the position of the bubble must be known, to investigate the bubble-particle interaction. Secondly, the slightly idealized system allowed to investigate separately and generically the defined turbulent inflow conditions on the bubble-particle interactions. Distortions from path instabilities or rotation, which are typical for freely rising bubbles in this size range, could be avoided. Finally, the water channel was suitable not only for the fine particle system (*PS33*), but also for the larger particle system (*PMMA200*). Due to the circulating of the fluid flow in the water channel, *PMMA200* particles did not sediment on the bottom of the cell.

The defined hydrodynamic conditions in these experimental setups cannot be generalized to the harsh conditions in a flotation cell. Instead, they aim to mimic the turbulence modulation from the dispersed phase in a flotation cell [208]. These setups enabled to generate a range of the turbulent length scales in the vicinity of the bubble. Thus, they gave a framework to study the particle motion and collision behavior between particles and bubbles with 4D PTV and PEPT.

The results of the measurements in the bubble column and water channel with 4D PTV and PEPT were the concern of questions **Q.3**, **Q.4** and **Q.5**. Question **Q.3** dealt with the influence of the bubble wake on the bubble-particle collision. The magnitude of the turbulent parameters in the liquid flow of the bubble wake was characterized by TPIV (Fig. 4.4 and Fig. 4.11). As shown in Fig. 5.3 and Fig. 5.9, the fine particle systems, *PS33* and *PS95*, not only collided with the leading edge, but also with the trailing edge of a bubble. This phenomenon was promoted by the turbulent bubble wake (Fig. 4.4 and Fig. 4.11). The combination of both, the flow field and the collision trajectories, confirmed that the turbulent kinetic energy (TKE) and dissipation rate in the bubble wake were sufficiently high to enable the trailing edge collisions for fine particles (Fig. 5.5 and Fig. 5.11). A similar effect was not observed for

the larger particle system, *PMMA200*. This indicated that the TKE and dissipation rate in the bubble wake were too low to affect the motion of *PMMA200* particles.

Until now, research focused mainly on fine particle entrainment due to the bubble wake [209], neglecting the influence of the bubble wake on the collision efficiency of fine particles [7]. However, the state of the art in fine particle flotation is that, besides the high dissipation rate, small spherical bubbles improve the collision probability [21]. These spherical bubbles do not form a wake [91]. Thus, the trailing edge collision phenomenon is insignificant for flotation cells forming bubble sizes below 2 mm. Nonetheless, the trailing edge collision could be interesting for modeling flotation columns. In these cells, the bubble diameter exceeds 2 mm e.g. due to the low concentration of added flotation reagents.

The influence of the turbulent liquid flow on the collision between a stagnant bubble and model particles was investigated for a range of turbulent length scales, which is the concern of question **Q.4**. The generated range of turbulent length scales in the liquid flow were characterized by TPIV. The turbulent intensity changed with the distance to the grid (5 %... 15 %), leading to different turbulent length scales upstream of each bubble position. Based on the power spectra, nearly isotropic turbulence had been achieved for the middle and lower bubble positions (Fig. 4.8). The collision behavior of two different particle systems, *PS33* and *PMMA200*, was investigated at the three positions of the stagnant bubble,  $p = 1 - 3$ , in the water channel.

Independently of the bubble position, a leading and trailing edge collision was observed for the fine particle system, *PS33*. In contrast, the distribution of the collision positions of the coarse particle system, *PMMA200*, remained mainly at the stagnation point of the leading edge of the bubble. A clear trend between the turbulent length scales upstream of each bubble on the bubble-particle interaction could not be shown. Possible limitations on the experimental setup and measurement methodologies were discussed.

Despite the fact that no dependency of the leading edge collision on the bubble position was observed, this dissertation extended understanding of influence of turbulence on the bubble-particle interaction. Previous studies [17, 30–34] only recorded particle trajectories colliding with a stagnant bubble in quiescent flow. This dissertation expanded their idea by adding a grid upstream of the stagnant bubble to generate different turbulent length scales in the liquid flow. Further, the analysis combined the colliding particle trajectories with the results of the liquid velocity field.

To answer question **Q.5**, the spatially resolved dissipation rate and TKE were fed into existing collision models developed by Saffman et al. [35], Abrahamson [36] and Kostoglou et al. [37] to obtain the collision frequency for each measurement configuration. The experimentally determined collision frequency followed Eq. 3.68, employing the number of detected collisions with 4D PTV (Fig. 4.4 and Fig. 4.11). Firstly, the experimentally determined collision frequencies were compared to the collision frequencies predicted by the models by Saffman et al. [35] and Abrahamson [36]. The experimentally determined collision frequencies were much smaller than those predicted by the models [35, 36]. Possible reasons for this outcome were that their assumptions (e.g. monodispersed particle sizes, isotropic turbulence and  $\rho_S \gg \rho_L$ ) were rarely met in the flotation process, where the collisions between various length scales of bubbles and particles are of great importance. Secondly, the experimentally determined collision frequencies were compared with the further developed collision

model of Kostoglou et al. [37], who adapted it for the process of froth flotation. In the case of an immobile stagnant bubble with a turbulent inflow, the collision frequencies were in the same order of magnitude as the prediction by the model proposed by Kostoglou et al. [37]. In the case of the freely rising bubbles with a mobile surface, the experimentally detected collision frequencies were considerably smaller than the prediction by the model proposed by Kostoglou et al. [37]. The discrepancy between the theoretical and experimental results was mainly attributed to the underestimation of the collision trajectories and to the spatial and temporal limitations of the TPIV in the experiments.

To sum up, the developed methodology and experimental setups are very promising to investigate the interaction between bubbles and particles. The conducted experiments extend the range of fundamental studies on bubble-particle interactions and allow a critical assessment of available collision models. As a consequence, this dissertation provides a foundation to enhance the understanding of turbulence in a flotation cell and gives a framework for further studies.

## 6.2. Outlook

While answering the questions Q.1 to Q.5 in this thesis, more questions arose for further research activities. These questions are structured into the following topics: the enhancement of the current measurement technique, the application of the developed methodology in future studies and other potential measurement techniques to investigate the bubble-particle interaction.

To overcome limitations of the current measurement technique, the setup could be improved as follows: During the shadowgraphy measurements, the reconstruction of the measured bubble shape could be enhanced by adding a camera to observe the bubble from the side. In detail, the  $x_3x_2$ -plane for the bubble column and the  $x_1x_2$ -plane for the water channel setup (Fig. 3.1). The side view of the bubble allows to analyze the tilt angle of the free rising bubble in  $x_1$ -direction and the exact shape of the stagnant bubble, respectively. However, a perpendicular side view of the bubble with a camera conflicts with the laser. Either the camera would block the laser light, or the laser light would directly radiate the camera and destroy it. Consequently, the side camera would be useful for an intensive study of the bubble shape with only shadowgraphy. For TPIV and 4D PTV measurements, the same behavior would be assumed due to the reproducibility of the experimental setup.

In the case of the TPIV and 4D PTV, the cameras could be equipped with objectives having a larger focal length to enhance the spatial resolution. The measurements could be recorded with a higher frame rate to increase the temporal resolution. Further, the uncertainty arising from ghost particles could be minimized by using a larger number of cameras. Additionally, the spectrum of suitable fluorescent particles could be enhanced by applying fluorescent minerals [210] or coating minerals with a fluorescent dye [211–213].

The PEPT measurements could be enhanced by either increasing the probability of an interaction between the stagnant bubble and the radio-labeled tracer particles or increasing the temporal resolution of the tracer position. An enhancement of the bubble-particle interaction could be achieved by the employment of a large number of tracers, the reduction

of the cross-section of the water channel or minimizing the residence time of a tracer by increasing the flow rate. Possible approaches that would enhance the temporal resolution include an increase of the initial tracer activity, the usage of different isotopes with longer half lives, and tailored PEPT cameras optimized for this particular study.

The application of 4D PTV and PEPT to analyze the bubble-particle interaction is manifold. In future studies, experimental setups could be developed to generate turbulence by randomly moving particles in a grid structure [143], by a round free jet [214] or Taylor-Couette flow [215]. The properties of the bubble surface could be modified by either adding varying concentrations of surfactants [109] or changing its surface coverage of particles [216]. Finally, the suspended particles could have different states of hydrophobization [217] or have a non-spherical shape [33].

Another promising measurement technique to analyze the bubble-particle interaction in the dense multiphase flow in industrial flotation cells would be neutron imaging [218]. Lapan et al. [218] applied neutron imaging to the opaque multiphase flows in liquid metal to investigate bubble - particle interactions. This technique allowed the simultaneous observation of multiple particles and a bubble. In this case, the used model particles were gadolinium, a rare earth element, offering the largest neutron attenuation coefficient.

# A. Appendix

## A.1. Physical properties of the model particle systems

Table A.1. Physical properties of the used particle systems *PS-FluoRed* and *PMMA-RhB*, denoted by  $\rho_s$  the particle density,  $\lambda_{abs}$  the absorption wavelength and  $\lambda_{em}$  the emission wavelength.

Product name	<i>PS-FluoRed</i>	<i>PMMA-RhB</i>
Material	polysterene (PS)	polymethylmethacrylate (PMMA)
$\rho_s$ in g/m <sup>3</sup>	1.05	1.2
$\lambda_{abs}$ in nm	530	560
$\lambda_{em}$ in nm	607	584

## A.2. Measurement of the contact angle with the Washburn method

To measure contact angle of the model particle systems in deionized (DI) water, the Washburn method for porous media [175] was used based on the measurement of the free surface energy with the force tensiometer K100 (KRÜSS GmbH, Germany). The main idea of the Washburn method is that a fluid moves upwards in a porous media due to capillarity, as shown in Fig. A.1a. During the measurements, the force tensiometer detects the increase of the mass of the probe over time which is related to advancing contact angle of the powder as follows

$$\cos \Theta = \frac{m_p^2}{t} \cdot \frac{\mu}{\rho_L^2 \cdot \sigma_{lg} \cdot c_c}, \quad (\text{A.83})$$

with  $\Theta$  as the contact angle,  $m_p$  as the mass of the probe,  $t$  as the flow time,  $\mu$  as the dynamic viscosity,  $\rho_L$  as the density of the liquid phase,  $\sigma_{lg}$  as the gas-liquid surface tension and  $c_c$  as the capillary constant of the powder. For the measurements, a homogeneous powder pack-



ing is crucial, thus the experiments were conducted with *PMMA-RhB* and *PS-FluoRed* particles in the diameter range between 1  $\mu\text{m}$  and 20  $\mu\text{m}$ . Each measurement used a particle powder mass of 0.35 g.

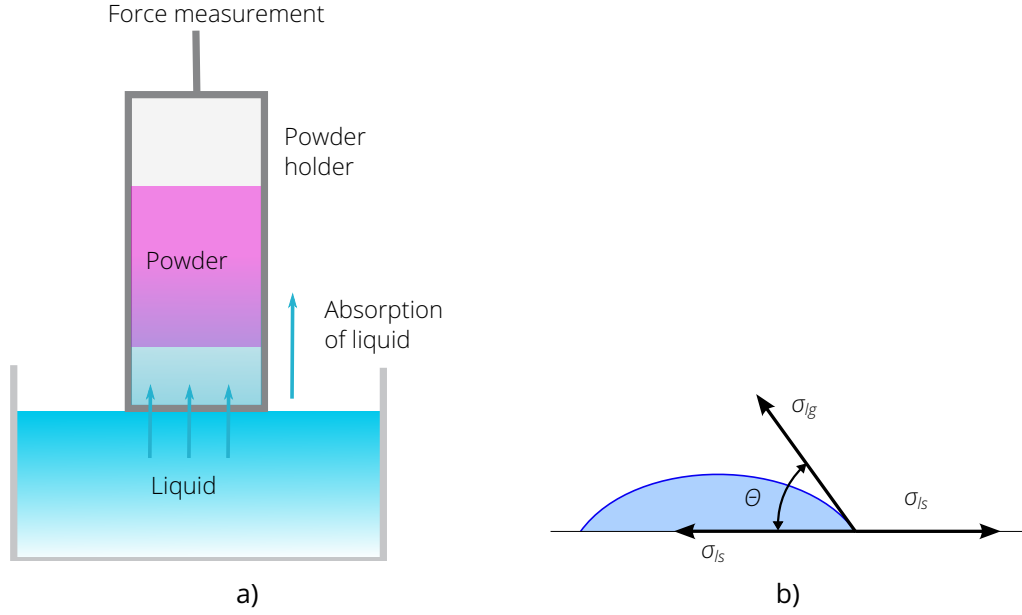


**Figure A.1.** Measurement of hydrophobicity. a) Schematic of the Washburn method. b) Schematic of a liquid drop illustration the variables of the Young equation, where  $\theta$  denotes the contact angle,  $\sigma_{lg}$  the interfacial tension between liquid and gas phase,  $\sigma_{ls}$  the interfacial tension between liquid and solid phase, and  $\sigma_{gs}$  the interfacial tension between gas and solid phase.

Firstly, the capillary constant of the *PS-FluoRed* and *PMMA-RhB* was quantified by using the highly hydrophilic n-heptane, assuming  $\theta = 0^\circ$ . Secondly, the contact angle of *PS-FluoRed* or *PMMA-RhB*, was measured with two reference liquids dimethyl sulfoxide (DMSO) and n-hexadecane or DMSO and 1-bromnaptalin (1-BN), respectively. A direct measurement of the contact angle between the powders and DI was impossible because the Washburn method is limited to hydrophilic powders [219]. The obtained contact angles are summarized in Tab. A.2. Thirdly, the surface free energy of the solid-gas interface,  $\sigma_{gs}$ , was computed with the Owens, Wendt, Rabel and Kaelble (OWRK) method [220–222]. This method approximates the interfacial tension between liquid and solid phase as a geometric mean of the dispersed part,  $\sigma_{ij}^d$ , and the polar part,  $\sigma_{ij}^p$ , of the surface tension as

$$\sigma_{ls} = \sigma_{gs} + \sigma_{lg} - 2 \cdot \left( \sqrt{\sigma_{gs}^d \cdot \sigma_{lg}^d} + \sqrt{\sigma_{gs}^p \cdot \sigma_{lg}^p} \right). \quad (\text{A.84})$$

Combining Eq. A.84 with Eq. 3.70, the surface free energy of the solid-gas interface can be calculated using the results of the two reference liquids (Tab. A.3). The measured surface free energy of the solid-gas interface,  $\sigma_{gs}$ , of both particle materials is listed in Tab. A.2. Consequently, the contact angle between *PS-FluoRed* or *PMMA-RhB* and DI water with 0.01 M potassium chloride (KCl) exceeded  $90^\circ$ , thus the applied particle systems were hydrophobic (Tab. A.2).

**Table A.2.** Interfacial properties of *PS-FluoRed* and *PMMA-RhB* particles from microParticles GmbH (Germany). The gas-liquid-solid interface is characterized by the contact angle,  $\theta$ . These values are either measured (row: 1–3) with the force tensiometer K100 (KRÜSS GmbH, Germany) and calculated (row: 4) using Eq. 3.70. The capillary constant,  $c_c$  was quantified by using the highly hydrophilic n-heptane. The required gas-solid surface tension,  $\sigma_{gs}$ , was calculated with the Owens, Wendt, Rabel and Kaelble (OWRK) method (Eq. A.84). The physical and chemical properties of the liquid phase are summarized in Tab. A.3.

Interfacial property	Liquid phase	<i>PS-FluoRed</i>	<i>PMMA-RhB</i>
$\theta$ in °	n-heptane	0	0
	DMSO	$87 \pm 1$	$66 \pm 9$
	n-hexadecane	$86 \pm 1$	-
	1-BN	-	$70 \pm 11$
	DI water 0.01 M KCl	130	128
$c_c$ in mm <sup>5</sup>	-	0.134	0.32
$\sigma_{gs}$ in mN/m	-	$12.3 \pm 0.4$	$22 \pm 10$
$\sigma_{gs}^d$ in mN/m	-	$7.9 \pm 0.1$	$20 \pm 6$
$\sigma_{gs}^p$ in mN/m	-	$4.4 \pm 0.3$	$2 \pm 5$

**Table A.3.** Physical and chemical properties of the used reference liquids and the results of the measurement of the surface free energy of the *PS-FluoRed* and *PMMA-RhB* particles with the force tensiometer K100 (KRÜSS GmbH, Germany). The properties comprise  $\mu$  the dynamic viscosity,  $\rho_L$  the density of the liquid phase and  $\sigma_{lg}$  the gas-liquid surface tension divided into  $\sigma_{lg}^d$  its dispersed and  $\sigma_{lg}^p$  its polar part.

	n-heptane	DMSO	n-hexadecane	1-BN	DI water 0.01 M KCl
$\mu$ in mPas	0.4	2.0	0.4	5.1	1.0
$\rho_L$ in g/cm <sup>3</sup>	0.6794	1.10004	0.7733	1.483	0.997
$\sigma_{lg}$ in mN/m	20.1	43.5	21.1	44.6	72.8
$\sigma_{lg}^d$ in mN/m	20.1	34.9	27.1	44.6	21.8
$\sigma_{lg}^p$ in mN/m	0.0	8.6	0.0	0.0	51.0

### A.3. Specifications of the calibration targets

### A.4. Collision models

To make the calculation behind the data points in Fig. 5.7 and Fig. 5.14 more transparent, the approximation of the turbulent particle fluctuation proposed by Abrahamson [36] and

**Table A.4.** Properties of the applied calibration targets. The location of the calibration targets in the experimental setups are shown in Fig. A.2.

Type	025-3.3	058-5
Dimensions in mm × mm	25 × 25	58 × 58
Dot distance in mm	3.3	5
Dot diameter in mm	0.9	1.2
Level separation in mm		1
Positioning	Water channel: $p = 1$ and $2$ : Fig. A.2b $p = 1$ and $3$ : Fig. A.2c	Bubble Column: Fig. A.2a

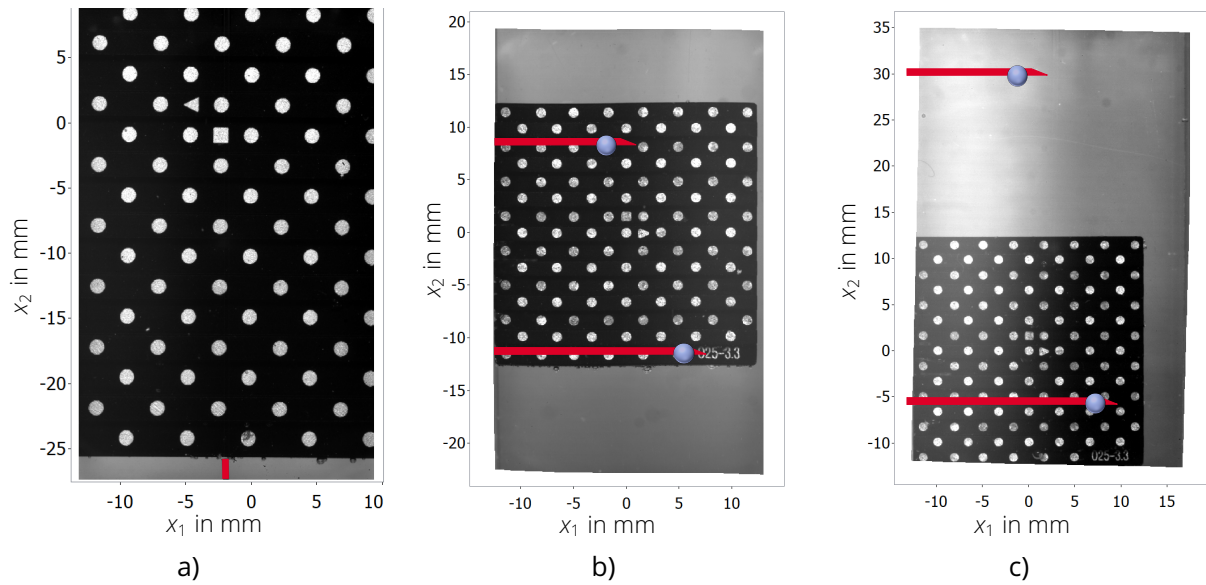


**Figure A.2.** Location of the calibration targets in the experimental setups. a) Bubble column. b) Water channel with the stagnant bubble localized at position  $p = 1$  and  $p = 2$ . c) Water channel with the stagnant bubble localized at position  $p = 1$  and  $p = 3$ . The positions of the needle are marked red.

the collision frequency model found in Kostoglou et al. [37] are described here in more detail. Abrahamson [36] approximated the turbulent particle fluctuation,  $W'_i$ , for the collision

frequency model (2.45) as

$$\overline{W_i'^2} = A_i \cdot \overline{U^2} \quad (\text{A.85a})$$

$$A_i = \frac{a_i \cdot T_L + b_i^2}{a_i \cdot T_L + 1} \quad (\text{A.85b})$$

$$a_i = \frac{36 \cdot \mu}{(2 \cdot \rho_{p,i} + \rho_l) \cdot 4 \cdot r_i^2} \quad (\text{A.85c})$$

$$b_i = \frac{3 \cdot \rho_l}{2 \cdot \rho_{p,i} + \rho_l} \quad (\text{A.85d})$$

$$T_L = \frac{1.4 \cdot k}{3 \cdot \varepsilon}, \quad (\text{A.85e})$$

with  $V'$  as the fluid turbulent velocity,  $T_L$  as the Lagrangian integral time scale,  $\mu$  as the dynamic viscosity,  $\rho_{p,i}$  as the particle and  $\rho_l$  as the liquid density,  $k$  as the turbulent kinetic energy and  $\varepsilon$  as the dissipation rate.

The collision frequency model found in Kostoglou et al. [37] and described in (Eq. 2.46) can be approximated in the following way. The model recreates the functional dependency,  $Z_{pb}^K(r_p, r_b, k, \varepsilon, |\overline{U}|, w_s)$ , of the collision frequency,  $Z_{pb}^K$ , depending on the bubble,  $r_b$ , and particle radii,  $r_p$ , the rising velocity of the bubble,  $|\overline{U}|$ , and the settling velocity of the particles,  $w_s$ . The aim is to simplify the one-dimensional integral in (Eq. 2.46) to solve it analytically.

Firstly, the function  $\Lambda$ , defined for positive  $x$  as  $\Lambda(x) = x$  and for negative  $x$  as  $\Lambda(x) = 0$ , is unfolded using the critical polar angle,  $\theta_c$ . The critical polar angle equals the polar angle along the bubble surface, where the relative velocity between the bubble and the particle changes its sign and becomes negative. Thus, a collision occurs only in the limits of  $\pm\theta_c$ , and outside this range  $Z_{pb}^K = 0$ . It is noted that  $\theta = 0^\circ$  is defined as the approaching direction of the far field liquid velocity. In the case of a mobile bubble surface, Kostoglou et al. [37] give the following solution for the critical angle,

$$\cos \theta_c = \frac{-N_2 + \sqrt{N_2^2 - 4 \cdot N_1 \cdot N_3}}{2 \cdot N_1}. \quad (\text{A.86})$$

In the case of an immobile bubble surface, a second critical angle is defined as

$$\cos \theta_d = \frac{-N_2 - \sqrt{N_2^2 - 4 \cdot N_1 \cdot N_3}}{2 \cdot N_1}, \quad (\text{A.87})$$

due to a formed wake downstream of the bubble. The variables  $N_1, N_2$  and  $N_3$  are a short form of

$$N_1 = 3 \cdot Y \cdot F \cdot |\Delta W_{bl}| \quad (\text{A.88a})$$

$$N_2 = 2 \cdot X \cdot F \cdot |\Delta W_{bl}| + |\Delta W_{pl}| \cdot f \quad (\text{A.88b})$$

$$N_3 = |\Delta W_{bp}| - Y \cdot F \cdot |\Delta W_{bl}|, \quad (\text{A.88c})$$

with  $X$ ,  $Y$  and  $F$  as the fitting parameters of the flow field approximation around a rising mobile bubble.

Secondly, the flow field around a rising bubble,  $\Omega(\theta)$ , is approximated using the equations employed by Nguyen et al. [49],

$$\Omega(\theta) = X \cdot \sin \theta + Y \cdot \sin \theta \cdot \cos \theta, \quad (\text{A.89})$$

with the fitting parameters  $X$  and  $Y$  and the dimensionless radial distance  $F$ . In the case of a mobile bubble surface, the fitting parameter are calculated as

$$X = 1 + \frac{0.0637 \cdot Re_w}{1 + 0.0438 \cdot Re_w^{0.976}} \quad (\text{A.90a})$$

$$Y = 0.0537 \frac{Re_w}{1 + 0.0318 \cdot Re_w^{1.31}} \quad (\text{A.90b})$$

$$F = \frac{1}{2} \cdot \left[ \frac{r_p}{r_b} - \left( \frac{r_p}{r_b} \right)^2 \right]. \quad (\text{A.90c})$$

In the case of an immobile bubble surface, the fitting parameter are calculated as

$$X = \frac{3}{2} + \frac{9}{32} \cdot \frac{Re_w}{1 + 0.31 \cdot Re_w^{0.7}} \quad (\text{A.91a})$$

$$Y = \frac{3}{8} \cdot \frac{Re_w}{1 + 0.217 \cdot Re_w^{0.518}} \quad (\text{A.91b})$$

$$F = \frac{1}{2} \cdot \left[ \frac{r_p}{r_b} \right]^2. \quad (\text{A.91c})$$

$$(\text{A.91d})$$

The Reynolds number of the relative motion between the bubble and the liquid phase is defined as

$$Re_w = \frac{r_b \cdot |\Delta W_{bl}|}{\nu}. \quad (\text{A.92})$$

Theses set of equations predict the normalized radial liquid velocity distribution along the bubble surface. The normalization is performed by the far-field liquid velocity in the rising direction of the bubble ( $\theta = 0^\circ$ ). Kostoglou et al. [37] used the normalized local radial liquid velocity distribution along the bubble surface at the radial position,  $r = r_b + r_p$ .

Combining the approach of the critical polar angle and the flow field approximation developed by Nguyen et al. [49], (Eq. 2.46) can be simplified as follows. In the case of a mobile bubble surface:

$$Z_{pb}^K = 2\pi \cdot (r_b + r_p)^2 \cdot \left[ N_1 \cdot \frac{1 - \cos^3 \theta_c}{3} + N_2 \cdot \frac{1 - \cos^2 \theta_c}{2} + N_3 \cdot (1 - \cos \theta_c) \right]. \quad (\text{A.93})$$

In the case of an immobile bubble surface:

$$Z_{pb}^K = 2\pi \cdot (r_b + r_p)^2 \cdot \left[ N_1 \cdot \frac{2 - \cos^3 \theta_c + \cos^3 \theta_d}{3} + N_2 \cdot \frac{-\cos^2 \theta_c + \cos^2 \theta_d}{2} + N_3 \cdot (2 - \cos \theta_c + \cos \theta_d) \right]. \quad (\text{A.94})$$

The three components of the relative velocity between the bubble, the particle and the liquid phase, which respectively enter into Eq. 2.46, Eq. A.88, Eq. A.93 and Eq. A.94, are approximated as follows. Each component is computed numerically for several values and fitted to a simple relation.

(i) The total relative velocity between the bubble and the liquid phase,  $|\Delta W_{bl}|$ :

$$|\Delta W_{bl}| = \Phi \cdot V \quad (\text{A.95a})$$

$$\Phi = \begin{cases} 1.6, & \alpha < 0.1 \\ 0.0181 \cdot \alpha^3 + 0.213 \cdot \alpha^2 - 0.1096 \cdot \alpha + 1.584, & 0.1 \leq \alpha < 5 \\ \alpha + \frac{1}{\alpha}, & \alpha \geq 5 \end{cases} \quad (\text{A.95b})$$

$$\alpha = \frac{|\bar{U}|}{V} \quad (\text{A.95c})$$

$$V = Z \cdot W \quad (\text{A.96a})$$

$$\Gamma = \frac{2.625}{\varepsilon} \sqrt{\frac{v \cdot W^5}{r_b^3}} \quad (\text{A.96b})$$

$$Z = \begin{cases} \frac{2}{\sqrt{1+\sqrt{2}\Gamma}}, & \Gamma < 0.01 \\ 0.000356 \cdot \ln^4 \Gamma + 0.005 \cdot \ln^3 \Gamma - 0.0184 \cdot \ln^2 \Gamma - 0.2875 \cdot \ln \Gamma + 1.3582, & 0.01 \leq \Gamma < 100 \\ \left(\frac{4}{\Gamma}\right)^{0.4}, & \Gamma \geq 100 \end{cases} \quad (\text{A.96c})$$

$$W = \sqrt{\frac{k}{1.5}}. \quad (\text{A.96d})$$

(ii) The turbulent relative velocity between the bubble and the particle,  $|\Delta W_{bp}|$ :

$$|\Delta W_{bp}| = 0.103 \cdot r_p \cdot \sqrt{\frac{\varepsilon}{v}} \quad (\text{A.97})$$

(iii) The gravitational relative motion between the particle and the liquid phase,  $|\Delta W_{pl}|$ :

$$|\Delta W_{pl}| = w_s \quad (\text{A.98a})$$

$$f = \begin{cases} \frac{a}{2}, & a < 1 \\ 0.5 + 0.5 \cdot (1 + \exp(-0.85 \cdot (a - 1))), & a \geq 1 \end{cases} \quad (\text{A.98b})$$

For a detailed derivation of this collision frequency model, see Kostoglou et al. [37].

## A.5. Calculation of the values of the box plot

For the visualization of a given sample of a distribution,  $x_1, \dots, x_N$ , the values of the box plot are computed as follows [223]. It is assumed that the values are sorted as  $x_1 < \dots < x_N$ . For any real number,  $p$ , with  $0 \leq p \leq 1$ , the percentile in the order of  $p$  is defined as

$$q(p) = \begin{cases} x_{([N \cdot p + 1])}, & \text{if } N \cdot p \text{ is an integer number} \\ 0.5 \cdot (x_{(N \cdot p)} + x_{(N \cdot p + 1)}), & \text{if } N \cdot p \text{ is not an integer number.} \end{cases} \quad (\text{A.99})$$

The median point,  $q(0.5)$ , is the 50th percentile of the sample data. The 25th,  $q(0.25)$ , and 75th percentile,  $q(0.75)$ , are calculated as described in Eq. A.99. The lower,  $q(0)$ , and upper whisker,  $q(1)$ , are defined as

$$q(0) = q(0.25) - 1.5 \cdot IQR \quad (\text{A.100a})$$

$$q(1) = q(0.75) + 1.5 \cdot IQR \quad (\text{A.100b})$$

with  $IQR = q(0.75) - q(0.25)$  as the interquartile range, which is the difference between 25th and 75th percentile. Every data point outside of the range between lower and upper whisker are classified as outlier.

# Bibliography

- [1] F. Herbert and K. D. Beheng. "Scavenging of airborne particles by collision with water drops – model studies on the combined effect of essential microdynamic mechanisms". In: *Meteorology and Atmospheric Physics* 35.4 (1986), pp. 201–211. DOI: 10.1007/bf01041812.
- [2] J. M. Champney, A. R. Dobrovolskis, and J. N. Cuzzi. "A numerical turbulence model for multiphase flows in the protoplanetary nebula". In: *Physics of Fluids* 7.7 (1995), pp. 1703–1711. DOI: 10.1063/1.868486.
- [3] M. Pinsky, A. Khain, and M. Shapiro. "Stochastic effects of cloud droplet hydrodynamic interaction in a turbulent flow". In: *Atmospheric Research* 53.1-3 (2000), pp. 131–169. DOI: 10.1016/s0169-8095(99)00048-4.
- [4] M. Balthasar, F. Mauss, A. Knobel, and M. Kraft. "Detailed modeling of soot formation in a partially stirred plug flow reactor". In: *Combustion and Flame* 128.4 (2002), pp. 395–409. DOI: 10.1016/s0010-2180(01)00344-3.
- [5] A. Kamp, A. Chesters, C. Colin, and J. Fabre. "Bubble coalescence in turbulent flows: A mechanistic model for turbulence-induced coalescence applied to microgravity bubbly pipe flow". In: *International Journal of Multiphase Flow* 27.8 (2001), pp. 1363–1396. DOI: 10.1016/s0301-9322(01)00010-6.
- [6] G. Narsimhan. "Model for drop coalescence in a locally isotropic turbulent flow field". In: *Journal of Colloid and Interface Science* 272.1 (2004), pp. 197–209. DOI: 10.1016/j.jcis.2003.11.057.
- [7] H. Schubert. "On the turbulence-controlled microprocesses in flotation machines". In: *International Journal of Mineral Processing* 56.1-4 (1999), pp. 257–276. DOI: 10.1016/s0301-7516(98)00048-9.
- [8] D. Deglon. "The effect of agitation on the flotation of platinum ores". In: *Minerals Engineering* 18.8 (2005), pp. 839–844. DOI: 10.1016/j.mineng.2005.01.024.



- [9] S. C. Chelgani, M. Rudolph, T. Leistner, J. Gutzmer, and U. A. Peuker. "A review of rare earth minerals flotation: monazite and xenotime". In: *International Journal of Mining Science and Technology* 25.6 (2015), pp. 877–883. DOI: 10.1016/j.ijmst.2015.09.002.
- [10] C. Marion, R. Li, and K. E. Waters. "A review of reagents applied to rare-earth mineral flotation". In: *Advances in Colloid and Interface Science* 279 (2020), p. 102142. DOI: 10.1016/j.cis.2020.102142.
- [11] B. A. Wills and J. A. Finch. "Chapter 12 - Froth Flotation". In: *Wills' Mineral Processing Technology (Eighth Edition)*. Ed. by B. A. Wills and J. A. Finch. Eighth Edition. Boston: Butterworth-Heinemann, 2016, pp. 265–380. DOI: 10.1016/B978-0-08-097053-0.00012-1.
- [12] M. Mankosa, J. Kohmuench, L. Christodoulou, and E. Yan. "Improving fine particle flotation using the StackCell™ (raising the tail of the elephant curve)". In: *Minerals Engineering* 121 (2018), pp. 83–89. DOI: 10.1016/j.mineng.2018.03.012.
- [13] R. H. Yoon and G. H. Luttrell. "The Effect of Bubble Size on Fine Particle Flotation". In: *Mineral Processing and Extractive Metallurgy Review* 5.1-4 (1989), pp. 101–122. DOI: 10.1080/08827508908952646.
- [14] W. Trahar and L. Warren. "The flotability of very fine particles — A review". In: *International Journal of Mineral Processing* 3.2 (1976), pp. 103–131. DOI: 10.1016/0301-7516(76)90029-6.
- [15] D. Tao. "Role of Bubble Size in Flotation of Coarse and Fine Particles—A Review". In: *Separation Science and Technology* 39.4 (2005), pp. 741–760. DOI: 10.1081/SS-120028444.
- [16] Z. Dai, D. Fornasiero, and J. Ralston. "Particle–Bubble Attachment in Mineral Flotation". In: *Journal of Colloid and Interface Science* 217.1 (1999), pp. 70–76. DOI: 10.1006/jcis.1999.6319.
- [17] H. J. Schulze. "Hydrodynamics of Bubble-Mineral Particle Collisions". In: *Mineral Processing and Extractive Metallurgy Review* 5.1-4 (1989), pp. 43–76. DOI: 10/b4vp6h.
- [18] N. Hooshyar, J. R. van Ommen, P. J. Hamersma, S. Sundaresan, and R. F. Mudde. "Dynamics of Single Rising Bubbles in Neutrally Buoyant Liquid-Solid Suspensions". In: *Physical Review Letters* 110.24 (2013). DOI: 10.1103/physrevlett.110.244501.
- [19] T. Miettinen, J. Ralston, and D. Fornasiero. "The limits of fine particle flotation". In: *Minerals Engineering* 23.5 (2010), pp. 420–437. DOI: 10.1016/j.mineng.2009.12.006.
- [20] S. Farrokhpay, L. Filippov, and D. Fornasiero. "Flotation of Fine Particles: A Review". In: *Mineral Processing and Extractive Metallurgy Review* (2020), pp. 1–11. DOI: 10.1080/08827508.2020.1793140.
- [21] G. J. Jameson. "New directions in flotation machine design". In: *Minerals Engineering* 23.11-13 (2010), pp. 835–841. DOI: 10.1016/j.mineng.2010.04.001.

- [22] J. Dickinson and K. Galvin. "Fluidized bed desliming in fine particle flotation – Part I". In: *Chemical Engineering Science* 108 (2014), pp. 283–298. DOI: 10.1016/j.ces.2013.11.006.
- [23] B. Pyke, D. Fornasiero, and J. Ralston. "Bubble particle heterocoagulation under turbulent conditions". In: *Journal of Colloid and Interface Science* 265.1 (2003), pp. 141–151. DOI: 10.1016/S0021-9797(03)00345-x.
- [24] C. J. Meyer and D. A. Deglon. "Particle collision modeling – A review". In: *Minerals Engineering* 24.8 (2011), pp. 719–730. DOI: 10.1016/j.mineng.2011.03.015.
- [25] L.-P. Wang, A. S. Wexler, and Y. Zhou. "Statistical mechanical description and modelling of turbulent collision of inertial particles". In: *Journal of Fluid Mechanics* 415 (2000), pp. 117–153. DOI: 10.1017/S0022112000008661.
- [26] H. E. Fayed and S. A. Ragab. "Direct Numerical Simulation of Particles-Bubbles Collisions Kernel in Homogeneous Isotropic Turbulence". In: *The Journal of Computational Multiphase Flows* 5.3 (2013), pp. 167–188. DOI: 10.1260/1757-482x.5.3.167.
- [27] Y. Zhou, A. S. Wexler, and L.-P. Wang. "On the collision rate of small particles in isotropic turbulence. II. Finite inertia case". In: *Physics of Fluids* 10.5 (1998), pp. 1206–1216. DOI: 10.1063/1.869644.
- [28] R. Onishi, K. Takahashi, and S. Komori. "Influence of gravity on collisions of monodispersed droplets in homogeneous isotropic turbulence". In: *Physics of Fluids* 21.12 (2009), p. 125108. DOI: 10.1063/1.3276906.
- [29] M. Ernst and M. Sommerfeld. "On the Volume Fraction Effects of Inertial Colliding Particles in Homogeneous Isotropic Turbulence". In: *Journal of Fluids Engineering* 134.3 (2012). DOI: 10.1115/1.4005681.
- [30] A. V. Nguyen and S. Kmeť. "Collision efficiency for fine mineral particles with single bubble in a countercurrent flow regime". In: *International Journal of Mineral Processing* 35.3-4 (1992), pp. 205–223. DOI: 10.1016/0301-7516(92)90034-t.
- [31] D. I. Verrelli, P. T. Koh, and A. V. Nguyen. "Particle–bubble interaction and attachment in flotation". In: *Chemical Engineering Science* 66.23 (2011), pp. 5910–5921. DOI: 10.1016/j.ces.2011.08.016.
- [32] Z. Brabcová, T. Karapantsios, M. Kostoglou, P. Basařová, and K. Matis. "Bubble–particle collision interaction in flotation systems". In: *Colloids and Surfaces A: Physicochemical and Engineering Aspects* 473 (2015), pp. 95–103. DOI: 10.1016/j.colsurfa.2014.11.040.
- [33] G. Lecrivain, G. Petrucci, M. Rudolph, U. Hampel, and R. Yamamoto. "Attachment of Solid Elongated Particles on the Surface of a Stationary Gas Bubble". In: *International Journal of Multiphase Flow* 71 (2015), pp. 83–93. DOI: 10.1016/j.ijmultiphaseflow.2015.01.002.
- [34] S. Li, M. P. Schwarz, W. Yang, Y. Feng, P. Witt, and C. Sun. "Experimental observations of bubble–particle collisional interaction relevant to froth flotation, and calculation of the associated forces". In: *Minerals Engineering* 151 (2020), p. 106335. DOI: 10.1016/j.mineng.2020.106335.

- [35] P. G. Saffman and J. S. Turner. "On the collision of drops in turbulent clouds". In: *Journal of Fluid Mechanics* 1.1 (1956), p. 16. DOI: 10.1017/s0022112056000020.
- [36] J. Abrahamson. "Collision rates of small particles in a vigorously turbulent fluid". In: *Chemical Engineering Science* 30.11 (1975), pp. 1371–1379. DOI: 10.1016/0009-2509(75)85067-6.
- [37] M. Kostoglou, T. D. Karapantsios, and S. Evgenidis. "On a generalized framework for turbulent collision frequency models in flotation: The road from past inconsistencies to a concise algebraic expression for fine particles". In: *Advances in Colloid and Interface Science* 284 (2020), p. 102270. DOI: 10.1016/j.cis.2020.102270.
- [38] A.-E. Sommer, M. Nikpay, S. Heitkam, M. Rudolph, and K. Eckert. "A novel method for measuring flotation recovery by means of 4D particle tracking velocimetry". In: *Minerals Engineering* 124 (2018), pp. 116–122. DOI: 10.1016/j.mineng.2018.05.006.
- [39] A.-E. Sommer, K. Ortmann, M. V. Heerden, T. Richter, T. Leadbeater, K. Cole, S. Heitkam, P. Brito-Parada, and K. Eckert. "Application of Positron Emission Particle Tracking (PEPT) to measure the bubble-particle interaction in a turbulent and dense flow". In: *Minerals Engineering* 156 (2020), p. 106410. DOI: 10.1016/j.mineng.2020.106410.
- [40] A.-E. Sommer, H. Rox, P. Shi, K. Eckert, and R. Rzehak. "Solid-liquid flow in stirred tanks: "CFD-grade" experimental investigation". In: *Chemical Engineering and Science* 245 (2021), p. 116743. DOI: 10.1016/j.ces.2021.116743.
- [41] A.-E. Sommer, S. Heitkam, and K. Eckert. "Particle-bubble collisions in a turbulent flow: an experimental study with 4D Particle Tracking Velocimetry and Tomographic Particle Image Velocimetry". Submitted to *Journal of Fluid Mechanics*. 2021.
- [42] K. Fallenius. "Turbulence in flotation cells". In: *International Journal of Mineral Processing* 21.1-2 (1987), pp. 1–23. DOI: 10.1016/0301-7516(87)90002-0.
- [43] S. B. Pope. *Turbulent flows*. Cambridge: Cambridge Univ. Press, 2011.
- [44] R. Clift, J. R. Grace, and M. E. Weber. *Bubbles, Drops, and Particles (Dover Civil and Mechanical Engineering)*. Dover Publications, 2005.
- [45] J. Magnaudet and I. Eames. "The Motion of High-Reynolds-Number Bubbles in Inhomogeneous Flows". In: *Annual Review of Fluid Mechanics* 32.1 (2000), pp. 659–708. DOI: 10.1146/annurev.fluid.32.1.659.
- [46] A. A. Kulkarni and J. B. Joshi. "Bubble Formation and Bubble Rise Velocity in Gas-Liquid Systems: A Review". In: *Industrial & Engineering Chemistry Research* 44.16 (2005), pp. 5873–5931. DOI: 10.1021/ie049131p.
- [47] C. T. Crowe, J. D. Schwarzkopf, M. Sommerfeld, and Y. Tsuji. *Multiphase flows with drops and bubbles*. Taylor & Francis Ltd., 2011.
- [48] M. Sommerfeld. "Numerical Methods for Dispersed Multiphase Flows". In: *Particles in Flows*. Springer International Publishing, 2017, pp. 327–396. DOI: 10.1007/978-3-319-60282-0\_6.

- [49] A. Nguyen and H. J. Schulze. *Colloidal Science of Flotation (Surfactant Science)*. CRC Press, 2003.
- [50] O. Reynolds. "On the dynamical theory of incompressible viscous fluids and the determination of the criterion". In: *Philosophical Transactions of the Royal Society of London. (A.)* 186 (1895), pp. 123–164. DOI: 10.1098/rsta.1895.0004.
- [51] B. Landers. "Mixing Characteristics of Turbulent Twin Impinging Axisymmetric Jets at Various Impingement Angles". PhD thesis. 2016. DOI: 10.13140/RG.2.1.1028.2482.
- [52] P. Davidson. *Turbulence: An Introduction for Scientists and Engineers*. Oxford University Press, 2015.
- [53] G. Taylor. "Statistical theory of turbulence, I-III". In: *Proceedings of the Royal Society A: Mathematical, Physical and Engineering Sciences* 421–464 (1935).
- [54] L. Richardson and P. Lynch. *Weather Prediction by Numerical Process*. Cambridge Mathematical Library. Cambridge University Press, 1922.
- [55] A. N. Kolmogorov. "The Local Structure of Turbulence in Incompressible Viscous Fluid for Very Large Reynolds Numbers". In: *Doklady Akademii Nauk SSSR* 30 (1941), pp. 299–303. DOI: 10.1098/rspa.1991.0075.
- [56] M. Lesieur. *Turbulence in Fluids*. Springer-Verlag GmbH, 2008.
- [57] T. Kurian and J. H. M. Fransson. "Grid-generated turbulence revisited". In: *Fluid Dynamics Research* 41.2 (2009), p. 021403. DOI: 10.1088/0169-5983/41/2/021403.
- [58] G. Comte-Bellot and S. Corrsin. "Simple Eulerian time correlation of full-and narrow-band velocity signals in grid-generated, 'isotropic' turbulence". In: *Journal of Fluid Mechanics* 48.2 (1971), pp. 273–337. DOI: 10.1017/s0022112071001599.
- [59] M. V. Dyke. *An Album of Fluid Motion*. The Parabolic Press, 1982.
- [60] R. Taghavi-Zenouz, M. Salari, M. M. Tabar, and E. Omid. "Hot-wire anemometry of transitional boundary layers exposed to different freestream turbulence intensities". In: *Proceedings of the Institution of Mechanical Engineers, Part G: Journal of Aerospace Engineering* 222.3 (2008), pp. 347–356. DOI: 10.1243/09544100jaero284.
- [61] V. Strouhal. "Ueber eine besondere Art der Tonerregung". In: *Annalen der Physik und Chemie* 241.10 (1878), pp. 216–251. DOI: 10.1002/andp.18782411005.
- [62] S. Rüttinger, M. Hoffmann, and M. Schlüter. "Experimental Analysis of a Bubble Wake Influenced by a Vortex Street". In: *Fluids* 3 (2018), p. 8. DOI: 10.3390/fluids3010008.
- [63] A. Roshko. "On the Development of Turbulent Wakes from Vortex Streets". In: *Supersedes NACA TN 2913* (1954), pp. 1–20.
- [64] M. V. Morkovin. "Flow around circular cylinder-kaleidoscope of challenging fluid phenomena". In: *Proceedings of the Symposium on Fully Separated Flows, Philadelphia* (1964), pp. 102–18.
- [65] W. Drenckhan and A. Saint-Jalmes. "The science of foaming". In: *Advances in Colloid and Interface Science* 222 (2015), pp. 228–259. DOI: 10.1016/j.cis.2015.04.001.

- [66] J. N. Lin, S. K. Banerji, and H. Yasuda. "Role of Interfacial Tension in the Formation and the Detachment of Air Bubbles. 1. A Single Hole on a Horizontal Plane Immersed in Water". In: *Langmuir* 10.3 (1994), pp. 936–942. DOI: 10.1021/1a00015a054.
- [67] S. Gnyloskurenko, A. Byakova, O. Raychenko, and T. Nakamura. "Influence of wetting conditions on bubble formation at orifice in an inviscid liquid. Transformation of bubble shape and size". In: *Colloids and Surfaces A: Physicochemical and Engineering Aspects* 218.1-3 (2003), pp. 73–87. DOI: 10.1016/s0927-7757(02)00592-7.
- [68] B. R. Jennings and K. Parslow. "Particle size measurement: the equivalent spherical diameter". In: *Proceedings of the Royal Society of London. A. Mathematical and Physical Sciences* 419.1856 (1988), pp. 137–149. DOI: 10.1098/rspa.1988.0100.
- [69] D. Legendre, R. Zenit, and J. R. Velez-Cordero. "On the deformation of gas bubbles in liquids". In: *Physics of Fluids* 24.4 (2012), p. 043303. DOI: 10.1063/1.4705527.
- [70] D. M. Sharaf, A. R. Premlata, M. K. Tripathi, B. Karri, and K. C. Sahu. "Shapes and paths of an air bubble rising in quiescent liquids". In: *Physics of Fluids* 29.12 (2017), p. 122104. DOI: 10.1063/1.5006726.
- [71] H. Mirsandi, W. J. Smit, G. Kong, M. W. Baltussen, E. A. J. F. Peters, and J. A. M. Kuipers. "Influence of wetting conditions on bubble formation from a submerged orifice". In: *Experiments in Fluids* 61.3 (2020). DOI: 10.1007/s00348-020-2919-7.
- [72] P. Basařová and M. Zedníková. "Effect of Surfactants on Bubble-Particle Interactions". In: *Surfactants and Detergents*. IntechOpen, 2019. DOI: 10.5772/intechopen.85436.
- [73] A. de Vries. "Path and wake of a Rising Bubble". PhD thesis. Netherlands, 2001.
- [74] J. Mercier, A. Lyrio, and R. Forslund. "Three-Dimensional Study of the Nonrectilinear Trajectory of Air Bubbles Rising in Water". In: *Journal of Applied Mechanics* 40 (1973), pp. 650–654. DOI: 10.1115/1.3423065.
- [75] J. C. Cano-Lozano, C. Martinez-Bazan, J. Magnaudet, and J. Tchoufag. "Paths and wakes of deformable nearly spheroidal rising bubbles close to the transition to path instability". In: *Physical Review Fluids* 1 (2016), p. 053604. DOI: 10.1103/PhysRevFluids.1.0536.
- [76] M. Wu and M. Gharib. "Experimental studies on the shape and path of small air bubbles rising in clean water". In: *Physics of Fluids* 14.7 (2002), p. L49. DOI: 10.1063/1.1485767.
- [77] W. L. Haberman and R. K. Morton. *An Experimental Investigation of the Drag and Shape of Air Bubbles Rising in Various Liquids*. Washington, D.C.: David W. Taylor Model Basin, 1953.
- [78] R. A. Hartunian and W. R. Sears. "On the instability of small gas bubbles moving uniformly in various liquids". In: *Journal of Fluid Mechanics* 3.1 (1957), pp. 27–47. DOI: 10.1017/s0022112057000464.
- [79] P. G. Saffman. "On the rise of small air bubbles in water". In: *Journal of Fluid Mechanics* 1 (1956), pp. 249–275. DOI: 10.1017/s0022112056000159.

- [80] P. C. Duineveld. "The rise velocity and shape of bubbles in pure water at high Reynolds number". In: *Journal of Fluid Mechanics* 292 (1995), pp. 325–332. DOI: 10.1017/s0022112095001546.
- [81] F. Mugele and J. Heikenfeld. *Electrowetting - Fundamental Principles and Practical Applications*. New York: John Wiley & Sons, 2019.
- [82] M. A. Cabrerizo-Vilchez, J. R. Fernández, M. A. Fernández-Rodríguez, L. García-Río, M. C. Muñoz, and C. Núñez. "Interfacial tension measurements using a new axisymmetric drop/bubble shape technique". In: *RSC Advances* 9.28 (2019), pp. 16187–16194. DOI: 10.1039/c9ra00940j.
- [83] P. Cheng, D. Li, L. Boruvka, Y. Rotenberg, and A. Neumann. "Automation of axisymmetric drop shape analysis for measurements of interfacial tensions and contact angles". In: *Colloids and Surfaces* 43.2 (1990), pp. 151–167. DOI: 10.1016/0166-6622(90)80286-D.
- [84] O. Río and A. Neumann. "Axisymmetric Drop Shape Analysis: Computational Methods for the Measurement of Interfacial Properties from the Shape and Dimensions of Pendant and Sessile Drops". In: *Journal of Colloid and Interface Science* 196.2 (1997), pp. 136–147. DOI: 10.1006/jcis.1997.5214.
- [85] F. Skinner, Y. Rotenberg, and A. Neumann. "Contact angle measurements from the contact diameter of sessile drops by means of a modified axisymmetric drop shape analysis". In: *Journal of Colloid and Interface Science* 130.1 (1989), pp. 25–34. DOI: 10.1016/0021-9797(89)90074-X.
- [86] H. Schlichting and K. Gersten. "Fundamentals of Boundary-Layer Theory". In: *Boundary-Layer Theory*. Springer Berlin Heidelberg, 2016, pp. 29–49. DOI: 10.1007/978-3-662-52919-5\_2.
- [87] S. Rüttinger. *Investigation of the influence of vortex structures on transport processes at fluidic interfaces*. Göttingen: Cuvillier Verlag, 2018.
- [88] I. Komazawa, T. Otake, and M. Kamojima. "Wake Behavior And Its Effect On Interaction Between Spherical-cap Bubbles". In: *Journal Of Chemical Engineering Of Japan* 13 (1980), pp. 103–109.
- [89] L.-S. Fan and K. Tsuchiya. *Bubble Wake Dynamics in Liquids and Liquid-Solid Suspensions (Butterworth-Heinemann Series in Chemical Engineering)*. Butterworth-Heinemann, 2013.
- [90] G. Mougin and J. Magnaudet. "Path Instability of a Rising Bubble". In: *Physical Review Letters* 88 (2002), p. 014502. DOI: 10.1103/PhysRevLett.88.014502.
- [91] A. Blanco and J. Magnaudet. "The structure of the axisymmetric high-Reynolds number flow around an ellipsoidal bubble of fixed shape". In: *Physics of Fluids* 7.6 (1995), pp. 1265–1274. DOI: 10.1063/1.868515.
- [92] S. Li, K. Jue, and C. Sun. "Effect of Bubble Surface Properties on Bubble-Particle Collision Efficiency in Froth Flotation". In: *Minerals* 10.4 (2020), p. 367. DOI: 10.3390/min10040367.

- [93] W. Abbassi, S. Besbes, H. B. Aissia, and J. Y. Champagne. "Study of the rise of a single/multiple bubbles in quiescent liquids using the VOF method". In: *Journal of the Brazilian Society of Mechanical Sciences and Engineering* 41.6 (2019). DOI: 10.1007/s40430-019-1759-y.
- [94] M. Gumulya, R. Utikar, G. Evans, J. Joshi, and V. Pareek. "Interaction of bubbles rising inline in quiescent liquid". In: *Chemical Engineering Science* 166 (2017), pp. 1–10. DOI: 10.1016/j.ces.2017.03.013.
- [95] M. Watanabe and T. Sanada. "In-Line Motion of a Pair of Bubbles in a Viscous Liquid". In: *JSME International Journal Series B* 49.2 (2006), pp. 410–418. DOI: 10.1299/jsmeb.49.410.
- [96] K. Lunde and R. J. Perkins. "Shape Oscillations of Rising Bubbles". In: *Applied Scientific Research* 58.1/4 (1997), pp. 387–408. DOI: 10.1023/a:1000864525753.
- [97] V. V. Buwa, D. Gerlach, F. Durst, and E. Schlücker. "Numerical simulations of bubble formation on submerged orifices: Period-1 and period-2 bubbling regimes". In: *Chemical Engineering Science* 62.24 (2007), pp. 7119–7132. DOI: 10.1016/j.ces.2007.08.061.
- [98] C. Brücker. "Structure and dynamics of the wake of bubbles and its relevance for bubble interaction". In: *Physics of Fluids* 11.7 (1999), pp. 1781–1796. DOI: 10.1063/1.870043.
- [99] S. Banisi, J. A. Finch, A. R. Laplante, and M. E. Weber. "Effect of Solid Particles on Gas Holdup in Flotation Columns—II. Investigation of Mechanisms of Gas Holdup Reduction in Presence of Solids". In: *Chemical Engineering Science* 50.14 (1995), pp. 2335–2342. DOI: 10.1016/0009-2509(95)00076-H.
- [100] T. Miyahara, K. Tsuchiya, and L.-S. Fan. "Effect of turbulent wake on bubble—bubble interaction in a gas—liquid—solid fluidized bed". In: *Chemical Engineering Science* 46.9 (1991), pp. 2368–2373. DOI: 10.1016/0009-2509(91)85137-m.
- [101] H. Kusuno and T. Sanada. "Wake-induced lateral migration of approaching bubbles". In: *International Journal of Multiphase Flow* 139 (2021), p. 103639. DOI: 10.1016/j.ijmultiphaseflow.2021.103639.
- [102] L. Miller. *Bubble and Drop Interfaces (Progress in Colloid and Interface Science)*. CRC Press, 2011.
- [103] H. Schulze. "Probability of particle attachment on gas bubbles by sliding". In: *Advances in Colloid and Interface Science* 40 (1992), pp. 283–305. DOI: 10.1016/0001-8686(92)80079-d.
- [104] R. Miller, P. Joos, and V. B. Fainerman. "Dynamic surface and interfacial tensions of surfactant and polymer solutions". In: *Advances in Colloid and Interface Science* 49 (1994), pp. 249–302. DOI: 10.1016/0001-8686(94)80017-0.
- [105] C.-H. Chang and E. I. Franses. "Adsorption dynamics of surfactants at the air/water interface: a critical review of mathematical models, data, and mechanisms". In: *Colloids and Surfaces A: Physicochemical and Engineering Aspects* 100 (1995), pp. 1–45. DOI: 10.1016/0927-7757(94)03061-4.

- [106] R. Miller, E. Aksenenko, and V. Fainerman. "Dynamic interfacial tension of surfactant solutions". In: *Advances in Colloid and Interface Science* 247 (2017), pp. 115–129. DOI: 10.1016/j.cis.2016.12.007.
- [107] M. Fukuta, S. Takagi, and Y. Matsumoto. "Numerical study on the shear-induced lift force acting on a spherical bubble in aqueous surfactant solutions". In: *Physics of Fluids* 20.4 (2008), p. 040704. DOI: 10.1063/1.2911040.
- [108] C. D. Eggleton, Y. P. Pawar, and K. J. Stebe. "Insoluble surfactants on a drop in an extensional flow: a generalization of the stagnated surface limit to deforming interfaces". In: *Journal of Fluid Mechanics* 385 (1999), pp. 79–99. DOI: 10.1017/s0022112098004054.
- [109] M. Eftekhari, K. Schwarzenberger, S. Heitkam, and K. Eckert. "Interfacial flow of a surfactant-laden interface under asymmetric shear flow". In: *Journal of Colloid and Interface Science* 599 (2021), pp. 837–848. DOI: 10.1016/j.jcis.2021.04.126.
- [110] Y. Tagawa, S. Takagi, and Y. Matsumoto. "Surfactant effect on path instability of a rising bubble". In: *Journal of Fluid Mechanics* 738 (2014), pp. 124–142. DOI: 10.1017/jfm.2013.571.
- [111] R. Gatignol. "The Faxén formulae for a rigid particle in an unsteady non-uniform Stokes flow". In: *Journal de Mécanique Théorique et Appliquée* 1 (0750-7240 1983), pp. 143–160.
- [112] M. R. Maxey. "Equation of motion for a small rigid sphere in a nonuniform flow". In: *Physics of Fluids* 26.4 (1983), p. 883. DOI: 10.1063/1.864230.
- [113] J. Magnaudet. "The forces acting on bubbles and rigid particles". In: *Proceedings of ASME Fluids Engineering Summer Meeting*. Vol. 3522. 1997.
- [114] H. Kürten, J. Raasch, and H. Rumpf. "Beschleunigung eines kugelförmigen Feststoffteilchens im Strömungsfeld konstanter Geschwindigkeit". In: *Chemie Ingenieur Technik* 38 (1966), pp. 941–948. DOI: 10.1002/cite.330380905.
- [115] L. Schiller and A. Naumann. "About the basic calculations in gravity processing". In: *Zeitschrift des Vereines deutscher Ingenieure* 77 (1933), pp. 318–321.
- [116] L. Tang, F. Wen, Y. Yang, C. T. Crowe, J. N. Chung, and T. R. Troutt. "Self-organizing particle dispersion mechanism in a plane wake". In: *Physics of Fluids A: Fluid Dynamics* 4.10 (1992), pp. 2244–2251. DOI: 10.1063/1.858465.
- [117] H. Martin. "A2 Dimensionslose Kenngrößen". In: *VDI-Wärmeatlas*. Berlin, Heidelberg: Springer Berlin Heidelberg, 2013, pp. 13–18. DOI: 10.1007/978-3-642-19981-3\_2.
- [118] S. Flows and M. Sommerfeld. *Best Practice Guidelines for Computational Fluid Dynamics of Dispersed Multi-Phase Flows*. European Research Community on Flow, Turbulence and Combustion (ERCOFTAC), 2008.
- [119] G. V. Messa, Q. Yang, O. E. Adedeji, Z. Chára, C. A. R. Duarte, V. Matoušek, M. G. Rasteiro, R. S. Sanders, R. C. Silva, and F. J. de Souza. "Computational Fluid Dynamics Modelling of Liquid–Solid Slurry Flows in Pipelines: State-of-the-Art and Future Perspectives". In: *Processes* 9.9 (2021). DOI: 10.3390/pr9091566.



- [120] C. T. Crowe. "On models for turbulence modulation in fluid-particle flows". In: *International Journal of Multiphase Flow* 26.5 (2000), pp. 719–727. DOI: 10.1016/S0301-9322(99)00050-6.
- [121] G. Montante, A. Paglianti, and F. Magelli. "Analysis of dilute solid-liquid suspensions in turbulent stirred tanks". In: *Chemical Engineering Research and Design* 90.10 (2012), pp. 1448–1456. DOI: 10.1016/j.cherd.2012.01.009.
- [122] H. Unadkat, C. Rielly, G. Hargrave, and Z. Nagy. "Application of fluorescent PIV and digital image analysis to measure turbulence properties of solid-liquid stirred suspensions". In: *Chemical Engineering Research and Design* 87.4 (2009), pp. 573–586. DOI: 10.1016/j.cherd.2008.11.011.
- [123] A. Gabriele, A. Tsofigkas, I. Kings, and M. Simmons. "Use of PIV to measure turbulence modulation in a high throughput stirred vessel with the addition of high Stokes number particles for both up-and down-pumping configurations". In: *Chemical Engineering Science* 66.23 (2011), pp. 5862–5874. DOI: 10.1016/j.ces.2011.08.007.
- [124] S. Hosokawa and A. Tomiyama. "Turbulence modification in gas-liquid and solid-liquid dispersed two-phase pipe flows". In: *International Journal of Heat and Fluid Flow* 25.3 (2004), pp. 489–498. DOI: 10.1016/j.ijheatfluidflow.2004.02.001.
- [125] T. Tanaka and J. K. Eaton. "Classification of turbulence modification by dispersed spheres using a novel dimensionless number". In: *Physical Review Letters* 101.11 (2008), p. 114502. DOI: 10.1103/PhysRevLett.101.114502.
- [126] S. Balachandar and J. K. Eaton. "Turbulent Dispersed Multiphase Flow". In: *Annual Review of Fluid Mechanics* 42.1 (2010), pp. 111–133. DOI: 10.1146/annurev.fluid.010908.165243.
- [127] A. Esteghamatian and T. A. Zaki. "The dynamics of dense particles in vertical channel flows: gravity, lift and particle clusters". In: *Journal of Fluid Mechanics* 918 (2021). DOI: 10.1017/jfm.2021.304.
- [128] A. Mühlbauer, M. W. Hlawitschka, and H.-J. Bart. "Models for the Numerical Simulation of Bubble Columns: A Review". In: *Chemie Ingenieur Technik* 91.12 (2019), pp. 1747–1765. DOI: 10.1002/cite.201900109.
- [129] M. Schlüter, S. Scheid, S. John, and N. Rübiger. "Fluidization of Fluid Particles in Bubble Wakes Affects Hydrodynamics in Three-Phase Flows". In: *Journal of Chemical Engineering of Japan* 37.8 (2004), pp. 947–954. DOI: 10.1252/jcej.37.947.
- [130] M. Schlüter, S. Scheid, S. John, and N. Rübiger. "Influence of local effects in three phase flows on power input in Jet-Loop Reactors". In: *Powder Technology* 151.1-3 (2005), pp. 68–76. DOI: 10.1016/j.powtec.2004.11.032.
- [131] B. Wang and Y. Peng. "The effect of saline water on mineral flotation – A critical review". In: *Minerals Engineering* 66-68 (2014), pp. 13–24. DOI: 10.1016/j.mineng.2014.04.017.
- [132] Y. Xing, M. Xu, X. Gui, Y. Cao, M. Rudolph, H.-J. Butt, and M. Kappl. "The role of surface forces in mineral flotation". In: *Current Opinion in Colloid & Interface Science* 44 (2019), pp. 143–152. DOI: 10.1016/j.cocis.2019.11.005.

- [133] A. V. Nguyen, D.-A. An-Vo, T. Tran-Cong, and G. M. Evans. "A review of stochastic description of the turbulence effect on bubble-particle interactions in flotation". In: *International Journal of Mineral Processing* 156 (2016), pp. 75–86. DOI: 10.1016/j.minpro.2016.05.002.
- [134] Z. Dai, D. Fornasiero, and J. Ralston. "Particle–bubble collision models — a review". In: *Advances in Colloid and Interface Science* 85.2-3 (2000), pp. 231–256. DOI: 10.1016/S0001-8686(99)00030-5.
- [135] J. Ralston, S. Dukhin, and N. Mishchuk. "Wetting film stability and flotation kinetics". In: *Advances in Colloid and Interface Science* 95.2-3 (2002), pp. 145–236. DOI: 10.1016/S0001-8686(00)00083-x.
- [136] M. Kostoglou, T. D. Karapantsios, and O. Oikonomidou. "A critical review on turbulent collision frequency/efficiency models in flotation: Unravelling the path from general coagulation to flotation". In: *Advances in Colloid and Interface Science* 279 (2020), p. 102158. DOI: 10.1016/j.cis.2020.102158.
- [137] D. Hewitt, D. Fornasiero, and J. Ralston. "Bubble–particle attachment". In: *Journal of the Chemical Society, Faraday Transactions* 91.13 (1995), pp. 1997–2001. DOI: 10.1039/ft9959101997.
- [138] J. Anfruns and J. Kitchener. "Rate of capture of small particles in flotation". In: *Transactions of the Institution of Mining and Metallurgy Sect. C* 86 (1977), pp. C9–C15.
- [139] H. J. Schulze. *Physikalisch-chemische Elementarvorgänge des Flotationsprozesses: eine Analyse aus kolloidwissenschaftlicher Sicht*. Deutscher Verlag der Wissenschaften, 1981.
- [140] J. Ralston, S. Dukhin, and N. Mishchuk. "Inertial hydrodynamic particle - bubble interaction in flotation". In: *International Journal of Mineral Processing* 56.1-4 (1999), pp. 207–256. DOI: 10.1016/S0301-7516(98)00049-0.
- [141] D. Whelan P.F. ; Brown. "Particle-bubble attachment in froth flotation". In: *Bulletin of the American Institute of Mining and Metallurgical Engineers* 591 (1956), pp. 181–192.
- [142] T. Ziegenhein, J. Zalucky, R. Rzehak, and D. Lucas. "On the Hydrodynamics of Airlift Reactors, Part I: Experiments". In: *Chemical Engineering Science* 150 (2016), pp. 54–65. DOI: 10.1016/j.ces.2016.04.039.
- [143] K. Haase, U. D. Kück, J. Thöming, and C. J. Kähler. "Emulation of Bubble-Induced Turbulence Using Randomly Moving Particles in a Grid Structure". In: *Chemical Engineering & Technology* 40.8 (2017), pp. 1502–1511. DOI: 10.1002/ceat.201600687.
- [144] A. Tokuhira, M. Maekawa, K. Iizuka, K. Hishida, and M. Maeda. "Turbulent flow past a bubble and an ellipsoid using shadow-image and PIV techniques". In: *International Journal of Multiphase Flow* 24.8 (1998), pp. 1383–1406. DOI: 10.1016/S0301-9322(98)00024-x.
- [145] M. Raffel, C. E. Willert, F. Scarano, C. J. Kähler, S. T. Wereley, and J. Kompenhans. *Particle Image Velocimetry: A Practical Guide (Experimental Fluid Mechanics)*. Springer, 2018.

- [146] F. Scarano. "Tomographic PIV: principles and practice". In: *Measurement Science and Technology* 24.1 (2012), p. 012001. DOI: 10.1088/0957-0233/24/1/012001.
- [147] G. T. Herman and A. Lent. "Iterative reconstruction algorithms". In: *Computers in Biology and Medicine* 6.4 (1976), pp. 273–294. DOI: 10.1016/0010-4825(76)90066-4.
- [148] G. E. Elsinga, F. Scarano, B. Wieneke, and B. W. van Oudheusden. "Tomographic particle image velocimetry". In: *Experiments in Fluids* 41.6 (2006), pp. 933–947. DOI: 10.1007/s00348-006-0212-z.
- [149] B. Wieneke. "Volume self-calibration for 3D particle image velocimetry". In: *Experiments in Fluids* 45.4 (2008), pp. 549–556. DOI: 10.1007/s00348-008-0521-5.
- [150] F. Scarano. "Iterative image deformation methods in PIV". In: *Measurement Science and Technology* 13.1 (2001), R1–R19. DOI: 10.1088/0957-0233/13/1/201.
- [151] M. Samimy and S. K. Lele. "Motion of particles with inertia in a compressible free shear layer". In: *Physics of Fluids A: Fluid Dynamics* 3.8 (1991), pp. 1915–1923. DOI: 10.1063/1.857921.
- [152] R. Lindken and W. Merzkirch. "A novel PIV technique for measurements in multiphase flows and its application to two-phase bubbly flows". In: *Experiments in Fluids* 33.6 (2002), pp. 814–825. DOI: 10.1007/s00348-002-0500-1.
- [153] H. G. Maas, A. Gruen, and D. Papantoniou. "Particle tracking velocimetry in three-dimensional flows". In: *Experiments in Fluids* 15.2 (1993), pp. 133–146. DOI: 10.1007/bf00190953.
- [154] S. Tokgoz, G. E. Elsinga, R. Delfos, and J. Westerweel. "Spatial resolution and dissipation rate estimation in Taylor–Couette flow for tomographic PIV". In: *Experiments in Fluids* 53.3 (2012), pp. 561–583. DOI: 10.1007/s00348-012-1311-7.
- [155] G. I. Taylor. "The Spectrum of Turbulence". In: *Proceedings of the Royal Society A: Mathematical, Physical and Engineering Sciences* 164.919 (1938), pp. 476–490. DOI: 10.1098/rspa.1938.0032.
- [156] J. Ortiz-Villafuerte, W. D. Schmidl, and Y. A. Hassan. "Three-dimensional ptv study of the surrounding flow and wake of a bubble rising in a stagnant liquid". In: *Experiments in Fluids* 29.7 (2000), S202–S210. DOI: 10.1007/s003480070022.
- [157] D. Bröder and M. Sommerfeld. "Planar shadow image velocimetry for the analysis of the hydrodynamics in bubbly flows". In: *Measurement Science and Technology* 18.8 (2007), pp. 2513–2528. DOI: 10.1088/0957-0233/18/8/028.
- [158] A. Sciacchitano and B. Wieneke. "PIV uncertainty propagation". In: *Measurement Science and Technology* 27.8 (2016), p. 084006. DOI: 10.1088/0957-0233/27/8/084006.
- [159] J. M. Foucaut, J. Carlier, and M. Stanislas. "PIV optimization for the study of turbulent flow using spectral analysis". In: *Measurement Science and Technology* 15.6 (2004), pp. 1046–1058. DOI: 10.1088/0957-0233/15/6/003.

- [160] C. Atkinson, S. Coudert, J.-M. Foucaut, M. Stanislas, and J. Soria. "The accuracy of tomographic particle image velocimetry for measurements of a turbulent boundary layer". In: *Experiments in Fluids* 50.4 (2010), pp. 1031–1056. DOI: 10.1007/s00348-010-1004-z.
- [161] G. E. Elsinga, J. Westerweel, F. Scarano, and M. Novara. "On the Velocity of Ghost Particles and the Bias Errors in Tomographic-PIV". In: *Experiments in Fluids* 50.4 (2011), pp. 825–838. DOI: 10.1007/s00348-010-0930-0.
- [162] K. P. Lynch and F. Scarano. "Experimental determination of tomographic PIV accuracy by a 12-camera system". In: *Measurement Science and Technology* 25.8 (2014), p. 084003. DOI: 10.1088/0957-0233/25/8/084003.
- [163] R. J. Adrian. "Particle-Imaging Techniques for Experimental Fluid Mechanics". In: *Annual Review of Fluid Mechanics* 23.1 (1991), pp. 261–304. DOI: 10.1146/annurev.fl.23.010191.001401.
- [164] T. Dracos, ed. *Three-Dimensional Velocity and Vorticity Measuring and Image Analysis Techniques*. Springer Netherlands, 1996. DOI: 10.1007/978-94-015-8727-3.
- [165] F. Ahmadi, M. Ebrahimian, R. S. Sanders, and S. Ghaemi. "Particle image and tracking velocimetry of solid-liquid turbulence in a horizontal channel flow". In: *International Journal of Multiphase Flow* 112 (2019), pp. 83–99. DOI: 10.1016/j.ijmultiphaseflow.2018.12.007.
- [166] M. Ebrahimian, R. Sean Sanders, and S. Ghaemi. "Dynamics and wall collision of inertial particles in a solid-liquid turbulent channel flow". In: *Journal of Fluid Mechanics* 881 (2019), pp. 872–905. DOI: 10.1017/jfm.2019.749.
- [167] T. Berk and F. Coletti. "Dynamics of small heavy particles in homogeneous turbulence: a Lagrangian experimental study". In: *Journal of Fluid Mechanics* 917 (2021), A47. DOI: 10.1017/jfm.2021.280.
- [168] W. Brevis, Y. Niño, and G. H. Jirka. "Integrating cross-correlation and relaxation algorithms for particle tracking velocimetry". In: *Experiments in Fluids* 50.1 (2010), pp. 135–147. DOI: 10.1007/s00348-010-0907-z.
- [169] C. Cierpka, B. Lütke, and C. J. Kähler. "Higher order multi-frame particle tracking velocimetry". In: *Experiments in Fluids* 54.5 (2013). DOI: 10.1007/s00348-013-1533-3.
- [170] D. Schanz, S. Gesemann, and A. Schröder. "Shake-The-Box: Lagrangian particle tracking at high particle image densities". In: *Experiments in Fluids* 57.5 (2016), p. 70. DOI: 10.1007/s00348-016-2157-1.
- [171] B. Wieneke. "Iterative reconstruction of volumetric particle distribution". In: *Measurement Science and Technology* 24.2 (2012), p. 024008. DOI: 10.1088/0957-0233/24/2/024008.
- [172] D. Schanz, S. Gesemann, A. Schröder, B. Wieneke, and M. Novara. "Non-Uniform Optical Transfer Functions in Particle Imaging: Calibration and Application to Tomographic Reconstruction". In: *Measurement Science and Technology* 24.2 (2013), p. 024009. DOI: 10.1088/0957-0233/24/2/024009.

- [173] T. Young. "An Essay on the Cohesion of Fluids". In: *Philosophical Transactions of the Royal Society of London* 95 (1805), pp. 65–87. DOI: 10.1098/rstl.1805.0005.
- [174] E. G. Shafrin and W. A. Zisman. "Constitutive relations in the wetting of low energy surfaces and the theory of the retraction method of preparing monolayers". In: *The Journal of Physical Chemistry* 64.5 (1960), pp. 519–524. DOI: 10.1021/j100834a002.
- [175] E. W. Washburn. "The Dynamics of Capillary Flow". In: *Physical Review* 17.3 (1921), pp. 273–283. DOI: 10.1103/physrev.17.273.
- [176] N. A. Malik, T. Dracos, and D. A. Papantoniou. "Particle tracking velocimetry in three-dimensional flows". In: *Experiments in Fluids* 15-15.4-5 (1993), pp. 279–294. DOI: 10.1007/bf00223406.
- [177] K. E. Waters, N. A. Rowson, X. Fan, and J. J. Cilliers. "Following the path of hydrophobic and hydrophilic particles in a Denver Cell using positron emission particle tracking". In: *Asia-Pacific Journal of Chemical Engineering* 4.2 (2009), pp. 218–225. DOI: 10.1002/apj.224.
- [178] D. Parker, C. Broadbent, P. Fowles, M. Hawkesworth, and P. McNeil. "Positron emission particle tracking - a technique for studying flow within engineering equipment". In: *Nuclear Instruments and Methods in Physics Research Section A: Accelerators, Spectrometers, Detectors and Associated Equipment* 326.3 (1993), pp. 592–607. DOI: 10.1016/0168-9002(93)90864-e.
- [179] T. W. Leadbeater, D. J. Parker, and J. Gargiuli. "Positron imaging systems for studying particulate, granular and multiphase flows". In: *Particuology* 10.2 (2012), pp. 146–153. DOI: 10.1016/j.partic.2011.09.006.
- [180] D. Boucher, A. Jordens, J. Sovechles, R. Langlois, T. W. Leadbeater, N. A. Rowson, J. J. Cilliers, and K. E. Waters. "Direct mineral tracer activation in positron emission particle tracking of a flotation cell". In: *Minerals Engineering* 100 (2017), pp. 155–165. DOI: 10.1016/j.mineng.2016.10.022.
- [181] K. Cole, A. Buffler, N. van der Meulen, J. Cilliers, J.-P. Franzidis, I. Govender, C. Liu, and M. van Heerden. "Positron emission particle tracking measurements with 50 micron tracers". In: *Chemical Engineering Science* 75 (2012), pp. 235–242. DOI: 10.1016/j.ces.2012.02.053.
- [182] K. Waters, N. Rowson, X. Fan, D. Parker, and J. Cilliers. "Positron emission particle tracking as a method to map the movement of particles in the pulp and froth phases". In: *Minerals Engineering* 21.12-14 (2008), pp. 877–882. DOI: 10.1016/j.mineng.2008.02.007.
- [183] K. Cole, K. Waters, X. Fan, S. Neethling, and J. Cilliers. "Combining Positron Emission Particle Tracking and image analysis to interpret particle motion in froths". In: *Minerals Engineering* 23.11-13 (2010), pp. 1036–1044. DOI: 10.1016/j.mineng.2010.05.012.

- [184] M. Maučec, R. Dusterhoft, R. Rickman, R. Gibson, A. Buffler, M. Stankiewicz, and M. van Heerden. "Dynamic Imaging of Fluid Mobility in Low-Permeability Matrices Using Positron Emission Tomography". In: *Unconventional Resources Technology Conference, Denver, Colorado, 12-14 August 2013*. Society of Exploration Geophysicists, American Association of Petroleum Geologists, Society of Petroleum Engineers, 2013. DOI: 10.1190/urtec2013-161.
- [185] E. R. Davies. *Machine Vision: Theory, Algorithms, Practicalities (Signal Processing and its Applications)*. Morgan Kaufmann, 2004.
- [186] H. K. Yuen, J. Princen, J. Illingworth, and J. Kittler. "Comparative study of Hough Transform methods for circle finding". In: *Image Vision Comput.* 8 (1990), pp. 71–77. DOI: 10.1016/0262-8856(90)90059-E.
- [187] K. Cole, A. Buffler, J. Cilliers, I. Govender, J. Heng, C. Liu, D. Parker, U. Shah, M. van Heerden, and X. Fan. "A surface coating method to modify tracers for positron emission particle tracking (PEPT) measurements of froth flotation". In: *Powder Technology* 263 (2014), pp. 26–30. DOI: 10.1016/j.powtec.2014.04.083.
- [188] J. M. Sovechles, D. Boucher, R. Pax, T. Leadbeater, A. P. Sasmito, and K. E. Waters. "Performance analysis of a new positron camera geometry for high speed, fine particle tracking". In: *Measurement Science and Technology* 28.9 (2017), p. 095402. DOI: 10.1088/1361-6501/aa7dce.
- [189] A. Buffler, K. Cole, T. Leadbeater, and M. van Heerden. "Positron emission particle tracking: A powerful technique for flow studies". In: *International Journal of Modern Physics: Conference Series* 48 (2018), p. 1860113. DOI: 10.1142/s2010194518601138.
- [190] A. Buffler, I. Govender, J. J. Cilliers, D. J. Parker, J.-P. Franzidis, A. Mainza, R. T. Newman, M. Powell, and A. V. D. Westhuizen. "PEPT Cape Town: a new positron emission particle tracking facility at iThemba LABS". In: *Proceedings of International Topical Meeting on Nuclear Research Applications and Utilization of Accelerators*. Vol. 173. 2009.
- [191] K. Cole, K. Waters, D. Parker, S. Neethling, and J. Cilliers. "PEPT combined with high speed digital imaging for particle tracking in dynamic foams". In: *Chemical Engineering Science* 65.5 (2010), pp. 1887–1890. DOI: 10.1016/j.ces.2009.10.010.
- [192] A. Buffler, I. Govender, J. Cilliers, D. Parker, J.-P. Franzidis, A. Mainza, A. P. V. der Westhuizen, R. Newman, and M. Powell. "A new positron emission particle tracking facility at iThemba LABS". In: *International Atomic Energy Agency* 41 (47 2010).
- [193] D. J. Parker and X. Fan. "Positron emission particle tracking—Application and labelling techniques". In: *Particuology* 6.1 (2008), pp. 16–23. DOI: 10.1016/j.cpart.2007.10.004.
- [194] J. Magnaudet and G. Mougin. "Wake instability of a fixed spheroidal bubble". In: *Journal of Fluid Mechanics* 572 (2007), p. 311. DOI: 10.1017/S0022112006003442.
- [195] C. H. K. Williamson. "Vortex Dynamics in the Cylinder Wake". In: *Annual Review of Fluid Mechanics* 28.1 (1996), pp. 477–539. DOI: 10.1146/annurev.fl.28.010196.002401.

- [196] S. Rüttinger, M. Hoffmann, and M. Schlüter. "How Do Vortex Structures Influence Boundary Layer Dynamics in Gas-Liquid Systems?" In: *Chemical Engineering & Technology* 42.7 (2019), pp. 1421–1426. DOI: 10.1002/ceat.201900035.
- [197] S. Li, K. J., and C. Sun. "Effect of Bubble Surface Properties on Bubble-Particle Collision Efficiency in Froth Flotation". In: *Minerals* 10.4 (2020), p. 367. DOI: 10.3390/min10040367.
- [198] G. Hetsroni. "Particles-turbulence interaction". In: *International Journal of Multiphase Flow* 15.5 (1989), pp. 735–746. DOI: 10.1016/0301-9322(89)90037-2.
- [199] J. Meng, W. Xie, M. Brennan, K. Runge, and D. Bradshaw. "Measuring turbulence in a flotation cell using the piezoelectric sensor". In: *Minerals Engineering* 66-68 (2014), pp. 84–93. DOI: 10.1016/j.mineng.2014.06.007.
- [200] E. Tabosa, K. Runge, and P. Holtham. "The effect of cell hydrodynamics on flotation performance". In: *Sustainable Minerals Institute, The University of Queensland*. 156 (2016), pp. 99–107. DOI: 10.1016/j.minpro.2016.05.019.
- [201] J. Meng, E. Tabosa, W. Xie, K. Runge, D. Bradshaw, and E. Manlapig. "A review of turbulence measurement techniques for flotation". In: *Minerals Engineering* 95 (2016), pp. 79–95. DOI: 10.1016/j.mineng.2016.06.007.
- [202] S. Sherif. "On the propagation of random errors of constant-temperature anemometers in nonisothermal flows". In: *Measurement* 22.3-4 (1997), pp. 75–86. DOI: 10.1016/s0263-2241(97)00069-9.
- [203] E. Amini, D. Bradshaw, J. Finch, and M. Brennan. "Influence of turbulence kinetic energy on bubble size in different scale flotation cells". In: *Minerals Engineering* 45 (2013), pp. 146–150. DOI: 10.1016/j.mineng.2013.01.015.
- [204] A.-E. Sommer, S. Heitkam, and K. Eckert. "Example videos of particles colliding with a rising bubble". In: (2020). DOI: 10.14278/rodare.610.
- [205] Z. Dai, S. Dukhin, D. Fornasiero, and J. Ralston. "The Inertial Hydrodynamic Interaction of Particles and Rising Bubbles with Mobile Surfaces". In: *Journal of Colloid and Interface Science* 197.2 (1998), pp. 275–292. DOI: 10.1006/jcis.1997.5280.
- [206] T. Jahn, D. Schanz, and A. Schröder. "Advanced iterative particle reconstruction for Lagrangian particle tracking". In: 62.8 (2021). DOI: 10.1007/s00348-021-03276-7.
- [207] X. Fan, D. Parker, and M. Smith. "Enhancing  $^{18}\text{F}$  uptake in a single particle for positron emission particle tracking through modification of solid surface chemistry". In: *Nuclear Instruments and Methods in Physics Research Section A: Accelerators, Spectrometers, Detectors and Associated Equipment* 558.2 (2006), pp. 542–546. DOI: 10.1016/j.nima.2005.12.186.
- [208] J. S. Curtis and B. van Wachem. "Modeling particle-laden flows: A research outlook". In: *AIChE Journal* 50.11 (2004), pp. 2638–2645. DOI: 10.1002/aic.10394.
- [209] A. V. Nguyen. "Hydrodynamics of liquid flows around air bubbles in flotation: a review". In: *International Journal of Mineral Processing* 56.1-4 (1999), pp. 165–205. DOI: 10.1016/s0301-7516(98)00047-7.

- [210] M. Robbins. *The Collector's Book of Fluorescent Minerals*. Springer, Boston, MA, 1983.
- [211] M. S. Helmberger, M. K. Frame, and M. Grieshop. "Counterstaining to Separate Nile Red-Stained Microplastic Particles from Terrestrial Invertebrate Biomass". In: *Environmental Science & Technology* 54.9 (2020), pp. 5580–5588. DOI: 10.1021/acs.est.0c00711.
- [212] E.-C. Gabriel, I. G. Matthew, C. T. Richard, and A. C.-O. Joseph. "Lost, but Found with Nile Red: A Novel Method for Detecting and Quantifying Small Microplastics (1 mm to 20  $\mu\text{m}$ ) in Environmental Samples". In: *Environmental Science & Technology* 51.23 (2017), pp. 13641–13648. DOI: 10.1021/acs.est.7b04512.
- [213] T. Maes, R. Jessop, N. Wellner, K. Haupt, and A. G. Mayes. "A rapid-screening approach to detect and quantify microplastics based on fluorescent tagging with Nile Red". In: *Scientific Reports* 7 (2017), p. 44501. DOI: 10.1038/srep44501.
- [214] C. Ball, H. Fellouah, and A. Pollard. "The flow field in turbulent round free jets". In: *Progress in Aerospace Sciences* 50 (2012), pp. 1–26. DOI: 10.1016/j.paerosci.2011.10.002.
- [215] S. Grossmann, D. Lohse, and C. Sun. "High-Reynolds Number Taylor-Couette Turbulence". In: *Annual Review of Fluid Mechanics* 48.1 (2016), pp. 53–80. DOI: 10.1146/annurev-fluid-122414-034353.
- [216] P. Wang, J. J. Cilliers, S. J. Neethling, and P. R. Brito-Parada. "The behavior of rising bubbles covered by particles". In: *Chemical Engineering Journal* 365 (2019), pp. 111–120. DOI: 10.1016/j.cej.2019.02.005.
- [217] J. Sygusch and M. Rudolph. "A contribution to wettability and wetting characterisation of ultrafine particles with varying shape and degree of hydrophobization". In: *Applied Surface Science* 566 (2021), p. 150725. DOI: 10.1016/j.apsusc.2021.150725.
- [218] T. Lappan, M. Sarma, S. Heitkam, P. Trtik, D. Mannes, K. Eckert, and S. Eckert. "Neutron radiography of particle-laden liquid metal flow driven by an electromagnetic induction pump". In: *Magnetohydrodynamics* 56.2-3 (2020), pp. 167–176. DOI: 10.22364/mhd.56.2-3.8.
- [219] G. Buckton. "Contact angle, adsorption and wettability — a review with respect to powders". In: *Powder Technology* 61.3 (1990), pp. 237–249. DOI: 10.1016/0032-5910(90)80090-1.
- [220] D. H. Kaelble. "Dispersion-Polar Surface Tension Properties of Organic Solids". In: *The Journal of Adhesion* 2.2 (1970), pp. 66–81. DOI: 10.1080/0021846708544582.
- [221] D. K. Owens and R. C. Wendt. "Estimation of the surface free energy of polymers". In: *Journal of Applied Polymer Science* 13.8 (1969), pp. 1741–1747. DOI: 10.1002/app.1969.070130815.
- [222] W. Rabel. "Einige Aspekte der Benetzungstheorie und ihre Anwendung auf die Untersuchung und Veränderung der Oberflächeneigenschaften von Polymeren". In: *Farbe u. Lack* 77 (1971), pp. 997–1006.
- [223] N. Henze. *Stochastik für Einsteiger*. 7th ed. Vieweg+Teubner, 2008.



# Statement of authorship

I hereby certify that I have authored this document entitled *The role of turbulence on the bubble-particle collision – An experimental study with particle tracking methods* independently and without undue assistance from third parties. No other than the resources and references indicated in this document have been used. I have marked both literal and accordingly adopted quotations as such. During the preparation of this document I was only supported by the following persons:

- Prof. Dr. rer. nat. et Ing. habil. Kerstin Eckert
- Dr.-Ing. Sascha Heitkam

Additional persons were not involved in the intellectual preparation of the present document. I am aware that violations of this declaration may lead to subsequent withdrawal of the academic degree.

Dresden, 14.01.2022

Anna-Elisabeth Sommer